UNIVERSITÀ DEGLI STUDI DI PAVIA

DEPARTMENT OF MATHEMATICS "FELICE CASORATI"

JOINT PhD PROGRAM IN MATHEMATICS PAVIA – MILANO BICOCCA – INdAM

Thesis submitted for the degree of Dottore di Ricerca

Mathematical Models for Chromonic Liquid Crystals

Supervisor
Prof. Epifanio G. Virga

Doctoral Dissertation of
Silvia Paparini

October, 2021

Contents

Acknowledgements

Abstract

This dissertation is concerned with a peculiar class of lyotropics: chromonic liquid crystals (CLCs). These are formed by certain dyes, drugs, and short nuclei acid oligomers in aqueous solutions [74, 23, 120, 76, 138, 84, 36]. Dyes, drugs, and DNA oligomers are the most common examples. Since these solutions are present where most normal biological processes take place, it is no wonder that CLCs have become of interest for possible applications in medical sciences. But this is not the only reason that makes them special (or rather unique). Aggregation of CLCs starts at very low concentrations and the aggregates are columns, although with variants [74]. Some of them are stacks of single flat molecules, others have more than a molecule in their cross-sections [92]. These might seem to be minor details, but they may have momentous consequences at the macroscopic scale [43]. More specifically, CLC molecules are typically plank-shaped with aromatic cores and polar groups on their peripheries [93]. They tend to stack face-to-face and their aggregates order into a fluid nematic (N) phase or (for high concentrations or low temperatures) even in a solid-like medium (M) phase, where columns are organised parallel to one another with their centres arranged in an hexagonal pattern [74]. It is the variability in size and shape of the supra-molecular columns that makes CLCs so unique: a change in the distribution of size in the assembly affects the elastic energy term favouring twist in a way that will be clear below.

Chromonics in the nematic phase enjoy the head-tail symmetry, that is, they are non-chiral materials with a tendency for their constitutive elements (the columns of assembled molecules described above) to bundle together so that a director n (or, more generally, an order tensor) can be defined at a mesoscopic scale and lacks polarity. Such a uniaxiality is also the optical signature of the material and reveals the fascinating textures that the director can exhibit in confined geometries.

The ground state of ordinary nematic liquid crystals, that is, a configuration into which the liquid crystal naturally relaxes when neither external actions nor anchoring conditions affect its orientation, is attained when n is uniform in space, i.e., when the director is the same everywhere and no distortion is to be seen at all. Central to this dissertation is that when CLCs are confined in capillary cylinders with degenerate boundary conditions (i.e. n is bound to be tangent to the boundary, but free to orient in any direction) that would be compatible with the uniform alignment of the director along the cylinder's axis, then they are instead observed to acquire a nonuniform arrangement [55, 56, 19, 86]. In particular, their ground state in a cylindrical capillary, often referred to as the *escaped twist* (ET) field [19], is two-fold; it consists of two symmetric twisted configurations (left- and right-handed), each variant occurring with the same likelihood, as was to be expected from the lack of chirality in the molecular aggregates that constitute these materials. Despite the clear indication that CLCs in three-dimensional space exhibit a different behaviour from common nematic liquid crystals, the Oseen-Frank theory for nematics has been applied to rationalize the experiments with capillary tubes and so to determine the configuration of the ET field. This is a variational theory which posits a free-energy density quadratic in the director gradient that penalizes all distortions of n away from a uniform alignment (in whatever direction). Four basic distortions are classically identified, which correspond to four independent elastic constants; these are the splay (K_{11}), twist (K_{22}), bend (K_{33}), and saddle-splay (K_{24}) constants [127], which have recently been re-interpreted in a new light [114]. This latter reinterpretation is of interest in this thesis since it goes beyond the usual representation of the saddle-splay contribution only in terms of surface elasticity.

Ericksen's inequalities [30] ensure that Oseen-Frank's energy density is positive definite, and the spontaneous emergence of chirality in the nematic texture is not conceivable when they hold. Thus, as expected, Oseen-Frank's elastic theory justifies the observed configurations of CLCs under cylindrical confinement only if the relevant Ericksen's inequality, $K_{22} \geq K_{24}$, is violated, and so only if Oseen-Frank's free-energy functional is unbounded below in $3D$ Euclidean space. Indeed, the configuration they fall in (first found in [10]) is an equilibrium one only if that inequality is violated. The alternative form of the Oseen-Frank's free-energy density proposed in [114] distributes the saddle-splay contribution in the other elastic modes. In so doing, the pure twist corresponds to the elastic constant $(K_{22} - K_{24})$ (instead of only K_{22}) and it is termed *double twist*, as it has no characteristic direction in the plane perpendicular to n. The negativity of $(K_{22} - K_{24})$ suggests that the pure *double-twisted configuration*, where only the double twist mode is excited, should be the ground state of CLCs in $3D$ space. Unfortunately, this peculiar director field does not belong to any of the families of uniform director fields [128], and so it cannot fill $3D$ Euclidean space; this ideal state is only attainable along a $1D$ curve and produces elastic frustration if requested to occupy a particular geometry with particular boundary conditions. As a result, extending the ideal double-twisted texture to a tubular region introduces by necessity a non-uniform texture which

results from the combination of other fundamental deformation modes with pure double twist only along the axis of the cylinder. This is precisely the ET field experimentally observed for CLCs in cylindrical capillaries subject to degenerate boundary conditions. Taking for granted that the ground state of CLCs is an ideal (unattainable), pure double-twist, we may say that the ET field is actually a 'pseudo-ground state' since it is the result of the confinement-induced extension of the pure double twist, which induces elastic frustration in the system. The following questions then arise: Is anything wrong in applying Oseen-Frank's elastic theory to these materials? Do we need a new elastic theory for CLCs?

It follows from the geometric representation in [66] for the energy term K_{24} when $\boldsymbol{n}$ is required to obey planar anchoring conditions on the boundary that even when one of the Ericksen's inequalities involving K_{24} is violated, as in this case, the stored Oseen-Frank's energy is bounded below as long as the elastic constants K_{11}, K_{22}, and K_{33} are all non-negative. Hence, hardly confining boundary conditions could ensure the existence of the minimum also when the free-energy functional is unbounded below. It can thus be legitimate to apply Oseen-Frank's theory to this particular class of materials under confinement when $K_{22} < K_{24}$. In particular, the local stability of ET field is established in this thesis through a general formula for the second variation of the free-energy functional. But, does this really always suffice? Even for free-boundary conditions? To resolve these issues, this thesis takes two converging avenues. It studies problems of CLC drops surrounded by an isotropic liquid to illuminate the role played by K_{24} in Oseen-Frank's theory; it examines the consequences of the violation of Ericksen's inequality $K_{22} \geq K_{24}$ to ascertain whether they are all harmless. The ultimate conclusion is that Oseen-Frank's free-energy is not apt to describe the elasticity of CLCs because it entails paradoxes that arise if above Ericksen's inequality is violated.

This is not only a destructive thesis; it also proposes an amendment to the Oseen-Frank's theory, in the form of a quartic correction to the free-energy density, which promises to reinterpret correctly all experimental findings without leading to any paradox.

The outline of this dissertation is as follows. The first chapter provides an introduction to the classical Oseen-Frank's theory intended for nematic liquid crystals and applied so far to chromonic liquid crystals as well. It also provides the theoretical background for the subsequent explorations. The Chapter ends with the illustration of the ET equilibrium configurations. A re-interpretation of them in terms of characteristic distortions and elastic frustration is addressed.

Four Chapters then follow about specific projects of my research; Chapter 2 and part of Chapter 3 have already been published, [99, 100].

The variational problem of determining the optimal shape of a nematic droplet surrounded by the nematic phase is formidable and has only been attacked in selected classes of shapes and director fields. In Chapter 2, by considering a special class of admissible solutions for a bipolar droplet, we study how the prevalence of a shape is affected by a dimensionless measure α of the drop's volume and the ratios of the saddle-splay constant K_{24} and the bending constant K_{33} to the splay constant K_{11}. Our class of shapes (and director fields) is sufficiently different from those employed so far to unveil a rather different role of K_{24}. Chapter 2 is not intended exclusively for chromonic liquid crystals, but it is primarily concerned with bipolar tactoids and with how they prevail over other possible equilibrium shapes. Here, we focus only on the untwisted bipolar configurations; the twist term in the elastic free-energy density vanishes identically.

In Chapter 3 we adapt the theory presented in Chapter 2 to confined two-dimensional systems; here too twist is suppressed by symmetry. These are chromonic drops squeezed between two parallel plates [63, 136]. In these systems no twist can reside in the drops (neither single nor double [114]), and so Oseen-Frank's theory suffices. Here we solve the free-boundary variational problem that has the shape of the drop as main unknown and try and use the solution to fit experiments and collect enough data to afford a reliable measure of the surface tension at the interface between various CLCs and their isotropic melt, for which there are but controversial estimates [63, 82]. This latter estimate is then employed to provide a measure of the anchoring strength at the nematic-polymer interface, when the substrates squeezing the drop are patterned with sub-micron scale line channels (with the bottom and the top channels parallel to each other) and the droplet's long axis is aligned well to the channels.

The second part of the thesis is illustrated in Chapters 4, 5 and 6. In Chapter 4 we take for granted that Oseen-Frank's theory is suitable to describe the elastic properties of CLCs and we start to examine the consequences that would arise in cylindrical symmetry (in connection with Burylov's solutions [10]) if the relevant Ericksen's inequality, $K_{22} \geq K_{24}$, is violated. The geometric frustration and the characteristic of non-universality of the ET equilibrium configurations likely to characterize the two-fold ground state

of CLCs within Oseen-Frank's theory are shown to be locally stable. This is achieved through a general formula for the second variation of the free-energy functional. We substantiate the claim that the ET configurations arise from the elastic frustration of the ideal double-twist configuration when requested to occupy the cylinder and to obey degenerate boundary conditions. It is the desire to relax this elastic frustration that inspires Chapter 5. Indeed, although ET configurations realize the minimum of Oseen-Frank's energy in a cylinder, two paradoxes arise in cylindrical symmetry if $K_{22} < K_{24}$. In particular we construct a sequence of configurations $(\mathscr{B}_k, \boldsymbol{n}_k)$, where $\mathscr{B}_k$ is the region in space occupied by a CLC with fixed volume, such that the limiting value of the free-energy as $k \to \infty$ diverges to $-\infty$. Moreover, a second paradox arises by inserting inside a given cylinder another hollow cylinder of smaller radius. The new configuration into which the nematic director relaxes has a discontinuity on the material surface which separates the two regions into which the larger cylinder is divided, but the minimum energy of the resulting system is less than the energy of the original system, making one wonder where the missing energy has gone.

The thesis ends in Chapter 6 with the proposal of a quartic free-energy which promotes a double-twist configuration as ground state to avoid the shortcomings of the existing theory. Since this spontaneous state is not uniform, a characteristic length a of molecular order is thus introduced in the model which measures the extension over which the equilibrium distortion is affected. More precisely, the spontaneous state could be attained unfortunately only in the ideal case of a cylinder subject to planar anchoring conditions whose radius is considerably smaller than a; otherwise, the confinement prevents the realization of the spontaneous value of the double twist. The new theory has the advantage of avoiding the paradoxes presented in Chapter 5 and to reproduce faithfully the experiments on CLCs under cylindrical confinements.

Chapter 1

Introduction to Chromonics

Liquid crystals are *mesophases*, that is, intermediate states of matter which may flow like a liquid, but have also properties of solid crystals: they are constituted by basic mesogens, which may either be molecules or molecular assemblies (that is, supra-molecular constructs), oriented in a crystal-like way. Indeed, the existence of these mesophases is due to a particular organization of the orientation of their constituents when they pass from a crystalline ordered arrangement, typical of a solid, to a disordered organization, typical of a liquid. The liquid crystal phases are characterized by orientational order of their mesogenic units with, in some cases, a limited amount of positional order, so that liquid crystals are *anisotropic fluids*[127].

There are essentially two distinct ways to induce the liquid crystalline phase in a *mesogenic substance*, an organic substance in which there could be the onset of a mesophase, namely by changing its temperature or its concentration in a solvent. Systems in which an ordered phase is induced by reducing the temperature of the isotropic fluid phase are called *thermotropic*. In these materials, the mesogenic units are single molecules. There is another class of liquid crystals, those in which the mesogenic units are molecular assemblies in a solvent, and concentration is the driving parameter for ordering. These are called *lyotropic*. Thermotropic liquid crystals are used in man-made displays, whereas lyotropic liquid crystals are found in detergents and living organisms like [92].

This dissertation is concerned with a very peculiar class of lyotropics: *chromonic liquid crystals* (CLCs). These are formed by certain dyes, drugs, and short nucleic acid oligomers in aqueous solutions[74, 23, 120, 76, 138, 84, 36]. Since these solutions are where most biological processes take function normally, it is no wonder that CLCs have become of interest for possible applications in medical sciences. But this is not the only reason that makes them special (or rather unique)[1]

In conventional amphiphile/water systems, the temperature/composition phase diagrams are often complex—and can show a wide range of patterns of aggregation—spherical micelles, cylindrical columns, layered structures complex cubic phases—with the additional factor of there being both oil-in-water and water-in-oil inverse structures. What perhaps distinguishes CLCs is that aggregation starts at very low concentrations and that aggregates are columns, although with variants [74]. Some are stacks of single molecules, others have more than a molecule in their cross-sections [92]. These might seem to be minor details, but they may have momentous consequences at the macroscopic scale [43].

More specifically, CLC molecules are typically plank-shaped with aromatic cores and polar groups on their peripheries [93]: dyes, drugs, and DNA oligomers are the most common examples. They tend to stack face-to-face and their aggregates order into a fluid nematic (N) phase or (for higher concentrations or lower temperatures) even in a solid-like medium (M) phase, where

---

[1]A number of informative, updated reviews are available on this topic [72, 73, 74, 24].

columns are organised parallel to one another with their centres arranged in an hexagonal pattern [74]. While the former is just the analogue of the nematic phase in ordinary thermotropics, the latter is the analogue of the columnar phase in discotic thermotropic (for this reason, it is also termed as C phase).

It is the variability in size and shape of the supra-molecular columns that makes CLCs so unique. The aggregation process is *isodesmic*, because the energy gain in adding a unit to a pre-existing column with at least two units (typically between 5 and 10 kT) does not depend on the length of the column[2]. Equilibrium is reached by minimising the free-energy, where entropy counteracts internal energy. The isodesmic nature of the process results in a broad length column distribution, which is prone to the action of temperature. When the temperature is increased, the mean length is expected to shift towards smaller values, so that the concentration of longer assemblies decreases, while that of shorter ones increases. This is reflected by the elastic properties of the phase, in a way that ordinary lyotropics do not exhibit [93]. Especially, this change in the distribution of assembly size affects the elastic energy terms resisting and favouring twist in a way that will be clear below. Further increasing the temperature results into a first order nematic-isotropic transition with a wide coexistence region (5-10 °C). Conversely, when the temperature is decreased, short, disordered columns in the isotropic phase tend to grow and aggregate, eventually separating from the parent isotropic solution to form islands of ordered phase. As customary, the nematic phase is described by the nematic director field $\boldsymbol{n}$, the mesoscopic unit vector field designating the local average orientation of the elementary constituents of the phase. Chapters 2 and 3 address the study of free-boundary problems for bipolar droplets of nematic phase surrounded by an isotropic environment.

The elastic vulnerability of CLCs previously described manifests itself in spontaneous injections of chirality in the nematic director texture, with its characteristic optical signature, in the absence of molecular chirality [25]. Contrarily, in the absence of any external field the orienting interactions would incline the average orientation of the constitutive elements of a NLC to be uniform in space. In the classical theory of liquid crystal elasticity as formulated for general NLCs by Oseen [97] and Frank [38], the distortional cost associated with the nematic ground state is everywhere zero, and all other states, which have a non-vanishing gradient $\nabla \boldsymbol{n}$, are distorted. What is wrong with the application of this theory, built on a notion of undistorted ground state, to CLCs (as done so far) and why we do need a new theory for this class of materials? The answer to these questions lies in the second part of this thesis, which consists in Chapters 4, 5 and 6, with the proposal of a quartic theory to avoid the shortcomings of the existing one. The new theory intended for CLCs describes their assumed ground state and reproduce the experiments.

1.1 Preliminaries

The continuum theory of liquid crystals is a variational theory based on the works of Oseen [97] and Zocher [144]. A free-energy functional is posited and, since the temperature is taken as given throughout our development, such a functional is indeed the Helmholtz free-energy. In this first Chapter, we outline the classical Oseen-Frank's theory intended for nematic and cholestic liquid crystals and applied so far to chromonic liquid crystals; it has been around for some time already [38]. This theory constitutes a solid basis for the successive investigations and represents the framework for our subsequent development. We also recall in Sec. 1.1.2 alternative form of Oseen-Frank's free-energy density intended for nematics proposed in [114]; it is of interest in this dissertation since demystifies some implications of the saddle-splay contribution, often only considered as surface elasticity. In [128] this thread is taken up to characterize uniform

---

[2]Computer atomistic simulations [12] have shown that this is indeed an acceptable approximation.

distortions. There exist only two families of them and any other director field would be geometrically frustrated and become by necessity non uniform if requested to occupy the whole space. Especially, the application of Oseen-Frank's theory to CLCs suggests that the ground state of CLCs is a characteristic double twist, a distortion field that cannot cover uniformly the whole space and thus induces spatial frustration in the system. We recall in Sec. 1.1.3 the notion of interfacial energy; when a droplet is surrounded by an isotropic fluid the Oseen-Frank elastic energy, which accounts for distortions in bulk, does not suffice to describe the whole energetic landscape. A surface energy at the interface separating the droplet from the surrounding fluid must also be included. Chapters 2, 3 and 5 elaborate on this notion. The equilibrium equations, in both weak and strong forms, of the free-energy functional are given in section 1.1.4 when the region $\mathscr{B}$ has been taken as given in deriving them. These equations apply to most situations that we encounter in this thesis; especially, Chapter 4 addresses questions of the stability of the free-energy functional at an equilibrium configuration. Finally, in Sec. 1.2 we find within Oseen-Frank theory the equilibrium configurations with opposite chirality that CLCs fall in (first found in [10]) when they are confined in a cylindrical cavity. These configurations are re-interpreted in terms of the distortion characteristics recalled in 1.1.2 with considerations on their elastic frustration.

1.1.1 Frank's Formula

In 1922 G. Friedel [39] proposed to classify liquid crystals into three wide categories according to the molecular organization intermediate between different types of order, which he called *nematic*, *cholesteric* and *smectic*. Of particular interest in this thesis is the nematic liquid crystalline phase.

The constitutive elements of both nematic and cholesteric liquid crystals enjoy the head-tail symmetry, which implies that if head and tail are exchanged, then their interaction with the neighbouring molecules remain unaffected. For cholesteric liquid crystals this property cannot be phrased in terms of mirror symmetry as for nematics, since reflections reverse the chirality characteristic of their molecules which resemble helical springs[3].

The basic mesogens of nematic and cholesteric liquid crystals possess orientational and not positional ordering, and the crystalline phase manifests itself when the interaction between them tends to make them parallel to one another so as to induce a partial orientational order at the microscopic scale. We suppose that the liquid crystal occupies a region $\mathscr{B}$ and the nematic and cholesteric phases are described by the vector field $\boldsymbol{n} : \mathscr{B} \to \mathbb{S}^2$, where $\mathbb{S}^2$ is the unit sphere in $\mathbb{R}^3$, which associates the vector $\boldsymbol{n}(p)$ to the point p, where $\boldsymbol{n}(p)$ is the average orientation of the elementary constituents that make up the macroscopic particle at $p \in \mathscr{B}$.

The spatial distortion of a director field $\boldsymbol{n}$ is measured by its gradient $\nabla \boldsymbol{n}$ and the classical theory takes the bulk free-energy, also called the *elastic free-energy*, of nematic and cholesteric liquid crystals as given by the following functional

$$\mathscr{F}_{\mathrm{b}}[\mathscr{B}, \boldsymbol{n}] := \int_{\mathscr{B}} W(\boldsymbol{n}, \nabla \boldsymbol{n}) \, \mathrm{d}V, \tag{1.1}$$

where V is the volume measure and $\mathscr{B}$ is to be regarded as a variable when the region occupied by the liquid crystal is unknown. W is the *elastic free-energy density* (per unit volume) and it must obey a list of requirements that represent the main physical features of the materials we intend to model. More precisely, W must be *frame-indifferent*, *even* and *positive definite*. The frame-indifference states that $W(\mathsf{Q}\boldsymbol{n}, \mathsf{Q}\nabla\boldsymbol{n}\mathsf{Q}^{\mathrm{T}}) = W(\boldsymbol{n}, \nabla\boldsymbol{n})$ for any orthogonal tensor $\mathsf{Q} \in \mathsf{O}(3)$, property which ensures that the free-energy for unit volume is the same in any two

---

[3]Expressed differently, exchanging head and tail of a helix by a rotation leaves it unchanged.

frames. The head to tail symmetry demands $\boldsymbol{n}$ to be equivalent to $-\boldsymbol{n}$ and so W is even, i.e. $W(-\boldsymbol{n}, -\nabla\boldsymbol{n}) = W(\boldsymbol{n}, \nabla\boldsymbol{n})$. The latter request of positive definiteness deals with the fact that the functional measures the cost associated with producing a distortion in a natural state, that is a configuration into which the liquid crystal naturally relaxes when neither external actions nor anchoring conditions affect its orientation and to which zero distortional cost is associated. Especially, the ground state of nematics is attained when $\boldsymbol{n}$ is uniform in space, and so $\nabla\boldsymbol{n}$ is zero, while the characteristic natural orientation of cholesterics possesses a uniform twist which can be described by the following formula[4]

$$\boldsymbol{n}_c := \cos(q_0 x_3 + \varphi_0)\boldsymbol{e}_1 + \sin(q_0 x_3 + \varphi_0)\boldsymbol{e}_2, \tag{1.2}$$

where $\boldsymbol{e}_1$ and $\boldsymbol{e}_2$ are unit vectors of a frame $(\boldsymbol{e}_1, \boldsymbol{e}_2, \boldsymbol{e}_3)$ such that $\boldsymbol{e}_3 = \boldsymbol{e}_1 \times \boldsymbol{e}_2$ and x_3 is the coordinate along it. Here, φ_0 is an angle in the interval $[0, 2\pi)$ depending only on the frame of reference employed, while the *twist* q_0 is a material modulus depending on the temperature in a way which is characteristic of each cholesteric liquid crystal. The tip of the vector in (1.2) describes a helix which winds around the *cholesteric axis* $\boldsymbol{e}_3$; it rotates clockwise if q_0 is positive, counterclockwise if it is negative. The distance between any two adjacent spirals is the *natural pitch* and is defined as $P := 2\pi/|q_0|$. When q_0 vanishes, the liquid crystal becomes nematic and the field defined by (1.2) accordingly reduces to a constant.

The simplest formula for $W(\boldsymbol{n}, \nabla\boldsymbol{n})$ was put forward by Frank [38]: it is the most general quadratic expression in $\nabla\boldsymbol{n}$ invariant under rotations and complying with the nematic symmetry, embodied by the director reversion, $\boldsymbol{n} \to -\boldsymbol{n}$. It is given by[5]

$$f_{\text{OF}}(\boldsymbol{n}, \nabla\boldsymbol{n}) = \frac{1}{2}K_{11}(\operatorname{div}\boldsymbol{n})^2 + \frac{1}{2}K_{22}(\boldsymbol{n} \cdot \operatorname{curl}\boldsymbol{n} + q_0)^2 + \frac{1}{2}K_{33}|\boldsymbol{n} \times \operatorname{curl}\boldsymbol{n}|^2 +$$
$$+ K_{24}\left[\operatorname{tr}(\nabla\boldsymbol{n})^2 - (\operatorname{div}\boldsymbol{n})^2\right], \tag{1.3}$$

where q_0 is the natural twist of cholesterics previously introduced and which vanishes for nematics, while K_{11}, K_{22}, K_{33}, and K_{24} are Frank's elastic constants and are material moduli characteristic of each liquid crystal. They are often referred to as the *splay, twist, bend,* and *saddle-splay* elastic constants, respectively, since they are interpreted by producing four different orientation fields, each with a distortion energy which is proportional to only one of the terms present in equation (1.3) when $q_0 = 0$. While K_{11}, K_{22} and K_{33} can be independently excited, the K_{24} elastic constant is different from the others since we can only exhibit an orientation field whose energy density is just approximately proportional to it in a neighbourhood of a point in space. Moreover, as we will see below, the K_{24} term is a *null Lagrangian*, which can be converted into a surface integral over the boundary $\partial\mathscr{B}$ of the domain occupied by the liquid crystal, not contributing to the equilibrium equation in the bulk for the energy functional. The constants K_{11}, K_{22} and K_{33} are instead genuine bulk terms. The saddle-splay term can be written in a number of equivalent forms (see e.g. [65, Ch. 5]),[6]

$$\operatorname{tr}(\nabla\boldsymbol{n})^2 - (\operatorname{div}\boldsymbol{n})^2 = \operatorname{div}\left((\nabla\boldsymbol{n})\boldsymbol{n} - (\operatorname{div}\boldsymbol{n})\boldsymbol{n}\right) = -\operatorname{div}\left((\operatorname{div}\boldsymbol{n})\boldsymbol{n} + \boldsymbol{n} \times \operatorname{curl}\boldsymbol{n}\right), \tag{1.4}$$

---

[4]Any other natural orientations for a given cholesteric liquid crystal is obtained by taking a different phase φ_0 and instead of $\boldsymbol{e}_3$ $\boldsymbol{Q}\boldsymbol{e}_3$ for $\boldsymbol{Q}$ a rotation.

[5]Here 'tr' denotes the *trace* of a (second-rank) tensor: in Cartesian components, $\operatorname{tr}(\nabla\boldsymbol{n})^2 = n_{i,j}n_{j,i}$, with the usual convention of summing over repeated indices. Recently, a different modal decomposition has been put forward for f_{OF} [114], which has also been given a graphical representation in terms of an *octupolar* (third-rank) tensor [103]. Such a novel decomposition, however, is not particularly germane to the topic at hand, and so here we shall stick to tradition.

[6]An instructive way to relate the saddle-splay energy to splay and twist energies was also offered by Nehring and Saupe [87, 88]. In a Cartesian frame where $\boldsymbol{n} = \boldsymbol{e}_3$ and the matrix $n_{i,j}$, with $n_{3,j} = 0$, represents $\nabla\boldsymbol{n}$, $(\operatorname{div}\boldsymbol{n})^2 = (n_{1,1} + n_{2,2})^2$ and $(\boldsymbol{n} \cdot \operatorname{curl}\boldsymbol{n})^2 = (n_{1,2} - n_{2,1})^2$, while $\operatorname{tr}(\nabla\boldsymbol{n})^2 - (\operatorname{div}\boldsymbol{n})^2 = -2(n_{1,1}n_{2,2} - n_{1,2}n_{2,1})$.

which also reveal its nature of a null Lagrangian, as an integration over the bulk reduces it to a surface energy,

$$\int_{\mathscr{B}} \left(\operatorname{tr}(\nabla \boldsymbol{n})^2 - (\operatorname{div} \boldsymbol{n})^2 \right) \mathrm{d}V = \int_{\partial \mathscr{B}} \left((\nabla_{\mathrm{s}} \boldsymbol{n})\boldsymbol{n} - (\operatorname{div}_{\mathrm{s}} \boldsymbol{n})\boldsymbol{n} \right) \cdot \boldsymbol{\nu} \, \mathrm{d}A, \tag{1.5}$$

where $\boldsymbol{\nu}$ is the outer unit normal to $\partial \mathscr{B}$, A is the area measure, ∇_{s} denotes the surface gradient and $\operatorname{div}_{\mathrm{s}}$ the surface divergence [29]. In particular, as pointed out in [66], (1.5) has an interesting consequence when (as will be done in the thesis) $\boldsymbol{n}$ is required to obey the *degenerate* boundary condition on $\partial \mathscr{B}$[7],

$$\boldsymbol{n} \cdot \boldsymbol{\nu} \equiv 0. \tag{1.6}$$

Since (1.6) implies that $(\nabla_{\mathrm{s}} \boldsymbol{n})^{\mathsf{T}} \boldsymbol{\nu} = -(\nabla_{\mathrm{s}} \boldsymbol{\nu})\boldsymbol{n}$, where $\nabla_{\mathrm{s}} \boldsymbol{\nu}$ is the (symmetric) curvature tensor of $\partial \mathscr{B}$, it follows from (1.5) that

$$\int_{\mathscr{B}} \left(\operatorname{tr}(\nabla \boldsymbol{n})^2 - (\operatorname{div} \boldsymbol{n})^2 \right) \mathrm{d}V = - \int_{\partial \mathscr{B}} (\kappa_1 n_1^2 + \kappa_2 n_2^2) \, \mathrm{d}A, \tag{1.7}$$

where κ_1 and κ_2 are the principal curvatures of $\partial \mathscr{B}$ and n_1 and n_2 are the components of $\boldsymbol{n}$ along the corresponding principal directions of curvature. Thus, for $K_{24} \geqq 0$, the saddle-splay energy would by itself induce $\boldsymbol{n}$ to align along the direction with *maximum* (signed) curvature.[8] We shall see in Chapter 2 that this surface feature is key to the role played by K_{24} in determining the population of different droplet shapes, while in Chapters 4, 5 and 6 it leads to an escaped twist ground state. Equation (1.3) will often be referred to as *Frank's formula*. When in (1.1) W is given by Frank's formula we call $\mathscr{F}_{\mathrm{b}}$ *Oseen-Frank's energy functional*.

As said above, the natural orientations in Oseen-Frank's theory represent on the same footing the ground state, and (1.1) attains its minimum on them, to which zero distortional cost is associated. Thus f_{OF} is required to be positive definite and for nematics for which $q_0 = 0$, this amounts to satisfy the so called Ericksen's inequalities [30]:

$$(K_{11} - K_{24}) > 0, \quad (K_{22} - K_{24}) > 0, \quad K_{33} > 0, \quad K_{24} > 0. \tag{1.8}$$

1.1.2 Selinger's Decomposition

Recently, a different modal decomposition has been put forward for f_{OF} by J. Selinger [114][9], who built on earlier work of T. Machon and G. P. Alexander, [75]. More precisely, the starting point of the decomposition of f_{OF} in independent elastic modes is a new decomposition of $\nabla \boldsymbol{n}$,

$$\nabla \boldsymbol{n} = -\boldsymbol{b} \otimes \boldsymbol{n} + \frac{1}{2} T \boldsymbol{W}(\boldsymbol{n}) + \frac{1}{2} S \boldsymbol{P}(\boldsymbol{n}) + \boldsymbol{D}. \tag{1.9}$$

Here $\boldsymbol{W}(\boldsymbol{n})$ denotes the skew-symmetric tensor associated with $\boldsymbol{n}$[10] and $\boldsymbol{P}(\boldsymbol{n}) = \mathbf{I} - \boldsymbol{n} \otimes \boldsymbol{n}$ is the projector onto the plane orthogonal to $\boldsymbol{n}$, while the vector $\boldsymbol{b} := -(\nabla \boldsymbol{n})\boldsymbol{n} = \boldsymbol{n} \times \operatorname{curl} \boldsymbol{n}$ is the bend, the pseudoscalar $T := \boldsymbol{n} \cdot \operatorname{curl} \boldsymbol{n}$ is the twist, the scalar $S := \operatorname{div} \boldsymbol{n}$ is the splay and $\boldsymbol{D}$ is a symmetric tensor such that $\boldsymbol{D}\boldsymbol{n} = \boldsymbol{0}$ and $\operatorname{tr} \boldsymbol{D} = 0$. Accordingly, when $\boldsymbol{D} \neq \boldsymbol{0}$ it can be given the form

$$\boldsymbol{D} = q \left(\boldsymbol{n}_1 \otimes \boldsymbol{n}_1 - \boldsymbol{n}_2 \otimes \boldsymbol{n}_2 \right) \tag{1.10}$$

---

[7]That is, when $\boldsymbol{n}$ is bound to be tangent to the boundary, but oriented in any direction.

[8]In [66], the curvature tensor of $\partial \mathscr{B}$ is defined as $-\nabla_{\mathrm{s}} \boldsymbol{n}$, so that the principal curvatures κ_i have opposite signs and (1.7) turns into orienting $\boldsymbol{n}$ along the direction with *minimum* (signed) curvature, see also [102].

[9]A graphical representation of this modal decomposition in terms of an *octupolar* tensor has been given in [103]

[10]$\boldsymbol{W}(\boldsymbol{n})$ acts on any vector $\boldsymbol{v}$ as a cross product, i.e. $\boldsymbol{W}(\boldsymbol{n})\boldsymbol{v} = \boldsymbol{n} \times \boldsymbol{v}$

where q is the positive eigenvalue of $\boldsymbol{D}$, and this choice of sign for q identifies (to within a sign) the eigenvectors $\boldsymbol{n}_1$ and $\boldsymbol{n}_2$ orthogonal to $\boldsymbol{n}$. Selinger [114] has proposed to call q the biaxial splay to emphasize the similarity of this deformation mode with the symmetry of a biaxial nematic phase[11]; however when the equivalence between $\pm\boldsymbol{n}$ is considered, an even better term might be *tetrahedral splay* [115], which represents the full symmetry of the deformation; indeed, this deformation has the symmetry of a tetrahedron, which splays outward in one direction with respect to $\boldsymbol{n}$, and outward in the orthogonal direction with respect to $-\boldsymbol{n}$. Finally, the relation between the q mode and the symmetry properties of an *octupolar potential* on the unit sphere [41, 40, 103] justifies why hereafter we call q the *octupolar splay*. More precisely, an alternative representation for all modes but the double twist is offered by an even scalar-valued function on the unit sphere. This may have either four or three directions along which it attains a local maximum (conjugated to a local minimum in the apposite direction). The former arrangement, with four maxima falling on the vertices of a (possibly distorted) tetrahedron, signals the predominance of the q mode, whereas the arrangement with only three maxima signals the depression of that mode.

In this decomposition the *pure twist* and *pure splay* are reinterpreted as local configurations which are strictly uniaxial in the plane perpendicular to $\boldsymbol{n}$ (and therefore have only T and S non zero among the four modes). Especially, the pure splay S is a scalar, with one degree of freedom; it indicates how $\boldsymbol{n}$ tilts inward or outward, isotropically in the plane perpendicular to $\boldsymbol{n}$. Thus, a pure splay is indeed a double splay, in both directions perpendicular to $\boldsymbol{n}$[12]. The pure twist T is a pseudoscalar, with one degree of freedom and indicates how $\boldsymbol{n}$ changes in a right- or left-handed way, isotropically in the plane perpendicular to $\boldsymbol{n}$. Thus, a pure twist is indeed a double twist, since it has no characteristic direction in the plane perpendicular to $\boldsymbol{n}$. The canonical twist structure (e.g. $\boldsymbol{n}$ given in (1.2) and winding around a single fixed axes), is instead a mixture of pure (double) twist and biaxial splay.

The eigenvectors $\boldsymbol{n}_1$, $\boldsymbol{n}_2$, $\boldsymbol{n}$ of $\boldsymbol{D}$ are called the *distortion frame*. This can be defined for any sufficiently regular director field $\boldsymbol{n}$ and it changes from point to point, thus defining a movable frame. Since $\boldsymbol{b} \cdot \boldsymbol{n} = 0$, the bend vector $\boldsymbol{b}$ can be decomposed in the distortion frame as follows:

$$\boldsymbol{b} = b_1\boldsymbol{n}_1 + b_2\boldsymbol{n}_2. \tag{1.11}$$

Thus, seen from the distortion frame, the director field is locally characterized by the scalars (S, T, b_1, b_2, q), which depend on position in space and are called collectively *distortion characteristics* of the nematic director. The following identity, inferred from $\text{tr}\,\boldsymbol{D}^2 = 2q^2$, plays an important role in the theory,

$$2q^2 = \text{tr}(\nabla\boldsymbol{n})^2 + \frac{1}{2}T^2 - \frac{1}{2}S^2. \tag{1.12}$$

By its use we can give Oseen-Frank's energy density for nematics the equivalent form

$$f_{\text{OF}}(\boldsymbol{n}, \nabla\boldsymbol{n}) = \frac{1}{2}(K_{11} - K_{24})S^2 + \frac{1}{2}(K_{22} - K_{24})T^2 + \frac{1}{2}K_{33}B^2 + 2K_{24}q^2, \tag{1.13}$$

where $B^2 := \boldsymbol{b} \cdot \boldsymbol{b}$; the bend B indicates how $\boldsymbol{n}$ varies as one moves along the $\boldsymbol{n}$ direction. It is a vector in the plane perpendicular to $\boldsymbol{n}$. It has two degrees of freedom, because $\boldsymbol{n}$ may

---

[11]In this deformation mode $\boldsymbol{n}$ tips out-ward along one axis perpendicular to the local $\boldsymbol{n}$, and tips inward along the other axis perpendicular to the local $\boldsymbol{n}$, and so there is a combination of positive splay along one axis and negative splay along the other axis. The symmetry of this deformation is similar to a biaxial nematic liquid crystal, because of the two distinct axes perpendicular to $\boldsymbol{n}$

[12]It must be double splay because it is a scalar, which has no characteristic direction in the plane perpendicular to $\boldsymbol{n}$

change in either of the two directions perpendicular to $\boldsymbol{n}$. From (1.13), since (S, T, B, q) are all independent measures of distortions, it readily follows that f_{OF} is positive definite whenever Ericksen's inequalities (1.8) are satisfied. Accordingly, (1.13) admits as global minimizer the state

$$S = T = B = q = 0, \tag{1.14}$$

which corresponds to any constant field.

By (1.12), in (1.13), the standard K_{24} gets split into its constituent elements of splay, twist and biaxial splay and in so doing, converts the free-energy density into the sum of the squared of these four bulk modes. Thus, this not only reinterprets the notion of *pure twist* and *pure splay*, but it also reinterprets the saddle-splay contribution, often considered as surface elasticity, in terms of the sum of octupolar splay, double twist and double splay. Moreover, beyond its algebraic elegance, this decomposition is of interest since, as argued in [114], it demystifies some implications of the K_{24} in terms of purely elastic theory. Arguably it contributes to the stability of the blue phase, as well as to the spontaneous chirality in chromonic liquid crystals, which occurs for $K_{24} > K_{22}$ (as we will see below).

Based on this decomposition of orientation gradients, new questions arise about the compatibility of the Euclidean space with uniform distortions for the director field $\boldsymbol{n}$, which intuitively are director fields filling the whole space for which we could not tell where we are in space by sampling their local nematic distortion. To make this idea precise, they are the possible textures in $3D$ space that allow uniform gradient and thus whose distortion characteristics (S, T, b_1, b_2, q) are the same everywhere although the distortion frame my change from place to place. It was shown in [128] that there exist two families of *uniform director fields*: these families are realized by tipping the directors of a cholesteric up along its pitch axis by a constant angle; they are classified as follows and are distinguished by the sign of the twist:

$$S = 0, \; T = 2q, \; b_1 = b_2 = b, \tag{1.15a}$$

$$S = 0, \; T = -2q, \; b_1 = -b_2 = b, \tag{1.15b}$$

where q and b are constant assigned parameters.

1.1.3 Interfacial Energy

Like all lyotropic systems, CLCs have a large coexistence area in their phase diagram, where the ordered component can be surrounded at equilibrium by the isotropic one. When the liquid crystal comes in contact with the isotropic environment that surrounds it[13], as for the nematic tactoids discussed in Chapters 2 and 3, the bulk elastic energy distributed over $\mathscr{B}$ does not suffice to describe the whole energetic landscape. A surface energy at the interface separating the droplet from the surrounding fluid must also be included

$$\mathscr{F}_{\mathrm{s}}[\mathscr{B}, \boldsymbol{n}] = h \int_{\partial \mathscr{B}} \gamma_{\mathrm{a}} \, \mathrm{d}A; \tag{1.16}$$

there, an anisotropic surface tension γ_{a} which depends on the orientation of $\boldsymbol{n}$ relative to the outer unit normal $\boldsymbol{\nu}$ to $\partial \mathscr{B}$ comes into play and we assume that for a uniaxial nematic it is represented by the Rapini-Papoular formula [109]

$$\gamma_{\mathrm{a}} := \gamma \big(1 + \omega (\boldsymbol{n} \cdot \boldsymbol{\nu})^2 \big), \tag{1.17}$$

---

[13]This could either be the isotropic melt (or vapour) of the same substance (in thermotropic materials) or the isotropic component in phase-coexistence (in lyotropic materials).

where $\gamma > 0$ is the *isotropic* surface tension of the liquid crystal in contact with the isotropic solution and ω is a dimensionless *anchoring strength*.

We gave here the most elementary form of the interfacial energy; there exist symmetry allowed terms for either chiral or biaxial nematics that do not appear in the traditional Rapini-Papoular surface energy form, [48]. In particular, when the substrate in contact with the liquid crystal is regarded as consisting of 'frozen' liquid crystal molecules, chirality leads to the deviation at equilibrium from the rubbing direction. Generally, the alignment of the director at the interface depends on various intermolecular forces between the nematic liquid crystal and the surrounding melt (or the substrate), such as dispersion forces, i.e. van der Waals forces, dipolar interactions and steric interactions [51, 94].

Here we shall assume that $\boldsymbol{n}$ obeys degenerate boundary conditions (1.6) at the nematic/isotropic interface in agreement with the purely entropic argument of Onsager [95]. This model only accounts for steric, excluded-volume interactions between the particles constituting the phase and holds that at the interface particles would tend to lie parallel to the boundary of the droplet, as this would enhance their mutual sliding and so increase the entropy of the interface (a proper statistical model arriving at the same conclusion was also offered in [101]). Thus, at the nematic/isotropic interface, an orientation-dependent surface tension arises that favours the (degenerate) tangential orientation of $\boldsymbol{n}$ and we take ω to satisfy $\omega \geqq 0$, so that $\mathscr{F}_{\mathrm{s}}$ is minimized when $\boldsymbol{n}$ lies tangent to $\partial\mathscr{B}$.

As also shown in [105], for sufficiently small droplets, the assumption of tangential anchoring is untenable, as $\boldsymbol{n}$ tends to be uniform throughout $\mathscr{B}$, making (1.6) impossible (see also [127, Ch. 5]). A precise estimate that also involves the droplet's size and ω will be presented in Chapters 2 and 3.

The first part of the thesis assumed an axisymmetric shape for the nematic droplets in the isotropic phase with $\boldsymbol{n}$ along the meridians on their boundaries. This configuration of the nematic director is called *bipolar* and it is characterized by point defects of $\boldsymbol{n}$ at the poles. I recall that if $\boldsymbol{n}$ is not everywhere smooth, or it is not defined in some points, we say that a *defect* of $\boldsymbol{n}$ occurs in these points. A defect may be concentrated in isolated points, lines or surfaces, but only point defects are well explained within such a theory.

1.1.4 Energy Minimization

Neglecting the work done by body forces, we write the total energy of a drop of nematic liquid crystal surrounded by an isotropic fluid as

$$\mathscr{F}\left[\mathscr{B}, \boldsymbol{n}\right] := \mathscr{F}_{\mathrm{b}}\left[\mathscr{B}, \boldsymbol{n}\right] + \mathscr{F}_{\mathrm{s}}\left[\mathscr{B}, \boldsymbol{n}\right], \tag{1.18}$$

where $\mathscr{F}_{\mathrm{b}}$ and $\mathscr{F}_{\mathrm{s}}$ are as in (1.1) and (1.16). The shape $\mathscr{B}$ is not prescribed and it is allowed to vary like the orientation field within it; thus, the following isoperimetric constraint arises which assigns the volume of the shape:

$$V(\mathscr{B}) = V_0, \tag{1.19}$$

where V_0 is a given positive constant. Chapters 2 and 3 concern free-boundary problems of this type.

When $\mathscr{B}$ is given, the director field chooses the configuration that minimizes the free-energy functional $\mathscr{F}\left[\boldsymbol{n}\right]$ in (1.18) where $\mathscr{B}$ is no more a variable. We want to minimize the functional in the Sobolev space $W^{1,2}\left(\mathscr{B}, \mathbb{S}^2\right)$ [7] in the case in which no anchoring condition for $\boldsymbol{n}$ are prescribed on $\partial\mathscr{B}$; the director fields that represent possible equilibria make the elastic free-energy *stationary*, i.e.

$$\delta\mathcal{F}\left(\boldsymbol{n}\right)\left[\boldsymbol{v}\right] := \frac{\mathrm{d}}{\mathrm{d}\varepsilon}\mathcal{F}\left(\boldsymbol{n}_\varepsilon\right)|_{\varepsilon=0} = 0, \tag{1.20}$$

as ε spans in the interval $[-\varepsilon_0, \varepsilon_0]$, with $\varepsilon_0 > 0$ given, and $\boldsymbol{n}_\varepsilon$ describes a path of configurations about $\boldsymbol{n}$ which depend on $\boldsymbol{v} \in W^{1,2}\left(\mathscr{B}, \mathbb{R}^3\right) \cap L^\infty\left(\mathscr{B}, \mathbb{R}^3\right)$[14], and

$$\boldsymbol{n}_\varepsilon(p) := \frac{\boldsymbol{n}(p) + \varepsilon\boldsymbol{v}(p)}{|\boldsymbol{n}(p) + \varepsilon\boldsymbol{v}(p)|} \tag{1.21}$$

for every p in $\mathscr{B}$.

For a general isotropic and even free-energy density the *weak form of the Euler Lagrange equation* of $\mathscr{F}[\boldsymbol{n}]$ (see e.g. [127, Ch. 3]) is

$$\int_\mathscr{B} \left[\frac{\partial W}{\partial\nabla\boldsymbol{n}} \cdot \nabla\left(\boldsymbol{P}\left(\boldsymbol{n}\right)\boldsymbol{v}\right) + \frac{\partial W}{\partial\boldsymbol{n}} \cdot \boldsymbol{P}\left(\boldsymbol{n}\right)\boldsymbol{v} \right] \mathrm{d}V = 0. \tag{1.22}$$

where $\boldsymbol{v}$ can be chosen arbitrarily in $W^{1,2}\left(\mathscr{B}, \mathbb{R}^3\right) \cap L^\infty\left(\mathscr{B}, \mathbb{R}^3\right)$ and where $\boldsymbol{P}\left(\boldsymbol{n}\right) = \mathbf{I} - \boldsymbol{n} \otimes \boldsymbol{n}$ is the projection onto the plane orthogonal to $\boldsymbol{n}$. The *weak natural boundary condition* for $\boldsymbol{n}$ is

$$\int_{\partial\mathscr{B}} \left(\frac{\partial W}{\partial\nabla\boldsymbol{n}} + \frac{\partial\gamma_a}{\partial\boldsymbol{n}} \right) \boldsymbol{\nu} \cdot \boldsymbol{v} \, \mathrm{d}A = 0. \tag{1.23}$$

The corresponding *strong forms* of (1.22) and (1.23) are, respectively,

$$\boldsymbol{P}\left(\boldsymbol{n}\right)\left(\operatorname{div}\frac{\partial W}{\partial\nabla\boldsymbol{n}} - \frac{\partial W}{\partial\boldsymbol{n}} \right) = 0, \quad \text{in } \mathscr{B} \tag{1.24a}$$

$$\left(\frac{\partial W}{\partial\nabla\boldsymbol{n}} + \frac{\partial\gamma_a}{\partial\boldsymbol{n}} \right) \boldsymbol{\nu} = 0, \quad \text{on } \partial\mathscr{B} \tag{1.24b}$$

where $\boldsymbol{n}$ is at least a map of class $\mathcal{C}^2$ and so the derivatives exist in the strong sense.

Deciding the stability of the free-energy functional in the vicinity of an equilibrium solution presumes the analysis of its second variation at the configuration. In Chapter 4 we provide a general formula for the second variation $\delta^2\mathscr{F}_\mathrm{b}$, where $\mathscr{F}_\mathrm{b}$ is Frank's free-energy functional, for a solution $\boldsymbol{n}$ to the weak form of the Euler Lagrange equations for $\mathscr{F}_\mathrm{b}$ (c.f. (1.22) and (1.23) with W given by (1.3)).

1.2 Chromonic Liquid Crystals

CLCs in three-dimensional space have become of interest because in cylindrical capillary tubes subject to degenerate tangential boundary conditions, (1.6), the director $\boldsymbol{n}$ has been seen to steer away from the uniform alignment along the cylinder's axis [55, 56, 19, 86, 54][15], unlike any common NLC. Two symmetric twisted configurations (left- and right-handed) have been observed in capillaries, each variant occurring with the same likelihood, as was to be expected from the lack of chirality in the molecular aggregates that constitute these materials. Despite the clear indication that CLCs' ground state differs from the uniform alignment presumed in f_OF, the Oseen-Frank theory has been applied to rationalize the experiments with capillary tubes [55, 56, 19, 86], at the cost of violating one of Ericksen's inequalities (1.8), as we will see below.

According to the problem first studied analytically in [10], when $\mathscr{B}$ is a cylinder of radius R and height L, cylindrical coordinates with the unit vector $\boldsymbol{e}_z$ directed along the capillary axis are used to parametrize the director field $\boldsymbol{n}$,

$$\boldsymbol{n} = \sin\beta(\rho)\boldsymbol{e}_\theta + \cos\beta(\rho)\boldsymbol{e}_z \tag{1.25}$$

---

[14]If anchoring conditions are imposed on $\boldsymbol{n}$, also $\boldsymbol{n}_\varepsilon$ must obey them, and so $\boldsymbol{v}$ perturbs $\boldsymbol{n}$ according to the anchoring conditions prescribed by the prolem.

[15]Expressed differently, cylindrical capillaries have broken symmetry around the normal.

which is assumed to depend only on how far it is from the axis, i.e. on the radial coordinate $r \in [0, R]$, through the following scaled variable

$$\rho := \frac{r}{R} \in [0, 1]. \tag{1.26}$$

Here $\beta = \beta(\rho)$ is the angle between $\boldsymbol{n}$ and the capillary axis[16]; the cylindrical symmetry sets $\beta(0) = 0$, while the degenerate boundary condition (1.6) are satisfied for every value of $\beta(1)$, which is thus free to vary. Since

$$\nabla \boldsymbol{n} = \frac{1}{R}\left(-\frac{\sin\beta}{\rho}\boldsymbol{e}_r \otimes \boldsymbol{e}_\theta + \cos\beta\beta'\boldsymbol{e}_\theta \otimes \boldsymbol{e}_r - \sin\beta\beta'\boldsymbol{e}_z \otimes \boldsymbol{e}_r\right), \tag{1.27}$$

the distortion characteristics result as

$$S = 0, \tag{1.28a}$$

$$T = \frac{1}{R}\left(\beta' + \frac{\cos\beta\sin\beta}{\rho}\right), \tag{1.28b}$$

$$2q = \frac{1}{R}\left(\beta' - \frac{\cos\beta\sin\beta}{\rho}\right), \tag{1.28c}$$

$$\boldsymbol{b} = \frac{1}{R}\left(\frac{\sin^2\beta}{\rho}\right)\boldsymbol{e}_r, \tag{1.28d}$$

where a prime denotes differentiation with respect to ρ. At the end of the section, the re-interpretation of the equilibrium configurations in terms of these non-uniform distortion characteristics will become fundamental to the understanding of the CLCs ground state. By the change of variables $r \to \rho(r)$ where $\rho(r)$ is given by (1.26), and making use of (1.28) in (1.13), we arrive at the following reduced functional, $\mathcal{F}[\beta]$, which is an appropriate dimensionless form of Oseen-Frank's free-energy functional:

$$\mathcal{F}[\beta] := \frac{\mathscr{F}_{\mathrm{B}}[\boldsymbol{n}]}{2\pi K_{22}L} = \int_0^1 \left(\frac{\rho\beta'^2}{2} + \frac{1}{2\rho}\cos^2\beta\sin^2\beta + \frac{k_3}{2\rho}\sin^4\beta\right)\mathrm{d}\rho + \frac{(1 - 2k_{24})}{2}\sin^2\beta(1). \tag{1.29}$$

The following scaled elastic constants have been introduced in (1.29):

$$k_3 := \frac{K_{33}}{K_{22}}, \quad k_{24} := \frac{K_{24}}{K_{22}}. \tag{1.30}$$

We seek the orientation fields $\boldsymbol{n}$ which make Oseen-Frank's free-energy stationary within the class described by (1.25) subject to $\boldsymbol{n}|_{\rho=0} = \boldsymbol{e}_z$, under the assumption that $\boldsymbol{n}$ is a map at least of class $\mathcal{C}^2$. This amounts to seek the functions $\beta = \beta(\rho)$ of class $\mathcal{C}^2$ in $[0, 1]$ which satisfy the condition at $\rho = 0$ and make (1.29) stationary.

Here the functional defined by (1.29) can be regarded as an instance of the functionals represented by the general formula

$$I[u] := \int_a^b f(t, \chi(t), \chi'(t))\,\mathrm{d}t + \varphi(\chi(t))|_{t=b} \tag{1.31}$$

---

[16] Actually, Davidson considers in [19] the more general case in which $\boldsymbol{n} = \cos\alpha(r)\sin\beta(r)\boldsymbol{e}_r + \sin\alpha(r)\sin\beta(r)\boldsymbol{e}_\theta + \cos\beta(r)\boldsymbol{e}_z$ where $\alpha = \alpha(r)$ is the angle between the director projection on the plane $r\theta$ and $\boldsymbol{e}_r$ and $\beta = \beta(r)$ is defined in the main text. The planar degenerate anchoring condition (1.6) sets $\alpha(R) = \pi/2$, and it is proved that the equilibrium value of α is always $\pi/2$. Moreover, in (1.25) $\boldsymbol{n}$ is assumed to depend on ρ as suggested by the outcome of the analysis in [10] or in [19], where n was initially assumed to depend on r.

where f and φ are real function of class C^2 and the functions χ in the domain of I are of class C^2 on $[a, b]$ and satisfy

$$\chi(a) = \chi_a, \tag{1.32}$$

while $\chi(b)$ is free to vary. The equilibrium equations (1.24) reduce to

$$\left(\frac{\partial f}{\partial \chi'}\right)' - \frac{\partial f}{\partial \chi} = 0 \quad \text{in } [a, b] \tag{1.33a}$$

$$\frac{\partial f}{\partial \chi'} + \frac{\partial \varphi}{\partial \chi} = 0 \quad \text{for } t \in \{a, b\} \tag{1.33b}$$

The prime always denotes the derivative with respect to the argument. In our case, (1.29) is stationary at $\beta = \beta(\rho)$ of class C^2 if and only if

$$\frac{\cos \beta \sin \beta}{\rho} \left[1 + 2(k_3 - 1) \sin^2 \beta\right] - \beta' - \rho \beta'' = 0 \quad \rho \in (0, 1), \tag{1.34a}$$

$$\left[(1 - 2k_{24}) \cos \beta \sin \beta + \beta'\right]\big|_{\rho=1} = 0. \tag{1.34b}$$

The trivial solution $\beta(\rho) = 0$ always solves these equations. According to the sign of $(K_{22} - K_{24})$ other two nonuniform solutions to the problem could exist; multiplying both sides by $\rho \beta'$, we see that (1.34a) has an integral of motion

$$\left(\rho \beta'\right)^2 - \sin^2 \beta \left(\cos^2 \beta + k_3 \sin^2 \beta\right) = c, \tag{1.35}$$

where c is an arbitrary constant. By the assumption of regularity, the property $|\beta'(0)| < \infty$ holds, and so the constant c must vanish. Two branches of solution are emanated from $\rho = 0$ depending on wheter $\beta'(0)$ is positive or negative: they are obtained by integrating the equations

$$\beta' = \pm \frac{\sin \beta \cos \beta \sqrt{1 + k_3 \tan^2 \beta}}{\rho}. \tag{1.36}$$

We focus on the increasing branch with the plus sign holding in (1.36), and we substitute its evaluation for $\rho = 1$ into the boundary condition (1.34b); this yields an equation for the angle $\beta(1)$:

$$\sin \beta(1) \cos \beta(1) \left[\sqrt{1 + k_3 \tan^2 \beta(1)} + (1 - 2k_{24})\right]. \tag{1.37}$$

We note that $\beta(1) \neq 0$ exists only for $k_{24} > 1$; in this case

$$\beta(1) = \arctan\left(\frac{2\sqrt{k_{24} - 1}}{\sqrt{k_3}}\right). \tag{1.38}$$

Integrating (1.36) yields

$$\ln \rho = \int_0^\beta \frac{\mathrm{d}\eta}{\sin \beta \cos \beta \sqrt{1 + k_3 \tan^2 \beta}} = [\ln g(\eta)]_0^\beta, \tag{1.39}$$

where

$$g(\eta) = \frac{1}{2} - \frac{1}{\sqrt{1 + k_3 \tan^2 \eta} + 1}. \tag{1.40}$$

Taking into account the boundary value (1.38), we get an explicit solution. The same argument is employed for its mirror image, when the minus sign holds in (1.36). To sum up, there are one or three equilibrium solutions according to the value of k_{24}: the uniform solution

$$\beta = 0, \tag{1.41}$$

which exists for every $k_{24} > 0$, with the director $\boldsymbol{n}$ parallel to the capillary axis, and two other configurations

$$\beta(\rho) = \beta_0(\rho) := \arctan\left(\frac{2\sqrt{k_{24}(k_{24}-1)}\rho}{\sqrt{k_3}\left[k_{24} - (k_{24}-1)\rho^2\right]}\right), \tag{1.42}$$

with its mirror image solution:

$$\beta(\rho) = \pi - \beta_0(\rho). \tag{1.43}$$

These last two solutions are valid only if Ericksen's inequality $K_{22} \geq K_{24}$ (1.8) is violated. They describe how the director twists around the axis and have right and left handed chirality, respectively, according to whether the integral lines of the nematic director spiral clockwise or not. For $K_{24} < K_{22}$ the trivial solution is the only solution of the equilibrium equation and it is stable; as explained in Section 4.3.1 of Chapter 4 this is guaranteed by the validity of the Ericksen's inequality (1.8). The non-uniform configurations represent the branches of a bifurcation occurring at $K_{24} = K_{22}$ where they coincide with the trivial solution. They share the same bulk free-energy which is given by

$$\mathscr{F}^{ET} = 2\pi K_{22} L \left[-(k_{24}-1) + \frac{1}{2}\frac{k_3}{\sqrt{k_3-1}} \arctan\left(\frac{2\sqrt{k_3-1}(k_{24}-1)}{k_3 + 2(k_{24}-1)}\right)\right]. \tag{1.44}$$

As K_{24} increases beyond K_{22}, and thus as k_{24} increases beyond 1, (1.44) decreases continuously from zero, making the uniform configuration energetically disfavoured. This confirms that a spontaneous chirality in the nematic director texture manifests itself in the absence of molecular chirality, according to the experimental data. Thus, under the assumption that $\boldsymbol{n}$ is at least a map of class $\mathcal{C}^2$, the non-uniform equilibrium director configurations for Oseen-Frank's free-energy functional, (1.42) and its mirror image (1.43) are the candidates to rationalize the ground state of CLCs in cylindrical capillaries subject to degenerate boundary conditions, which is termed *escaped-twist* (ET) ground state in [19]. Since they are valid only if the related Ericksen's inequality $(K_{22} - K_{24}) \geq 0$ is violated, the experimental data seem to be justified only if Oseen-Frank's free-energy functional in $3D$ Euclidean space is unbounded below. The inequality $K_{22} < K_{24}$ in (1.13) would suggest that the pure *double-twist configuration*, that is, the director configuration having only the double twist mode T non-zero among all modes, is the ground state of CLCs. Henceforth in this dissertation we take this for a fact. This ideal mode belongs to neither of the two families of uniform director fields (1.15) and so it is necessarily frustrated (in a flat space) [134]; a constant T is only possible along a $1D$ curve. Accordingly, we may say that the so-called escaped twist ground state is actually a 'pseudo-ground state' since it is the result of the confinement-induced extension of the pure double twist when requested to occupy the cylinder and to satisfy degenerate boundary conditions, which injects elastic frustration in the system.

As rationalized within Oseen-Frank's theory, this induced state has non-uniform distortion characteristics, and only in the limit as ρ tends to 0, explicit calculations of (1.28) for the ET solutions (1.42) and (1.43) give

$$S = q = b_1 = b_2 = 0, \quad T \approx \pm\frac{4\sqrt{k_{24}-1}}{R\sqrt{k_3 k_{24}}}. \tag{1.45}$$

The double twist deformation mode can indeed be achieved, but only along the axis of the cylinder.

Chapter 2

Nematic Tactoid Population

Large saddle-splay elastic constants K_{24} compared with twist elastic constant K_{22} are necessary to justify within Oseen-Frank's theory the spontaneous emergence of chirality recently observed in achiral CLCs. This suggests the issue treated here connected to this elastic constant: to interpret and to re-investigate problems of drops of nematic phase surrounded by an isotropic liquid to document better the role played by K_{24} in Oseen-Frank's theory. We focus on the untwisted bipolar configurations; the twist term in the elastic free-energy density vanishes identically and makes the problem well posed also for CLCs, although this Chapter is not intended exclusively for them. What makes the saddle-splay constant K_{24} elusive is its being related to a surface (elastic) energy. Heuristically, since surface evokes shape, one expects K_{24} to be the elastic constant that most determines how a droplet looks like. By considering a novel class of admissible solutions for a bipolar droplet, we study the prevalence in the population of all equilibrium shapes of each of the three that may be optimal (tactoids primarily among them). In particular, we show how this prevalence is affected by a dimensionless measure α of the drop's volume and the ratios k_{24} and k_3, which here correspond to the ratios of K_{24} and K_{33} to K_{11}, since K_{22} plays no role. Tactoids, in particular, prevail for $\alpha \lessgtr 16.2 + 0.3k_3 - (14.9 - 0.1k_3)k_{24}$. This Chapter has been published in an article [99].

2.1 Tactoids in the Literature

Tactoids have a long and intriguing history. The name *tactoid* (in German, *taktoid*) comes from the Greek τακτός, meaning *ordered*; it was coined by Zocher and Jacobsohn [147] to designate spindle-like aggregates of elongated colloidal particles dispersed in sols (typically aqueous). Originally, such particles were composed of monocrystals of vanadium pentoxide (V_2O_5) grown by aging, first[1] studied in [143] and further characterized in [130].[2]

Later, once Stanley [118] had succeeded in extracting tobacco mosaic virus (TMV) from infected plants, tactoids made again their appearance in aqueous sols where TMV had been dispersed with a concentration higher than 2% by weight [4].[3] Remarkable is the evidence of tactoids in TMV sols collected in [5], whose diagrams and pictures of pointed shapes we found inspirational.[4] Onsager himself says that explaining the formation of TMV was one motivation

---

[1]We learn, however, in the historical review [117] (which is highly recommended to the reader) that an earlier experiment performed in 1904 by Q. Majorana had already found magnetically induced birefringence in a sol of inorganic particles (FeOOH).

[2]In this connection, the reader is referred to the interesting review [98] on a class of mineral liquid crystals, where tactoids also formed.

[3]A more recent study attempting to characterize this special system can be found in [37].

[4]The original aim of [5] was to measure inter-tactoid distances as a function of pH and ionic strength.

for his seminal paper [95] on the coexistence of nematic and isotropic phases as sole consequence of steric interactions.[5] Chromonic liquid crystals,[6] which are constituted by molecular aggregates whose length distribution is affected by both temperature and concentration, have shown hosts of tactoids [85, 123, 63, 55, 104].[7]

2.2 Introduction

Although there is experimental evidence showing that spherical droplets of (mostly thermotropic) liquid crystals may have normal as well as tangential anchoring at the interface [11, 129, 67], since the earliest works [13, 27] tactoids have been studied under the assumption that the nematic director n is tangent to the boundary. Actually, most studies have assumed an axisymmetric shape for tactoids with n along the meridians on their boundaries. In such *bipolar* configurations, the poles are doubly singular, because both the surface normal and the nematic director have there *defects*.

Williams [132] made the first systematic attempt to find both the equilibrium shape of droplets subject to tangential surface anchoring and the equilibrium director field inside them.[8] In its most general formulation, the problem soon appeared formidable. Nonetheless, analytic estimates and numerical computations suggested that tactoids "are difficult to observe, since very small drops and very low surface tension interface are required" [132, p. 12].[9]

Such a disheartening conclusion did not deter further studies. Tactoids and their mathematical description have recently witnessed a surge of interest in a series of papers by several authors [60, 105, 61, 106, 107]. Despite a number of differences, they have one feature in common: being directly or indirectly influenced by the work of Williams [132], they adopt a special representation for both the droplet's shape and the nematic director that makes the saddle-splay constant of the Oseen-Frank's energy, the most elusive to experimental detection, feature as mere renormalization of the splay constant, thus playing a marginal role in the occurrence of tactoids.

We are primarily interested in tactoids and on how they prevail over other possible equilibrium shapes, a notion which, borrowing from the language of demography, we describe as *tactoid population*. This is precisely what this Chapter is about: to widen the class of admissible droplet's shapes and directors to identify the agents responsible for the growth and decay of tactoid population. We shall show how a change in the class of admissible shapes may alter considerably the whole scene.

2.2.1 Plan

Section 2.3 is devoted to the illustration of the class of shapes (and director fields) adopted in this Chapter. In particular, we realize that in our class there are both *genuine* tactoids (those with pointed tips) and shapes that, although perfectly smooth, look very much like sharply pointed spindles. We introduce a full shape taxonomy that helps us navigate the configuration space. Not all admissible shapes are convex, but it is shown in Sec. 3.3 that all optimal shapes

---

[5]Although the connection between colloidal aggregates and liquid crystals was already clear to Onsager, it took Zocher a longer time to include what he had called nematic (and smectic) *superphases* [145, 148] "into the realm of liquid crystals, though their physico-chemical nature is very different from that of relatively low molecular organic substances exhibiting mesophases" [146, p. 178].

[6]Disparate materials can be classified as chromonic liquid crystals; they include dyes, drugs [23, 120], nucleotides [76], and DNA oligomers [138, 84]. See also the review [74] and the thesis [139].

[7]Examples of tactoids in other materials can also be found in [89, 124].

[8]In the special case where all elastic constants in the Oseen-Frank theory are equal.

[9]It is perhaps for this reason that in a subsequent paper Williams [133] considered only bipolar spherical droplets.

are so. They can be tactoids or spheroids (or something in between), depending on the values of two dimensionless parameters, one related to the droplet's size and the other related to the saddle-splay constant. In Sec. 2.5, we collect the main results of this Chapter by examining the circumstances that determine the prevalence of one shape over the others. In Sec. 2.6, we summarize our findings and see how Williams' pessimistic conclusion about the scarcity of tactoids can be mellowed. The Chapter is closed by three mathematical appendices, where we illustrate the details of our development that in the main text could have easily hampered the reader.

2.3 Class of Shapes

Ericksen's inequalities (1.8) will be taken as valid throughout this Chapter. Twist instability is suppressed for bipolar configurations, and K_{22} plays no role. In the present setting, Oseen-Frank's functional can be safely minimized.

Here we study a free-boundary problem, where a given quantity of nematic liquid crystal occupying the volume V_0 (we treat liquid crystals as incompressible fluids) is surrounded by an isotropic fluid (which could well be its own melt) and can take on any desired shape. The shape of the region $\mathscr{B}$ occupied by the material at equilibrium will be the primary unknown of our problem. Equilibrium is attained whenever the total free-energy is minimized, that is, whenever $\mathscr{B}$ minimizes the shape functional

$$\mathscr{F}[\mathscr{B}] := \int_{\mathscr{B}} f_{\mathrm{OF}} \, \mathrm{d}V + \gamma A(\partial \mathscr{B}), \tag{2.1}$$

subject to the isoperimetric constraint (1.19), where f_{OF} is as in (1.3). Minimizers of $\mathscr{F}$ will be sought for in a special class of shapes and director fields, which we now describe in detail.

2.3.1 Shape Representation and Director Retraction

We shall represent $\mathscr{B}$ as a region in three-dimensional space axisymmetric about the z-axis of a standard cylindrical frame $(\boldsymbol{e}_r, \boldsymbol{e}_\vartheta, \boldsymbol{e}_z)$ and mirror-symmetric relative to the equatorial plane $(\boldsymbol{e}_r, \boldsymbol{e}_\vartheta)$. As shown in Fig. 2.1, the boundary $\partial \mathscr{B}$ is obtained by rotating the graph of a function of class C^1, $R = R(z)$, which describes the radius of the drop's cross-section at height $z \in [-R_0, R_0]$. R is taken to an even function,

$$R(z) = R(-z), \quad z \in [-R_0, R_0]. \tag{2.2}$$

The points on the z-axis at $z = \pm R_0$, where R vanishes, are the *poles* of the drop. On the equator, which falls at $z = 0$, smoothness and symmetry require that $R'(0) = 0$, where a prime denotes differentiation.

Whenever $R'(R_0)$ is finite, the shape $\mathscr{B}$ has pointed poles, it is a *tactoid*, which we shall call *genuine* to distinguish it from similar elongated shapes with a smooth boundary. On the other hand, whenever R' is unbounded at the end-points of the interval $[-R_0, R_0]$, $\mathscr{B}$ has a smooth boundary; as shown below, its shape may appear in different forms and guises. Figure 2.1 depicts the cross-section with a meridian plane (say, at $\vartheta = 0$) of a region $\mathscr{B}$ in the class we are considering; the full shape is generated by a 2π-rotation around the z-axis.

The director field $\boldsymbol{n}$ on $\partial \mathscr{B}$ is taken to be oriented along the meridians. This is an additional hypothesis, also made in [105, 106], which is expected to be justified provided that the splay constant K_{11} does not exceed a combination of twist and bend constants. For spherical droplets, Williams [133] showed that when $K_{11} \geq K_{22} + 0.43 K_{33}$ a twisted configuration (with the director
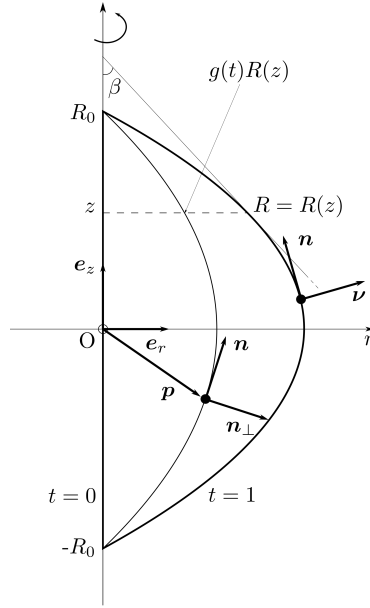
Figure 2.1: Cross-section of the drop with a meridian plane. The function $R(z)$ represents the boundary $\partial\mathscr{B}$, while the function $R_t(z) = g(t)R(z)$ is the retraction of $R(z)$ described in the text. The director field $\boldsymbol{n}$ is everywhere tangent to the retracted curves; $\boldsymbol{n}_\perp = \boldsymbol{e}_\vartheta \times \boldsymbol{n}$ is the orthogonal field that agrees with the outer unit normal $\boldsymbol{\nu}$ on $\partial\mathscr{B}$. The tangent to $R(z)$ for $z \geq 0$ makes the angle β with the z-axis; it is instrumental to the definition of the tactoidal measure τ illustrated in Appendix 2.B.

spiraling at an angle with the meridians) is energetically more favorable than the bipolar configuration. Heuristically, this is understood by considering that when the splay component of the nematic distortion becomes too energetic, it can be relaxed at the expenses of both twist and bend distortions, if they are less energetic. As pointed out in [105], since in elongated shapes, such as tactoids, the splay component is likely to be less prominent than in spherical droplets, one expects that in this context the twisting instability would require even larger values of K_{11} compared to Williams' original estimate.[10]

For any given ϑ, the boundary curve is represented by the position vector (issued from the center of symmetry of $\mathscr{B}$)

$$\boldsymbol{p}_1(\vartheta, z) := R(z)\boldsymbol{e}_r + z\boldsymbol{e}_z, \quad -R_0 \leqq z \leqq R_0, \tag{2.3}$$

which is *retracted* inside $\mathscr{B}$ as the curve

$$\boldsymbol{p}(t, \vartheta, z) := g(t)R(z)\boldsymbol{e}_r + z\boldsymbol{e}_z, \quad -R_0 \leqq z \leqq R_0, \tag{2.4}$$

where t is the *retraction parameter* ranging in $[0, 1]$ and g is any function of class C^1 strictly increasing on $[0, 1]$ and such that $g(0) = 0$ and $g(1) = 1$ (an example would be $g(t) = t$). Clearly, for $t = 1$, $\boldsymbol{p}(t, \vartheta, z)$ reduces to $\boldsymbol{p}_1(\vartheta, z)$ in (2.3), whereas for $t = 0$ it describes the polar axis $\boldsymbol{p}_0(z) = z\boldsymbol{e}_z$ (see Fig. 2.1). The family of retracted curves fill the whole of $\mathscr{B}$ by letting ϑ vary

---

[10]The fact, however, remains that a thorough stability analysis of the nematic distortions considered here is still lacking.

in $[0, 2\pi)$. Thus, $(t, \vartheta, z) \in [0, 1] \times [0, 2\pi) \times [-R_0, R_0]$ are the new set of *retracted coordinates* for the region $\mathscr{B}$.

We not only retract the boundary $\partial\mathscr{B}$ by letting t vary in $[0, 1]$, we also retract the meridian director field on $\partial\mathscr{B}$, which is thus defined in the whole of $\mathscr{B}$ as the unit vector field tangent to the lines with given (t, ϑ) and varying z (see Fig. 2.1). The director field produced with such a geometric construction possesses two point defects at the poles; they are two *boojums* with equal topological charge $m = +1$. By differentiating $\boldsymbol{p}$ in (3.43) with respect to z, keeping (t, ϑ) fixed, we easily obtain

$$\boldsymbol{n} = \frac{gR'\boldsymbol{e}_r + \boldsymbol{e}_z}{\sqrt{1 + (gR')^2}}. \tag{2.5}$$

Letting $\boldsymbol{n}_\perp$ be the unit vector orthogonal to $\boldsymbol{n}$ in the meridian plane, oriented so as to coincide with the outer unit normal $\boldsymbol{\nu}$ on $\partial\mathscr{B}$, we see form (3.44) that

$$\boldsymbol{n}_\perp = \frac{\boldsymbol{e}_r - gR'\boldsymbol{e}_z}{\sqrt{1 + (gR')^2}}. \tag{2.6}$$

A positively oriented orthonormal frame $(\boldsymbol{n}, \boldsymbol{n}_\perp, \boldsymbol{e}_z)$ is then obtained by appending the unit vector $\boldsymbol{e}_\vartheta = \boldsymbol{n} \times \boldsymbol{n}_\perp$, everywhere orthogonal to the local meridian plane. This frame, however, is not the frame associated with the new coordinates (t, ϑ, z), as we now proceed to show.

Imagine a smooth curve in $\mathscr{B}$ parametrized as $\xi \mapsto (t(\xi), \vartheta(\xi), z(\xi))$. It follows from (3.43) that

$$\dot{\boldsymbol{p}} = (g'R\dot{t} + gR'\dot{z})\boldsymbol{e}_r + gR\dot{\vartheta}\boldsymbol{e}_\vartheta + \dot{z}\boldsymbol{e}_z, \tag{2.7}$$

where a superimposed dot denotes differentiation with respect to the parameter ξ.[11] A glance at (3.44) suffices to show that (3.46) can also be rewritten as

$$\dot{\boldsymbol{p}} = g'R\dot{t}\boldsymbol{e}_r + gR\dot{\vartheta}\boldsymbol{e}_\vartheta + \sqrt{1 + (gR')^2}\,\dot{z}\boldsymbol{n}, \tag{2.8}$$

showing that $(\boldsymbol{e}_x, \boldsymbol{n}, \boldsymbol{e}_z)$ is the (non-orthogonal) frame associated with the retracted coordinates (t, ϑ, z).

Equation (2.8) is especially expedient to derive the elementary volume $\mathrm{d}V$ of $\mathscr{B}$ and the elementary area $\mathrm{d}A_t$ for the retracted boundary $\partial\mathscr{B}_t$ in $\mathscr{B}$. For the former we have that

$$\mathrm{d}V = \mathrm{d}t\,\mathrm{d}\vartheta\,\mathrm{d}z(g'R)(gR)\sqrt{1 + (gR')^2}\,\boldsymbol{e}_r \cdot \boldsymbol{e}_\vartheta \times \boldsymbol{n} = gg'R^2\,\mathrm{d}t\,\mathrm{d}\vartheta\,\mathrm{d}z, \tag{2.9}$$

where use has also been made of (3.44), while for the latter,

$$\mathrm{d}A_t = \mathrm{d}\vartheta\,\mathrm{d}z(gR)\sqrt{1 + (gR')^2}\,\boldsymbol{e}_\vartheta \times \boldsymbol{n} \cdot \boldsymbol{n}_\perp = gR\sqrt{1 + (gR')^2}\,\mathrm{d}\vartheta\,\mathrm{d}z. \tag{2.10}$$

Thus, the volume of a droplet $\mathscr{B}$ will be expressed in terms of the function R as

$$V(\mathscr{B}) = \int_0^1 gg'\,\mathrm{d}t \int_0^{2\pi} \mathrm{d}\vartheta \int_{-R_0}^{R_0} R^2\,\mathrm{d}z = \pi \int_{-R_0}^{R_0} R^2\,\mathrm{d}z = V_0, \tag{2.11}$$

and the area of the boundary $\partial\mathscr{B}$ as

$$A(\partial\mathscr{B}) = 2\pi \int_{-R_0}^{R_0} R\sqrt{1 + R'^2}\,\mathrm{d}z, \tag{2.12}$$

---

[11]With a slight abuse of language, here a prime denotes differentiation both with respect to t (in g') and with respect to z (in R'). No confusion should arise since, apart from $\boldsymbol{p}$, no other instance will occur of a function depending on both (t, z).

which follows from (3.47) for $t = 1$.

It is shown in Appendix 2.A how to derive from (3.43) the form taken by $\nabla \boldsymbol{n}$ in the orthonormal frame $(\boldsymbol{n}, \boldsymbol{n}_\perp, \boldsymbol{e}_z)$; this reads as

$$\nabla \boldsymbol{n} = \frac{gR''}{\left(1 + (gR')^2\right)^{3/2}} \boldsymbol{n}_\perp \otimes \boldsymbol{n} + \left(\frac{R'}{R} \frac{1}{\sqrt{1 + (gR')^2}} - \frac{g^2 R' R''}{\left(1 + (gR')^2\right)^{3/2}} \right) \boldsymbol{n}_\perp \otimes \boldsymbol{n}_\perp$$
$$+ \frac{R'}{R} \frac{1}{\sqrt{1 + (gR')^2}} \boldsymbol{e}_\vartheta \otimes \boldsymbol{e}_\vartheta. \tag{2.13}$$

The following expressions for the traditional measures of distortion are easy consequences of (3.57):

$$\operatorname{div} \boldsymbol{n} = \frac{R'}{\sqrt{1 + (gR')^2}} \left(\frac{2}{R} - \frac{g^2 R''}{1 + (gR')^2} \right), \tag{2.14a}$$

$$\operatorname{curl} \boldsymbol{n} = \frac{gR''}{\left(1 + (gR')^2\right)^{3/2}} \boldsymbol{e}_\vartheta, \tag{2.14b}$$

$$\boldsymbol{n} \cdot \operatorname{curl} \boldsymbol{n} = 0, \tag{2.14c}$$

$$\boldsymbol{n} \times \operatorname{curl} \boldsymbol{n} = -\frac{gR''}{\left(1 + (gR')^2\right)^{3/2}} \boldsymbol{n}_\perp, \tag{2.14d}$$

$$\operatorname{tr}(\nabla \boldsymbol{n})^2 - (\operatorname{div} \boldsymbol{n})^2 = -\frac{2R'^2}{R\left(1 + (gR')^2\right)} \left(\frac{1}{R} - \frac{g^2 R''}{1 + (gR')^2} \right). \tag{2.14e}$$

In particular, (3.58c) shows that, as expected, no twist is associated with the class of retracted meridian fields that we are considering.

Inserting (4.89) in (1.3), we arrive at

$$f_{\mathrm{OF}} = \frac{1}{2} K_{11} \frac{g^4 R'^2 R''^2}{\left(1 + (gR')^2\right)^3} + (K_{11} - K_{24}) \frac{2R'^2}{R\left(1 + (gR')^2\right)} \left(\frac{1}{R} - \frac{g^2 R''}{1 + (gR')^2} \right)$$
$$+ \frac{1}{2} K_{33} \frac{g^2 R''^2}{\left(1 + (gR')^2\right)^3}, \tag{2.15}$$

which shows how in our setting, at variance with [105, 107, 106, 60, 61], the saddle-splay constant does not merely renormalize the splay constant. For given g, the function R represents here both the shape $\mathscr{B}$ of a droplet and the nematic director field inside it.

Before building upon (3.3) and (2.15) the free-energy functional that we shall study in the following, we find it useful to rescale all lengths to the one dictated by the volume constraint. We call R_{e} the radius of the *equivalent* sphere, which has volume V_0, and we rescale to R_{e} both z and $R(z)$, keeping their names unaltered.[12] Letting

$$\mu := \frac{R_0}{R_{\mathrm{e}}}, \tag{2.16}$$

by use of (3.3), (2.15), (2.9), and (3.49), we arrive at the following reduced functional, $F[\mu; R]$, which is an appropriate dimensionless form of $\mathscr{F}$,

---

[12] An abuse of notation that we hope the reader will tolerate.

$$F[\mu; R] := \frac{\mathscr{F}[\mathscr{B}]}{2\pi K_{11} R_{\mathrm{e}}} = \int_0^1 \mathrm{d}t \int_{-\mu}^{\mu} gg' R^2 \left[\frac{1}{2} \frac{g^4 R'^2 R''^2}{\left(1 + (gR')^2\right)^3} + \frac{2(1 - k_{24}) R'^2}{R\left(1 + (gR')^2\right)} \left(\frac{1}{R} - \frac{g^2 R''}{1 + (gR')^2} \right) \right.$$

$$\left. + \frac{k_3}{2} \frac{g^2 R''^2}{\left(1 + (gR')^2\right)^3} \right] \mathrm{d}z + \alpha \int_{-\mu}^{\mu} R\sqrt{1 + R'^2}\, \mathrm{d}z$$

$$= \int_{-\mu}^{\mu} \left\{ \frac{R^2 R''^2}{4R'^2} \left(\frac{\ln(1 + R'^2)}{R'^2} - \frac{1}{(1 + R'^2)^2} \right) + (1 - k_{24}) \left[\left(1 - \frac{RR''}{R'^2} \right) \ln(1 + R'^2) + \frac{RR''}{1 + R'^2} \right] \right.$$

$$\left. + (k_3 - 3) \frac{R^2 R''^2}{8(1 + R'^2)^2} \right\} \mathrm{d}z + \alpha \int_{-\mu}^{\mu} R\sqrt{1 + R'^2}\, \mathrm{d}z, \tag{2.17}$$

where the integration in t is shown to be independent of the specific function g, provided it is monotonic and obeys the prescribed boundary conditions. The following scaled elastic constants have been introduced in (2.17),

$$k_3 := \frac{K_{33}}{K_{11}}, \quad k_{24} := \frac{K_{24}}{K_{11}}, \tag{2.18}$$

the former is non-negative and the latter is subject to $0 \leqq k_{24} \leqq 1$, as a consequence of (1.8). Moreover,

$$\alpha := \frac{\gamma R_{\mathrm{e}}}{K_{11}} \tag{2.19}$$

is a reduced (dimensionless) volume.[13]

The variational problem that we thus face can be phrased as follows: Find a positive μ and a smooth, even function R that obeys

$$R(-\mu) = R(\mu) = 0 \tag{2.20}$$

so as to minimize F subject to the isoperimetric constraint (2.11), which in the scaled variables reads simply as

$$\int_{-\mu}^{\mu} R^2(z)\, \mathrm{d}z = \frac{4}{3}. \tag{2.21}$$

2.3.2 Special Family of Shapes

The variational problem just stated is rather challenging, especially if we wish to discuss the role played by the constitutive parameters k_3 and k_{24} and by the reduced volume α in the population of minimizing shapes. Instead of embarking in a thorough numerical minimization of F, we rather resort to a special family of shapes described by a small number of parameters. We shall take the function R in the special form

$$R(z) = a(\mu^2 - z^2) + b\sqrt{\mu^2 - z^2}, \tag{2.22}$$

which exhibits defects at the poles when $b = 0$, while it is everywhere smooth otherwise. For $b = 0$, R in (2.22) reduces to the parabolic profile considered as an ansatz in [132].

We now illustrates and classify the relatively large variety of shapes that can be represented through (2.22). We begin by considering the constraints that the parameters (a, b, μ) are subject to.

---

[13]When we say that a drop is either small or large, we mean precisely that either $\alpha \ll 1$ or $\alpha \gg 1$, respectively.

First, $R(z)$ must be non-negative for all $-\mu \leqq z \leqq \mu$. It a simple matter to check that this requirement is equivalent to the inequalities

$$b \geq -\mu a \quad \text{and} \quad b^2 \geq (\mu a)^2 \quad \text{or} \quad ab > 0, \tag{2.23}$$

which can be represented by letting

$$\mu a = \rho \cos \phi \quad \text{and} \quad b = \rho \sin \phi, \quad \text{with} \quad \rho > 0 \quad \text{and} \quad 0 \leqq \phi \leqq \frac{3\pi}{4}. \tag{2.24}$$

Second, the isoperimetric constraint (5.5) requires that

$$\mu^3 \left(b^2 + \frac{9\pi}{16}(\mu a)b + \frac{4}{5}(\mu a)^2 \right) = 1. \tag{2.25}$$

Inserting (2.24) into (2.25), we obtain ρ and conclude that all admissible values of a and b are represented by

$$a = \frac{1}{\mu^{5/2}} \frac{\cos \phi}{\sqrt{h(\phi)}}, \quad b = \frac{1}{\mu^{3/2}} \frac{\sin \phi}{\sqrt{h(\phi)}}$$
$$\text{with} \quad h(\phi) := \sin^2 \phi + \frac{9\pi}{16} \sin \phi \cos \phi + \frac{4}{5} \cos^2 \phi > 0, \quad 0 \leqq \phi \leqq \frac{3\pi}{4}. \tag{2.26}$$

Thus, (ϕ, μ) are the only independent parameters that describe all admissible shapes in the special class (2.22). We now explore the qualitative features of these shapes, corresponding to different regions in configuration space $\mathsf{S} := \{(\phi, \mu) : 0 \leqq \phi \leqq \frac{3\pi}{4}, \ \mu > 0\}$.

We first distinguish *prolate* from *oblate* shapes, the former are characterized by having height larger than width, that is, by the inequality $\mu \geq R(0)$, which by (2.22) and (3.20) becomes

$$\mu \geq \varpi(\phi) := \sqrt[3]{\frac{(\cos \phi + \sin \phi)^2}{h(\phi)}}. \tag{2.27}$$

The graph of $\varpi(\phi)$ is shown in Fig. 3.4: all shapes above it are prolate, all shapes below it are oblate. The round sphere, corresponding to the point to $(\frac{\pi}{2}, 1)$, falls on the graph of ϖ (it is denoted by a circle in Fig. 3.4).

We distinguish convex from concave shapes. The latter arise whenever R' has an extra root in $-\mu \leqq z \leqq \mu$, besides $z = 0$. It is easily seen that such an extra root requires that

$$a < 0 \quad \text{and} \quad b < 2\mu|a|. \tag{2.28}$$

By (3.20), these inequalities reduce to $\phi > \phi_{\mathrm{c}} := \text{arccot}\left(-\frac{1}{2}\right) \doteq 2.03\,\text{rad}$. Thus the pink strip in S depicted in Fig. 3.4 is where we find all concave shapes represented by (2.22). The corresponding three-dimensional droplets $\mathscr{B}$ are axisymmetric *dumbbells*, with a neck that narrows as ϕ approaches the boundary of S at $\phi = \frac{3\pi}{4}$, where it vanishes altogether and the droplet is severed. The strip of dumbbells is also traversed by the graph of $\varpi(\phi)$ (see Fig. 3.4), which means that some dumbbells are prolate (if they fall above the graph of ϖ), while others are oblate (if they fall below the graph of ϖ), although here this simply means that their height is either larger or smaller than their neck.

2.3.3 Droplet Taxonomy

Strictly speaking, as already remarked above, a three-dimensional shape $\mathscr{B}$ represented by (2.22) has pointed tips at the poles only for $\phi = 0$, which according to (3.20) is the only value of ϕ
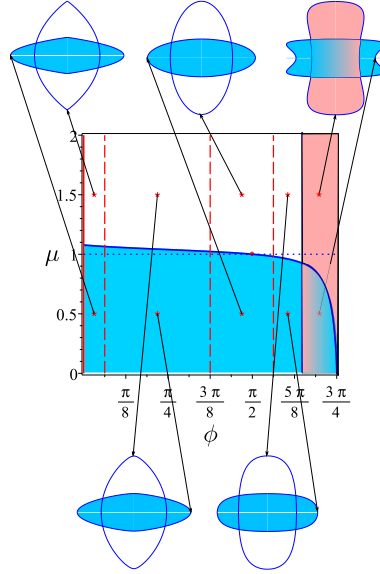
Figure 2.2: Configuration space with all admissible shapes described by (2.22). The blue region below the graph of the function $\varpi(\phi)$ in (3.21) represents all prolate shapes. The pink vertical strip for $\phi_c \leqq \phi \leqq \frac{3\pi}{4}$ represents the concave shapes that we have called *dumbbells*; all shapes falling on the left of this strip are convex. The sphere is represented by the point $(\frac{\pi}{2}, 1)$, marked by a red circle. According to the taxonomy introduced in Sec. 2.3.3, we also call *tactoids* the shapes for $0 \leqq \phi \leqq \frac{\pi}{16}$ (*genuine* tactoids, only those for $\phi = 0$, marked by a red line), *bumped spheroids* those for $\frac{\pi}{16} \leqq \phi \leqq \frac{6\pi}{16}$, simply *spheroids* those for $\frac{6\pi}{16} \leqq \phi \leqq \frac{9\pi}{16}$, and *barrels* those for $\frac{9\pi}{16} \leqq \phi \leqq \phi_c$, see also Table 3.1, and Fig. 3.5 for a fuller gallery of shapes. The barriers marking transitions from one family of shapes to another are represented by vertical dashed lines.

that makes b vanish. We wonder whether for small enough values of ϕ the shape represented by (2.22) via (3.20) can be visually distinguished from a tactoid (in accord with the etymology of the word recalled in the Introduction). The answer to this question is vital to our "demographic" quest. If we want to know how tactoids feature in the whole droplet population, we need to have a clear criterion to classify as tactoids also those shapes which may not have pointed tips, but look like they have.

In Appendix 2.B, we build a quantitative criterion on a certain qualitative observation. There, we arrive at a *tactoidal* measure, which here translates into a conventional classification rule. We propose to call simply tactoids all shapes represented by the strip $0 \leqq \phi \leqq \frac{\pi}{16}$ in configuration space S. Other strips are conventionally identified in S, which describe other shape variants. Our full taxonomy is summarized in Table 3.1 below.

In this section, we shall be contented with illustrating our taxonomic criterion by drawing shapes for which $\mu = 1$. We have two good reasons to do so. First, we have drawn a number of shapes for very different values of μ and always found our criterion qualitatively accurate. Second, as will be clear in Sec. 3.3 below, the equilibrium shapes that minimize the free-energy functional never fall too far away from $\mu = 1$.

Figure 3.5 presents a gallery of meridian cross-sections of a droplet obtained from (2.22) and (3.20) for $\mu = 1$ and a number of values of ϕ falling in the different categories listed in Table 3.1, including the transition shapes. Clearly, the shapes in Figs. 3.6a-3.6b are tactoids. On the other hand, the shapes shown in Figs. 2.3e-2.3h are definitely *not* tactoidal, but they are not completely spherical either. We call them *bumped spheroids* to highlight the fact that

Table 2.1: We identify five strips in configuration space S, which correspond to five qualitatively different shapes for a droplet $\mathscr{B}$ represented by (2.22) via (3.20). The names given below are somewhat self-explanatory; a visual illustration is provided by the gallery of shapes drawn in Fig. 3.5 for $\mu = 1$. The transition shapes, which somehow belong to two adjacent classes, are characterized by the following values of ϕ: $\frac{\pi}{16}$, $\frac{6\pi}{16}$, $\frac{9\pi}{16}$, and $\phi_c = \operatorname{arccot}\left(-\frac{1}{2}\right) \doteq 2.03\,\mathrm{rad}$.

Tactoids	Bumped Spheroids	Spheroids	Barrels	Dumbbells
$0 \leqq \phi \leqq \dfrac{\pi}{16}$	$\dfrac{\pi}{16} \leqq \phi \leqq \dfrac{6\pi}{16}$	$\dfrac{6\pi}{16} \leqq \phi \leqq \dfrac{9\pi}{16}$	$\dfrac{9\pi}{16} \leqq \phi \leqq \phi_c$	$\phi_c \leqq \phi \leqq \dfrac{3\pi}{4}$

they exhibit a smooth bump where a tactoid would have a tapered tip. The difference between tactoids and bumped spheroids is just a matter of how polar protrusions look like: pointed in the former, smoother in the latter. Keeping increasing ϕ from $\frac{6\pi}{16}$ to $\frac{9\pi}{16}$, the representative shapes gradually lose their bumps, justifying calling them simply *spheroids*, see Figs. 2.3j,2.3k. At $\phi = \frac{9\pi}{16}$, however, spheroids evolve into something else: they start resembling cylinders; we call them *barrels*, see Fig. 3.6d. Beyond the transition shape at $\phi = \phi_c$ shown in Fig. 2.3n, the gallery of shapes is closed by a dumbbell falling in the pink region of the configuration space in Fig. 3.4, see Fig. 3.6e.

We shall see in the following sections where in configuration space S the free-energy functional F in (2.15) attains its minimum, for given values of k_3 and k_{24}, and variable α. We shall learn which among the shapes illuminated in Fig. 3.5 will be privileged as energy minimizers. In preparation for that, here we have set the language to describe a variety of possible shape transitions.

2.4   Optimal Shapes

Our study is confined to bipolar droplets, for which the anchoring at the interface is successfully holding up a tangential, albeit degenerate alignment of the nematic director. It is well-known [126] that for sufficiently small droplets the nematic orientation inside them tends to be uniform and the anchoring at their boundary is accordingly broken, so that the equilibrium shape is delivered by the classical Wulff's construction [135]. We need to make sure that the parameters are chosen in a range where such a configuration would be energetically disfavored. We shall see that this can be achieved provided that the reduced volume α in(3.12) is sufficiently large.

2.4.1   Admissible Volumes

To identify the safeguard value of α below which it would be unwise to push our analysis, we perform here an energy comparison based on two simple estimates.

We begin by estimating the free-energy $\mathscr{F}$ in (3.3) for a uniformly aligned cylindrical drop with (constant) radius R and height L delivered by

$$L = \frac{4}{3}\frac{R_e^3}{R^2}, \tag{2.29}$$

for the constraint on the volume in (1.19) to be obeyed. Suppose that $\boldsymbol{n}$ is along the cylinder's axis; since $\nabla\boldsymbol{n}$ vanishes identically, no distortion energy is stored in the body $\mathscr{B}$ of the drop: all
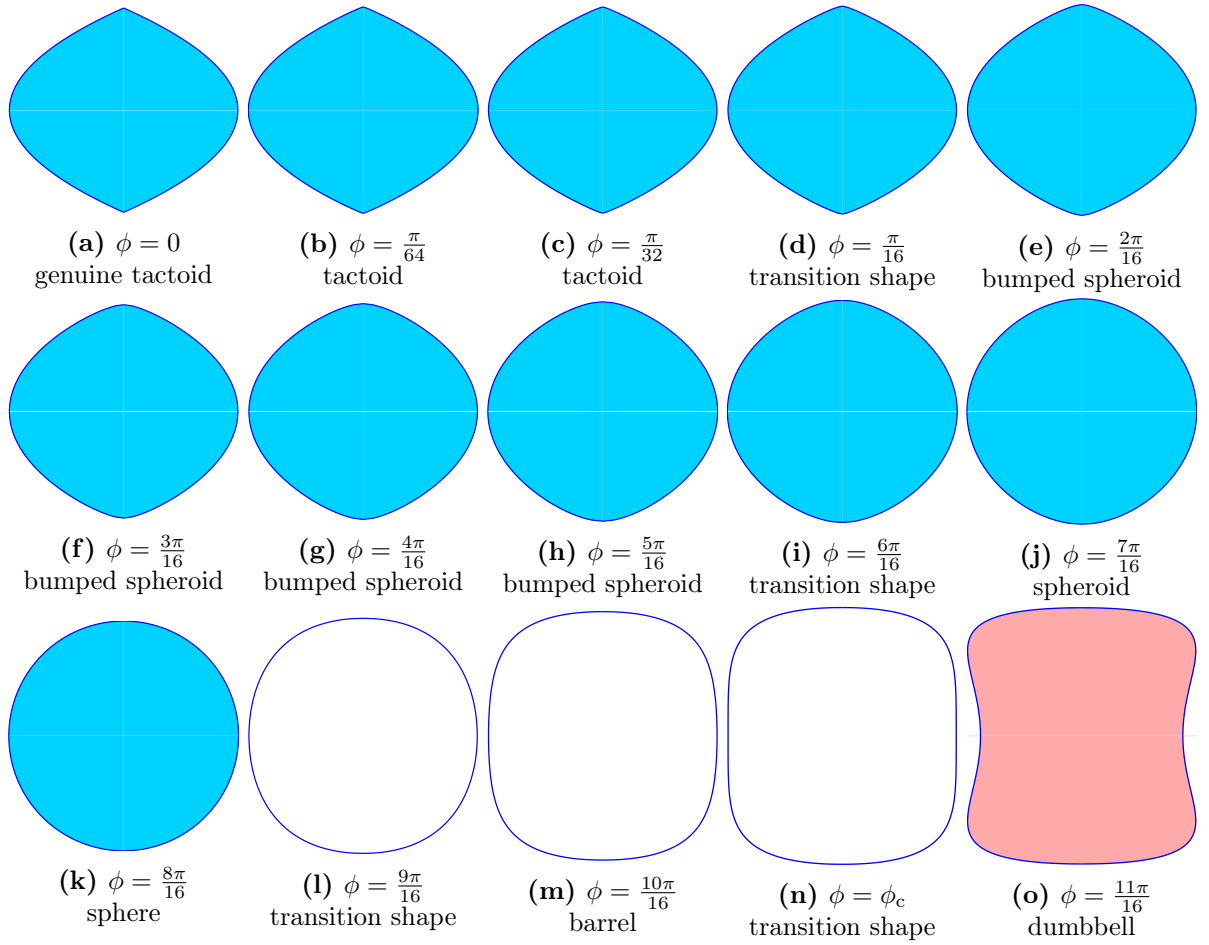
Figure 2.3: Gallery of shapes illustrating for $\mu = 1$ the taxonomy introduced in Table 3.1. In particular, the four transition shapes that somehow share features of two adjacent categories are also shown. The color coding of the shapes is the same used in Fig. 3.4.

the free-energy comes from the boundary $\partial \mathscr{B}$; it is given by

$$F_{\mathrm{c}} = 2\pi\gamma \left(\frac{4}{3} \frac{R_{\mathrm{e}}^3}{R} + (1 + \omega)R^2 \right), \tag{2.30}$$

where use has been made of (2.29) and account has been taken of the different orientation of $\boldsymbol{n}$ relative to $\boldsymbol{\nu}$ on the lateral surface and on the bases of the cylinder. It is a very simple matter to see that F_{c} is minimized for

$$R = R_{\mathrm{e}} \sqrt[3]{\frac{2}{3(1 + \omega)}} \tag{2.31}$$

and that the corresponding value of F_{c} is

$$F_{\mathrm{c}} = 2\pi\gamma R_{\mathrm{e}}^2 \sqrt[3]{12(1 + \omega)}. \tag{2.32}$$

This energy is to be compared with that estimated for a sphere with the bipolar director field emanating from the poles. Letting all constants K_{11}, K_{22}, and K_{33} be equal to K in the elastic energy computed in equation (2.18) of [133], for the total free-energy F_{s} of a spherical drop of

radius R_e we obtain

$$F_s = \left(7 - \frac{\pi^2}{4}\right)\pi K R_e - 4\pi K_{24}R_e + 4\pi\gamma R_e^2. \tag{2.33}$$

The demand that $F_s < F_c$ for all admissible K_{24}, which would make it unfavorable breaking the tangential surface anchoring, is thus reverted into an inequality for α,

$$\alpha > \alpha_s(\omega) := \frac{7 - \frac{\pi^2}{4}}{2(\sqrt[3]{12(1+\omega)} - 2)}, \tag{2.34}$$

which shows how the *bipolar safeguard* value α_s for α depends on ω. Clearly, the larger is ω, the smaller is α_s. Estimating ω in the range[14] 1-10, we shall take[15] $\alpha > \alpha_s(5) \doteq 1.0$.

In view of (3.12), the latter inequality can be interpreted as a lower bound for the linear size R_e of the drops admissible in our theory.[16] Taking $K \sim$ 1-10 pN as typical value for all elastic constants[17] and $\gamma \sim 10^{-5}\,\mathrm{Nm}^{-1}$ as typical value for the interfacial energy of a nematic liquid crystal in contact with its melt,[18] the lower bound for α translates into $R_e \gtrsim$ 0.1-1 μm, which expresses in physical terms the appropriate range of validity of the theory presented here.[19]

2.4.2   Mininizing Trajectories

Finding the minimum of the functional $F[\mu; R]$ in (2.17) is not a problem that can be solved analytically, even in the class of shapes (and retracted meridian fields) described in (2.22) with a and b expressed as in (3.20) in terms of the configuration parameters (ϕ, μ).

For a given choice of the elastic parameters (k_3, k_{24}), we evaluated numerically $F[\mu; R]$ for increasing values of $\alpha > 1$ as a *reduced* function $F_\alpha(\phi, \mu)$ on the configuration space S. Figure 2.4 illustrates the generic situation that we encountered. As shown in Fig. 2.4a, F_α has a convex graph and attains a single minimum in S, which is easily identified through the level sets of F_α depicted in Fig. 2.4b; the corresponding equilibrium shape, a bumped spheroid according to the taxonomy of Sec. 2.3.3, is illustrated in Fig. 2.4c.

We performed a systematic search for the minimizer of F_α upon increasing $\alpha > 1$, for given elastic parameters (k_3, k_{24}). Each search delivered a path of minimizers in the configuration space S, parameterized in α. These paths are shown in Fig. 2.5 for $k_3 = 1$ and a sequence of values of k_{24} in the admissible interval $[0, 1]$. They all have a number of features in common.

First, they reside on the μ-axis (for $\phi = 0$) until α reaches a critical value, α_c, upon crossing which they leave the boundary of S and dive into its interior. Clearly, for $1 < \alpha < \alpha_c$, the equilibrium shape of the drop is a *genuine* tactoid (with sharply pointed tips). For $\alpha > \alpha_c$, the minimizing trajectory traverses the domain of generic tactoids, until ϕ reaches the conventional

---

[14]See, for example, [108] and [63].

[15]This threshold is to some extent conventional, but cannot be "too" wrong, as for other values of ω we would obtain $\alpha_s(1) \doteq 2.6$ and $\alpha_s(10) \doteq 0.7$.

[16]Thus making it clear in what sense this applies to sufficiently *large* drops.

[17]This estimate is supported by a number of contributions that span a long time interval, from early works [111, 110, 96, 58, 59, 78, 116] to more recent ones [9, 2, 50, 121, 81, 69, 70, 122, 53], both experimental and computational in nature, for liquid crystals ranging from thermomotropic to lyotropic, with both low and high molecular weight, see also [132] and [105]. That elastic constants are not too dissimilar for lyotropic and thermotropic liquid crystals has also been confirmed by a recent study on chromonics [141], see also [63].

[18]This estimate is supported by the now classical experimental works [35, 34] on cyano-biphenyls and a number of more recent works [15, 16, 17, 14] on other materials, see also [57, 68, 137] for further earlier sources.

[19]It is perhaps worth noting that such a range changes dramatically when the isotropic fluid surrounding the drop is not its melt. For example, the early measurements of Naggiar [83] and Schwartz [113] gave $\gamma \sim 10^{-2}\mathrm{Nm}^{-1}$ for the surface tension of nematic liquid crystals in contact with its vapor. Correspondingly, an estimate for the admissible R_e would then give $R_e \gtrsim 10^{-11}$m, which makes our theory applicable to drops of virtually all sizes in that environment.
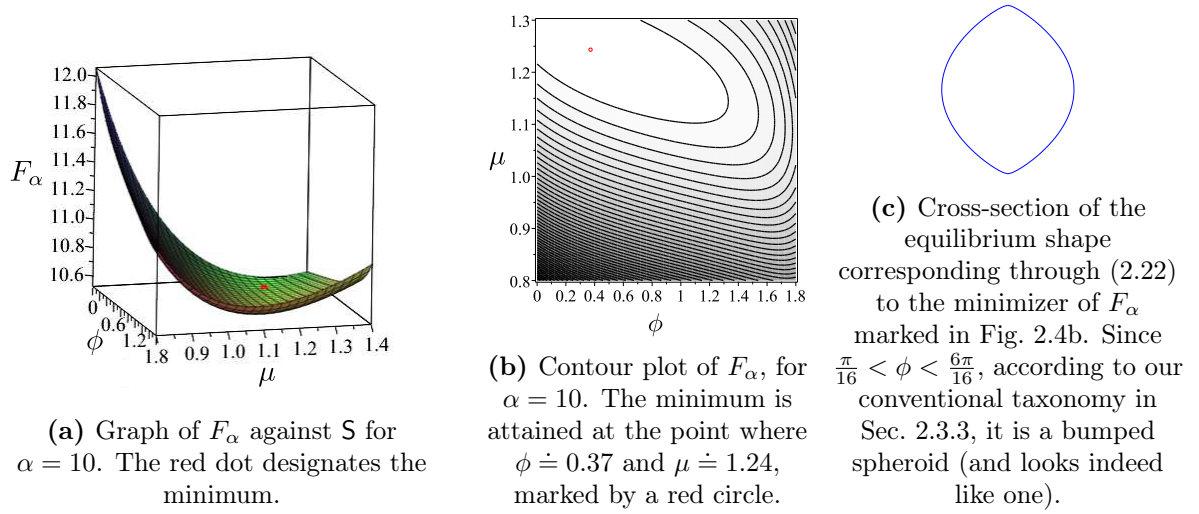
(a) Graph of F_α against S for $\alpha = 10$. The red dot designates the minimum.

(b) Contour plot of F_α, for $\alpha = 10$. The minimum is attained at the point where $\phi \doteq 0.37$ and $\mu \doteq 1.24$, marked by a red circle.

(c) Cross-section of the equilibrium shape corresponding through (2.22) to the minimizer of F_α marked in Fig. 2.4b. Since $\frac{\pi}{16} < \phi < \frac{6\pi}{16}$, according to our conventional taxonomy in Sec. 2.3.3, it is a bumped spheroid (and looks indeed like one).

Figure 2.4: For given $\alpha > 1$, the function F_α is defined in configuration space $S = \{(\phi, \mu) : 0 \leqq \phi \leqq \frac{3\pi}{4}, \mu > 0\}$ by reducing the functional $F[\mu; R]$ in (2.17) to the special families of shapes in (2.22). Reduced elastic constants are $k_3 = 1$, $k_{24} = \frac{1}{2}$.

barrier $\phi = \frac{\pi}{6}$. Such a crossing takes place for $\alpha = \alpha_c'$; there, the equilibrium drop undergoes a (smooth) shape transition, becoming a bumped spheroid. The whole territory of these latter shapes is then traversed by the minimizing trajectories, which enter the realm of spheroids for $\alpha = \alpha_c''$ (where $\phi = \frac{6\pi}{11}$). Upon further increasing α, all trajectories converge towards the point that in S represents the sphere of radius R_e (marked by a red dot in Fig. 2.5).

Qualitatively, this scenario remains the same for different values of k_{24}. As shown by the panels in Fig. 2.5, the only appreciable difference is that the minimizing trajectory resides on the line of genuine tactoids for a *longer* stretch when k_{24} is *smaller*. This feature has two consequences. First, for a given (sufficiently small) value of α, genuine tactoids are more *slender* for smaller k_{24}. Second, the critical value α_c, which marks the extinction of genuine tactoids, decreases as k_{24} increases. Actually, as shown in Fig. 2.6, this is a property that α_c shares with both α_c' and α_c''. This means that as k_{24} increases both tactoids and bumped spheroids persist only in smaller and smaller intervals for α, giving way to larger colonies of spheroids. In brief, we may say that k_{24} is an *antidote* to slender shapes. In particular, the tactoidal population prospers only as k_{24} decreases.

Figure 2.7 shows how this characteristic is quantitatively affected by changes in k_3. While the graph of α_c' against k_{24} is essentially the same for $k_3 = \frac{1}{2}, 1, 2$, it moves upward for $k_3 = 10$; correspondingly, all four graphs of α_c'' are orderly one above the other, keeping their features unchanged. A quantitative inspection shows that the data reported in Fig. 2.7 for α_c' and α_c'' can be given the following approximate linear representation,

$$\alpha_c' \approx 16.2 + 0.3k_3 - (14.9 - 0.1k_3)k_{24}, \tag{2.35a}$$

$$\alpha_c'' \approx 31.6 + 3.7k_3 - (21.3 - 0.02k_3)k_{24}, \tag{2.35b}$$

which show how k_3 has but a moderate role in determining the distribution of equilibrium droplet shapes. Thus, α and k_{24} remain the only effective (dimensionless) parameters of our analysis.

In Sec. 2.5, we shall detail such a shape distribution, which is one distinctive feature of this work. Other works have illuminated the multiplicity of shapes exhibited by bipolar nematic droplets. To close this section, we show how these works relate to ours.
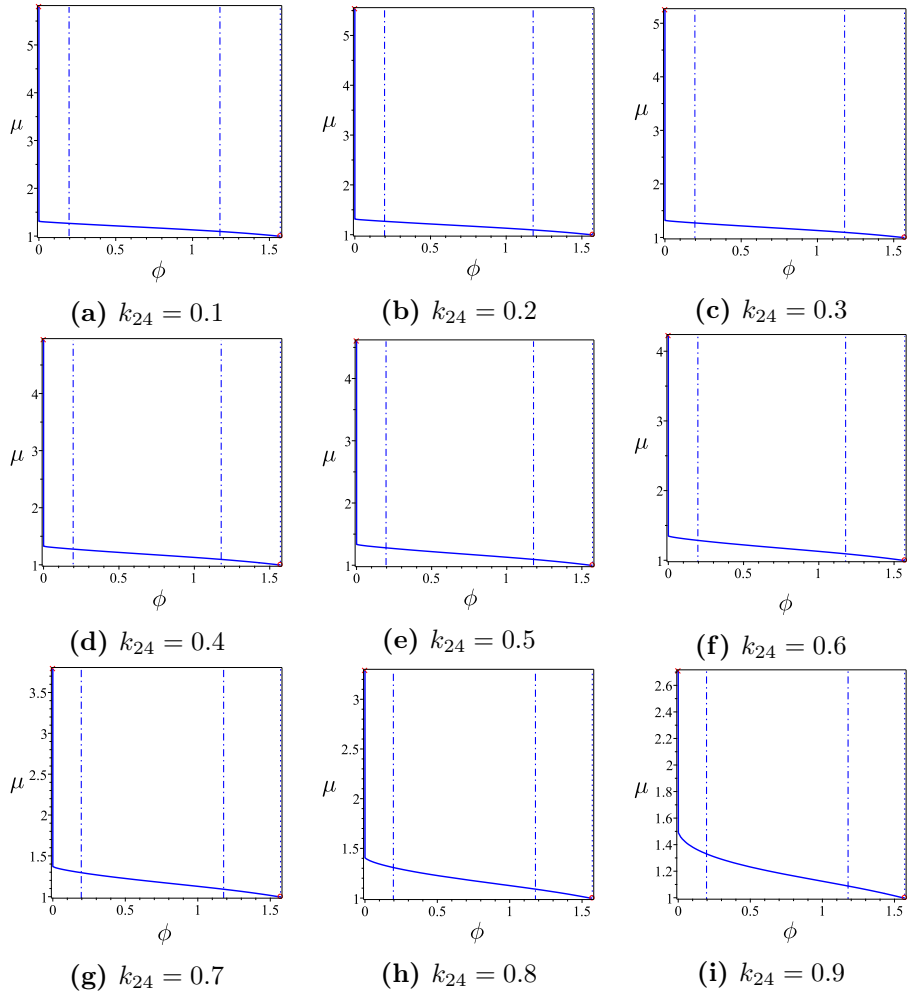
Figure 2.5: Minimizing trajectories (solid lines) in the configuration space S for $k_3 = 1$ and different values of k_{24}. All trajectories are parameterized in α and start from the configuration representing the minimum of F_α for $\alpha = 1$ (marked by a red cross); they all converge to the point representing in S the sphere of radius R_e (marked by a red circle). The dashed lines (at $\phi = \frac{\pi}{6}$ and $\phi = \frac{6\pi}{16}$) represent the barriers introduced in Sec. 2.3.3 to delimit different families of shapes.

2.4.3   Comparison with Previous Work

The variety of stable equilibrium shapes offered by nematic bipolar droplets has been the object of a remarkable series of theoretical papers, inspired by the seminal work of Williams [133]. In particular, the papers [105, 106, 107, 60, 61] have followed in the same footsteps, sharing the original geometrical approach, which, as we shall see here, is unrelated to ours.

The class of admissible droplet shapes suggested by Williams includes spindles and spheres, all obtained by rotating about the z-axis a circular segment hinged at the points $z = \pm R_0$ (the poles of the drop), see Fig. 2.8. On a meridian cross-section of the drop, the integral lines of the family of admissible director fields are Apollonian circles passing through both poles with radius increasing on approaching the z-axis (see, for example, §2 of [91]). Thus, in the parameterization introduced in Sec. 3.2, the boundary $\partial \mathscr{B}$ of the drop is described by the function

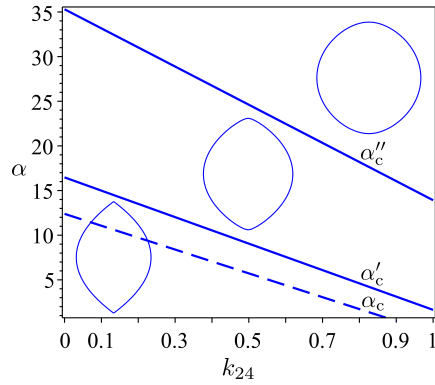$$R(z) = \sqrt{R_0^2 + x_0^2 - z^2} - x_0, \quad z \in [-R_0, R_0], \tag{2.36}$$

Figure 2.6: Critical values of α plotted against k_{24} for $k_3 = 1$. The lowest (dashed) line, α_{c}, designates the extinction of genuine (sharply pointed) tactoids; the middle line, α'_{c}, marks the extinction of tactoids (pointed or not) and the onset of bumped spheroids; the upper line, α''_{c}, marks the extinction of bumped spheroids and the onset of spheroids.
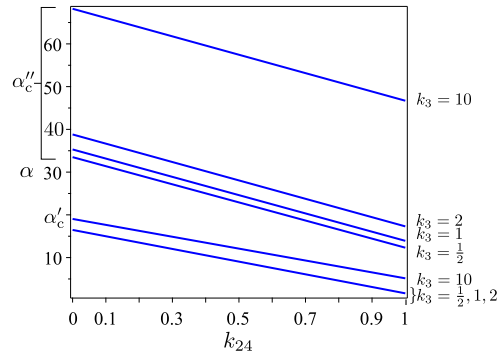
Figure 2.7: The critical values α'_{c} and α''_{c} plotted against k_{24} as in Fig. 2.6, but for four different values of k_3, namely, $k_3 = \frac{1}{2}, 1, 2, 10$. While the first three graphs of α'_{c} virtually coalesce on one another and are not discernible at this scale, the corresponding graphs of α''_{c} are one above the other, ordered like the values of k_3.

Figure 2.8: Apollonian family of shapes. The boundary $\partial \mathscr{B}$ is obtained by rotating a circular segment about the z-axis, so that the profile $R(z)$ is described by (2.36). The integral lines of the director field $\boldsymbol{n}$ are a family of circles represented by $R_t(z)$ in (2.37). For $t \to \infty$, R_t tends to the z-axis, whereas it represents the droplet's boundary for $t = 0$.

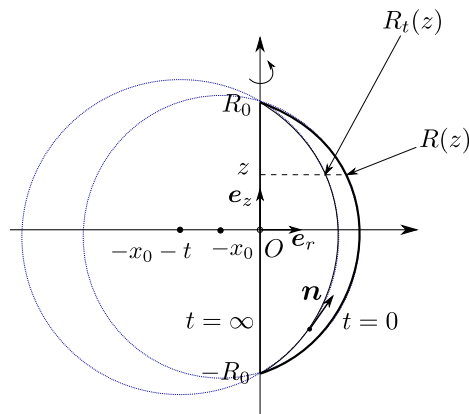where the point $(-x_0, 0)$ in the $(\boldsymbol{e}_r, \boldsymbol{e}_z)$ plane is the center of the bounding Apollonian circle (for $x_0 = 0$, the drop is spherical). Accordingly, the integral lines of the director field $\boldsymbol{n}$ are circles in a family parameterized by $t \in [0, +\infty)$:

$$R_t(z) = \sqrt{R_0^2 + (x_0 + t)^2 - z^2} - (x_0 + t), \tag{2.37}$$

where the point $(-(x_0 + t), 0)$ in the $(\boldsymbol{e}_r, \boldsymbol{e}_z)$ plane is the center of a circle passing through the poles. The curves of this family at $t = 0$ and $t = +\infty$ correspond to the boundary of the drop and to its symmetry axis, respectively.

It is now a simple exercise to show that this family of shapes does not fall within that introduced in Sec. 3.2, as there is no function $g(t)$ such that $R_t(z)$ in (2.37) could be expressed as $R_t(z) = g(t)R(z)$, with $R(z)$ as in (2.36). To afford a fair comparison between our approach and this one, we need to compare the minima of the total free-energy $\mathscr{F}[\mathscr{B}]$ computed with the two methods.

The total free-energy in (2.17) associated with a droplet described by R in (2.36) has been computed in [107], see in particular their equation (12), which we now transliterate in our language. Instead of μ, defined in (3.8), Prinsen and van der Schoot [107] used the aspect ratio $\varepsilon := R(0)/R_0 \leqq 1$ to parameterize tactoids in their class of shapes. By letting the droplet's volume V_0 be expressed as in (A.14) of [107] (where, incidentally, R is to be identified with our R_e), we easily arrive at the relation

$$\mu(\varepsilon) := \frac{2}{\sqrt[3]{\left(\frac{1+\varepsilon^2}{\varepsilon}\right)^2 \left(1 - \frac{1-\varepsilon^2}{\varepsilon} \arctan \varepsilon\right) - 4}}, \tag{2.38}$$

which shows how μ and ε are in a one-to-one correspondence, with $\mu(1) = 1$ and $\mu(\varepsilon) \to \infty$ as $\varepsilon \to 0$. In [107], the dimensionless strength of surface energy is defined as

$$\upsilon := V_0 \left(\frac{\gamma \omega}{\widetilde{K}_{11}}\right)^3, \tag{2.39}$$

where $\widetilde{K}_{11} := K_{11} - K_{24}$ is the *reduced* splay constant[20] and we replaced their τ with our γ (with the same physical meaning). Making use of (2.39), (2.38), and (3.12) in (12) of [107], having noted that there $\widetilde{F} = \mathscr{F}/\gamma V_0^{2/3}$, we arrive at the following form for the reduced total free-energy in terms of ε,

$$F_\mathrm{t}(\varepsilon) := \frac{\mathscr{F}[\mathscr{B}]}{2\pi K_{11} R_\mathrm{e}} = \mu(\varepsilon) \left\{ \left(2(1 - k_{24}) + \frac{3}{2}k_3 + \alpha \frac{1+\varepsilon^2}{\varepsilon} \mu(\varepsilon) \right) \left(1 - \frac{1-\varepsilon^2}{\varepsilon} \arctan \varepsilon \right) \right.$$
$$\left. - 2k_3 \arctan^2 \varepsilon \right\}. \tag{2.40}$$

It is not difficult to show that F_t is a function that diverges like $1/\varepsilon^{1/3}$ as $\varepsilon \to 0$ and has a single minimum for $0 < \varepsilon < 1$, which approaches $\varepsilon = 1$ as $\alpha \to \infty$. Moreover,

$$F_\mathrm{t}(1) = 2 + \left(\frac{3}{2} - \frac{\pi^2}{8}\right) k_3 + 2(\alpha - k_{24}), \tag{2.41}$$

which agrees with formula (2.18) of [133] for the reduced free-energy of a bipolar sphere. Thus, in this theory, the minimum of the free-energy is attained on a bipolar tactoid.[21] Differently said,

---

[20]As already recalled, in this theory, K_{24} enters only through a renormalization of K_{11}.

[21]Leaving aside the possibility that it undergoes the twisting instability first predicted in [133] for sufficiently large values of K_{11}.

there is no critical value of α above which the equilibrium shape of the droplet becomes smooth, although remaining elongated, which is a feature of the theory presented in this Chapter.

To ascertain whether the smoothening transition that we predict is real or not, we need compare the minimum of $F_t(\varepsilon)$ for ε in $[0,1]$ and the minimum of $F_\alpha(\phi, \mu)$ in S. Unfortunately, we do not have a general closed-form formula for $F_\alpha(\phi, \mu)$ to be compared with (2.40), and so generically the comparison between minima is to be performed numerically.

There are two instances worth mentioning for which we can provide closed-form expressions for $F_\alpha(\phi, \mu)$. These are for $\phi = 0$ and any μ, corresponding to genuine tactoids, and for $\phi = \frac{\pi}{2}$ and $\mu = 1$, corresponding to the sphere of radius R_e. We record both formulae in Appendix 2.C, for the reader's convenience; the energy of the sphere in (2.51) is the one that especially interests us here. Contrasting it with (2.41) shows that the asymptotic behavior as $\alpha \to \infty$ of $F_t(1)$ and $F_\alpha(\frac{\pi}{2}, 1)$ is the same. Now, since the minimizing shapes for both F_t and F_α converge to the sphere as $\alpha \to \infty$, we conclude that for sufficiently large α we cannot distinguish between the two theories. But we can for finite values of α.

We computed the relative energy difference ΔF defined as

$$\Delta F(\alpha) := \frac{\min_{(\phi, \mu)} F_\alpha(\phi, \mu) - \min_\varepsilon F_t(\varepsilon)}{\min_\varepsilon F_t(\varepsilon)}. \tag{2.42}$$

The graph of ΔF against α for $k_{24} = 0.7$ and three values of k_3 is plotted in Fig. 2.9; it
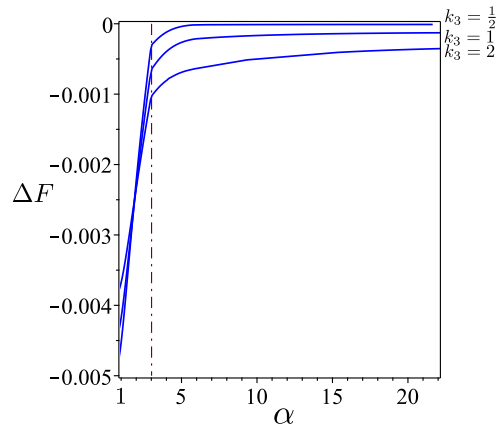

Figure 2.9: Plots of the relative energy difference ΔF against α, according to (2.42), for $k_{24} = 0.7$ and $k_3 = \frac{1}{2}, 1, 2$. The dashed straight line marks the critical value $\alpha_c \doteq 3.02$ (virtually identical in the three cases) where our theory predicts that the minimizing droplet's shape ceases to be a genuine tactoid.

shows that ΔF, although tiny in absolute value, is always *negative*. This property has been confirmed for similar numerical computations performed for $k_{24} = 0.2$ and $k_{24} = 0.4$. We have thus good reasons to hold that smooth shapes, be they generic tactoids or bumped spheroids, are energetically more favorable than genuine tactoids. We shall substantiate this claim more quantitatively in the following section.

2.5   Shape Populations

Typical methods for generating liquid crystal droplets produce a wide range of droplet sizes. For simplicity, we assume that droplets are uniformly distributed in size within a certain volume interval $(V_0, V_0 + \delta V)$. Correspondingly, in view of (3.12), for given isotropic interfacial tension and elastic constants, α ranges in an interval $(\alpha_0, \alpha_0 + \delta\alpha)$.

We have already seen in Figs. 2.6 and 2.7 how the width of the strips in (k_{24}, α) plane inhabited by different droplet's shapes depends on k_{24}. Assuming uniform distribution of droplets in a probe volume interval (parameterized in α), we convert this information into a frequency of occurrence in the whole equilibrium shape population of the three distinctive shapes that we have identified as most easily recognizable, namely, tactoids (either genuine or not), bumped spheroids, and spheroids. Formally, for given k_{24}, the frequency of occurrence f of a shape is defined as the ratio of the span of values of α where the selected shape occurs at equilibrium over the whole explored range $\delta\alpha$. These frequencies depend non-trivially on k_{24}; they suggest themselves as possible statistical measures for k_{24}, based on shape recurrence.

Figure 2.10 shows the graphs of f for the three shape populations as functions of k_{24}, for $0 < \alpha < 100$. It is clear that the population of tactoids is depleted as k_{24} grows; the same
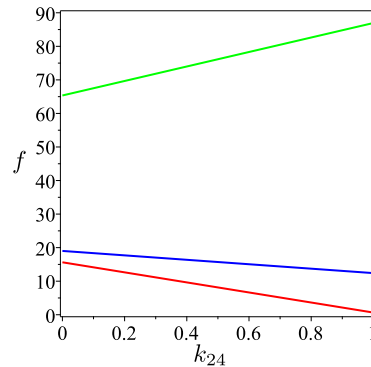

Figure 2.10: Relative frequencies (in percentage) for the occurrence of tactoids (red), bumped spheroids (green) and spheroids (blue) in the population of equilibrium shapes. The three functions f are plotted against k_{24}; they have been computed for $k_3 = 1$ under the assumption that the droplet size is uniformly distributed in a range of volumes corresponding to $1 < \alpha < 100$.

trend (but with higher values) is exhibited by the population of bumped spheroids; the majority always lies with spheroids when α ranges in an interval large enough to allow them to arise. Unlike tactoids and bumped spheroids (the elongated kin), spheroids are increased in number as k_{24} increases. Thus, k_{24} depresses slim shapes, while fostering fat ones.

In Fig. 2.11, we illustrate a finer analysis of the frequencies of shapes, performed on a sequence of elementary volume intervals of equal amplitude, $\delta\alpha = 3.5$. Such a splitting of the whole range of droplet volumes in smaller intervals around increasing values reveals different scenarios in shape populations. When the average volume is small, tactoids dominate over bumped spheroids, for a wide range in k_{24}, the *equal population* point being close to $k_{24} = 1$. As the average volume increases, the equal population point decreases, until bumped spheroids displace tactoids completely. As the average volume further increases, bumped spheroids are challenged by spheroids, which first reach an equal population point with bumped spheroids close to $k_{24} = 1$ and then eventually dominate the scene completely, as the volume is further increased.

The simple morale of the whole story is that in bipolar nematic droplets the population of tactoids (and elongated shapes, in general) is favored by small saddle-splay elastic constants (compared to the splay constant), provided that the droplet (dimensionless) volume is not too large.

To isolate the role played by the droplet's volume in the distribution of equilibrium shapes, in Fig. 2.12 we plot the relative frequency of the three shapes as functions of α. These graphs are extracted from Fig. 2.6, as were those in Fig. 2.10, but assuming uniformity in the distribution of k_{24}. Again, we may say that small, intermediate, and large volumes promote tactoids, bumped
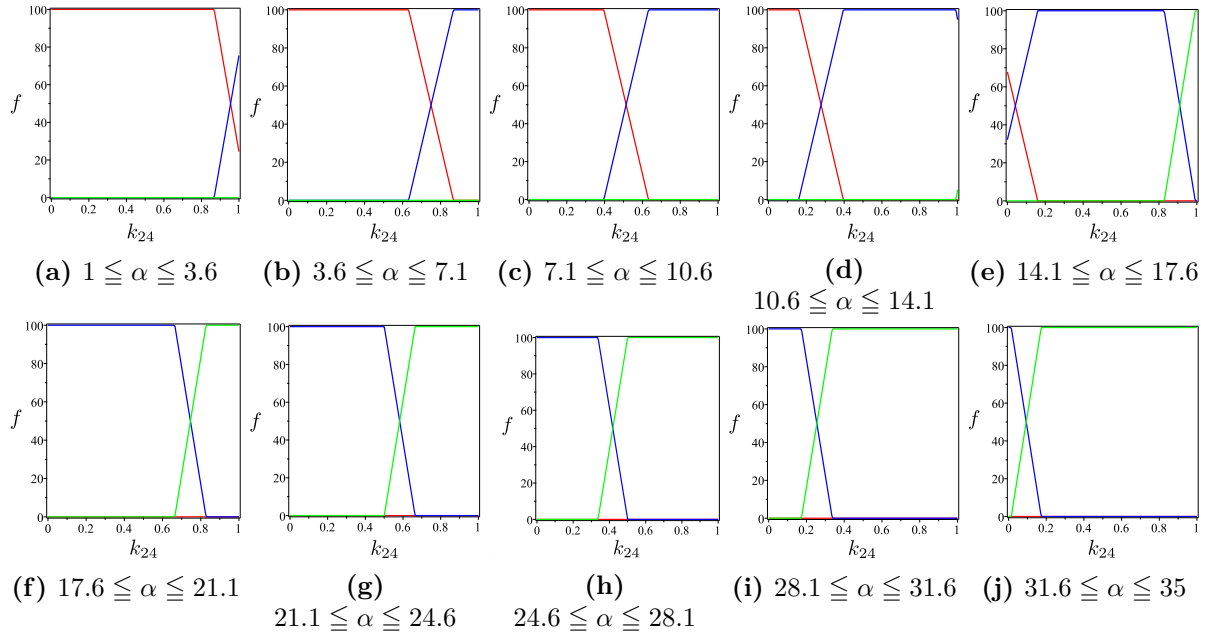
Figure 2.11: Relative frequencies (in percentage) for the occurrence of tactoids (red), bumped spheroids (green) and spheroids (blue) as functions of k_{24}, for $k_3 = 1$ and increasing values of the average volume in the specified range, under the assumption of uniform distribution in droplet size.

spheroids, and spheroids, respectively. But, perhaps, the most interesting feature shown in Fig. 2.12 is the coexistence of all shapes for moderate volumes.

2.6   Conclusions

This Chapter took a census of all possible shapes that a bipolar droplet of nematic liquid crystal can have upon varying its volume and the elastic constants of the material that constitutes it. In the adopted class of shapes, we found that either tactoids (genuine or not), bumped spheroids, and spheroids can be optimal. The prevalence in population of one shape is determined by the volume V_0 and the saddle-splay constant K_{24} (appropriately scaled). One may say that tactoids prevail when both volume and saddle-splay constant are small (with the bend constant K_{33} acting as a moderate amplifying factor). But there is more to it: for a given average volume V_0, the prevalence in shape population changes upon increasing K_{24}, shifting first from tactoids to bumped spheroids, and then from the latter to spheroids, as V_0 is increased. It may be a stretch to think that our "demographic" analysis has the potential to indicate the ballpark where to find the ratio K_{24}/K_{11} of a specific material, provided we can produce droplets in a range of wide enough volumes.

In comparing our work with others, we saw that the optimal shapes we find in our class may have slightly less energy than shapes found in other classes, but the qualitative difference in shapes was substantial even if the gain in energy was marginal. This adds to the difficulty of the problem tackled here, indicating that the energy minimum is rather shallow.

Williams [133] studied the stability of a bipolar spherical droplet against twisting distortions. This study was sharpened and extended to tactoids by Prinsen and van der Schoot [107]. As expected, large values of the splay constant K_{11} (relative to K_{22} and K_{33}) promote a twisting instability in the director field, which start exhibiting a chiral pattern around the symmetry axis.
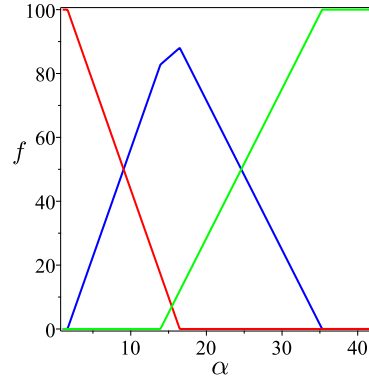
Figure 2.12: Relative frequencies (in percentage) for the occurrence of tactoids (red), bumped spheroids (green) and spheroids (blue) as functions of the (reduced) volume α, for $k_3 = 1$ and under the assumption of uniform distribution in the (dimensionless) saddle-splay constant k_{24}.

It would be desirable to find the critical value of K_{11} below which the bipolar droplets studied in this Chapter are stable, as our conclusions are valid only in this regime. In light of the role played by K_{24} in determining the optimal bipolar droplet, we expect that their range of stability would also be affected in novel ways. This is likely to shed new light on the chiral symmetry breaking exhibited by tactoids in some chromonic liquid crystals [123, 55, 104].

2.A   Retracted Meridian Field

Our aim here is to justify the expression (3.57) for the gradient of the the retracted meridian field $\boldsymbol{n}$ in (3.44).

First, we remark that differentiating $\boldsymbol{n}$ along the smooth curve $\xi \mapsto (t(\xi), \vartheta(\xi), z(\xi))$ introduced in Sec. 2.3 we easily obtain from (3.44) that

$$\dot{\boldsymbol{n}} = \frac{g'R'\dot{t} + gR''\dot{z}}{1 + (gR')^2}\boldsymbol{n}_\perp + \frac{gR'\dot{\vartheta}}{\sqrt{1 + (gR')^2}}\boldsymbol{e}_\vartheta, \tag{2.43}$$

where a superimposed dot denotes differentiation with respect to ξ and use also been made of (3.45).

Now, $\nabla\boldsymbol{n}$ must be such that

$$\dot{\boldsymbol{n}} = (\nabla\boldsymbol{n})\dot{\boldsymbol{p}}, \tag{2.44}$$

where $\dot{\boldsymbol{p}}$ is as in (2.8) for arbitrary $(\dot{t}, \dot{\vartheta}, \dot{z})$. Since $\boldsymbol{n}$ is a unit vector field and we wish to express its gradient $\nabla\boldsymbol{n}$ in the orthonormal frame $(\boldsymbol{n}, \boldsymbol{n}_\perp, \boldsymbol{e}_z)$, we can write

$$\nabla\boldsymbol{n} = \boldsymbol{n}_\perp \otimes \boldsymbol{a} + \boldsymbol{e}_\vartheta \otimes \boldsymbol{b}, \tag{2.45}$$

where $\boldsymbol{a} = a_1\boldsymbol{n} + a_2\boldsymbol{n}_\perp + a_3\boldsymbol{e}_\vartheta$ and $\boldsymbol{b} = b_1\boldsymbol{n} + b_2\boldsymbol{n}_\perp + b_3\boldsymbol{e}_\vartheta$, with a_i and b_i scalar components to be determined. Thus, (3.52) also reads as

$$\dot{\boldsymbol{n}} = (\boldsymbol{a} \cdot \dot{\boldsymbol{p}})\boldsymbol{n}_\perp + (\boldsymbol{b} \cdot \dot{\boldsymbol{p}})\boldsymbol{e}_\vartheta. \tag{2.46}$$

Making use of (2.8) and both (3.44) and (3.45), we readily see that

$$\boldsymbol{x} \cdot \dot{\boldsymbol{p}} = \frac{g'R(gR'x_1 + x_2)\dot{t}}{\sqrt{1 + (gR')^2}} + gRx_3\dot{\vartheta} + \sqrt{1 + (gR')^2}x_1\dot{z}, \tag{2.47}$$

for any vector $\boldsymbol{x} = x_1\boldsymbol{n} + x_2\boldsymbol{n}_\perp + x_3\boldsymbol{e}_\vartheta$. Specializing (3.55) for $\boldsymbol{x} = \boldsymbol{a}$ and $\boldsymbol{x} = \boldsymbol{b}$ and inserting both resulting equations in (3.54) alongside with (3.51), we obtain an identity for arbitrary $(\dot{t}, \dot{\vartheta}, \dot{z})$ only if the components of $\boldsymbol{a}$ and $\boldsymbol{b}$ in the frame $(\boldsymbol{n}, \boldsymbol{n}_\perp, \boldsymbol{e}_z)$ are given by

$$a_1 = \frac{gR''}{\left(1 + (gR')^2\right)^{3/2}}, \quad a_2 = \frac{R'}{R}\frac{1}{\sqrt{1 + (gR')^2}} - \frac{g^2 R' R''}{\left(1 + (gR')^2\right)^{3/2}}, \quad a_3 = 0, \tag{2.48a}$$

$$b_1 = b_2 = 0, \quad b_3 = \frac{R'}{R}\frac{1}{\sqrt{1 + (gR')^2}}, \tag{2.48b}$$

which with the aid of (3.53) deliver (3.57) in the main text.

2.B   Tactoidal Measure

In this Appendix, we introduce a tactoidal measure to justify the conventional choices made in Sec. 2.3.3 to classify the different shapes that inhabit the special family represented by (2.22).

Consider the angle β that the tangent to the drop's profile makes with the symmetry axis (see Fig. 2.1). If for $\mu = 1$ we draw the graph of β as a function of z, we observe a drastic difference in the two cases $\phi = 0$ and $\phi = \frac{\pi}{2}$, corresponding to a shape $\mathscr{B}$ that is a genuine tactoid and the round sphere, respectively. In the former case, the graph is concave, whereas it is convex in the latter. There is indeed more to that: as also shown in Fig. 2.13, as soon as $\phi > 0$, the graph of β exhibits an inflection point at $z = \tau > 0$, which slides gradually towards $z = 0$ (corresponding to the equator of the drop) as ϕ increases towards $\frac{\pi}{2}$.[22]
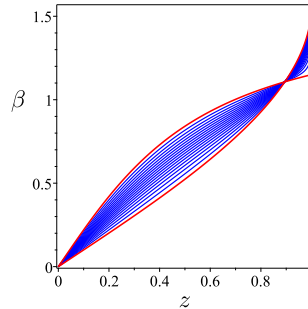
Figure 2.13: Graphs of β against z according to (2.49) for several values of $0 \leqq \phi \leqq \frac{\pi}{2}$. The concave red curve corresponds to $\phi = 0$, whereas the convex red curve corresponds to $\phi = \frac{\pi}{2}$. All other (blue) curves in the pencil interpolating the red curves have an inflection point (besides that at $z = 0$), which defines τ.

It is precisely τ that we take as a *tactoidal measure*. The closer is τ to unity, the more likely is $\mathscr{B}$ to look like a tactoid (even if its outer unit normal $\boldsymbol{\nu}$ is continuous throughout $\partial\mathscr{B}$). Formally,

$$\beta = \arctan\left(\frac{2\cos\phi}{\sqrt{h(\phi)}}z + \frac{\sin\phi}{\sqrt{h(\phi)}}\frac{z}{\sqrt{1 - z^2}}\right) \tag{2.49}$$

and τ is defined as the positive root of the equation $\beta''(z) = 0$.

Figure 2.14 illustrates how τ depends on ϕ. A simple asymptotic analysis shows that $1 - \tau = O(\phi^{2/5})$ as $\phi \to 0$ and that a bifurcation of τ occurs out of the trivial inflection point of β at $z = 0$ for $\phi \doteq 1.46\,\mathrm{rad}$. It is remarkable how the graph of τ in Fig. 2.14 exhibits a nearly linear behavior between two "knees", the first upward and the second downward, which are approximately placed

---

[22]It is perhaps in order to remark that $z = 0$ is an inflection point for $\beta(z)$, for all values of ϕ, see also (2.49).

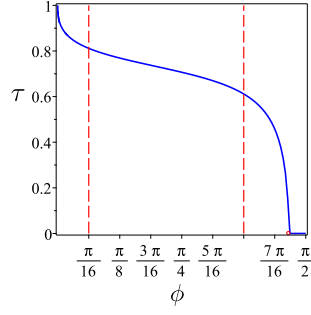**Figure 2.14:** The graph of the tactodial measure τ against ϕ. The circle marks the point at $\phi \doteq 1.46\,\mathrm{rad}$, where τ bifurcates off the trivial inflection point for β at $z = 0$. The two dashed vertical (red) lines delimit the nearly linear behavior of τ between two "knees" (one upward and the other downward); they are placed approximately at $\phi = \frac{\pi}{16}$ and $\phi = \frac{6\pi}{16}$, which are precisely the barriers conventionally introduced in configuration space to delimit the range of bumped spheroids, see Fig. 3.4.

at $\phi = \frac{\pi}{16}$ and $\phi = \frac{6\pi}{16}$. In Sec. 2.3.3, we interpreted the former as the upper limit for a tactoidal shape and the latter as the upper limit for what we called a bumped spheroid.

We fully appreciate that a good deal of conventionality remains attached to this choice of ours and to the taxonomy of shapes that ensued in Sec. 2.3.3. Perhaps, the best way to convince the reader that it has some merit is to see it at work in Fig. 3.5. In any event, here we have recounted the (possibly meandering) path that we took to identify the barriers that delimit the range of bumped spheroids in the configuration space shown in Fig. 3.4.

2.C The Energy of Genuine Tactoids and Sphere

Here we record the closed-form formulae that can be obtained by performing the integrals in (2.17) for special values of the parameters (ϕ, μ) featuring in (2.22) via (3.20).

For genuine tactoids, corresponding to $\phi = 0$ and any μ,

$$
\begin{aligned}
F_\alpha(0,\mu) = \sqrt{5\mu}\arctan\sqrt{\frac{5}{\mu^3}} &\left[\frac{1}{5}\left(\frac{47}{32} - \frac{3}{32}k_3 - k_{24}\right)\mu^2 + \left(\frac{1}{16}(13 - k_3) - k_{24}\right)\frac{1}{\mu} + \frac{5}{32}\left(\frac{1}{3} + k_3\right)\frac{1}{\mu^4}\right] \\
&+ \left(\frac{1}{3}\ln\left(1 + \frac{5}{\mu^3}\right) + \frac{1}{32}(3k_3 - 47) + k_{24}\right)\mu + \frac{5}{32}\left(\frac{1}{3} + k_3\right)\frac{1}{\mu^2} \\
&+ \frac{1}{2}\alpha\left[\ln\left(\sqrt{\frac{5}{\mu^3}} + \sqrt{1 + \frac{5}{\mu^3}}\right)\left(1 + \frac{1}{20}\mu^3\right)\mu^2 + \frac{\sqrt{5}}{2}\sqrt{\mu^3 + 5}\left(\frac{1}{\mu} - \frac{\mu^2}{10}\right)\right].
\end{aligned}
\tag{2.50}
$$

In complete analogy to formula (2.40) for F_t in the main text, this function has a unique minimum for μ in $[0, \infty)$; it diverges to $+\infty$ like $1/\mu^{7/2}$ as $\mu \to 0$, and like $\sqrt{\mu}$ as $\mu \to \infty$.

For a sphere of radius R_e, corresponding to $\phi = \frac{\pi}{2}$ and $\mu = 1$,

$$
F_\alpha(\tfrac{\pi}{2}, 1) = \frac{1}{3}\ln 2 + \frac{23}{12} + \frac{1}{4}k_3 + 2(\alpha - k_{24}).
\tag{2.51}
$$

Chapter 3

Shape Bistability in 2D Chromonic Droplets

The preceding Chapter provides a theory for the representation of tactoids, which here is adapted to two-dimensional systems. These are droplets of chromonic liquid crystals squeezed between parallel plates inducing degenerate tangential anchoring on the nematic director; in the absence of a privileged orientation on the bounding plates, they are referred to as *degenerate substrates*, while when an easy nematic axis is prescribed they are called *aligning substrates*. According to the experimental observations in [63, 136], the droplets have both a shape and a director field uniform across the gap. Twist (both single and double [114]) is thus suppressed by symmetry and Oseen-Frank's theory should suffice. Since K_{22} plays no role but splay distortion contributes to the free-energy, we shall rescale the elastic constants to K_{11}. The solutions of the free-boundary problem of finding the optimal droplet shape at fixed area are put to the test by interpreting experimental data provided by [63] and [136]; we found a fairly good quantitative agreement between experiment and theory. Moreover, a regime of shape coexistence for larger droplets than those in the experiments is predicted: here tactoids (pointed, zeppelin-shaped droplets) and smooth-edged droplets are both local minima of the free-energy. The mathematical model for degenerate substrates included in the Chapter produces what promises to be a more accurate estimate for the isotropic surface tension at the nematic/isotropic solution interface, estimate then employed to provide a measure of the anchoring strength at the nematic polymer interface, when the substrates squeezing the drop are aligning.

3.1 Introduction

Like all lyotropic systems, CLCs have a large coexistence area in their phase diagram, where droplets in the nematic phase are at equilibrium with the surrounding melt. We shall be concerned with a two-dimensional problem, inspired by the experimental settings explored by Kim et al. [63] and by Yi & Clark [136]. Most droplets reported in [63] and [136] were *bipolar*, with point defects of $\boldsymbol{n}$ at the pointed poles. Especially, two-dimensional bipolar droplets of the chromonic N nematic phase of disodium cromoglycate (DSCG) sandwiched between glass degenerate plates, i.e. plates on which the director is bound to lie but oriented in any direction, have been the object of a thorough experimental study [63]. This Chapter includes mainly a mathematical model of this system, obtained by adapting to the two-dimensional setting the theory presented in the preceding Chapter[1]. The model first predicts a *shape bistability*, which seems characteristic of

---

[1]In the two dimensional thin film context, other models reminiscent of Landau de Gennes, which do not preclude the possibility of capturing the coexistence of nematic and isotropic states, are proposed in [44, 45] in

the two-dimensional setting and identifies a range of droplet's areas where two distinct shapes could be observed, one tactoidal, as expected, and the other *discoidal* (smooth), both bearing a bipolar arrangement of $\boldsymbol{n}$. A sort of *shape* coexistence thus parallels the phase coexistence observed in these materials. This regime manifests itself for droplets larger than those reported in [63]; to our knowledge, it has not yet been observed. Second, we use the very detailed data of [63] to compare the observed tactoidal (spindle-like) shapes with those predicted by our theory. We extract an estimate for the isotropic component of the surface tension at the droplet's interface, which turns out to be comparable in order of magnitude to the typical values measured for standard thermotropic liquid crystals ($\sim 10\,\mu\mathrm{N/m}$, see [65, p. 495]). All these results related to degenerate substrates have recently been published in [100].

At the end of each section, the model employed for degenerate substrates is extended to predict the equilibrium shapes for CLC droplets squeezed between aligning substrates, which induce a planar anchoring with a preferred surface orientation. There, too two-dimensional bipolar CLC droplets in the nematic phase appeared surrounded by the isotropic phase, but the plates bounding both the droplet and the surrounding isotropic solution are patterned with sub-micron scale line channels (with the bottom and the top channels parallel to each other) and the droplet's long axis is well aligned to the channels. The easy nematic axis coincides with the direction of the channels, and the observed shapes are rectangular cuboids with hemicylindrical ends. The regime of shape bistability for sufficiently large bipolar droplets is also predicted for aligning substrates, with the following novelty: there is a range of droplet's size where the optimal shape resemble a little baton, which is in good qualitative agreement to the experimental data. In addition, the model accounts for the elongation of the optimal drop along the channels of the substrates when its size sufficiently increases. Finally, the data collected by fitting the experiments through the solutions of the model, combined with the estimate extracted for the isotropic surface tension in the case of degenerate substrates, allow us to measure the anchoring strength at the nematic-polymer interface. The orders of magnitude of these two estimates coincide.

At the end of the Chapter, to put the theory for degenerate substrate to the test for another lyotropic system, the bipolar tactoids observed in solutions of F-actin filaments [89] are also considered. For the isotropic surface tension, we estimate a value three orders of magnitude less than for CLCs, but comparable to that measured for some phase-separated colloid-polymer dispersions [1].

In this two-dimensional setting, we can spare the trouble of the non legitimacy of the theoretical treatment of chromonics through the Oseen-Frank theory. Indeed, every out of plane distortion of the director field, including twist instability, is suppressed when the droplet is squeezed between two substrates and so neither K_{22} nor K_{24} play a role; in the present setting f_{OF} is bounded from below. The legitimacy of this theoretical treatments in three-dimensional space is considered in the second part of the thesis, namely Chapters 4, 5 and 6.

3.1.1 Plan

The Chapter is organized as follows. In Sec. 3.2, the theory presented in the preceding Chapter is adapted to the present two-dimensional settings. The optimal shapes of bipolar droplets that minimize the total free-energy functional are derived and discussed in Sec. 3.3, where we illustrate in detail the bistability scenario that we envision. We show, in particular, how the critical values of the droplet's area that delimit the corresponding shape hysteresis depend on the elastic constants of the material and also of the substrates in the aligning case. Section 3.4 is devoted to

---

order to examine the interaction between the nematic defects and isotropic-to-nematic interfaces during phase transitions.

the comparison with experiments. We contrast our predicted shapes to the observed ones and, encouraged by their agreement, we estimate the isotropic component of the surface tension for CLCs through the model proposed for the case of degenerate substrates. This latter estimate is then employed to provide a measure of the anchoring strength at the nematic-polymer interface, making use of the model which is fit to describe aligning substrates as bounding plates. Finally, in Sec. 3.6, we summarize our conclusions and comment on possible further extensions of our study. The Chapter is closed by three mathematical appendices, where we collect computational details and auxiliary results needed in the main text, but inessential to its comprehension.

3.2 Two-Dimensional Setting

Here, we set our theoretical scene; we shall first recall the energetics of a CLC drop squeezed between two parallel degenerate plates and we shall then describe both its outer profile and inner director field. Separate subsections deal with the extensions needed to study the aligning case.

The region $\mathscr{B}$ will be a thin blob representing a droplet of CLC surrounded by the isotropic solution, squeezed between two parallel plates at the distance h from one another.

Formally, $\mathscr{B} = \mathscr{R} \times [-\frac{h}{2}, \frac{h}{2}]$, where $\mathscr{R}$ is a region with piecewise smooth boundary $\partial \mathscr{R}$ in the (x, y) plane of a Cartesian frame $(\boldsymbol{e}_x, \boldsymbol{e}_y, \boldsymbol{e}_z)$ (see Fig. 3.1).

(a) No preferred orientation is present on the substrates and the axis of the drop could be orientated in any direction

(b) There is a privileged orientation on the bounding substrates, which are patterned with sub-micron scale line channels. The anchoring energy they provide is sufficiently large to align well the droplet long axis to the channels.
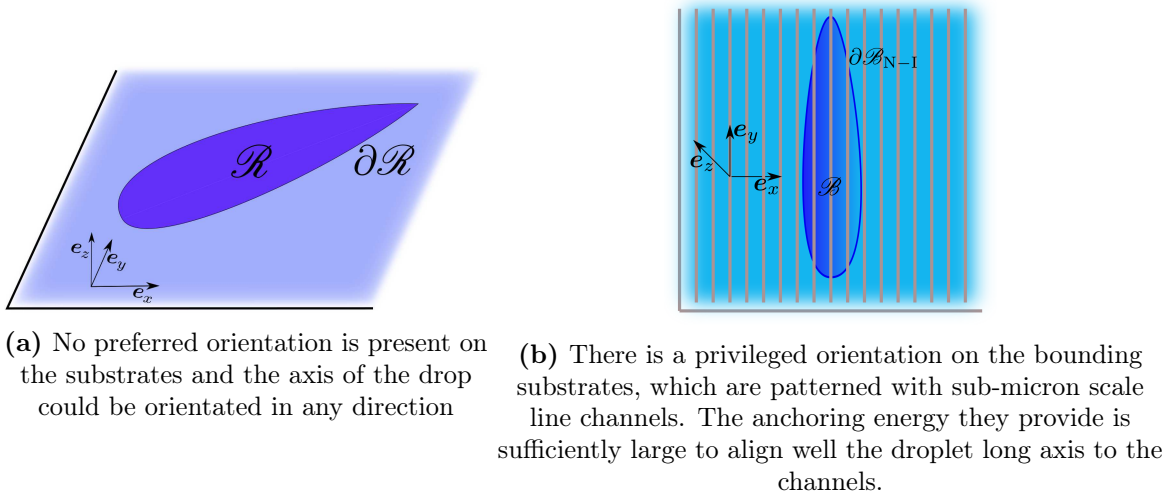
Figure 3.1: Two-dimensional domain $\mathscr{R}$ with area A_0 in the (x, y) plane. It represents the cross-section of a drop squeezed between two parallel substrates h apart and surrounded laterally by the isotropic phase. In accord with the experimental observations in [63] and in [136], both shape and director field are uniform across the gap of thickness h along $\boldsymbol{e}_z$.

The field $\boldsymbol{n}$ lies in the same plane as $\mathscr{R}$ and it is thought of as being extended uniformly through the blob's thickness. For a *planar* field of this sort, the twist term in (1.3) vanishes identically, as curl $\boldsymbol{n} \parallel \boldsymbol{e}_z$, as also does the saddle-splay term (see Appendix 3.A). Thus, leaving aside the possibly controversial issue arising in general from the violation of one of Ericksen's inequality, we remain assured that in the present setting the Oseen-Frank energy-density f_{OF} is bounded below and the free-energy $\mathscr{F}_{\mathrm{b}}$ can be safely minimized.

3.2.1   Energetics

We assume that a given mass of material constitute the blob $\mathscr{B}$, and so its volume V_0 is prescribed by the incompressibility constraint (which is satisfied to a large degree of approximation). Consequently, the area A_0 of $\mathscr{R}$ is prescribed, as $V_0 = A_0 h$. We further assume that the plates bounding both $\mathscr{B}$ and the surrounding isotropic solution exert a degenerate tangential anchoring on the nematic director $\boldsymbol{n}$, so that, in light of the constraint on the area of $\mathscr{R}$, the additional anchoring energy can be treated as an inessential additive constant.

   This is not the case for the surface energy $\mathscr{F}_{\mathrm{s}}$ at the interface between $\mathscr{B}$ and the surrounding isotropic solution, represented by (1.16) in Chapter 1. Here, this energy results as

$$\mathscr{F}_{\mathrm{s}}[\mathscr{R}, \boldsymbol{n}] = h \int_{\partial\mathscr{R}} \gamma(1 + \omega(\boldsymbol{n} \cdot \boldsymbol{\nu})^2) \, \mathrm{d}\ell, \tag{3.1}$$

where $\gamma > 0$ is the isotropic surface tension of the liquid crystal in contact with the isotropic solution, $\omega \geq 0$ is a dimensionless anchoring strength, $\boldsymbol{\nu}$ is the outer unit normal to $\partial\mathscr{R}$, and $\mathrm{d}\ell$ is the length element. Thus $\mathscr{F}_{\mathrm{s}}$ is minimized when $\boldsymbol{n}$ lies tangent to $\partial\mathscr{R}$. Henceforth, we shall enforce this minimum requirement as a constraint on $\boldsymbol{n}$,

$$\boldsymbol{n} \cdot \boldsymbol{\nu} \equiv 0, \quad \text{on} \quad \partial\mathscr{R}, \tag{3.2}$$

save checking ultimately this assumption with appropriate energy comparisons (see Appendix 3.B) which ensure that such a *tangential anchoring* is not broken. In short, the validity of (3.2) requires that the droplet is not too *small* when the substrates are both degenerate and aligning, and also not too big for the latter case. The sense of these estimates will be made precise below.

   Thus, the total free-energy of the system is given by the functional

$$\mathscr{F}[\mathscr{R}, \boldsymbol{n}] := h \left(\int_{\mathscr{R}} f_{\mathrm{OF}} \, \mathrm{d}A + \gamma\ell(\partial\mathscr{R}) \right), \tag{3.3}$$

subject to (3.2) and to the isoperimetric constraint

$$A(\mathscr{R}) = A_0, \tag{3.4}$$

where A and ℓ are the area and length measures, respectively.

Aligning Substrates

Here the plates bounding $\mathscr{B}$ and the surrounding isotropic solution are aligning: $\boldsymbol{e}_y$ is the unit vector which lies along the preferred direction, which coincides with the orientation of the channels that patter the substrates; this means that $\boldsymbol{e}_y$ is the prescribed easy axis, as all distortions of $\boldsymbol{n}$ away from it are energetically disfavorable. Considering the isoperimentric constraint (3.4), the anchoring energy $\mathscr{F}_{\sigma_0}$ for the two substrates can be defined as:

$$\mathscr{F}_{\sigma_0}[\mathscr{R}, \boldsymbol{n}] := -2\sigma_0 \int_{\mathscr{R}} (\boldsymbol{n} \cdot \boldsymbol{e}_y)^2 \, \mathrm{d}A, \tag{3.5}$$

where $\sigma_0 > 0$ is the *anchoring strength* at the N-polymer interface. In accord to the experimental setting of [136], this contribution is sufficiently large to guarantee that the droplet long axis is aligned well to $\boldsymbol{e}_y$. $\mathscr{F}_{\sigma_0}[\mathscr{R}, \boldsymbol{n}]$ is to be added to the total energy of the system when the substrates are degenerate, (3.3), and, to sum up, the total free-energy of the system bounded by two aligning substrates is given by

$$\mathscr{F}^{\mathrm{align}}[\mathscr{R}, \boldsymbol{n}] := \mathscr{F}[\mathscr{R}, \boldsymbol{n}] + \mathscr{F}_{\sigma_0}[\mathscr{R}, \boldsymbol{n}] = h \left(\int_{\mathscr{R}} f_{\mathrm{OF}} \, \mathrm{d}A + \gamma\ell(\partial\mathscr{R}) \right) - 2\sigma_0 \int_{\mathscr{R}} (\boldsymbol{n} \cdot \boldsymbol{e}_y)^2 \, \mathrm{d}A. \tag{3.6}$$

3.2.2 Admissible Shapes

No preferred direction is present on the substrates that bound the drop, and so, contemplating tactoids among the possible equilibrium shapes of $\mathscr{R}$ (as well as other smooth shapes), we assume that these are mirror symmetric about two orthogonal axes, one joining the possible sharp tips of the boundary $\partial\mathscr{R}$. We denote by y the latter axis and by x the orthogonal symmetry axis.[2] Thus, only half of the curve that bounds $\mathscr{R}$ needs to be described, the other half being obtained by mirror symmetry. We take this curve to be represented as $x = R(y)$, where y ranges in the interval $[-R_0, R_0]$, with R_0 to be determined, and R is a smooth, even function such that

$$R(R_0) = 0 \quad \text{and} \quad R'(0) = 0, \tag{3.7}$$

where a prime $'$ denotes differentiation with respect to y (see Fig. 3.2). The points where R
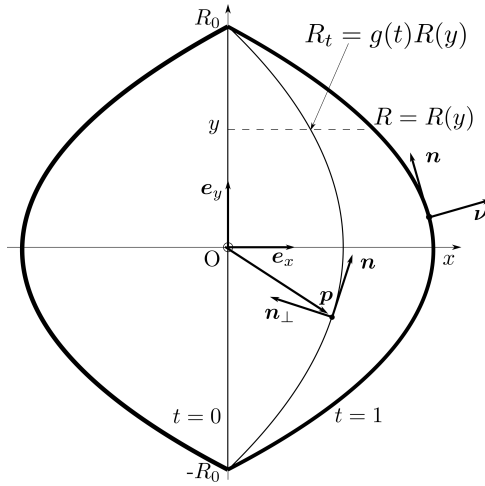

Figure 3.2: The function $R(y)$ and its retraction $R_t(y) = g(t)R(y)$ represent (half) the boundary $\partial\mathscr{R}$ and retracted inner curves $\partial\mathscr{R}_t$ for generic $t \in [0, 1]$. The nematic director $\boldsymbol{n}$ is the unit vector field everywhere tangent to the retracted curves; $\boldsymbol{n}_\perp = \boldsymbol{e}_z \times \boldsymbol{n}$ is the orthogonal field, and $\boldsymbol{\nu}$ is the outer unit normal to $\partial\mathscr{R}$, where $\boldsymbol{\nu} = -\boldsymbol{n}_\perp$. The function R represents half a drop; the other half is obtained by mirror symmetry about the y axis.

vanishes correspond to the *poles* of $\mathscr{R}$. Whenever $R'(R_0)$ is finite, R represents a tactoid, as the outer unit normal $\boldsymbol{\nu}$ to $\partial\mathscr{R}$ is discontinuous at the poles. Smooth shapes correspond to $R'(R_0) = -\infty$.

We call R_e the radius of the *equivalent* disc, which has area A_0, and we denote by μ the dimensionless length of the semi-axis of the drop,

$$\mu := \frac{R_0}{R_e}. \tag{3.8}$$

Hereafter, we shall rescale all lengths to R_e (while keeping their names unchanged, to avoid typographical clutter). With this normalization, the area constraint (3.4) reads simply as

$$\int_{-\mu}^{\mu} R(y)\,\mathrm{d}z = \frac{\pi}{2}. \tag{3.9}$$

---

[2]Clearly, due to the absence of a privileged orientation on the bounding substrates, the y axis could indeed be oriented in any direction. If several drops are present, their axes would be isotropically distributed. For aligning substrates with sufficiently high anchoring energy, their axes would be all oriented in the direction of the easy axis, $\boldsymbol{e}_y$.

Aligning substrates

The assumption of mirror symmetry about the orthogonal axes x and y of the shape of $\mathscr{R}$ is here justified by the preferred direction present on the bounding substrates designates by $\boldsymbol{e}_y$ which is directed as the axis of the drop.

3.2.3   Director Retraction

The shape of $\mathscr{R}$ is unknown and needs to be determined. Since $\boldsymbol{n}$ is tangent to $\partial\mathscr{R}$, following [99] we devise a method that also derives $\boldsymbol{n}$ inside $\mathscr{R}$ from the knowledge of $\partial\mathscr{R}$, thus reducing the total free-energy $\mathscr{F}$ to a pure *shape* functional. This is achieved by *retracting* $\partial\mathscr{R}$ inside $\mathscr{R}$ with its tangent field $\boldsymbol{n}$.

Formally, we define a function $R_t(y) := g(t)R(y)$, where $t \in [0,1]$ and g is an increasing monotonic function such that $g(0) = 0$ and $g(1) = 1$. The graph of R_t, shown in Fig. 3.2, represents the *retraction* of $\partial\mathscr{R}$ that borders an inner domain $\mathscr{R}_t \subseteq \mathscr{R}$. All domains $\mathscr{R}_t$ are nested one inside the other as t decreases towards 0. For $t = 0$, $\mathscr{R}_t$ reduces to the y axis. The advantage of this method is that it also affords to describe the inner director $\boldsymbol{n}$ as the field everywhere tangent to the family of curves $\partial\mathscr{R}_t$. All director fields obtained by this geometric construction are *bipolar*, in that they have two point defects at the poles; in the language of Mermin [79], they are *boojums* with topological charge $m = +1$ (see also [65, p. 501]).

It is shown in Appendix 3.A how to compute the area element $\mathrm{d}A$ in the (t, y) coordinates and how to express $\nabla\boldsymbol{n}$ in the orthonormal frame $(\boldsymbol{n}, \boldsymbol{n}_\perp)$, where $\boldsymbol{n}_\perp := \boldsymbol{e}_z \times \boldsymbol{n}$, in terms of the functions $R(y)$ and $g(t)$.

In the rescaled variables y and $R(y)$, an appropriate dimensionless form of $\mathscr{F}$ in (3.3) is then given by

$$F[\mu; R] := \frac{\mathscr{F}[\mathscr{B}]}{K_{11}h} = \int_{-\mu}^{\mu} \left\{ \left[\frac{R'}{R} - \frac{R''}{R'} + \frac{1}{8}\frac{RR''^2}{R'^3}(3 + k_3) \right] \arctan R' + \frac{R''}{1 + R'^2} \right.$$
$$\left. + \frac{1}{8}\frac{RR''^2}{(1 + R'^2)^2}\left[(k_3 - 5) - \frac{1}{R'^2}(k_3 + 3) \right] \right\} + 2\alpha\sqrt{1 + R'^2}\,\mathrm{d}y, \quad (3.10)$$

where

$$k_3 := \frac{K_{33}}{K_{11}} \tag{3.11}$$

is a *reduced bend* constant and

$$\alpha := \frac{\gamma R_\mathrm{e}}{K_{11}} \tag{3.12}$$

is a *reduced area*. Equivalently, $\alpha = R_\mathrm{e}/\xi_\mathrm{e}$, where ξ_e is the de Gennes-Kleman *extrapolation length* [65, p. 159].[3]

The reduced functional F in (3.10) suffers from a typical pathology of two-dimensional director theory: it diverges logarithmically to $+\infty$ near defects. Here, the culprit is the integrand $\frac{R'}{R}\arctan R'$, which is not integrable at $y = \pm\mu$. Following a well established practice (see, e.g.,[20, p. 171]), we imagine that the energy concentration near defects causes a localized transition to the isotropic phase, which constitutes a *defect core* (whose fine structure is better explored within Ericksen's theory [31]). The energy associated with such a phase transition is proportional to the core's area and will be taken as approximately fixed. Moreover, for simplicity, instead of considering a circular core, which in the most common choice, we take it in the shape

---

[3]Thus, a drop is either small or large, whether $\alpha \ll 1$ or $\alpha \gg 1$, respectively.

of the tapering drop's tip. Letting r_c denote the core's size, we set $r_c = \varepsilon R_e$ and restrict y to the interval $[-\eta, +\eta]$, where η is defined by

$$R(\eta) = R(-\eta) = \varepsilon, \tag{3.13}$$

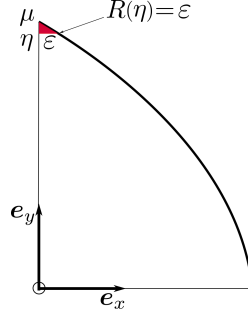and so depends indirectly on ε (see Fig. 3.3). For R_e of the order of 10μm, it is reasonable to

Figure 3.3: Isotropic defect core (in red) at the tip of a drop (only a quarter is shown). In our dimensionless units (rescaled to R_e), η is defined by (3.13). A sensible value for the parameter ε, which here is out of scale, is $\varepsilon \approx 10^{-3}$. A similar construction also applies to a drop with smooth poles (not shown here).

take $\varepsilon \approx 10^{-3}$, as we shall do here, which corresponds to r_c of the order of 10nm. The integral in (3.10) will hereafter be limited to the interval $[-\eta, +\eta]$, so that it will always converge. The extra energy stored in the defects, being approximately constant, will play no role in our quest for the equilibrium shape of squeezed drops.

Aligning substrates

The same arguments about shape representation and director retraction could be employed also for this case and in the scaled variables y and $R(y)$. We compute in Appendix 3.A the dimensionless form of the anchoring energy (3.5):

$$\mathcal{F}_{\sigma_0} := \frac{\mathscr{F}_{\sigma_0}}{K_{11}h} = -4\widetilde{\beta} \int_{-\mu}^{\mu} \frac{R}{R'} \arctan R' \, dy, \tag{3.14}$$

where $\widetilde{\beta}$ is the dimensionless parameter defined by

$$\widetilde{\beta} = \frac{\sigma_0}{K_{11}h} R_e^2. \tag{3.15}$$

Equations (3.12) and (3.15) highlight the dependence of α and $\widetilde{\beta}$ on R_e and, for fixed constitutive parameters K_{11}, γ, σ_0 and h, $\widetilde{\beta}$ can be seen as a quadratic form of α:

$$\widetilde{\beta} = \beta \alpha^2, \tag{3.16}$$

where β is the (reduced) dimensionless anchoring strength of the substrates and is defined as

$$\beta := \frac{\sigma_0 K_{11}}{h\gamma^2}. \tag{3.17}$$

The scaled total free-energy of the system in the aligning case is an appropriate dimensionless form of $\mathscr{F}^{\text{align}}$ in (3.6) and is given by

$$
F^{\text{align}}[\mu; R] := \frac{\mathscr{F}^{\text{align}}[\mathscr{B}]}{K_{11}h} = \int_{-\mu}^{\mu} \left\{ \left[(1 - 4\beta\alpha^2)\frac{R'}{R} - \frac{R''}{R'} + \frac{1}{8}\frac{RR''^2}{R'^3}(3 + k_3) \right] \arctan R' + \frac{R''}{1 + R'^2} \right.
$$
$$
\left. + \frac{1}{8}\frac{RR''^2}{(1 + R'^2)^2}\left[(k_3 - 5) - \frac{1}{R'^2}(k_3 + 3) \right] \right\} + 2\alpha\sqrt{1 + R'^2}\,\mathrm{d}y.
$$

$$(3.18)$$

It corresponds to the sum of the contribution in the degenerate case (3.10) and that provided by the aligning channels (3.14); it suffers from the same pathology as the two-dimensional director field, and so the integral in (3.18) will be limited to $[-\eta, \eta]$.

3.2.4   Special Family of Shapes

Here, we follow closely [99], albeit in a two-dimensional setting, in an attempt to restrict the admissible shapes of drops to a special family amenable to a simple analytical treatment. The admissible drop profiles will be described by the function[4]

$$
R(y) = a(\mu^2 - y^2) + b\sqrt{\mu^2 - y^2}, \tag{3.19}
$$

where a and b are real parameters that must be chosen subject to the requirements that $R(y) \geqq 0$ for all $-\mu \leqq y \leqq \mu$ and that (3.9) is satisfied. It is a simple matter to show (see also [99]) that a and b can be expressed in terms of the free parameters (ϕ, μ) that span the configuration space $\mathsf{S} := \{(\phi, \mu) : 0 \leqq \phi \leqq \frac{3\pi}{4},\ \mu > 0\}$. Precisely,

$$
a = \frac{1}{\mu^3}\frac{\pi\cos\phi}{h(\phi)}, \quad b = \frac{1}{\mu^2}\frac{\pi\sin\phi}{h(\phi)} \quad \text{with} \quad h(\phi) := \frac{8}{3}\cos\phi + \pi\sin\phi > 0, \quad 0 \leqq \phi \leqq \frac{3\pi}{4}. \tag{3.20}
$$

Shapes with different qualitative features correspond to different regions of S, as illustrated in Fig. 3.4. *Prolate* shapes are characterized by

$$
\mu \geqq \varpi(\phi) := \sqrt{\frac{\pi(\cos\phi + \sin\phi)}{h(\phi)}}, \tag{3.21}
$$

whereas *oblate* shapes are characterized by $\mu < \varpi(\phi)$. Moreover, shapes represented by (3.20) are convex for $0 \leqq \phi \leqq \phi_c := \text{arccot}\left(-\frac{1}{2}\right) \doteq 2.03$ and concave for $\phi_c < \phi \leqq \frac{3\pi}{4}$. The latter are represented by the red strip in Fig. 3.4; we call them *butterflies*: their waist narrows as ϕ approaches the boundary of S at $\phi = \frac{3\pi}{4}$, where it vanishes altogether and the droplet splits in two.

$\mathscr{R}$ has pointed tips only whenever $R'(\mu)$ is finite; according to (3.20), the only value of ϕ that makes b vanish is $\phi = 0$. We call *genuine* these tactoids. For small enough values of ϕ the shape represented by (3.19) via (3.20) cannot be visually distinguished from pointed tactoids; we find the conventional barrier at $\phi = \frac{\pi}{16}$ appropriate to delimit the realm of tactoids (genuine or not). Further increasing ϕ, $\mathscr{R}$ has tips that look smoother, justifying our calling them *discoids*. A conventional barrier is set at $\phi = \frac{9\pi}{16}$ to mark where discoids evolve into little batons, for which we use the French word *bâtonnet*. The names used to identify different shapes of $\mathscr{R}$ and the corresponding strips in S where they are found are recalled in Table 3.1.

Fig. 3.5 illustrates a gallery of shapes for $\mathscr{R}$ obtained from (3.19) and (3.20) for $\mu = 1$ and a number of values of ϕ falling in the different types listed in Table 3.1.

---

[4]For $b = 0$, R in (3.19) reduces to the parabolic profile considered in [132].
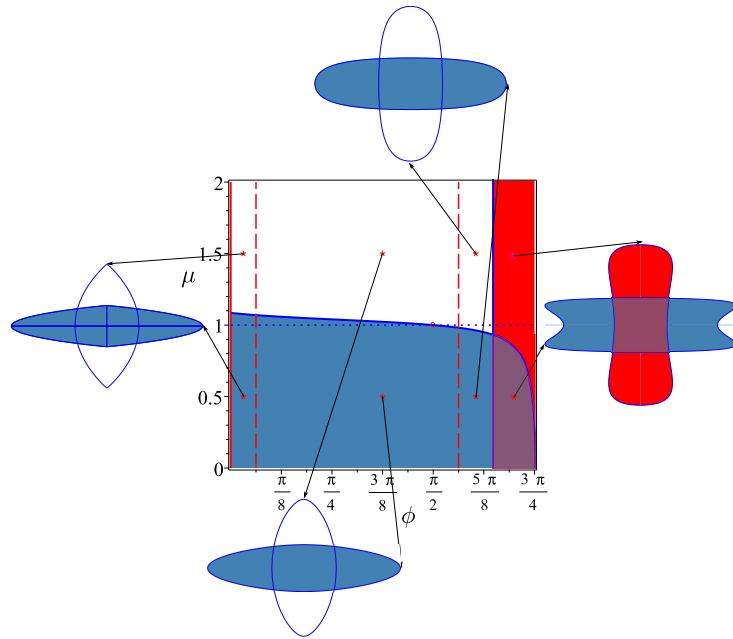
Figure 3.4: Configuration space S with the admissible shapes described by (3.19). All prolate shapes are represented by the blue region below the graph of the function $\varpi(\phi)$ in (3.21). The concave shapes that we call *butterflies* are represented by the red strip for $\phi_{\mathrm{c}} \leqq \phi \leqq \frac{3\pi}{4}$; all shapes falling on the left of this strip are convex. The circular disc is represented by the point $(\frac{\pi}{2}, 1)$ (red circle). We also call tactoids the shapes for $0 \leqq \phi \leqq \frac{\pi}{16}$ (*genuine* tactoids, only those for $\phi = 0$—red line), *discoids* those for $\frac{\pi}{16} \leqq \phi \leqq \frac{9\pi}{16}$, and *bâtonnet* those for $\frac{9\pi}{16} \leqq \phi \leqq \phi_{\mathrm{c}}$, see also Table 3.1, and Fig. 3.5 for a fuller gallery of shapes. Vertical dashed lines represent the barriers marking transitions from one family of shapes to another.

Aligning Substrates

As will be clear in Section 3.3.2, the equilibrium drops are strongly elongated in the direction of the channels and their optimal value for μ is nearly 2 for the relevant values of α. Fig. 3.6 presents a gallery of droplets obtained from (3.19) and (3.20) for $\mu = 2$ and for the values of ϕ used in Figure 3.5. It is worth mentioning that the barriers conventionally introduced in S to delimit the ranges of qualitatively different shapes do not suffer noticeable changes by changing μ.

3.3 Optimal Shapes

This section is devoted to the study of the minimizers of the free-energy functional in (3.10) for the degenerate case and in (3.18) for the aligning case. Our major result will be the prediction of a shape bistability, which has not yet been observed in this setting. Before describing this phenomenon, however, we need to make sure that the droplets we consider are of the right dimensions for the tangential anchoring condition in (3.2) to be valid; for degenerate substrates, droplets only need to be not too small, while for aligning substrates also an upper bound on their size is to be determined.

Table 3.1: We identify four strips in configuration space S, which correspond to four qualitatively different shapes for a region $\mathscr{R}$ represented by (3.19) via (3.20). Here $\phi_c = \text{arccot}\left(-\frac{1}{2}\right) \doteq 2.03$.
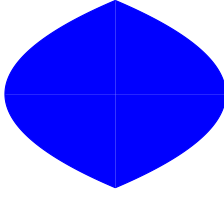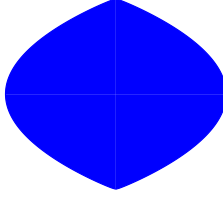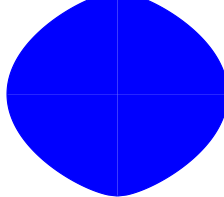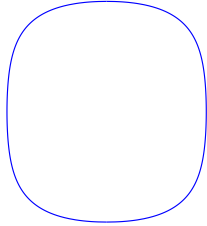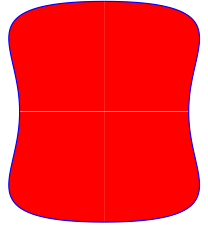
Tactoids	Discoids	Bâtonnet	Butterflies
$0 \leqq \phi < \dfrac{\pi}{16}$	$\dfrac{\pi}{16} < \phi < \dfrac{9\pi}{16}$	$\dfrac{9\pi}{16} < \phi < \phi_c$	$\phi_c < \phi \leqq \dfrac{3\pi}{4}$

(a) $\phi = 0$ **(b)** $\phi = \frac{\pi}{32}$ **(c)** $\phi = \frac{\pi}{4}$ **(d)** $\phi = \frac{10\pi}{16}$ **(e)** $\phi = \frac{11\pi}{16}$
genuine tactoid   tactoid   discoid   bâtonnet   butterfly

Figure 3.5: Gallery of shapes illustrating for $\mu = 1$ the taxonomy introduced in Table 3.1. The color coding of the shapes is the same used in Fig. 3.4.

3.3.1 Admissible Drop Sizes

It is known [126] that drops sufficiently small in three-dimensional space tend to break the director's tangential anchoring on their boundary, favouring the uniform alignment of $\boldsymbol{n}$ in their bulk. A simple heuristic argument tells us that a similar breaking would also take place in the present two-dimensional setting.

The elastic cost of the bulk deformation scales as Kh, where K is a typical elastic constant, while the surface anchoring energy scales as $\gamma \omega h R_e$, and so α in (3.12) estimates the ratio of the latter to the former. Thus, when α is sufficiently small, the bulk energy becomes dominant and it is minimized by the uniform alignment of $\boldsymbol{n}$, which breaks the tangential anchoring, undermining our analysis. In Appendix 3.B, we perform an energy comparison that provides an estimate for the *safeguard* value α_s of α, above which tangential anchoring is expected to remain unbroken. We obtained the following explicit formula for α_s,

$$\alpha_s := \frac{\frac{\pi}{4}\left(k_3 - 1 - k_3 \ln 2 - \ln \varepsilon\right) + \varepsilon}{j(\omega) - \left(\frac{\pi}{2} - \varepsilon\right) - \frac{\omega}{2}\pi\varepsilon}, \tag{3.22}$$

where $j(\omega)$ is the function defined in (3.63). For $\omega = 5$, which is a choice supported by some evidence,[5] $\alpha_s \approx 0.2k_3 - 0.5(1 + \ln \varepsilon)$. In particular, for $k_3 = 1$ and $\varepsilon = 10^{-3}$, $\alpha_s \approx 3$, which will be our reference choice henceforth. Taking $K \sim$ 1-10 pN as typical value for all elastic constants[6] and $\gamma \sim 10\,\mu\text{N/m}$ as typical value for the surface tension of a chromonic liquid crystal in contact with the isotropic solution,[7] by (3.12) taking $\alpha > 3$ means taking $R_e \gtrsim 0.3$-3 μm, which provides a lower bound on the admissible size of the droplets that can be treated within our theory.

---

[5]See, for example, [108] and [63].

[6]This estimate is supported for example by [142] for material such as DSCG, SSY, and PBG.

[7]Discordant estimates of γ have been given in the literature [63, 82, 123]. Here we take the average order of magnitude found in these works (see also Sec. 3.4.1 below for an independent justification of this choice).
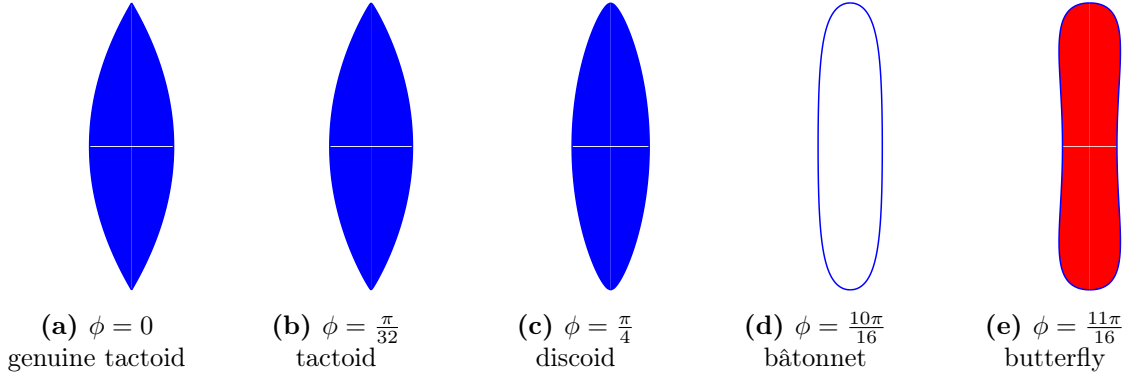
(a) $\phi = 0$
genuine tactoid

(b) $\phi = \frac{\pi}{32}$
tactoid

(c) $\phi = \frac{\pi}{4}$
discoid

(d) $\phi = \frac{10\pi}{16}$
bâtonnet

(e) $\phi = \frac{11\pi}{16}$
butterfly

Figure 3.6: Gallery of shapes illustrating for $\mu = 2$ the taxonomy introduced in Table 3.1. The color coding of the shapes is the same used in Fig. 3.4.

Aligning Substrates

It would be unwise to push our analysis beyond a further critical threshold of α. Indeed, for large values of α the anchoring term of the energy due to the aligning substrates (3.14), which is multiplied by α^2, prevails over the others and needs to be minimized by a uniform orientation of the director field along $\boldsymbol{e}_y$.

In Appendix 3.B we prove that, to ensure the planar alignment of the nematic director at the interface, the following quadratic function of α must be positive for the given values of k_3, ω, ε and β:

$$
\begin{aligned}
f_\alpha = &- 2\beta\alpha^2 \frac{\delta^2}{6} + \alpha \left[4j(\omega) - 4\delta\left(\frac{\pi}{2} + \varepsilon\right) - \frac{\pi}{\delta}\left(1 - \delta^2\right) - 2\omega\delta\pi\varepsilon \right] \\
&- 4\left[\frac{\pi}{4}\left(k_3 - 1 - k_3\ln(2) - \ln(\varepsilon)\right) + \varepsilon\right] \geq 0,
\end{aligned}
\tag{3.23}
$$

where $j(\omega)$ is the function of ω in (3.66) and $\delta \in (0, 1]$ is a parameter to be determined to make the interval of α in which the tangential surface anchoring is mantained as big as possible.

This function has two real roots, α_s^1 and α_s^2, and the condition (3.23) is equivalent to require:

$$
\alpha_s^1 \leqq \alpha \leqq \alpha_s^2,
\tag{3.24}
$$

with α_s^2 considerably affected by η (see Fig.3.22b).

For $\beta = 10^{-2}$ and for the choices of parameters made in the preceding section, i.e. $k_3 = 1$, $\varepsilon = 10^{-3}$ and $\omega = 5$, it is shown in Appendix 3.B, through the graph in Fig. 3.22b, that $\alpha_s^1 \approx 6$ and $\alpha_s^2 \approx 6057$.

By considering as in preceding Section $K_{11} \sim$ 1-10 pN and $\gamma \sim 10^{-5}\,\mathrm{Nm}^{-1}$, in view of the definition of α in (3.12) the inequalities for the admissible values of α can be interpreted as lower and upper bounds for the linear size R_e of the drops which are admissible in the theory: $(0.6 - 6)\mathrm{mm} \gtrsim R_e \gtrsim (0.6 - 6)\mu\mathrm{m}$.

3.3.2 Shape Bistability

Finding analytically the minima of the *reduced* free-energy $F_\alpha(\phi, \mu)$, the function defined on the configuration space S by computing the functional $F[\mu; R]$ in (3.10) on the special family of shapes in (3.19), is simply impractical. Thus, for a given choice of the elastic parameter k_3, we evaluated numerically F_α and we sought its minimizers in S for increasing $\alpha > \alpha_s$.

We found out that there are two critical values of α, α_1 and $\alpha_2 > \alpha_1$, such that for either $\alpha < \alpha_1$ or $\alpha > \alpha_2$, F_α attains a single (absolute) minimum in S, whereas it attains two (relative)
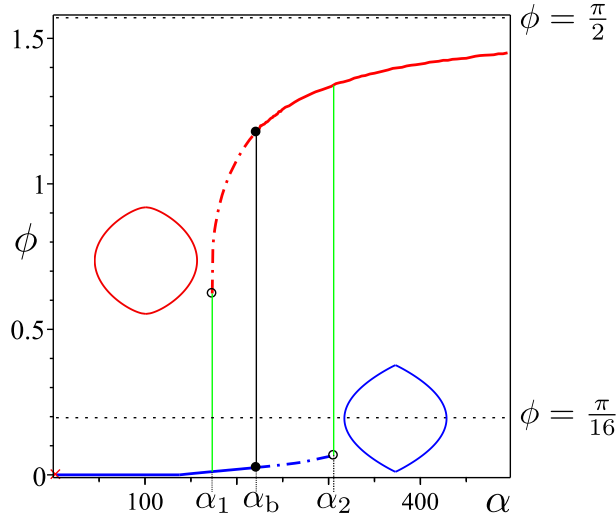
Figure 3.7: Bifurcation diagram for the parameter ϕ that describes the equilibrium profile (3.19) as a function of the bifurcation parameter α. For every k_3, there are three critical values of α, namely, α_1, α_b, and α_2. Solid lines represent global minima, while broken lines represent local minima. Open circles mark the appearance or disappearance of a local minimum at $\alpha = \alpha_1$ and $\alpha = \alpha_2$. Two green lines delimit the coexistence interval $[\alpha_1, \alpha_2]$. At $\alpha = \alpha_b$, both local minima are also global minima; two black dots mark the jump of the global minimum from one branch to the other. Here $k_3 = 1$, $\alpha_1 = 172$, $\alpha_b = 221$, and $\alpha_2 = 305$. Droplet's equilibrium shapes are drawn for the critical values α_1 and α_2.

minima for $\alpha_1 \leqq \alpha \leqq \alpha_2$. There is a third critical value, $\alpha_b \in (\alpha_1, \alpha_2)$, such that for $\alpha = \alpha_b$ the two minima of F_α are equal and its absolute minimizer abruptly shifts from one point in S to another. Were the points of S to represent the different phases of a condensed system, this scenario would be described as a (first-order) *phase transition*. In our setting, it more simply describes the (local) stability of two equilibrium shapes for a squeezed drop: for $\alpha_1 < \alpha < \alpha_2$, both a tactoid and a discoid are local energy minimzers, the global minimum shifting from the former to the latter at $\alpha = \alpha_b$. For $\alpha < \alpha_1$, the only equilibrium shape is a tactoid, whereas it is a discoid for $\alpha > \alpha_2$. The *shape bistability* exhibited by this two-dimensional system will now be documented in more detail.

We start by representing the equilibrium landscape in the language of bifurcation theory. Taking α as a bifurcation parameter and ϕ as an equilibrium shape representative, in Fig. 3.7 we illustrate the minima of F_α for $k_3 = 1$: one falls in $0 < \phi < \frac{\pi}{16}$ (blue line), and so it is a tactoid, while the other falls in $\frac{\pi}{16} < \phi < \frac{\pi}{2}$ (red line) and is a discoid. Solid lines represent global minima, while broken lines represent local minima. Two separate local minima are also global minima for $\alpha = \alpha_b$, where a perfect bistability is established between the two equilibrium branches. The tacoidal branch can be further continued, as it is locally stable, until α reaches the critical value α_2, where it ceases to exist altogether. Similarly, as soon as α exceeds α_1, the discoidal branch comes first into life as a locally stable equilibrium, which then becomes globally stable for $\alpha > \alpha_b$. For $\alpha \in [\alpha_1, \alpha_2]$, tactoids and discoids coexist as optimal shapes; both are metastable, one or the other is globally stable, according to whether $\alpha < \alpha_b$ or $\alpha > \alpha_b$.

The dimensionless parameter α is ultimately related through (3.12) to the amount of material trapped in the drop. So the coexistence interval $[\alpha_1, \alpha_2]$ corresponds to a window of areas A_0 for which two different shapes could be observed, more likely (and frequently) the one corresponding to the global minimum. If, ideally, one could gently pump material into a tactoidal drop, so as

to follow the blue branch in Fig. 3.7, the drop would continue to grow as a tactoid until the critical volume corresponds to α_2, where a dynamical instability would presumably prompt the transition towards a discoid. Conversely, if material could be gently removed from the latter, this would keep its discoidal shape until the critical volume corresponds to α_1, where it would dynamically evolve into a tactoid. The green lines in Fig. 3.7 delimit such a hysteresis loop.

Figure 3.8 illustrates the energy landscape for $\alpha < \alpha_1$; F_α is convex, and so it attains a single

(a) Graph of F_α against S; the red dot designates its single minimum.

(b) Contour plot of F_α. The minimum is attained for $\phi \doteq 0.01$ and $\mu \doteq 1.11$ (red circle).

(c) Equilibrium tactoidal shape corresponding through (3.19) to the minimizer of F_α.

Figure 3.8: For $\alpha < \alpha_1$, the reduced free-energy F_α is convex on the configuration space S and attains a single minimum in $0 < \phi < \frac{\pi}{16}$. Here, $k_3 = 1$, $\alpha = 170$, $\alpha_1 = 172$.

minimum, which falls in $0 < \phi < \frac{\pi}{16}$, corresponding to a tactoid. The scene changes in Fig. 3.9, where $\alpha = \alpha_b$ and F_α attains two equal minima, corresponding to a tactoid and a discoid. For

(a) Graph of F_α against S. F_α is no longer convex: it attains two equal minima designated by red dots.

(b) Contour plot of F_α. One minimum is attained for $\phi \doteq 0.025$ and $\mu \doteq 1.11$ (tactoid), while the other is attained for $\phi \doteq 1.2$ and $\mu \doteq 1.04$ (doscoid); both are marked by red circles.

(c) Tactoidal equilibrium shape.

(d) Discoidal equilibrium shape.
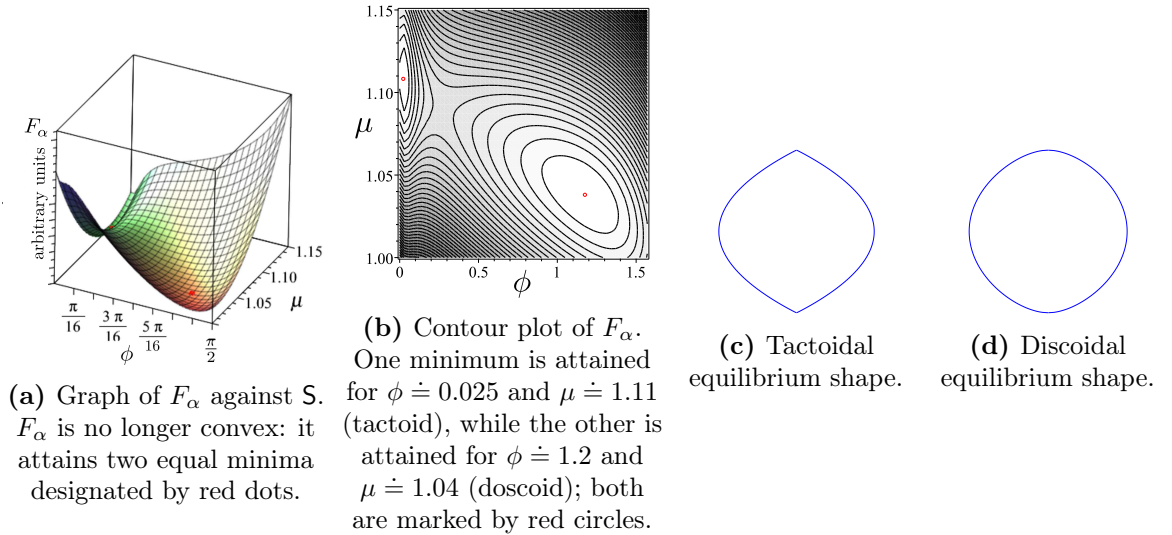
Figure 3.9: For $\alpha = \alpha_b$, the reduced free-energy F_α has two (equal) global minima, one for $0 < \phi < \frac{\pi}{16}$ (tactoid) and the other for $\frac{\pi}{16} < \phi < \frac{\pi}{2}$ (discoid). Here, $k_3 = 1$ and $\alpha_b = 221$.

$\alpha > \alpha_2$, F_α is again convex, with a single minimum on a discoid, which gets closer and closer to the round disc, represented by the point $(\frac{\pi}{2}, 1)$ in S, as α grows indefinitely.

We have computed the three critical values, α_1, α_b, and α_2 for several values of k_3. Fig. 3.11 shows that, to within a good approximation, they all grow linearly with k_3. The best linear fit

(a) Graph of F_α against S; the red dot designates its single minimum.

(b) Contour plot of F_α. The minimum is attained for $\phi \doteq 1.34$ and $\mu \doteq 1.02$ (red circle).

(c) Equilibrium discoidal shape corresponding through (3.19) to the minimizer of F_α.
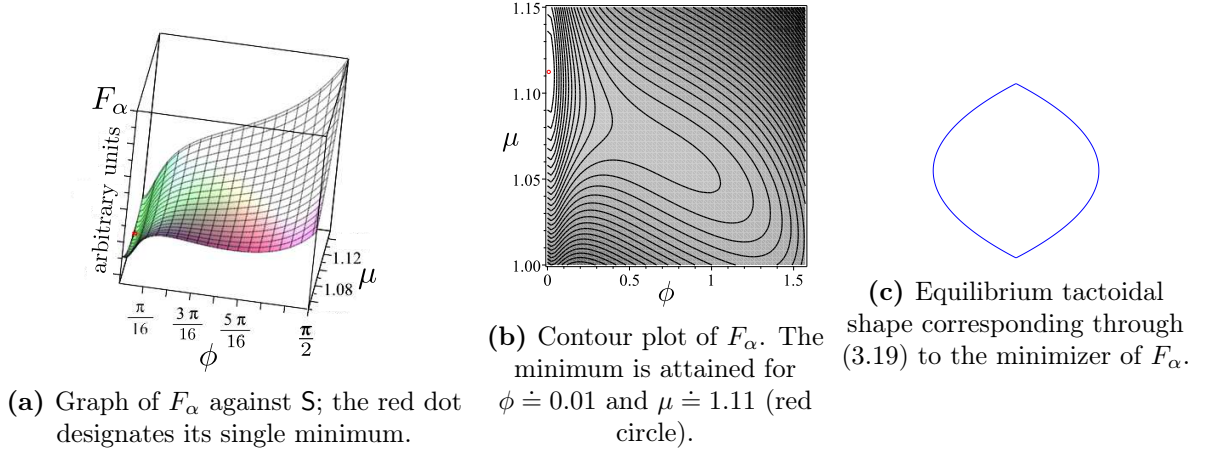
Figure 3.10: For $\alpha > \alpha_2$, the reduced free-energy F_α is gain convex on the configuration space S and attains a single minimum for $\frac{\pi}{16} < \phi < \frac{\pi}{2}$. Here, $k_3 = 1$, $\alpha = 307$, $\alpha_2 = 305$.

Figure 3.11: Critical values of α for different values of k_3. To within a good approximation, they all depend linearly on k_3. Red and blue ranges refer to discoids and tactoids, respectively, according to the same color coding adopted in Fig. 3.7. The broken lines represent the best linear fits in (3.25).

is provided by the following functions,

$$\alpha_1 \approx 157 + 15k_3, \tag{3.25a}$$
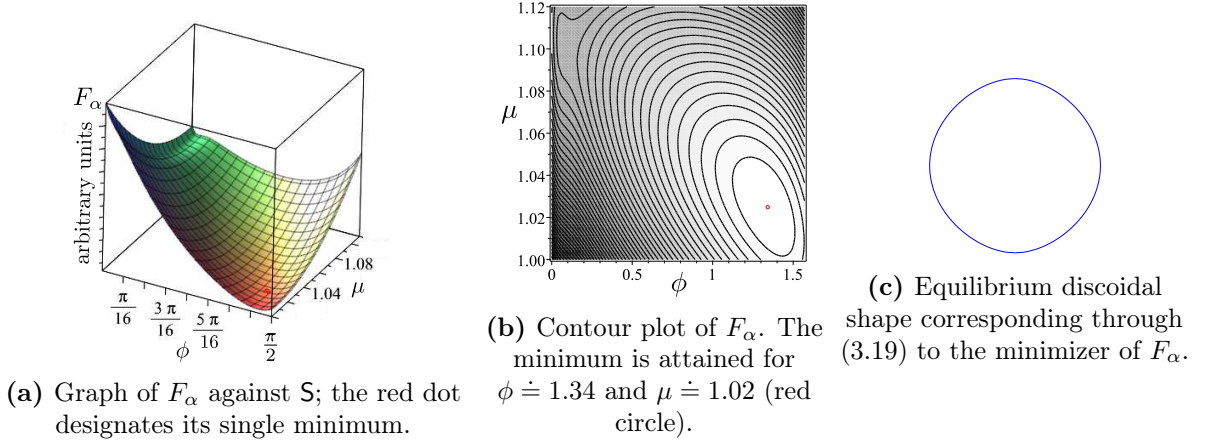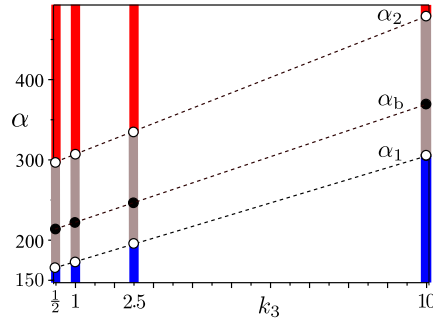
$$\alpha_b \approx 205 + 16k_3, \tag{3.25b}$$

$$\alpha_2 \approx 289 + 19k_3. \tag{3.25c}$$

Aligning Substrates

For a given choice of the elastic paramenters (k_3, β) and upon increasing values of $\alpha_s^1 < \alpha < \alpha_s^2$, we evaluate numerically $\mathcal{F}_\alpha^{\text{align}}[\phi, \mu]$, defined on the configuration space S by reducing the functional $F^{\text{align}}[\mu; R]$ in (3.18) to the special families of shapes in (3.19). Through the systematic search for the minimizers of this functional, the three critical values α_1, α_b and α_2 are also in the case of aligning substrates; this system too exhibits a regime of shape coexistence. We document this phenomenon through the language of bifurcation analysis as in the preceding section; figures 3.12a and 3.12b illustrate the bifurcation diagram for $k_3 = 1$ and $\beta = 10^{-2}$ where α is the bifurcation parameter; ϕ and μ are taken, respectively, as the parameters which represent the minima of the functional $\mathcal{F}_\alpha^{\text{align}}[\phi, \mu]$, one for $\phi < \frac{\pi}{16}$ (blue lines) and the other for $\phi > \frac{\pi}{16}$ (red lines). ϕ as a function of α suggests how equilibrium shapes are classified. In both Figures 3.12a and 3.12b, solid lines refer to the stable solution, while dashed lines represent the metastable
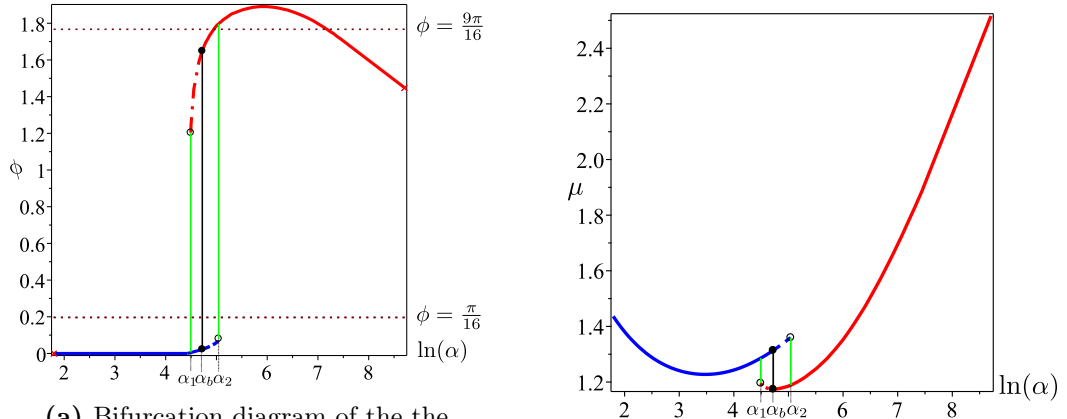
(a) Bifurcation diagram of the the representation parameter ϕ, which concerns the classification of the equilibrium profile (3.19), as a function of $\ln \alpha$. Second order transitions of the equilibrium drop, identified by the second minimum (for $\phi > \pi/16$), from coins to bâtonnet and vice versa occur when the graph in figure crosses the conventional barrier $\phi = 9\pi/16$.

(b) Bifurcation diagram of the the representation parameter μ, which refers to the length of the long-axis of the equilibrium profile (3.19) scaled to R_{e}, and so to the area of the drop, as a function of $\ln \alpha$. A growth of the optimal μ of the first and of the second minimum of $\mathcal{F}_\alpha^{\mathrm{align}}[\phi, \mu]$ occurs when α is great enough.

Figure 3.12: For each k_3, there are three characteristic values of $\alpha_s^1 \leqq \alpha \leqq \alpha_s^2$ (marked by a red crosses): α_1, α_b and α_2. Heavy lines refer to the stable solution, while the region of metastability is indentified by dashed lines. Black circles delimit the interval of coexistence of the two minimizers, since they mark the rise of the second minimum at $\alpha = \alpha_1$ and the disappearance of the first one at $\alpha = \alpha_2$. Precisely at these two last values, the green lines represent the hysteresis limits. For $k_3 = 1$ and $\beta = 10^{-2}$, the values provided by the model for aligning substrates are $\alpha_1 = 90$, $\alpha_b = 112$ and $\alpha_2 = 157$, while the range in which the equilibrium drops are bâtonnet is $[141, 1308]$.

one. The green lines delimit the hysteresis loop. Moreover, figure 3.13 illustrates the situation we encounter for $\alpha = \alpha_{\mathrm{b}}$, when the two corresponding equilibrium shapes share the same energy.

A different scenario appears as soon as α is large enough. Figure 3.12b illustrates that the anchoring term due to the substrates in (3.18) begins to play an important role in the minimization problem and induces a growth of the optimal value of μ of both the minima; it starts to increase monotonically with increasing α. This accounts for the elongation of the optimal drops along the channels of the substrates when their size increases sufficiently. In addition, not only the coins are the equilibrium shapes priviledged by the second minimum of the energy, but for a range of values of α the trajectory of the second minimum crosses the domain of the bâtonnet. For these values of α, the graph of the optimal value of ϕ in Fig. 3.12a is indeed above the barrier $\phi = \frac{9\pi}{16}$. Especially, the equilibrium drop undergoes two smooth shape transitions from a coin to a bâtonnet and vice versa. The energy landscape when α ranges in this special range is illustrated in figure 3.14.

Upon further increasing $\alpha_2 < \alpha < \alpha_s^2$, the unique minimum of $\mathcal{F}_\alpha^{\mathrm{align}}[\phi, \mu]$ does not converge towards the point representing in S the disk of radius R_{e}, but crosses the region of coins becoming more and more elongated as α increases. Figure 3.15 shows this characteristic for a large enough value of α.

(a) Graph of $\mathcal{F}_\alpha^{\mathrm{align}}[\phi, \mu]$ against S for $\alpha_b = 112$. The red dots designate the minima.

(b) Contour plot of $\mathcal{F}_\alpha^{\mathrm{align}}[\phi, \mu]$, for $\alpha_b = 112$. The first minimum is attained at the point where $\phi \doteq 0.025$ and $\mu \doteq 1.317$, while the second minimum at the point where $\phi \doteq 1.67$ and $\mu \doteq 1.17$, marked by red circles.

(c) Equilibrium shape corresponding through (3.19) to the first minimizer of $\mathcal{F}_\alpha^{\mathrm{align}}[\phi, \mu]$ marked in Fig. 3.13b. Since $\phi < \frac{\pi}{16}$, according to our conventional taxonomy, it is a tactoid

(d) Equilibrium shape corresponding through (3.19) to the second minimizer of $\mathcal{F}_\alpha^{\mathrm{align}}[\phi, \mu]$ marked in Fig. 3.13b. Since $\frac{\pi}{16} < \phi < \frac{9\pi}{16}$, according to our conventional taxonomy, it is a coin.
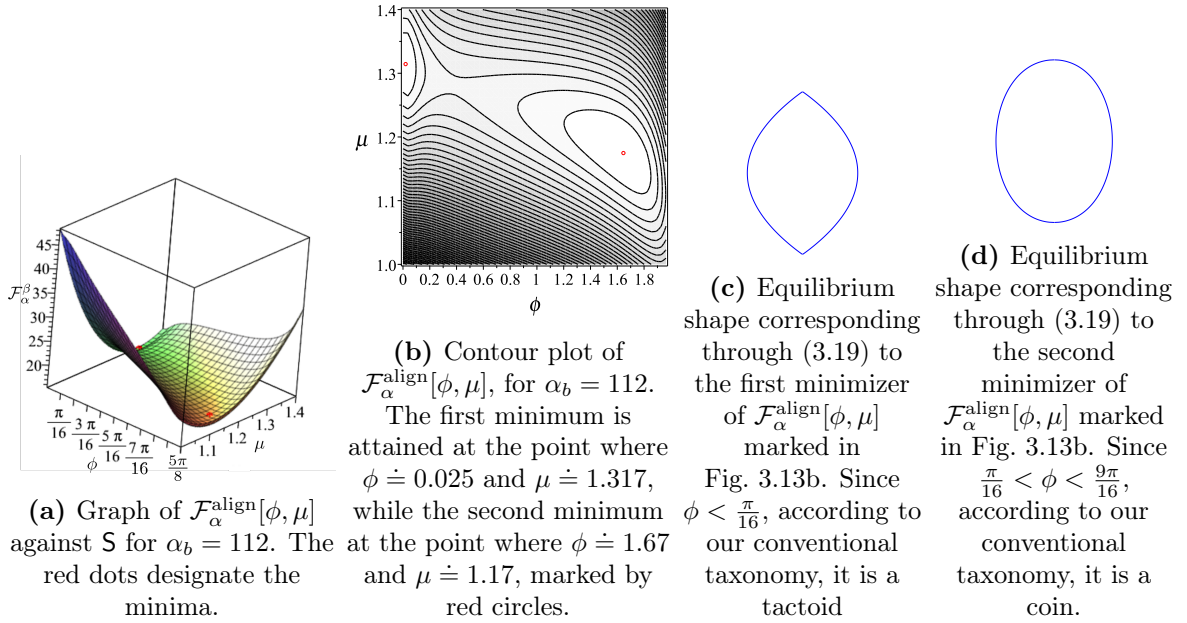
Figure 3.13: Bistability phenomenon: the two minima, the former for $\phi < \frac{\pi}{16}$ (tactoid) and the latter for $\phi > \frac{\pi}{16}$, minimize $\mathcal{F}_\alpha^{\mathrm{align}}[\phi, \mu]$. Here a first-order transition takes place. For $k_3 = 1$ and $\beta = 10^{-2}$ it occurs at $\alpha_b = 112$.

(a) Graph of $\mathcal{F}_\alpha^{\mathrm{align}}[\phi, \mu]$ against S for $\alpha = 250$. The red dot designates the unique minimum.

(b) Contour plot of $\mathcal{F}_\alpha^{\mathrm{align}}[\phi, \mu]$, for $\alpha = 250$. The minimum is attained at the point where $\phi \doteq 1.87$ and $\mu \doteq 1.25$, marked by a red circle.

(c) Equilibrium shape corresponding through (3.19) to the minimizer of $\mathcal{F}_\alpha^{\mathrm{align}}[\phi, \mu]$ marked in Fig. 3.14b. Since $\phi > \frac{9\pi}{16}$, according to our conventional taxonomy in Sec. 3.2.4, it is a bâtonnet.

Figure 3.14: For a given $\alpha > \alpha_2$, the reduced function $\mathcal{F}_\alpha^{\mathrm{align}}[\phi, \mu]$ on S has a convex graph and attains a single minimum for $\phi > \frac{\pi}{16}$. For this particular α the minimum is attained in the region of the bâtonnet.

(a) Graph of $\mathcal{F}_\alpha^{\text{align}}[\phi, \mu]$ against S for $\alpha = 1600$. The red dot designates the unique minimum.

(b) Contour plot of $\mathcal{F}_\alpha^{\text{align}}[\phi, \mu]$, for $\alpha = 1600$. The minimum is attained at the point where $\phi \doteq 1.728$ and $\mu \doteq 1.857$, marked by a red circle.

(c) Equilibrium shape corresponding through (3.19) to the minimizer of $\mathcal{F}_\alpha^{\text{align}}[\phi, \mu]$ marked in Fig. 3.15b. Since $\frac{\pi}{16} < \phi < \frac{9\pi}{16}$, according to our conventional taxonomy, it is a coin.
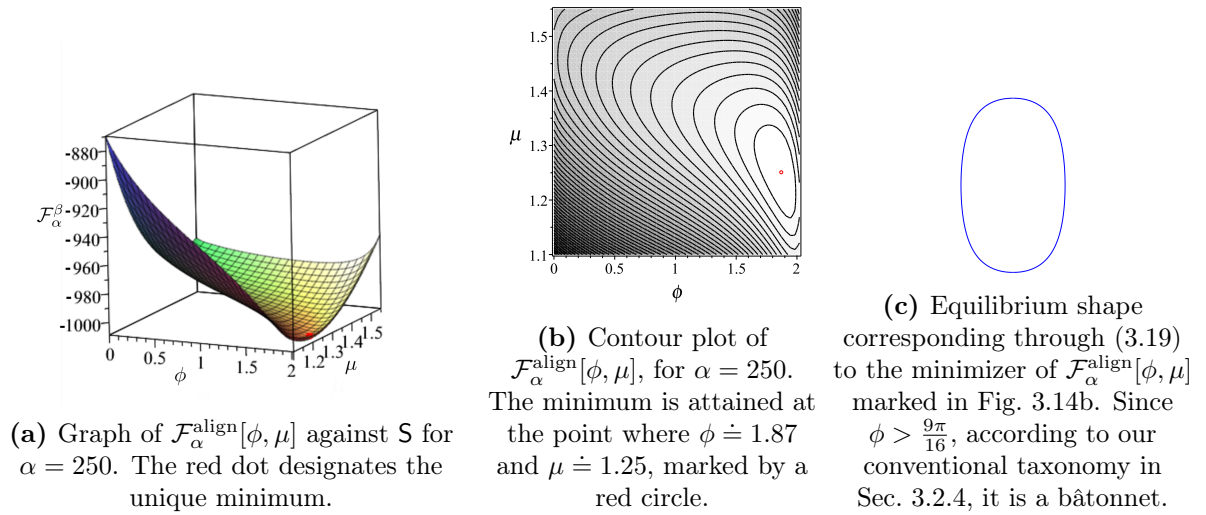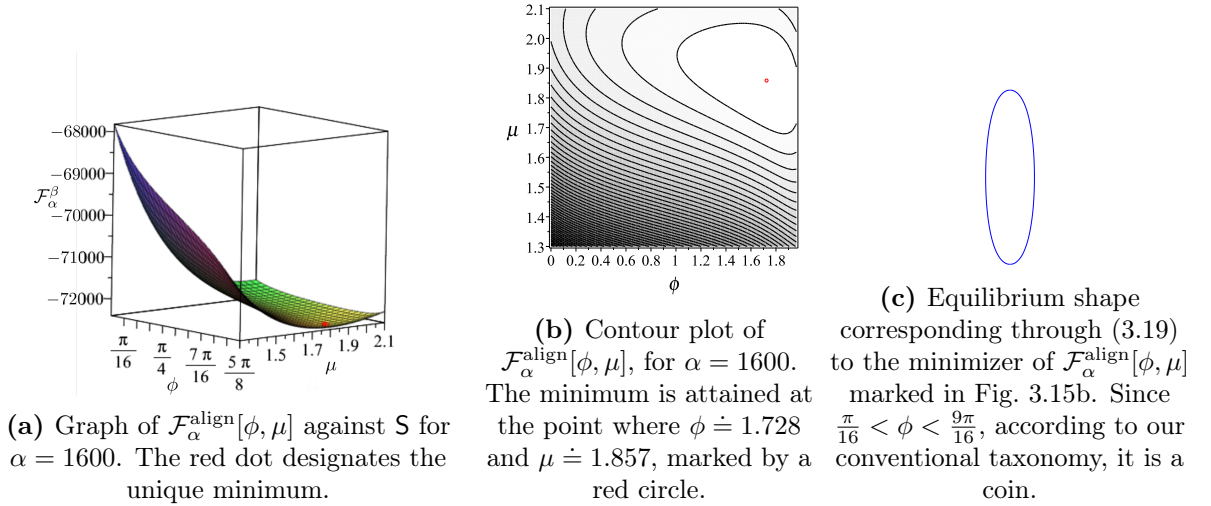
Figure 3.15: For a given $\alpha > \alpha_2$, the reduced function $\mathcal{F}_\alpha^{\text{align}}[\phi, \mu]$ on S has a convex graph and attains a single minimum for $\phi > \frac{\pi}{16}$. For this particular α the minimum returns to be attained in the region of the coins.

3.4 Comparison With Experiments

A major motivation for this Chapter was offered by the experiments conducted in [63] for degenerate substrates and in [136] for aligning substrates with water solutions of disodium cromoglycate (DSCG). By applying our theory to interpret the experiments of Kim et al. in [63], we show how to extract from them an estimate for the isotropic surface tension γ at the interface between the nematic phase of a DSCG solution at a given concentration and its isotropic liquid phase. With this estimate, we are then in position to interpret the experimental observations of [136] within the extended model proposed for the case of aligning substrates; we then achieve an estimate of the anchoring strength at the Nematic-Polymer interface.

To illustrate the generality of our method, we shall also apply it in Section 3.5 to estimate γ at the interface between the tactoids formed in an F-actin solution at equilibrium with the isotropic phase [89].

3.4.1 DSCG Solution

Among many other things, Kim et al. [63] explored water solution of DSCG at concentration $c = 16 \, \text{wt}\%$ confined between two parallel glass plates at a distance ranging in the interval 1-5 μm; the plates were spin-coated with a polymide layer, SE-7511, which exerts a degenerate tangential anchoring on the nematic director. This system can be treated as two-dimensional since the bounding plates suppress the out-of-plane distortions in the observed samples, as required by our theory.

Upon quenching the system from the isotropic phase into the coexistence regime, tactoidal droplets were observed, surrounded by the parent isotropic phase. In particular (see, Fig. 6a of [63]), a tactoid with bipolar nematic orientation was observed more closely, for which the area $A_0 = 200 \, \mu\text{m}^2$ and the aspect ratio $\Delta = 1.3 \pm 1$ were measured at the temperature $T = 37.5 \,°\text{C}$, which we read off from Fig. 2c of [63]. We wish to make use of these data to validate our theory. To this end, we need to estimate the elastic constants K_{11} and K_{33} at $T = 37.5 \,°\text{C}$.

Interpolating the curves representing in [142] the temperature dependence of the elastic con-

stants of the nematic phase of DSCG at $c = 16\,\text{wt}\%$, we readily arrived at

$$K_{11} = 4\,\text{pN}, \quad K_{33} = 9\,\text{pN}, \quad \text{at} \quad T = 37.5\,°\text{C} \quad \text{and} \quad c = 16\,\text{wt}\%, \tag{3.26}$$

and so we take $k_3 \doteq 2.25$. We can also obtain α from the measured aspect ratio Δ. It follows from (3.19) that in our theory Δ can be given the form

$$\Delta := \frac{\mu}{R(0)} = \frac{\mu^2 \left(\frac{8}{3}\cos\phi + \pi\sin\phi\right)}{\pi(\cos\phi + \sin\phi)}, \tag{3.27}$$

where use has also been made of (3.20). The plot of Δ computed on the minima of F_α over S is drawn against α in Fig. 3.16 for $k_3 = 2.25$. It shows the typical behaviour also found in other
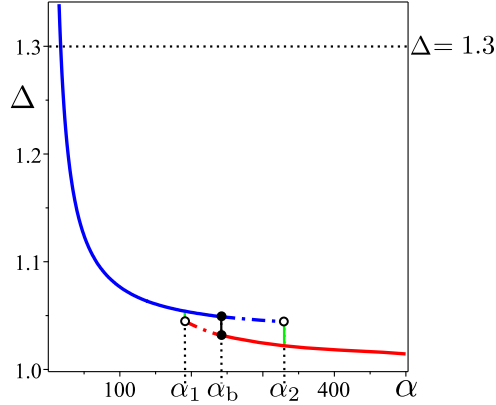

Figure 3.16: The droplet's aspect ratio Δ computed on the minima of F_α, plotted against α for $k_3 = 2.25$. The broken horizontal line designates the level $\Delta = 1.3$, which is attained for $\alpha = 17.2$. Local and global minima are marked with the same symbols as in Fig. 3.7. The critical values of α are $\alpha_1 = 192$, $\alpha_2 = 330$, and $\alpha_b = 243$. Equilibrium tactoids are genuine for $\alpha \lesssim 137$.

theoretical studies [105, 106]: the aspect ratio of a bipolar droplet decreases as its linear size increases. We see that the value $\Delta = 1.3$ is attained by the tactoidal branch (as expected) for $\alpha \doteq 17.2$; the corresponding coordinates in S of the minimum of F_α are $\phi \doteq 0$ and $\mu \doteq 1.24$, and so the equilibrium shape is a genuine tactoid (with pointed tips). For $k_3 = 2.25$, equilibrium tactoids cease to be genuine at $\alpha \approx 137$.

Since the equivalent radius R_e is known from the isoperimetric constraint (3.4), $R_e \approx 8\mu\text{m}$, we readily obtain for the long axis l of the droplet $l = 2R_0 = 2\mu R_e \approx 20\,\mu\text{m}$. The equilibrium tactoid predicted by our theory is plotted in Fig. 3.17 against the observed shape. Our expected value for l also agrees quite well with the measurement performed in [63] on the reconstructed shape, as does the *cusp angle* τ_N marked in Fig. 3.17. In our formalism, for a genuine tactoid, the latter can be expressed as

$$\tau_N = -2\arctan(R'(\mu)) = 2\arctan\left(\frac{3\pi}{4\mu^2}\right), \tag{3.28}$$

which for $\mu = 1.24$ delivers $\tau_N \doteq 1.99$. The value of τ_N reported in [63] for the shape in Fig. 3.17 is $\tau_N = 1.05 \pm 0.05$, whereas a direct measurement on Fig. 3.17 would suggest that this value is indeed $\tau_N/2$, in good agreement with our theoretical prediction. Moreover, by use of equation (3.12), we can give the following estimate for the surface tension at the nematic/isotropic interface of an aqueous DSCG solution at $16\,\text{wt}\%$,

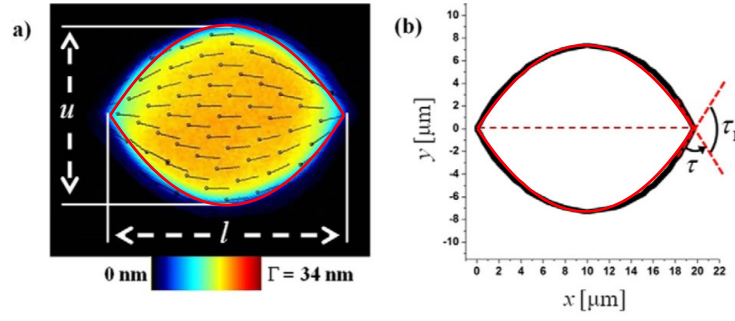$$\gamma \approx 8.9\,\mu\text{N/m}. \tag{3.29}$$

Figure 3.17: The droplet's equilibrium shape (in red) corresponding to $\alpha = 17.2$, $\phi = 0$, and $\mu = 1.24$ is contrasted against the shape observed in [63] (see their Figs. 6a and 6b). Our estimate for the long axis is $l \approx 20\,\mu$m. On the left: PolScope image. On the right: reconstructed shape.

Different, discordant estimates have been given in the literature for the order of magnitude of γ. For example, in [82] they estimate $\gamma \sim 1\,\mu$N/m, whereas in [63] they give $\gamma \sim 10^2\,\mu$N/m, an estimate obtained by applying the pendant drop technique [16, 17]. We trust that the measurements based on the theory presented in this Chapter might be more accurate. The value in (3.29) is closer to that found in [33] at the nematic-isotropic interface of 5CB (see also [34, 35]).

The critical values of α corresponding to $k_3 = 2.25$ are $\alpha_1 = 192$, $\alpha_2 = 330$, and $\alpha_b = 243$, while the observed droplet shown in Fig. 3.17 corresponds to $\alpha = 17.2$. According to our theory, one would then expect coexistence of tactoids and discoids for R_e in the range $90\,\mu\text{m} \lessapprox R_e \lessapprox 153\,\mu\text{m}$, that is, for an area A_0 in the range $0.3\,\text{mm}^2 \lessapprox A_0 \lessapprox 0.7\,\text{mm}^2$, a regime of large drops, for which no data are available in [63].

Aligning Substrates

The sample setting of [136] consists in two replicas of 250nm line channels with 250nm spacing overlaid with 7μm spacers between them, such that the bottom and the top channels are parallel. A DSCG solution (11wt%) or a SSY solution (27wt%), prepared by dissolving the chromonic liquid crystal in deionized water, are injected into the assembled cell.

At $T = 25°$C Yi et al. experimentally detect N sandwiched tactoids, that is, flat-sided droplets whose shape is a rectangular cuboid with hemi cylindrical ends and their director field $\boldsymbol{n}$ has a bipolar configuration with only in plane components. They are well aligned to the channels. Especially, the study of a DSCG cell with initial concentration of 11wt% distinctly shows a droplet with this particular geometry and we read off from [136, Fig.12a] its area A_0 and aspect ratio Δ:

$$A_0 = 3217\mu\text{m}^2, \quad \Delta = 2.4. \tag{3.30}$$

As before, we interpolate the curves in [142] which represents the temperature dependence of the elastic constants of the nematic phase of DSCG at $c = 11$wt%, and we readily arrive at

$$K_{11} = 1.5pN, \quad k_3 = 4.1, \quad \text{at} \quad T = 25°C \quad \text{and} \quad c = 11\%. \tag{3.31}$$

Here, we resort to the estimate of the surface tension at the nematic/isotropic interface of an aqueous DSCG solution found in Sec 3.4.1 through the model presented for degenerate substrates. This estimate combines with the equivalent radius $R_e \approx 32\mu$m, known from the isoperimetric constraint (3.4), and the value of K_{11} in (3.31) and gives by (3.12):

$$\alpha = 193. \tag{3.32}$$
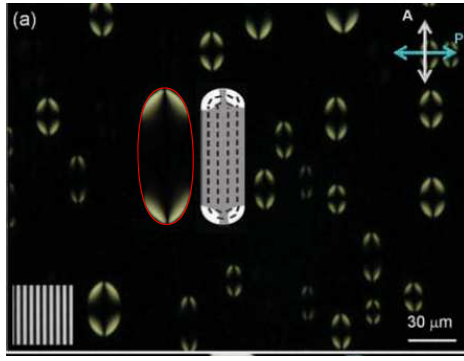
(a) Comparison with the experiment in [136] in a 11wt% DSCG cell; the metod for aligning substrates agrees with the experimental data available.
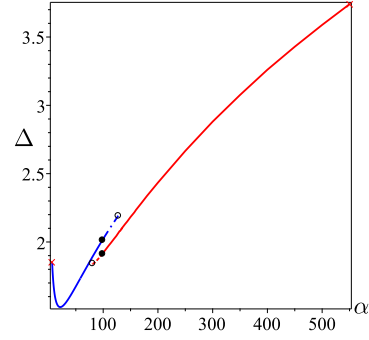
(b) Graph of the aspect ratio Δ of the two minima of F_α^β against α for $\varepsilon = (10)^{-3}$, $k_3 = 4.1$, $\beta = 3.3 \times 10^{-2}$. The colors, the style of the lines and the symbols are those used in Figures 3.12a and 3.12b

Figure 3.18: Comparison with the experiment in [63] in a 16wt% DSCG cell; the equilibrium cross-section obtained with the metod for degenerate substrates fits the experimental picture.

For the values of the elastic pararmeter (k_3, α) fixed by the experimental setting as in (3.31) and (3.32), we sougth the value of β at which the functional $\mathcal{F}^{\text{align}}[\mu, R]$ has minimum in S of aspect ratio experimentally observed (3.30). This value of Δ is attained by the discoidal branch for

$$\beta = 3.3 \times 10^{-2}; \tag{3.33}$$

coordinates in S for this minimum are $\mu = 1.52$ and $\phi = 1.8$, and so the equilibrium shape is a bâtonnet. The comparison between the predicted shape and the experimentally observed droplet is reported in Fig. 3.19. A fairly good qualitative agreement between experiments and theory is found. By the use of the definition of β (3.33) as a function of σ_0, we can provide the following estimate for the anchoring strength at the nematic/polymer interface of an acqueous DSCG solution

$$\sigma_0 = 1.21 \times 10^{-5} \text{J/m}^2. \tag{3.34}$$

We note that γ and σ_0 have the same order of magnitude. Different discordant estimate have been given in literature also for the order of magnitude of σ_0. For example, in [62] $\sigma_0 \sim 10^{-4} \text{J/m}^2$ is estimated using secondary sputtering lithography (SSL), whereas in [18] $\sigma_0 \sim 10^{-6} \text{J/m}^2$ results on different rubbed polyimide alignment layers.

The sistematic search for the minimizer of $\mathcal{F}^{\text{align}}$ for increasing α when β is given by the estimated value (3.33) and k_3 is as in (3.31) leads to the following three critical values: $\alpha_1 = 80.3$, $\alpha_b = 98.6$, and $\alpha_2 = 127.5$, while the equilibrium shape is a bâtonnet when α ranges in $[131, 321]$.

According to the model proposed for aligning substrates, one would then expect coexistence of tactoids and discoids for R_e in the range $13 \, \mu\text{m} \lessapprox R_e \lessapprox 21 \, \mu\text{m}$, a regime of small drops, for which no data are available in [136]. For $R_e \geq 21.18 \mu\text{m}$, only smooth shapes are observed; they are coins except for $21.7 \mu\text{m} \leq R_e \leq 53.3 \mu\text{m}$, where they are bâtonnet. The shape transitions from coins to bâtonnet and vice versa are smooth. Beyond $R_e = 3 \mu\text{m}$ and $R_e = 15 \mu\text{m}$.

When $\omega = 5$ and the parameters of the model are as in (3.31) and (3.33), the safeguard values of α are in $\alpha_s^1 \approx 7$ and $\alpha_s^2 \approx 1853$; in accord with experiments, for α in (3.32) the uniform configuration is energetically disfavored.

The plot of Δ computed on the minima of F_α over S is drawn against α in Fig. 3.16 for $k_3 = 4.1$.

Aligning Substrates: SSY Solution

In [136, Fig.10b] a N sandwiched tactoid with a in-plane bipolar director field is experimentally observed in a 29wt% SSY cell at the room temperature $T = 25°C$. Its aspect ratio is $\Delta = 2.5$, while its linear dimension $R_e \approx \sqrt{\frac{A_0}{\pi}} = 80\mu$m is known from the isoperimetric constraint (3.4).

The value of σ_0, (3.34), for the interface between the substance and the nematic phase of DSCG, could be employed when the liquid crystal in the cell is SSY instead; the experimental cell is precisely the same as in [63] and σ_0 follows from the action of a dense substrate (polymer) on a liquid crystal solution, and so depends more on the source of the interaction. According to the measurments in [142] for a SSY solution, we have

$$K_{11} = 4.3\text{pN}, \quad k_3 = 1.42, \quad \text{at} \quad T = 25°C \quad \text{and} \quad c = 29\%. \tag{3.35}$$

Substituting (3.35) and the given values of R_e and h in (3.15), we get

$$\widetilde{\beta} = 2573\mu\text{m}, \tag{3.36}$$

and the model for aligning substrates provides $\alpha = 502$. As above, by (3.12) we provide an estimate for the surface tension at the nematic/isotropic interface of SSY at 29wt%:

$$\gamma^{SSY} = 2.72 \times 10^{-5}\text{J/m}^2. \tag{3.37}$$

Fig. 3.19 illustrates a comparison between the observed droplets and the equilibrium shape for $\alpha = 550$.
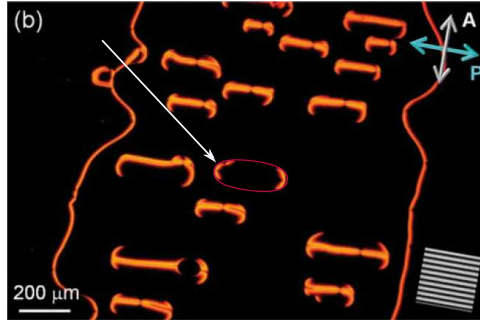

Figure 3.19: Comparison with the experiment in [136] in a 29wt% SSY cell; The droplet's equilibrium shape (in red) corresponding to $\alpha = 550$, $\phi = 1.84$ and $\mu = 1.53$ is constrasted against the shape observed in [136]. The metod for aligning substrates agrees with the available experimental data.

3.5 F-actin Solution

Highly concentrated solutions of short ($\lesssim 2\,\mu$m) F-actin filaments form liquid crystal phases which may coexist with their isotropic liquid phase [89].[8] The two-dimensional islands of ordered phase are bipolar tactoids, just like those considered in this Chapter. Although it is suggestive to use liquid crystal theory to interpret the spindle shape exhibited in the process of cellular mitosis [8], to our knowledge no direct proof is available that this actually applies to physiological conditions [131]. Typical 2D tactoidal shapes have been observed in solutions of F-actin filaments at equilibrium with the isotropic phase in the presence of physiological cross-linkings (filamin)

---

[8]For longer filaments, the ordering transition is continuous and no coexistence has been observed [125].

at concentration 100-fold lower than in the case of free filaments [131]. However, contrary to the hypotheses of our theory, these tactoids, which are presumably closer to physiological conditions, were seen with a *homogeneous* alignment of the director throughout the droplets. For this reason, we shall use for a comparison the experimental observations of two-dimensional bipolar tactoids in [89].

To apply our theory to the F-actin solutions studied in [89], we need to estimate the elastic constants K_{11} and K_{33} at the appropriate concentration; unlike chromonics, direct experimental determinations are lacking for them. Here we shall resort to rigid-rod theory. For filament lengths less than 2μm, as in this case, good agreement with rigid-rod theory is found in [125], and as highlighted in [131], short actin filaments (average length between 180nm and 2μm) behave as rigid rods because they are appreciably shorter than the persistence length of F-actin polymers, which is approximately 15-18μm [52, 42].

The bare excluded volume theory, which treats filaments as rigid cylinders of diameter d and height ℓ, predicts the following expressions for the elastic constants [90],

$$K_{11} = \frac{7}{8\pi}\frac{kT}{d}q, \quad K_{33} = \frac{4}{3\pi^2}\frac{kT}{d}q^3, \tag{3.38}$$

where k is the Boltzmann constant, T is the absolute temperature and q is the *dimensionless* concentration, defined as

$$q := bc_\ell = \eta\frac{\ell}{d}, \tag{3.39}$$

where c_ℓ and η are the filament's number density and volume fraction, respectively, and $b := \pi\ell^2 d/4$ is the average isotropic excluded volume.

F-actin filaments are charged; the extra mutual repulsion that they feel affects the elastic constants. As already observed by Onsager [95], this effects can be taken into account in a purely steric theory by replacing d with an effective diameter $d_e > d$. Thus, in (3.38) d needs to be replaced by d_e and q by $q_e := qb_e/b$, where $b_e := bd_e/d$ is the effective average excluded volume. It is easily seen that these corrections leave K_{11} unchanged, while increasing K_{33}:

$$K_{11} = \frac{7}{8\pi}\frac{kT}{d}\left(\eta\frac{\ell}{d}\right), \quad K_{33} = \frac{32}{21\pi}K_{11}q_e^2, \quad \text{with} \quad q_e = \eta\frac{\ell}{d}\frac{d_e}{d}, \tag{3.40}$$

so that

$$k_3 = \frac{K_{33}}{K_{11}} = \frac{32}{21\pi}q_e^2. \tag{3.41}$$

As first pointed out in [119], the electrostatic repulsion among filaments also affects the critical concentration q^* at which the isotropic phase becomes unstable (which is a good estimate of the coexistence region), in a way that depends on the ratio κ of the Debye screening length to the effective diameter. Thus, from $q^* = 4$ for $\kappa = 0$ [69], q^* may increase up to $q^* \approx 6$ for $\kappa = 0.5$ [119]. Taking as in [80] $q_e \approx 6$ in (3.41), we estimate $k_3 \approx 17.5$ for F-actin filaments.

To obtain K_{11}, we need to estimate η, ℓ, and d. From [22], we get $d \approx 8\,$nm. As for ℓ and η, we rely on the data of [89]: they estimate $\ell \approx 1.2\,\mu$m and produce solutions with a mass density $\rho = 10.8\,$mg/ml $= 10.8\,$Kg/m^3. Since the molecular mass of a monomer of actin is $M = 4.2\,$Kg/mol and its volume is $v_m = 50.1\,$nm^3 [22], the molar concentration of the solution is $c_M = \rho M \approx 259 \times 10^{-3}\,$mol/m^3, which gives $\eta = c_M N_A v_m \approx 7.8 \times 10^{-3}$ (where $N_A = 6.02 \times 10^{23}$ is the Avogadro number) and, by (3.40), $d_e/d \approx 5$. Thus, again by (3.40), we obtain that at room temperature $K_{11} \approx 0.17\,$pN and $K_{33} \approx 2.93\,$pN.

With these data we are now in a position to interpret within our theory the observations of [89]. Their Fig. 7 collects a number of tactoids by their aspect ratio Δ and axial length l. We select as a representative observation one around which most data seem to be clustered, namely

$\Delta = 2.7$ and $l = 50\,\mu$m. Following the same steps as in Sec. 3.4.1, for the estimated k_3 we find that $\alpha \approx 3.9$. To extract finally γ from this, we only need to estimate the equivalent radius R_e of the representative tactoid. Taking this as the region bounded by two symmetric arcs of circle, equation (3.71) from Appendix 3.C delivers $A_0 \approx 634\,\mu$m^2 for its area. Thus, $R_\mathrm{e} \approx 14.2\,\mu$m and

$$\gamma_\mathrm{actin} = \frac{\alpha K_{11}}{R_\mathrm{e}} \approx 46\,\mathrm{nN/m}, \tag{3.42}$$

which is an order of magnitude less than the value ($\gamma_\mathrm{actin} \approx 300\,\mathrm{nN/m}$) estimated experimentally in [131] with a dynamical relaxation method for tactoids formed at a concentration 100-fold lower (in the presence of a cross-linking physiological ligand), but consistent with the measurements at the interfaces of some phase-separated colloid-polymer dispersions [1]. For a further comparison, we note that our estimate for γ_actin is appreciably less than the surface tension reported for other protein-based liquid droplets, which ranges from $\gamma \sim 1\,\mu\mathrm{N/m}$ [6] to $\gamma \approx 100\,\mu\mathrm{N/m}$ [28].

As for the regime of coexistence between tactoids and discoids as equilibrium shapes, which is the main object of this Chapter, for $k_3 = 17.5$ equations (3.25) deliver $\alpha_1 \approx 420$ and $\alpha_2 \approx 622$ as delimiters of the coexistence window (with perfect bistability at $\alpha_\mathrm{b} \approx 485$). They correspond to the following values of the equivalent radius, $R_\mathrm{e} \approx 1528\,\mu$m and $R_\mathrm{e} \approx 1768\mu$m, respectively, more than two orders of magnitude larger than for the observed tactoids. According to our theory, this makes it highly unlikely the observation of equilibrium shapes of condensates of F-actin filaments other than tactoids, at least at the given concentration.

3.6 Conclusion

We studied chromonic droplets in two space dimensions. Our major motivation was the thorough experimental investigation both in [63] and in [136] of thin cells with degenerate tangential anchoring for the nematic director in the first case and with a tangential anchoring inducing a preferred direction in the second case. In particular, a solution of DSCG in water was quenched in the temperature regime where nematic and isotropic phases coexist in equilibrium, the former forming islands with a peculiar shape. We introduced a wide class of two-dimensional shapes for the equilibrium droplets, which includes tactoids, discoids, bâtonnet, and butterflies, the latter of which are concave, whereas the former three are convex. For the first case of degenerate substrates, our analysis revealed that upon increasing the droplet's area a tactoidal equilibrium branch gives way to a discoid branch, while neither bâtonnet nor butterflies can ever be equilibrium shapes. Bâtonnet can be observed when the substrates are aligning. Moreover, there is a regime of shape coexistence, where a tactoid and a discoid are both local minima of the free-energy, the global minimum shifting from one to the other at a critical value of the droplet's area, where perfect bistability is established. This shows another, possibly less usual incarnation of a phenomenon broadly present in physics (think of optical bistability, for example). A typical bifurcation diagram with hysteresis describes the situation, reminiscent of a first-order phase transition with super-heating and super-cooling temperatures (replaced here by corresponding values of the area).

We put our theory to the test by interpreting experimental data provided by [63] and [136]. We found a fairly good quantitative agreement between experiment and theory, although further data should be collected to establish on firmer grounds the degree of confidence of the theory. In particular, we could extract from the data available in [63] an estimate for the isotropic component γ of the surface tension at the interface between coexisting nematic and isotropic phases of DSCG in 16\%wt aqueous sol. An estimate of the measurement of the anchoring strength at the nematic/polymer interface for a DSCG in 11\%wt aqueous sol is provided by the model proposed for aligning substrates. Both the estimates seems to promise more accuracy

than the rough evaluation of order of magnitude available in the literature for this material and its chromonic siblings. We hope that the theory proposed here could be used for a systematic determination of γ and σ_0 for different temperatures and concentrations.

To illustrate the generality of our method, we also used it to estimate the isotropic surface tension γ_{actin} for tactoids shown in solutions of F-actin filaments [89]. We estimated the elastic constants for the nematic phase of F-actin filaments taking them as charged, rigid cylinders; we obtained a value of γ_{actin} comparable to the one measured for some phase-separated colloid-polymer dispersions [1].

The data available for both systems do not cover the range of predicted bistability. We estimated the area that a droplet should reach to display an abrupt transition from tactoid to discoid. It remains to be seen whether a controlled growth in the droplet's size can be realized to observe neatly this transition.

We have shown that the critical values of the area that delimit the shape hysteresis are (increasing) linear functions of the ratio K_{33}/K_{11} between bend and splay elastic constants. If this critical phenomenon could be explored experimentally, our theory would also offer an independent way to measure K_{33}/K_{11}. This might be especially welcome for non conventional new lyotropic phases.

3.A   Retracted Tangential Field

In this Appendix, we justify the expression for the free-energy functional (3.10) associated with the bipolar director field $\boldsymbol{n}$ defined as the unit vector field tangent to the lines with given t and varying y (see Fig. 3.2). A generic curve in that family is represented by the position vector

$$\boldsymbol{p}_t(y) := g(t)R(y)\boldsymbol{e}_x + y\boldsymbol{e}_y, \quad -R_0 \leqq y \leqq R_0, \tag{3.43}$$

where g is any function of class C^1 strictly increasing on $[0,1]$ and such that $g(0) = 0$ and $g(1) = 1$. For given $t \in [0,1]$, the tangent vector field $\boldsymbol{n}$ is given by

$$\boldsymbol{n} = \frac{gR'\boldsymbol{e}_x + \boldsymbol{e}_y}{\sqrt{1 + (gR')^2}}, \tag{3.44}$$

where a prime denotes differentiation. The unit vector field

$$\boldsymbol{n}_\perp := \boldsymbol{e}_z \times \boldsymbol{n} = \frac{-\boldsymbol{e}_x + gR'\boldsymbol{e}_y}{\sqrt{1 + (gR')^2}} \tag{3.45}$$

is everywhere orthogonal to $\boldsymbol{n}$ and such that $\boldsymbol{n}_\perp|_{\partial\mathscr{R}} = -\boldsymbol{\nu}$, where $\boldsymbol{\nu}$ is the outer unit normal to $\partial\mathscr{R}$ (see again Fig. 3.2).

Imagine now a smooth curve in $\mathscr{R}$ parameterized as $\xi \mapsto (t(\xi), y(\xi))$; it follows from (3.43) and (3.44) that

$$\dot{\boldsymbol{p}} = g'R\dot{t}\boldsymbol{e}_x + \dot{y}(gR'\boldsymbol{e}_x + \boldsymbol{e}_y) = g'R\dot{t}\boldsymbol{e}_x + \sqrt{1 + (gR')^2}\dot{y}\boldsymbol{n}, \tag{3.46}$$

where a superimposed dot denotes specifically differentiation with respect to ξ. Thus, the elementary area dA is

$$dA = dt\,dy\,g'R\sqrt{1 + (gR')^2}\boldsymbol{e}_x \times \boldsymbol{n} \cdot \boldsymbol{e}_z = g'R\,dt\,dy, \tag{3.47}$$

and the elementary length $d\ell_t$ on the retracted curve $\partial\mathscr{R}_t$, for given t, is

$$d\ell_t = \sqrt{1 + (gR')^2}\,dy. \tag{3.48}$$

In particular, the area of $\mathscr{R}$ and the length of its boundary are given by

$$A(\mathscr{R}) = 2 \int_0^1 g' \, dt \int_{-R_0}^{R_0} R \, dy = 2 \int_{-R_0}^{R_0} R \, dy \tag{3.49}$$

and

$$\ell(\partial\mathscr{R}) = 2 \int_{-R_0}^{R_0} \sqrt{1 + R'^2} \, dy. \tag{3.50}$$

Differentiating $\boldsymbol{n}$ in (3.44) along the smooth curve $\xi \mapsto (t(\xi), y(\xi))$, we find that

$$\dot{\boldsymbol{n}} = -\frac{g'R'\dot{t} + gR''\dot{y}}{1 + (gR')^2}\boldsymbol{n}_\perp. \tag{3.51}$$

Assuming that $\boldsymbol{n}$ is differentiable in $\mathscr{R}$, $\dot{\boldsymbol{n}}$ and $\dot{\boldsymbol{p}}$ must be related through

$$\dot{\boldsymbol{n}} = (\nabla\boldsymbol{n})\dot{\boldsymbol{p}}. \tag{3.52}$$

Since $\boldsymbol{n}$ is a unit vector field, $(\nabla\boldsymbol{n})^\mathsf{T}$ annihilates $\boldsymbol{n}$, and so there exists a vector $\boldsymbol{a} = a_1\boldsymbol{n} + a_2\boldsymbol{n}_\perp$ such that

$$\nabla\boldsymbol{n} = \boldsymbol{n}_\perp \otimes \boldsymbol{a}. \tag{3.53}$$

To determine the scalar components a_i of $\boldsymbol{a}$, we observe that, by (3.53), (3.52) also reads as

$$\dot{\boldsymbol{n}} = (\boldsymbol{a} \cdot \dot{\boldsymbol{p}})\boldsymbol{n}_\perp. \tag{3.54}$$

Making use of (3.46) and both (3.44) and (3.45), we readily see that

$$\boldsymbol{a} \cdot \dot{\boldsymbol{p}} = \frac{g'R(gR'a_1 + a_2)\dot{t}}{\sqrt{1 + (gR')^2}} + \sqrt{1 + (gR')^2}a_1\dot{y}, \tag{3.55}$$

and inserting this into (3.54) alongside with (3.51), we obtain an identity for arbitrary $(\dot{t}, \dot{y})$ only if

$$a_1 = -\frac{gR''}{[1 + (gR')^2]^{3/2}}, \quad a_2 = \frac{R'}{R}\frac{1}{\sqrt{1 + (gR')^2}} - \frac{g^2R'R''}{[1 + (gR')^2]^{3/2}}, \tag{3.56}$$

which leads us to

$$\nabla\boldsymbol{n} = -\frac{gR''}{[1 + (gR')^2]^{3/2}}\boldsymbol{n}_\perp \otimes \boldsymbol{n} + \left(\frac{R'}{R}\frac{1}{\sqrt{1 + (gR')^2}} - \frac{g^2R'R''}{[1 + (gR')^2]^{3/2}}\right)\boldsymbol{n}_\perp \otimes \boldsymbol{n}_\perp. \tag{3.57}$$

The following expressions for the traditional measures of distortion then follow from (3.57),

$$\operatorname{div}\boldsymbol{n} = \frac{R'}{\sqrt{1 + (gR')^2}}\left(\frac{1}{R} - \frac{g^2R''}{1 + (gR')^2}\right), \tag{3.58a}$$

$$\operatorname{curl}\boldsymbol{n} = -\frac{gR''}{[1 + (gR')^2]^{3/2}}\boldsymbol{e}_z, \tag{3.58b}$$

$$\boldsymbol{n} \cdot \operatorname{curl}\boldsymbol{n} = 0, \tag{3.58c}$$

$$\boldsymbol{n} \times \operatorname{curl}\boldsymbol{n} = \frac{gR''}{[1 + (gR')^2]^{3/2}}\boldsymbol{n}_\perp, \tag{3.58d}$$

$$\operatorname{tr}(\nabla\boldsymbol{n})^2 - (\operatorname{div}\boldsymbol{n})^2 = 0. \tag{3.58e}$$

We found it useful to rescale all lengths to the radius R_e of the disc of area A_0. Letting μ as in (3.8) and using (3.3) and (3.49), we arrive at the following reduced functional,

$$F[\mu; R] := \frac{\mathscr{F}[\mathscr{B}]}{K_{11}h} = \int_{-\mu}^{\mu} dy \int_0^1 g' \left[\frac{g^4 R R'^2 R''^2}{\left(1 + (gR')^2\right)^3} + \frac{R'^2}{R} \frac{1}{\left(1 + (gR')^2\right)} - 2 \frac{g^2 R'^2 R''}{\left(1 + (gR')^2\right)^2} \right.$$
$$\left. + k_3 \frac{g^2 R R''^2}{\left(1 + (gR')^2\right)^3} \right] dt + 2\alpha \int_{-\mu}^{\mu} \sqrt{1 + R'^2} \, dy, \qquad (3.59)$$

where k_3 and α are as in (5.8) and in (3.12). The integration in t, which delivers (3.10) in the main text, is independent of the specific function g, provided it is monotonic and obeys the prescribed boundary conditions.

Retracted Tangential Field

By rescaling all lengths to the radius R_e of the disc of area A_0, letting μ as in (3.8) and using (3.49), we obtain the following dimensionless form of $\mathscr{F}_{\sigma_0}$ in (3.5)

$$F_{\sigma_0}[\mu; R] := \frac{\mathscr{F}_{\sigma_0}[\mathscr{B}]}{K_{11}h} = -4\widetilde{\beta} \int_{-\mu}^{\mu} dy \int_0^1 \frac{g'R}{1 + (gR')^2} \, dt, \qquad (3.60)$$

where $\widetilde{\beta}$ is the dimensionless parameter defined by (3.15). The integration in t is shown in (3.14) to be independent of the specific function g, provided it is monotonic and obeys the prescribed boundary conditions.

3.B   Preventing Anchoring Breaking

Here, we perform an energy comparison to identify the *safeguard* value α_s of α, that is, the lower bound that should be exceeded for a drop to be bipolar at equilibrium. It is known that for α sufficiently small the tangential anchoring favored by the interfacial energy (3.1) is bound to be broken, so that the nematic alignment becomes uniform throughout the droplet. Uniform and bipolar alignments will indeed be the terms of comparison for our estimate of α_s.

For drops with uniform alignment, the total free-energy reduces to (3.1), subject to the area constraint (3.9). The optimal shape is delivered by the classical Wulff's construnction [135] (see also [65, p. 490]). Assuming that $\boldsymbol{n} \equiv \boldsymbol{e}_y$ and that $\mathscr{R}$ is mirror-symmetric with respect to both axes $\boldsymbol{e}_x$ and $\boldsymbol{e}_y$, one needs only determine the equilibrium shape of $\mathscr{R}$ in the positive (x, y) quadrant. We let $y = y_W(x) \geqq 0$ represent the profile of $\mathscr{R}$ and define $\lambda > 0$ by setting $y_W(\lambda) = 0$. Here, as in the main text, all lengths are scaled to R_e. The method illustrated in [127, Ch.5] and [105] delivers Wulff's shape through the following explicit function

$$y_W\left(x\lambda^{-1}\right)\lambda^{-1} = \frac{1 + \omega\left(1 - \xi^2\right) - \xi x\lambda^{-1}}{\sqrt{1 - \xi^2}}, \qquad (3.61a)$$

where ξ is given in terms of x by solving the algebraic equation

$$\omega\xi^3 + (1 - \omega)\xi - x\lambda^{-1} = 0 \qquad (3.61b)$$

and λ is determined by the isoperimetric constraint (3.9), which here reads as

$$4\int_0^\lambda y_W(x)\, dx = 4\lambda^2 \int_0^1 y_W\left(x\lambda^{-1}\right)\lambda^{-1}\, d\left(x\lambda^{-1}\right) = \pi. \qquad (3.61c)$$

Correspondingly, by computing the free-energy in (3.1) on Wulff's shape, we obtain that

$$\mathscr{F}_{\mathrm{W}} = 4K_{11}h\alpha j(\omega), \tag{3.62}$$

where the function j, defined by

$$j(\omega) := \frac{1}{2}\sqrt{\frac{\pi}{\int_0^1 y_{\mathrm{W}}\,\mathrm{d}x}} \left(\int_0^1 \sqrt{1 + y_{\mathrm{W}}'^2}\,\mathrm{d}x + \omega \int_0^1 \frac{1}{\sqrt{1 + y_{\mathrm{W}}'^2}}\,\mathrm{d}x \right), \tag{3.63}$$

is computed on the solution y_{W} of (3.61), renormalized so that $y_{\mathrm{W}}(1) = 0$. Figure 3.20 illustrates the Wulffian shape obtained with this method for $\omega = 5$ and the graph of j for $0 \leqq \omega \leqq 10$.

(a) Wulffian shape obtained by solving equations (3.61) for $\omega = 5$. With lengths scaled to R_{e}, $\lambda = 0.51$.

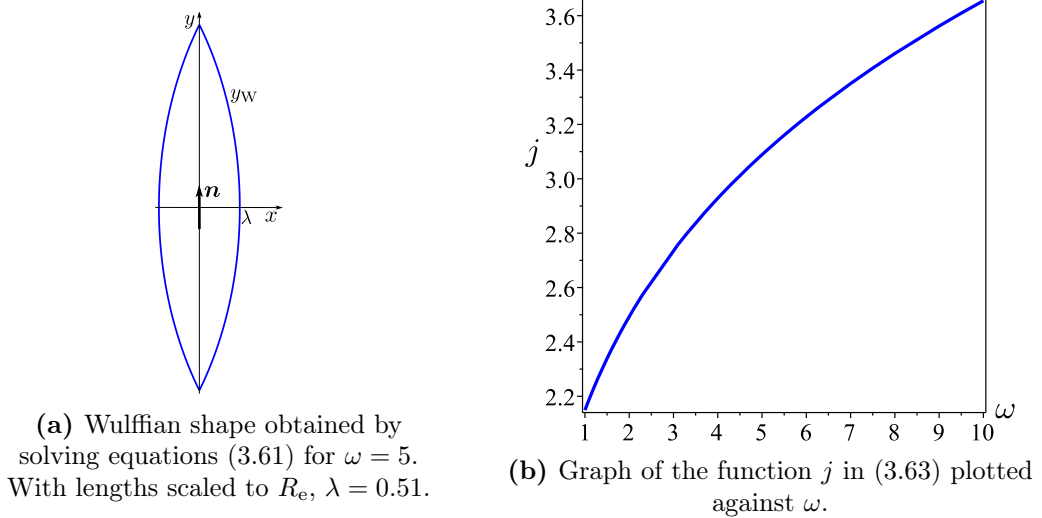(b) Graph of the function j in (3.63) plotted against ω.

Figure 3.20: Shape and (scaled) energy for the fully aligned droplet.

We now compare this energy to that of a disc with an in-plane bipolar director field whose integral lines are Apollonian circles passing through the poles (see, for example, §2 of [91]); their radius increases to $+\infty$ upon approaching the y-axis, as shown in Fig. 3.21, which represents a quadrant of the disc. Adapting the computations in bipolar coordinates (ξ, η) of Williams [133]
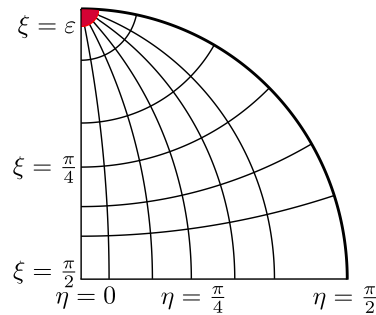

Figure 3.21: A quarter of a unit disc described in bipolar coordinates (ξ, η). Apollonian circles correspond to different values of η; they are orthogonal to the coordinate lines with ξ constant. As in Fig. 3.3, also here ε is out of scale.

to the present two-dimensional setting, we arrive at

$$\mathscr{F}_{\text{bip}} := K_{11}h \left\{ 4 \int_{\varepsilon}^{\frac{\pi}{2}} \mathrm{d}\xi \int_0^{\frac{\pi}{2}} \mathrm{d}\eta \left[\frac{1}{2} \frac{\cos^2 \xi}{\sin \xi} \frac{1}{(1 + \sin \xi \cos \eta)^2} + \frac{k_3}{2} \frac{\sin^2 \eta \sin \xi}{(1 + \sin \xi \cos \eta)^2} \right] + 2\alpha\pi \right\}$$

$$= 4hK_{11} \left\{ \left[\frac{\pi}{4} \left(k_3 - 1 - k_3 \ln 2 - \ln \varepsilon \right) + \varepsilon + \alpha \left(\frac{\pi}{2} - \varepsilon \right) \right] + \frac{\alpha\omega\pi\varepsilon}{2} \right\}, \tag{3.64}$$

where the defect core has been identified with the region $0 \leqq \xi \leqq \varepsilon$. The estimate in (3.22) follows from requiring that $\mathscr{F}_{\text{bip}} < \mathscr{F}_{\text{W}}$.

Aligning Substrates

The aim of this Appendix is to perform an energy comparison to identify the two safeguard values of α which delimit the range of α for which the breaking of the tangential anchoring is prevented.

For drops with an homogeneous director field oriented along $\boldsymbol{e}_y$ no distortion is produced in the bulk, and the total free-energy (3.3)[9] results as the sum of the contributions of the interfacial energies:

$$\mathscr{F}_h = \mathscr{F}_{\text{s}} - 2\sigma_0 A(\mathscr{B}) = \mathscr{F}_{\text{s}} - 2\sigma_0 A_0, \tag{3.65}$$

where $\mathscr{F}_s$ is given here by (3.1). The anchoring energy due to the substrates does not contribute to the minimization process since A_0 is fixed, and the optimal shape is delivered with the help of the classical Wulff's construnction [135], as for the degenerate case in Appendix 3.B.

Thus, by computing the free-energy in (3.65) on Wulff's shape, we obtain that

$$\mathscr{F}_h = 4K_{11}h \left[\alpha j(\omega) - 2\beta\alpha^2\pi \right], \tag{3.66}$$

where the function j is defined by (3.63).

As pointed out in the main text, as soon as α is great enough the equilibrium drop starts to elongate along the channels of the substrates and the surface free-energy, given by the sum of (1.16) and (3.5), is no more minimized by a disk. Thus, here we compare (3.66) to the energy of a droplet of area A_0 whose shape is made up by a rectangle, inside which the director field is uniform along $\boldsymbol{e}_y$, equipped with two semi-disk ends, where the vector lines mimic those of the disk previously introduced in Section 3.B, and so join the poles along Apollonian circles filling the whole of the semi-disks with radius increasing on approaching the y-axis. This shape is physically plausible, since it resembles that experimentally oserved in [136], and it is illustrated, together with the associated in-plane bipolar director field associated, in Figure 3.22a.

We can choose the radius of the semi-disks on the top of the rectangle which could grow until it reaches R_{e}, value at which our shape returns a disk of radius R_{e}. Thus, we define the radius of the hemi-disks by $R_{\text{e}}^{\delta} := \delta R_{\text{e}}$, where δ is an arbitrary parameter ranging in $(0, 1]$, and the length L of the vertical side of the rectangle is automatically identified by the isoperimetric constraint (3.4):

$$L = \frac{\pi R_{\text{e}}}{2\delta} \left(1 - \delta^2 \right), \quad \delta \in (0, 1]. \tag{3.67}$$

The free-energy associated with the hemi-disks is obtained adapting the argument of Williams to a disk of radius R_{e}^{δ}, and the total free-energy (3.3) comprising also the free-energy associated to the rectangle with a uniform director field results, with the aid of (3.67), as:

---

[9]We perform an energy comparison between droplets subject to the isoperimetric constraint, and so we compare their shape functional (3.3), where all the terms which take the same value for all shapes and fields with planar degenerate anchoring on $\partial\mathscr{B}_{\text{N-I}}$, (1.6), are not considered.
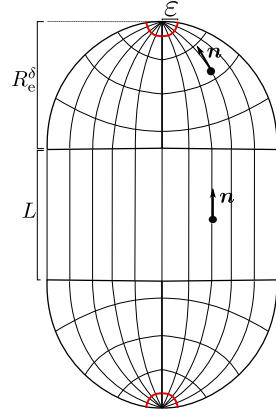
(a) Drop of fixed area A_0 whose shape is physically plausible, [136]. The $\boldsymbol{n}$ field, which forms two boojums at the poles, has only in-plane components and is everywhere tangent to the retraced curves in figure to allow the angle between the director $\boldsymbol{n}$ and the $y-$axis to be zero for a variable portion of the region.
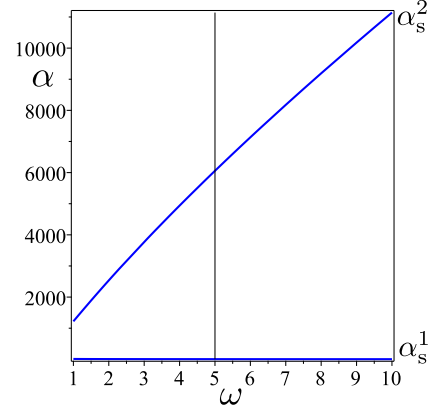
(b) Graph of the two safeguard values of α as functions of $\omega \in [1, 10]$ obtained for the optimal value of δ and which delimit the range of α for which the director field inside the drop is bipolar.

Figure 3.22: In the main text we find the optimal value of $\delta \in [0, 1]$, with $R_{\text{e}}^\delta = \delta R_{\text{e}}$, which maximizes α_s^2 to render the energy of this bipolar configuration energetically favourable in the greatest range of α.

$$\mathscr{F}_{\text{bip}} := K_{11}h \left\{ 4 \int_0^{\frac{\pi}{2}} \mathrm{d}\xi \int_0^{\frac{\pi}{2}} \mathrm{d}\eta \left[\frac{1}{2} \frac{\cos^2 \xi}{\sin \xi} \frac{1}{(1 + \sin \xi \cos \eta)^2} + \frac{k_3}{2} \frac{\sin^2 \eta \sin \xi}{(1 + \sin \xi \cos \eta)^2} \right. \right.$$
$$\left. \left. -2\beta\alpha^2 \frac{\sin \xi(\sin \xi + \cos \eta)^2}{(1 + \cos \eta \sin \xi)^4} \right] \mathrm{d}\eta + \alpha \left[2\delta\pi + \frac{\pi}{\delta}(1 - \delta^2) \right] - 2\beta\alpha^2(1 - \delta^2) \right\}. \quad (3.68)$$

As above, the splay term diverges logarithmically for the defect points $\xi \in \{0, \pi\}$ and we exclude from the nematic domain a core of critical radius $r_{\text{c}} = \varepsilon R_{\text{e}}$ around them to make their energy finite.

$$F_{\text{bip}}^\varepsilon \approx \left\{ 4 \left[\frac{\pi}{4}(k_3 - 1 - k_3 \ln(2) - \ln(\varepsilon)) + \varepsilon \right] + \alpha \left[4\delta \left(\frac{\pi}{2} - \varepsilon \right) + \frac{\pi}{\delta}(1 - \delta^2) \right] \right\}$$
$$+ 2\alpha\delta\omega\pi\varepsilon - 2\beta\alpha^2\pi \left(1 - \frac{\delta^2}{6} \right). \quad (3.69)$$

The demand that $F_{\text{bip}}^\varepsilon < F_{\text{a}}$ is reverted into the request that the quadratic function of α in (3.23) is positive for the given values of k_3, ε, and β. This function has two rooths, α_s^1 and α_s^2 and the positivity of f_α in (3.23) is ensured whenever $\alpha_s^1 \le \alpha \le \alpha_s^2$. For $k_3 = 1$, $\varepsilon = 10^{-3}$, $\omega = 5$ and $\beta = 10^{-2}$ as in the main text, α_s^1 is not considerably affected by changes in $\delta \in (0, 1]$ and we aim at the optimal value of δ which maximizes α_s^2 to make the range of α for which it is unfavorable breaking the tangential surface anchoring as big as possible. In Fig 3.22b it is illustrated the two graphs of this safeguard values of α obtained by the optimal value of δ as a function of $\omega \in [1 - 10]$.

3.C   Spindle Area

In the bipolar coordinates (ξ, η) adopted by Williams [133], a *spindle* is the region between two Apollonian circles symmetrically located relative to the axis joining the poles (Fig.3.21 shows quarters of the members in a single family of such Apollonian circles). Half a spindle is described by letting ξ range in $[0, \pi]$ and η in $[0, \eta_0]$, where η_0 is related to the aspect ratio $\delta > 1$ by $\eta_0 = 2 \arctan(1/\delta)$. Denoting by l the distance between the poles, the area element is given by

$$\mathrm{d}A = \left(\frac{l}{2} \right)^2 \frac{\sin \xi}{(1 + \sin \xi \cos \eta)^2} \, \mathrm{d}\xi \, \mathrm{d}\eta.$$ (3.70)

The area of a spindle will then be expressed as

$$A_0 = 2 \left(\frac{l}{2} \right)^2 \int_0^\pi \mathrm{d}\xi \int_0^{\eta_0} \mathrm{d}\eta \frac{\sin \xi}{(1 + \sin \xi \cos \eta)^2} = \left(\frac{l}{2} \right)^2 \frac{(1 + \delta^{-2})^2 \arctan \delta + \delta^{-3} - \delta^{-1}}{\delta^{-2}},$$ (3.71)

which is the formula used in Sec. 3.5 to estimate the area of a tactoid representing a cluster of observations in [89].

Chapter 4

Second Variation
of Oseen-Frank's Free-Energy

Since the divergence to $-\infty$ of Oseen-Frank's free-energy when $K_{22} - K_{24} < 0$ is prevented in confined geometry subject to degenerate boundary conditions, we can apply here Oseen-Frank's theory to CLCs. We provide a general formula for the second variation of Oseen-Frank's functional, through which we learn that an exchange of stability is expected in the system at $K_{22} = K_{24}$. For $K_{24} > K_{22}$ the trivial solution becomes unstable and two ET solutions sharing the same energy arise, which are stable. They thus characterize the two-fold 'pseudo' ground state of CLCs within Oseen-Frank's theory. We substantiate the claim that they are spurred up by the adjustment of the double twist mode to fit the cylinder with the imposed boundary. The local stability of the ET configurations explored in this Chapter seems to support the legitimacy of this theoretical treatment.

4.1   Introduction

CLCs in cylindrical capillaries subject to degenerate tangential boundary conditions (1.6) have been observed in [55, 56, 19, 86, 54] to exhibit chiral director configurations in the absence of intrinsic chirality. A theoretical treatment of this class of materials through Oseen-Frank's theory for nematic is not entirely justified, since it is built on a notion of undistorted ground state; it posits a free-energy density which measures the cost associated with producing a distortion in the nematic natural state, which is attained when $\boldsymbol{n}$ is constant in space, and so $\nabla\boldsymbol{n} = \boldsymbol{0}$. As a result, under the assumption that $\boldsymbol{n}$ is at least a map of class $\mathcal{C}^2$, the ET equilibrium configurations, (1.42) and its mirror immage (1.43) (first found in [10]), likely to rationalize configurations of the chromonics' confinement-induced ground state, are valid only if Ericksen's inequality $K_{22} \geq K_{24}$ is violated. Such a violation would make Oseen-Frank's free-energy unbounded below in $3D$ Euclidean space, but boundary conditions could still ensure the existence of a minimum; for planar anchoring, it follows from the geometric representation in terms of the principal curvatures (1.7) for the energy term K_{24} that even when one of Ericksen's inequalities involving K_{24} is violated, as in this case, Oseen-Frank's energy stored in the cylinder is bounded below as long as the elastic constants K_{11}, K_{22} and K_{33} are all non-negative. It is thus legitimate to apply Oseen-Frank's theory to this particular class of materials under cylindrical confinement when $K_{22} < K_{24}$.

In this Chapter we thus take for granted that this theory is suitable to describe the elastic properties of CLCs and we start to examine the consequences that would arise in cylindrical symmetry (in connection with Burylov's solutions [10]) if the relevant Ericksen's inequality,

$K_{22} \geq K_{24}$, is violated.

As pointed out in Chapter 1, the non-uniform double twist configuration is the ground state of CLCs in $3D$ space. According to the locality of this ideal mode, ET configurations rather characterize a 'pseudo' ground state of CLCs. The geometric frustration and the characteristic of non-uniformity [77] of these equilibrium configurations give rise to the following questions: does the uniform state still have the characteristics of a local minimizer of the free-energy? Are the two nonuniform equilibrium configurations for Oseen-Frank's free-energy functional at least locally stable? The study of local stability of the critical points thus becomes a tool for identification of the minimum.

Here, the problem tackled in [10, 19] of seeking the orientation fields $\boldsymbol{n}$ at least of class $\mathcal{C}^2$ which make Oseen-Frank's free-energy stationary, is reduced to an analogous infinite horizon variational problem, whose analysis resorts to *Weierstrass' theory* for the dynamics of a one-dimensional Lagrangian conservative system. The new bulk free-energy density is mechanically interpreted as the Lagrangian of this peculiar dynamical system given by the sum of a kinetic and a potential energy. The first section illustrates the features of these motions through the phase diagram of the system. This infinite horizon system admits a conservation law and the orbits all have an explicit representation on the phase space; they all are solutions to the equation of motion in the bulk departing from a curve of natural conditions. When $K_{22} < K_{24}$ there are two non-trivial trajectories in the phase space departing from the curve of natural conditions that possess finite energy. One of them evolves toward the origin and reaches it in an infinite time, while the other orbit corresponds to its mirror image. They are the dynamical analogues of the ET solutions (1.42) and (1.43).

Deciding the stability of the free-energy functional in the vicinity of an equilibrium solution presumes the analysis of its second variation at the configuration. We thus provide a general formula for the second variation $\delta^2 \mathscr{F}_{\mathrm{b}}$, where $\mathscr{F}_{\mathrm{b}}$ is Oseen-Frank's free-energy functional, for $\boldsymbol{n}$ a solution to the weak form of the Euler-Lagrange equations for $\mathscr{F}_{\mathrm{b}}$ (c.f. (1.22) and (1.23) with W given by (1.3) and $\gamma_{\mathrm{a}} = 0$). It is a quadratic functional in the perturbation $\boldsymbol{v}$ of $\boldsymbol{n}$, where $\boldsymbol{v}$ is constrained to obey $\boldsymbol{v} \cdot \boldsymbol{n}$. Here $\boldsymbol{v}$ is assumed to be absolutely continuous and to perturb $\boldsymbol{n}$ according to the anchoring conditions prescribed by the problem. This formula for the second variation is then applied to the uniform configuration which results unstable whenever one of the Ericksen's inequalities is violated (1.8).

The aim of the second section is to explore the local stability within Oseen-Frank's theory of the ET configurations when the CLC is confined in a cylinder. It is found that when perturbations are assumed to preserve the cylindrical symmetry of the problem, the second variation functional at these equilibrium configurations can be regarded as a sum of two independent functionals: one is associated with azhimutal perturbations, the other with radial ones. Sections 4.4.1 and 4.4.2 are devoted to the study of their positivity whenever k_1, $k_3 \geq 1$ (according to the experimetal investigations reported for ordinary CLCs), which ensures the local stability of the escaped twist configurations with respect to these two types of perturbations within Oseen-Frank's theory. For completeness, the argument in Appendix 4.C involves the values of $k_3 \in (0, 1)$.

Escaped twist (ET) solutions are valid only if the Ericksen's inequality $K_{22} \geq K_{24}$ (1.8) is violated. For $K_{24} < K_{22}$ the trivial solution is the only solution of the equilibrium equation and it is stable; as explained in Section 4.3.1 this is guaranteed by the validity of the Ericksen's inequality (1.8). The ET configurations represent the branches of a bifurcation occurring at $K_{24} = K_{22}$ where they coincide with the trivial solution. They share the same bulk free-energy given by (1.44), which decreases continuously from zero as K_{24} increases beyond K_{22}: this makes the uniform configuration unstable with respect to generic perturbations and the system settles in one of the two locally stable configurations with the same probability, (1.42) or (1.43).

4.2 Dynamical Problem

As first found in [10], when $\mathscr{B}$ is a capillary of radius R and height L, then Oseen-Frank's free-energy functional within the class of orientation fields described by (1.25) is given by (1.29). We reduce this functional to an analogous autonomous dynamical problem by the change of variables

$$t(\rho) := -\ln(\rho), \tag{4.1}$$

where t has the meaning of artificial time and maps $[0,1]$ onto $[0,+\infty]$. In particular, the axis of the cylinder at $\rho = 0$ is approached in the new variable when t is sent to infinity, while $t = 0$ corresponds to the surface of the cylinder at $\rho = 1$. Moreover β becomes a function on $[0,\infty)$, which is defined by

$$b(t(\rho)) := \beta(\rho), \tag{4.2}$$

and inserting (4.2) into (1.29), by use of

$$\mathrm{d}t = -\frac{1}{\rho}\,\mathrm{d}\rho, \tag{4.3}$$

we give $\mathscr{F}$ in (1.29) the following dimensionless form:

$$\mathcal{F}[b] := \frac{\mathscr{F}_{\mathrm{b}}}{2\pi K_{22} L} = \int_0^\infty \left(\frac{\dot{b}^2}{2} + \phi(b) \right) \mathrm{d}t - \varphi_0(b(0)), \tag{4.4}$$

for which we have employed the notations

$$\phi(b) := \frac{\sin^2 b \cos^2 b}{2} + \frac{k_3 \sin^4 b}{2}. \tag{4.5}$$

$$\varphi_0(b) := -\frac{(1 - 2k_{24})}{2} \sin^2 b \tag{4.6}$$

Our analysis will resort here to *Weierstass' theory* for one dimensional Lagrangian conservative motions; the functional in (4.4) is quadratic in $\dot{b}$ and bounded for $b \in [0, b(0)]$, and the bulk free-energy density is interpreted as the Lagrangian of this peculiar dynamical system given by the sum of a kinetic and a potential energy,

$$\mathcal{L} := \frac{\dot{b}^2}{2} + \phi(b). \tag{4.7}$$

Here, $b = b(t)$ is the single Lagrangian parameter which describes the configuration of the Lagrangian system under the assumptions that the holonomic constraints acting upon it do not depend explicitly on time and that the active force exerted on the system is conservative and can be derived from the potential $\phi = \phi(b)$. The kinetic energy of this system is $T(\dot{b}) = \dot{b}^2/2$.

We call orbits all solutions to the *equation of motion*

$$\frac{\mathrm{d}}{\mathrm{d}t} \frac{\partial \mathcal{L}}{\partial \dot{b}} = \frac{\partial \mathcal{L}}{\partial b}, \tag{4.8}$$

which here reads as

$$\ddot{b} = \phi'(b), \tag{4.9}$$

and which obey the natural condition at the boundary obtained through vanishing the conjugate moment in order to have no moment flow at both initial t_i and final t_f instants

$$\left(\frac{\partial \mathcal{L}}{\partial \dot{b}} + \frac{\partial \varphi_0(b)}{\partial b} \right) = 0 \quad \text{for } t \in \{t_i, t_f\}; \tag{4.10}$$

making use of the formulae (4.7), (4.5) and (4.6), (4.10) gives

$$\dot{b}_n = \dot{b}_n(b) := (1 - 2k_{24}) \sin b \cos b, \quad \text{for } t \in \{0, \infty\}. \tag{4.11}$$

At first, the surface term $\varphi_0(b_0)$ in (4.4), which is an additive constant depending only on the initial condion q_0, is not taken into account. Multiplying both sides of (4.9) by $\dot{b}$ and integrating, we arrive at the *conservation law*

$$\frac{\dot{b}^2}{2} = \phi(b) + \frac{c}{2}, \tag{4.12}$$

where c is an integration constant. Here, the integral of energy given by the difference of the kinetic and the potential energies evaluated on the orbits takes throughout the motion one and the same value, $E_c = c/2$, which depends on the particular level curve for the value of c selected.

The first qualitative feature of the motion we learn from (4.12) is that, since the kinetic function is a positive function vanishing only if $\dot{b} = 0$, the motion is confined to the regions where $\phi(b) \geq -E$, or, equivalently, to the regions where $\phi(b) \geq -c/2$. When $c \leq 0$ the range of the values of the parameter b may attain splits into allowed and prohibited intervals, separated by *barriers*, that is configurations $\bar{b}$ such that $\phi(\bar{b}) = -c/2$. When $c > 0$ and due to the non-negativity of ϕ in (4.5), no barriers exists and the system is not confined to the interval of b where the initial condition happens to lie.

We read the equations (4.9) and (4.11) in the phase space $(b, \dot{b})$; the phase diagrams of these system for the representative values $k_3 = 30$, $k_{24} = 7.5$ [32] is depicted in Figure 4.1. We restrict to values of b which spans $[0, \pi]$ and the b-axis, being angular, wraps onto itself after π radians. Moreover, we overlook for a moment (4.11), by taking a generic initial condition $b_0 := b(0)$ away from a barrier, if there are any. In this case, two branches of solutions depart from b_0, depending on whether $\dot{b}_0 := \dot{b}(0)$ is positive or negative. Through the conservation law (4.12), these solutions are obtained by solving by separation of variables

$$\dot{b} := \pm\sqrt{2\phi(b) + c}, \tag{4.13}$$

with ϕ as in (4.5). For a fixed value of c, the two curves in the phase space given by (4.13) are symmetric under reflections about the axis $\dot{b} = 0$. We suppose, for sake of argument, that $\dot{b}_0 < 0$ and by (4.13) the time needed to reach a generic configuration $b < b_0$ is given by the inverse of function $b = b(t)$, which is delivered by

$$t = -\int_{b_0}^{b} \frac{1}{\sqrt{2\phi(\eta) + c}} \, d\eta. \tag{4.14}$$

We note that the integrand of (4.22) can diverge only at the barriers, if there are any, where its denominator vanishes.

After this brief introduction, we recall that the orbits verify the natural boundary conditions at $t = 0$ and so they must depart from a point $(b_0, \dot{b}_n(b_0))$ on the curve (4.11) in the phase space (red line in Fig 4.1). Whenever $k_{24} > 1$, if b_0 spans $[0, \pi/2]$, then $\dot{b}_n(b_0)$ is negative and the orbit starts following the negative branch of the solution (4.13). We confine attention to this case.

The admissible values of c are always greater than $-k_3$ in order to ensure the positivity of the radicand in (4.13), while not all values of $c > 0$ guarantee an initial value b_0 at which the corrisponding orbit crosses the curve of the natural conditions. As illustrated in Figure 4.1, trajectories for $c < 0$ always intersect the curve (4.11) in

$$b_1 := \arcsin\sqrt{\frac{2k_{24}(k_{24} - 1) + \sqrt{4k_{24}^2(k_{24} - 1)^2 - c[k_3 + 4k_{24}(k_{24} - 1)]}}{k_3 + 4k_{24}(k_{24} - 1)}}, \tag{4.15}$$
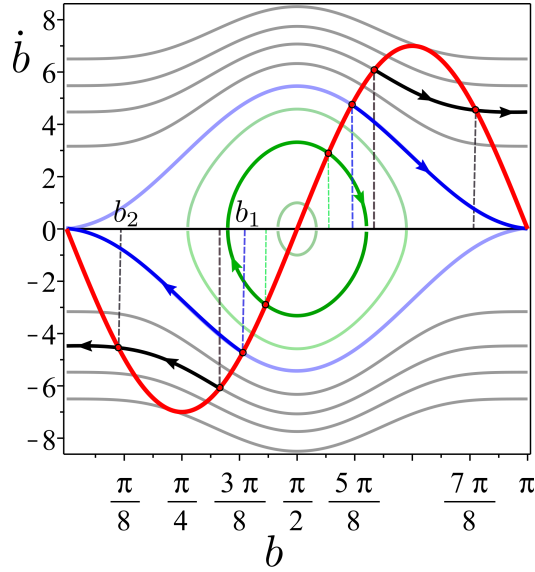
Figure 4.1: Reduced elastic constants are $k_3 = 30$ and $k_{24} = 7.5$; phase portrait for $b \in [0, \pi]$ of the dynamical system generated by the minimized Lagrangian. The b-axis wraps onto itself after π radians. Here, the orbits for $c = -20$ (dark green line), $c = 0$ (blue line) and $c = 20$ (black line) have been underlined, with attention to the orientation. Generally, an orbit, which follows the level curve for an admissible value of c, departs from a point on the curve of the natural conditions (4.11) (red line). When $c > 0$, there are four possible orbits. When $c < 0$, the motion is periodic and the more c decreases towards $-k_3$, the more the corresponding orbit embraces the point $(\pi/2, 0)$ in the phase space. Finally, for $c = 0$, the blue orbits are the unique solutions to the equation of motion which depart from and reach the manifold (4.11) in an infinite time and with a finite energy. By considering $t = -\ln \rho$, these latter orbits coincide with the *ET* configuration in (1.42) and (1.43)

while whenever $c \geq 0$ another intersection is attained between the manifold and the negative branch of solutions (4.13)

$$b_2 := \arcsin \sqrt{\frac{2k_{24}(k_{24} - 1) - \sqrt{4k_{24}^2(k_{24} - 1)^2 - c[k_3 + 4k_{24}(k_{24} - 1)]}}{k_3 + 4k_{24}(k_{24} - 1)}}. \tag{4.16}$$

These intersections could exist when the range of the admissible values of c is bounded above by

$$c_{\max} := \frac{4k_{24}^2(k_{24} - 1)^2}{[k_3 + 4k_{24}(k_{24} - 1)]}. \tag{4.17}$$

When $c = 0$, b_2 in (4.16) degenerates into 0 and the trajectory for $c = 0$ separates orbits with qualitatively different features: for $c < 0$ the orbits are periodic, while for $c > 0$ they are open. This is achieved by the following property: by expanding the potential $\phi(b)$ in Taylor series about a barrier $\bar{b}$, the Weierstrass theory for one-dimensional Lagrangian motion shows that the time needed to arrive at the barrier is finite when $\phi'(\bar{b}) \neq 0$, and so when there is no generalized force exerted on the system in $\bar{b}$, whereas it is infinite when $\phi'(\bar{b}) = 0$. Here ϕ' is given by

$$\phi'(b) = 2 \cos b \sin b \left[\cos^2 b + (2k_3 - 1) \sin^2 b \right], \tag{4.18}$$

and whenever $k_3 > 1$ and $b \in [0, \pi]$ it vanishes at $b \in \{0, \pi/2, \pi\}$. We now restrict attention to the non-positive values of c, for which barriers $\bar{b}$ at which $2\phi(\bar{b}) = c$ correspond through (4.13)

to the values of b at which the orbits cross the b- axis as $c \leq 0$ varies, and so to the equilibrium configurations of the system with $\dot{b} = 0$. Whenever $c < 0$, by evaluating (4.9) for the barrier $\bar{b}$, we obtain that $\ddot{b} = \phi'(\bar{b}) \neq 0$ and the system cannot remain in the equilibrium configuration $\bar{b}$; since $\dot{b} = 0$ there, the solution jumps from the equation in (4.13) for $\dot{b} < 0$ to the other, without suffering discontinuity in b or $\dot{b}$. Thus, $\dot{b}$ reverses its sign while b traverses the same values attained before, until it takes again the initial value b_0 for $\dot{b} > 0$. Then, the analysis of the equation of motion is essentially the same illustrated above, but now applied to the equation with positive sign in (4.13); b reaches the other barrier at $\pi - \bar{b}$ in a finite time since $\phi'(\pi - \bar{b}) \neq 0$ and the motion is one more time reversed and evolves again towards b_0. This is the reason why every barrier as $\bar{b}$ or $\pi - \bar{b}$ for $c < 0$ is called *inversion point*. The evolution of b follows this pattern just described in a finite time T and repeats it over and over again. Thus the motion is periodic with a period T. The more c decreases, the more the corresponding orbits embrace $b = \pi/2$ without degenerate into it.

A different situation arises when $c \in (0, c_{\max}]$; $b(t)$ decreases towards $b = 0$ in a finite time, since by (4.13) $\dot{b} = -\sqrt{c}$ and the denominator of (4.22) does not vanish although $\ddot{b} = 0$. Since $b = 0$ is not a barrier when $c > 0$, the motion will continue for $b < 0$ following the same periodic pattern but driven forward to π radians, and so on for all the other windows.

Finally, the barrier of the level curve for $c = 0$ falls in 0 and $\phi'(0) = 0$ by (4.18); this means that $b(t)$ approaches this barrier indefinetly at a steadily decreasing speed. Every barrier where ϕ' vanishes is called *asymptotic limit*.

The smooth optimal orbits of the infinite horizon problem minimize the dimensionless functional (4.4) among all admissible orbits of the Lagrangian system (4.13) starting from the curve of natural conditions (4.11). Making use of (4.12) in (4.4), the scaled free-energy functional evaluated on the the solutions to the equation of motion is expressed as

$$\mathcal{F}_c := \frac{\mathscr{F}}{2\pi K_{22} L} = \int_0^\infty \left[2\phi(b) + \frac{c}{2} \right] \mathrm{d}t + \varphi_0(b_0). \qquad (4.19)$$

There are three possible situations according to the value of c which ranges in the interval $(-k_3, c_{\max}]$. When $c < 0$, the equilibrium paths in the phase space exist only if $\phi(b) > -c/2 = |c|/2$ and so (4.19) is

$$\mathcal{F}_{c<0} \geq \int_0^\infty \frac{|c|}{2} \mathrm{d}t + \varphi_0(b_0), \qquad (4.20)$$

which diverges to $+\infty$. When $c > 0$, the positivity of the function $\phi(b)$ leads to the conclusion reached above.

This analysis shows that for the initial configuration $b_0 \in (0, \pi/2)$ there is only one solution departing from (4.11) with a finite energy, that is the orbit corresponding to $c = 0$. (the same arguments holds for the mirror trajectory when b_0 is assumed to be $> \pi/2$). The negative branch in the phase space given by (4.13) for the minus sign, departs from $(b_1^0, \dot{b}_n(b_1^0))$ where by (4.16)

$$b_1^0 := \arctan\left(\frac{2\sqrt{k_{24}(k_{24}-1)}}{\sqrt{k_3}} \right), \qquad (4.21)$$

and approaches the asymptotic limit $b = 0$, while the positive branch starting from $(\pi - b_0^1, \dot{b}_n(b_0^1))$ evolves towards the asymptotic limit $b = \pi$. For $k_3 = 30$ and $k_{24} = 7.5$, in fig 4.2 blue lines represent the optimal orbits in the window $[0, \pi]$ of the phase space, while the red line represents the curve of the natural condition. These two orbits, as we will see below, correspond to the ET configuration and its mirror image found in [10, 19], respectively (1.42) and (1.43).

We specialize the analysis to the negative branch of (4.13) when $c = 0$. This orbit exists only if $k_{24} > 1$, since its slope in the origin of the phase space is -1, while that of the curve of the
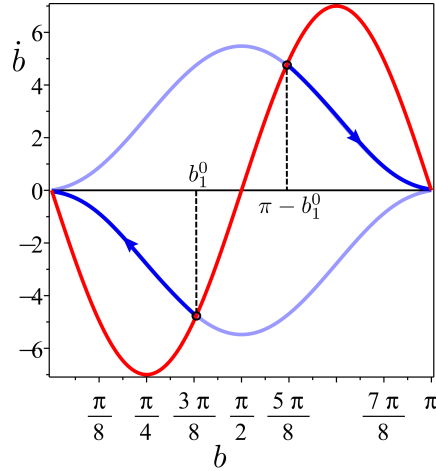
Figure 4.2: Reduced elastic constants are $k_3 = 30$ and $k_{24} = 7.5$; whenever $k_{24} > 1$ and $b \in (0, \pi/2)$, the level curve for $c = 0$ crosses the curve of the natural conditions (4.11) (red line) at $b \neq 0$ besides $b = 0$, the asymptotic limit. When $b \in (\pi/2, \pi)$ the same argument holds for $b = \pi$ instead of 0. The negative branch in the phase space given by (4.13) for the minus sign, departs from $(b_1^0, \dot{b}_n(b_1^0))$ and approaches $b = 0$ in an infinite time, while the positive branch starting from $(\pi - b_1^0, \dot{b}_n(\pi - b_1^0))$ evolves toward $b = \pi$, and it will never arrive at it.

natural condition (4.11) is $(1 - 2k_{24})$. When $k_{24} = 1$ the two curves are tangent at $b = 0$ and the equilibrium configuration coincided with the trivial one, while whenever $k_{24} > 1$ an additional intersection in $b \neq 0$ verifies. Thus, the two solutions for $c = 0$ represent the branches of a bifurcation occurring at $k_{24} = 1$, where they coincide with the trivial solution $b = 0$ or $b = \pi$ respectively. The time lapse needed for b to go backwards from $\widetilde{b}_1^0$ to a generic configuration $b > 0$ is delivered by (4.22) when c=0

$$t = -\int_{b_1^0}^b \frac{\mathrm{d}\eta}{\sqrt{2\phi(\eta)}} = -\int_{b_1^0}^b \frac{\mathrm{d}\eta}{\sin \eta \cos \eta \sqrt{1 + k_3 \tan^2 \eta}} = -[\ln g(\eta)]_{b_1^0}^b = -\ln g(b) + \ln g(b_1^0), \quad (4.22)$$

where

$$g(b) = \frac{1}{2} - \frac{1}{\sqrt{1 + k_3 \tan^2 b} + 1}. \quad (4.23)$$

By truncating the expansion about $b = 0$ of the second term of (4.22), the time lapse exhibits the following asymptotic behaviour

$$T_{c=0} \approx -\ln \left(\frac{k_3}{8} b^2 \right). \quad (4.24)$$

and diverges logarithmically as b approaches 0. Thus $b(+\infty) = 0$ when $c = 0$ and by interpreting (4.22) for $c = 0$ as a change of variables, we express the energy (4.19) of this orbit as an integral of a bounded and monotone function over the bounded interval $[0, b_1^0]$:

$$\mathcal{F}_0[b] = \int_0^{b_1^0} \sqrt{2\phi(b)} \, \mathrm{d}b = \int_0^{b_1^0} \left(\sin b \cos b \sqrt{1 + k_3 \tan^2 b} \right) \mathrm{d}b. \quad (4.25)$$

This scales functional is finite and gives precisely (1.29) found before. Moreover, by solving (4.22) we get the explicit solution

$$b(t) := \arctan \left(\frac{2\sqrt{k_{24}(k_{24} - 1)} e^{-t}}{\sqrt{k_3} \left[k_{24} - (k_{24} - 1) e^{-2t} \right]} \right) \quad (4.26)$$

which exactly coincides with $\beta_0(e^{-t})$ for β_0 as in (1.42).

4.3 Second Variation of Oseen-Frank's Free-Energy: General Formula

We write Oseen-Frank's free-energy intended for nematic and cholesteric liquid crystals as

$$\mathscr{F}[\boldsymbol{n}] = \int_{\mathscr{B}} \left\{ \frac{1}{2} K_{11}(\operatorname{div} \boldsymbol{n})^2 + \frac{1}{2} K_{22}(\boldsymbol{n} \cdot \operatorname{curl} \boldsymbol{n} + q_0)^2 + \frac{1}{2} K_{33}|\boldsymbol{n} \times \operatorname{curl} \boldsymbol{n}|^2 \right.$$
$$\left. + K_{24} \left[\operatorname{tr}(\nabla \boldsymbol{n})^2 - (\operatorname{div} \boldsymbol{n})^2 \right] \right\} \mathrm{d}V \tag{4.27}$$

where $\mathscr{B}$ is the region in space occupied by the material. We provide a general formula for the second variation $\delta^2 \mathscr{F}$ at a solution $\boldsymbol{n}$ to the weak form of the Euler-Lagrange equation for $\mathscr{F}$ in (4.27).

The mapping $t \to \boldsymbol{n}_p(t)$ defines for each $p \in \mathscr{B}$ a trajectory in $\mathbb{S}^2$, which for $t = 0$ crosses $\boldsymbol{n}|_p$, i.e. it satisfies $\boldsymbol{n}_p(0) = \boldsymbol{n}|_p$. Thus, as t spans $[0, \infty)$, we define the vector field $\boldsymbol{n}(t)$ on $\mathscr{B}$ defined by the instantaneous realizations in time of the collection of the trajectories $\boldsymbol{n}_p(t)$ for every point $p \in \mathscr{B}$. It describes a path of configurations about the director field $\boldsymbol{n}$ prescribed in $\mathscr{B}$, with the property that

$$\boldsymbol{n}(0) = \boldsymbol{n}. \tag{4.28}$$

Moreover, the constraint of unimodularity on $\boldsymbol{n}(t)$, i.e.

$$\boldsymbol{n}(t) \cdot \boldsymbol{n}(t) = 1 \tag{4.29}$$

must be respected as time elapses and differentiating both sides of (4.29) with respect to t, we get

$$\dot{\boldsymbol{n}}(t) \cdot \boldsymbol{n}(t) = 0, \tag{4.30}$$

where a dot denotes differentiation with respect to t. The vector field defined by

$$\boldsymbol{v} := \dot{\boldsymbol{n}}(t)|_{t=0} \tag{4.31}$$

is orthogonal to $\boldsymbol{n}$ thanks to the equation (4.30) evaluated at $t = 0$ and perturbs $\boldsymbol{n}$ in order to hold valid the unimodularity constraint. In order to satisfy the latter constraint even at the second order, we further differentiate (4.30) with respect to t arriving at

$$\ddot{\boldsymbol{n}}(t) \cdot \boldsymbol{n}(t) + |\dot{\boldsymbol{n}}(t)|^2 = 0 \quad \text{for every } t. \tag{4.32}$$

Here $\ddot{\boldsymbol{n}}(t)|_{t=0}$, named $\ddot{\boldsymbol{n}}$, fulfills the role of the perturbation of the second order of $\boldsymbol{n}$. By the equation (4.32) evaluated at $t = 0$, we write $\ddot{\boldsymbol{n}}$ as

$$\ddot{\boldsymbol{n}} = \boldsymbol{w} - v^2 \boldsymbol{n}, \tag{4.33}$$

introducing this new arbitrary vector field $\boldsymbol{w}$ with the property of being orthogonal to $\boldsymbol{n}$. Here v^2 denotes $\boldsymbol{v} \cdot \boldsymbol{v}$. In particular, we say that $\boldsymbol{v}$ and $\boldsymbol{w}$ are *outer variations* (of $\boldsymbol{n}$) since they perturb the trajectories $\boldsymbol{n}_p$ for every p from the outside.

Considering t as a perturbation parameter and making use of

$$\frac{\mathrm{d}}{\mathrm{d}t}\left[\operatorname{tr}(\nabla\boldsymbol{n}(t))^2\right] = \frac{\mathrm{d}}{\mathrm{d}t}\left[\mathbf{I} \cdot \nabla\boldsymbol{n}(t)^2\right] = \mathbf{I} \cdot \frac{\mathrm{d}}{\mathrm{d}t}\nabla\boldsymbol{n}(t)^2 = \mathbf{I} \cdot (\nabla\dot{\boldsymbol{n}}(t))\nabla\boldsymbol{n}(t) + \mathbf{I} \cdot \nabla\boldsymbol{n}(t)(\nabla\dot{\boldsymbol{n}}(t))$$
$$= 2\mathbf{I} \cdot \nabla\dot{\boldsymbol{n}}(t)\nabla\boldsymbol{n}(t), \tag{4.34}$$

and of

$$\frac{\mathrm{d}^2}{\mathrm{d}t^2}\left[\mathrm{tr}\left(\nabla\boldsymbol{n}(t)\right)^2\right] = 2\frac{\mathrm{d}}{\mathrm{d}t}\left[\mathbf{I}\cdot\nabla\dot{\boldsymbol{n}}(t)\nabla\boldsymbol{n}(t)\right] = 2\mathbf{I}\cdot\left[\nabla\ddot{\boldsymbol{n}}(t)\nabla\boldsymbol{n}(t) + (\nabla\dot{\boldsymbol{n}}(t))^2\right], \tag{4.35}$$

we evaluate the first and the second derivatives of the free-energy density (1.3) with respect to t as

$$\begin{aligned}\dot{W}(t) =& K_{11}\,\mathrm{div}\,\boldsymbol{n}(t)\,\mathrm{div}\,\dot{\boldsymbol{n}}(t) + K_{22}\left[\boldsymbol{n}(t)\cdot\mathrm{curl}\,\boldsymbol{n}(t) + q_0\right]\cdot\left[\dot{\boldsymbol{n}}(t)\cdot\mathrm{curl}\,\boldsymbol{n}(t) + \boldsymbol{n}(t)\cdot\mathrm{curl}\,\dot{\boldsymbol{n}}(t)\right] \\ &+ K_{33}\left[\boldsymbol{n}(t)\times\mathrm{curl}\,\boldsymbol{n}(t)\right]\cdot\left[\dot{\boldsymbol{n}}(t)\times\mathrm{curl}\,\boldsymbol{n}(t) + \boldsymbol{n}(t)\times\mathrm{curl}\,\dot{\boldsymbol{n}}(t)\right] \\ &+ 2K_{24}\left[\mathbf{I}\cdot\nabla\dot{\boldsymbol{n}}(t)\nabla\boldsymbol{n}(t) - \mathrm{div}\,\boldsymbol{n}(t)\,\mathrm{div}\,\dot{\boldsymbol{n}}(t)\right]\end{aligned} \tag{4.36}$$

and

$$\begin{aligned}\ddot{W}(t) =\ & K_{11}\left[\mathrm{div}\,\dot{\boldsymbol{n}}(t)^2 + \mathrm{div}\,\boldsymbol{n}(t)\,\mathrm{div}\,\ddot{\boldsymbol{n}}(t)\right] \\ &+ K_{22}\left\{\left[\dot{\boldsymbol{n}}(t)\cdot\mathrm{curl}\,\boldsymbol{n}(t) + \boldsymbol{n}(t)\cdot\mathrm{curl}\,\dot{\boldsymbol{n}}(t)\right]^2\right. \\ &\quad\left. + \left[\boldsymbol{n}(t)\cdot\mathrm{curl}\,\boldsymbol{n}(t) + q_0\right]\left[\ddot{\boldsymbol{n}}(t)\cdot\mathrm{curl}\,\boldsymbol{n}(t) + 2\dot{\boldsymbol{n}}(t)\cdot\mathrm{curl}\,\dot{\boldsymbol{n}}(t) + \boldsymbol{n}(t)\cdot\mathrm{curl}\,\ddot{\boldsymbol{n}}(t)\right]\right\} \\ &+ K_{33}\left\{\left|\dot{\boldsymbol{n}}(t)\times\mathrm{curl}\,\boldsymbol{n}(t) + \boldsymbol{n}(t)\times\mathrm{curl}\,\dot{\boldsymbol{n}}(t)\right|^2\right. \\ &\quad\left. + \left[\boldsymbol{n}(t)\times\mathrm{curl}\,\boldsymbol{n}(t)\right]\cdot\left[\ddot{\boldsymbol{n}}(t)\times\mathrm{curl}\,\boldsymbol{n}(t) + 2\dot{\boldsymbol{n}}(t)\times\mathrm{curl}\,\dot{\boldsymbol{n}}(t) + \boldsymbol{n}(t)\times\mathrm{curl}\,\ddot{\boldsymbol{n}}(t)\right]\right\} \\ &+ 2K_{24}\left\{\mathbf{I}\cdot\left[\nabla\ddot{\boldsymbol{n}}(t)\nabla\boldsymbol{n}(t)\right] + \mathbf{I}\cdot\nabla\dot{\boldsymbol{n}}(t)^2 - \mathrm{div}\,\dot{\boldsymbol{n}}(t)^2 - \mathrm{div}\,\boldsymbol{n}(t)\,\mathrm{div}\,\ddot{\boldsymbol{n}}(t)\right\}. \tag{4.37}\end{aligned}$$

The director field chooses the configuration that minimizes the Oseen-Frank's energy functional (1.1) in the admissible class

$$\mathcal{A}(\boldsymbol{n}_0) = \left\{\boldsymbol{n}\in\mathcal{H}^1(\mathscr{B},\mathbb{S}^2) : \boldsymbol{n}_0\in\mathcal{H}^1(\mathscr{B},\mathbb{S}^2) \text{ is the trace of } \boldsymbol{n} \text{ on } \partial\mathscr{B}\right\}. \tag{4.38}$$

We give the name first variation of $\mathscr{F}$ at the configuration $\boldsymbol{n}$ to the functional linear in $\boldsymbol{v}$

$$\delta\mathscr{F}(\boldsymbol{n})[\boldsymbol{v}] := \frac{\mathrm{d}}{\mathrm{d}t}\mathscr{F}[\boldsymbol{n}(t)]|_{t=0} = \int_\mathscr{B}\dot{W}\left(\boldsymbol{n}(t),\nabla\boldsymbol{n}(t)\right)|_{t=0}\,\mathrm{d}V, \tag{4.39}$$

and the director fields that represent possible equilibria make the elastic free-energy stationary at $t = 0$, i.e. make its first variation (4.39) identically zero. With the aid of (4.28) and (4.31) we evaluate (4.36) at $t = 0$ and by (4.39) we derive the weak form of the *Euler-Lagrange equation* solved by an equilibrium director field:

$$\begin{aligned}\int_\mathscr{B}&\left\{K_{11}\,\mathrm{div}\,\boldsymbol{n}\,\mathrm{div}\,\boldsymbol{v} + K_{22}\left(\boldsymbol{n}\cdot\mathrm{curl}\,\boldsymbol{n} + q_0\right)\cdot\left(\boldsymbol{v}\cdot\mathrm{curl}\,\boldsymbol{n} + \boldsymbol{n}\cdot\mathrm{curl}\,\boldsymbol{v}\right)\right. \\ &\left. + K_{33}\left(\boldsymbol{n}\times\mathrm{curl}\,\boldsymbol{n}\right)\cdot\left(\boldsymbol{v}\times\mathrm{curl}\,\boldsymbol{n} + \boldsymbol{n}\times\mathrm{curl}\,\boldsymbol{v}\right) + 2K_{24}\left[(\nabla\boldsymbol{n})^t\cdot\nabla\boldsymbol{v}\nabla\boldsymbol{n} - \mathrm{div}\,\boldsymbol{n}\,\mathrm{div}\,\boldsymbol{v}\right]\right\}\mathrm{d}V = 0\end{aligned} \tag{4.40}$$

where $\boldsymbol{v}$ is assumed to be sufficiently regular and to perturb $\boldsymbol{n}$ according to the anchoring conditions prescribed by the problem. This equation coincides with formula (1.22) when W is Oseen-Frank free-energy density (1.3).

Deciding the stability of $\mathscr{F}[\boldsymbol{n}]$ in the vicinity of an equilibrium solution of (4.40) presumes the analysis of its second variation at that configuration, i.e. of

$$\delta^2\mathscr{F}(\boldsymbol{n})[\boldsymbol{v}] := \frac{\mathrm{d}^2}{\mathrm{d}t^2}\mathscr{F}[\boldsymbol{n}(t)]|_{t=0} = \int_\mathscr{B}\ddot{W}\left(\boldsymbol{n}(t),\nabla\boldsymbol{n}(t)\right)|_{t=0}\,\mathrm{d}V, \tag{4.41}$$

where

$$
\ddot{W}\left(\boldsymbol{n}(t), \nabla \boldsymbol{n}(t)\right)|_{t=0} = +K_{11}\left[(\operatorname{div}\boldsymbol{v})^2 + \operatorname{div}\boldsymbol{n}\operatorname{div}\ddot{\boldsymbol{n}}\right]
$$
$$
+ K_{22}\left[(\boldsymbol{v}\cdot\operatorname{curl}\boldsymbol{n} + \boldsymbol{n}\cdot\operatorname{curl}\boldsymbol{v})^2 + (\boldsymbol{n}\cdot\operatorname{curl}\boldsymbol{n} + q_0)(\ddot{\boldsymbol{n}}\cdot\operatorname{curl}\boldsymbol{n} + 2\boldsymbol{v}\cdot\operatorname{curl}\boldsymbol{v} + \boldsymbol{n}\cdot\operatorname{curl}\ddot{\boldsymbol{n}})\right]
$$
$$
+ K_{33}\left[|\boldsymbol{v}\times\operatorname{curl}\boldsymbol{n} + \boldsymbol{n}\times\operatorname{curl}\boldsymbol{v}|^2 + (\boldsymbol{n}\times\operatorname{curl}\boldsymbol{n})\cdot(\ddot{\boldsymbol{n}}\times\operatorname{curl}\boldsymbol{n} + 2\boldsymbol{v}\times\operatorname{curl}\boldsymbol{v} + \boldsymbol{n}\times\operatorname{curl}\ddot{\boldsymbol{n}})\right]
$$
$$
+ 2K_{24}\left[\mathbf{I}\cdot(\nabla\ddot{\boldsymbol{n}}\nabla\boldsymbol{n}) + \mathbf{I}\cdot(\nabla\boldsymbol{v})^2 - (\operatorname{div}\boldsymbol{v})^2 + \operatorname{div}\boldsymbol{n}\operatorname{div}\ddot{\boldsymbol{n}}\right]. \tag{4.42}
$$

We note that $\ddot{W}\left(\boldsymbol{n}(t), \nabla\boldsymbol{n}(t)\right)|_{t=0}$ is linear in $\ddot{\boldsymbol{n}}$ and since the latter is of the form (4.33) the parts in $\boldsymbol{w}$ and in $-v^2\boldsymbol{n}$ are decoupled. Effectively, the integral over $\mathscr{B}$ of the part in $\boldsymbol{w}$ vanishes as it corresponds exactly to (4.40) for $\boldsymbol{n}$ an equilibrium solution and $\boldsymbol{w}$ orthogonal to $\boldsymbol{n}$. Thus, the second variation of $\delta^2\mathscr{F}[n]$ is the quadratic functional in the perturbation $\boldsymbol{v}$ of $\boldsymbol{n}$ delivered by

$$
\delta^2\mathscr{F}(\boldsymbol{n})[\boldsymbol{v}] = \int_{\mathscr{B}}\left\{(K_{11} - 2K_{24})\left[(\operatorname{div}\boldsymbol{v})^2 - v^2(\operatorname{div}\boldsymbol{n})^2 - (\operatorname{div}\boldsymbol{n})\boldsymbol{n}\cdot\nabla v^2\right]\right.
$$
$$
+ K_{22}(\boldsymbol{v}\cdot\operatorname{curl}\boldsymbol{n} + \boldsymbol{n}\cdot\operatorname{curl}\boldsymbol{v})^2
$$
$$
+ 2K_{22}(\boldsymbol{n}\cdot\operatorname{curl}\boldsymbol{n} + q_0)(-v^2\boldsymbol{n}\cdot\operatorname{curl}\boldsymbol{n} + \boldsymbol{v}\cdot\operatorname{curl}\boldsymbol{v})
$$
$$
+ K_{33}|\boldsymbol{v}\times\operatorname{curl}\boldsymbol{n} + \boldsymbol{n}\times\operatorname{curl}\boldsymbol{v}|^2
$$
$$
+ K_{33}(\boldsymbol{n}\times\operatorname{curl}\boldsymbol{n})\cdot(\ddot{\boldsymbol{n}}\times\operatorname{curl}\boldsymbol{n} - 2v^2\boldsymbol{n}\times\operatorname{curl}\boldsymbol{n} - \nabla v^2)
$$
$$
\left. + 2K_{24}\left[\operatorname{tr}(\nabla\boldsymbol{v})^2 - v^2\operatorname{tr}(\nabla\boldsymbol{n})^2 + (\boldsymbol{n}\times\operatorname{curl}\boldsymbol{n})\cdot\nabla v^2\right]\right\}dV, \tag{4.43}
$$

where use has been made of the identities in Appendix 4.A (see, e.g., [127, Ch. 2])

4.3.1   Application

We put on test the general formula (4.43) found in the preceding section. In Sec. 4.3.1, when $q_0 = 0$ the study of $\delta^2\mathscr{F}$ for a constant director field provides the stability of the undistorted configuration if and only if Ericksen's inequalities (1.8) are satisfied. In the special case of the radial hedgehog, treated in Sec. 4.3.1, (4.43) reduces to formula (2.3) of Kinderlehrer & Ou in [64] when $q_0 = 0$, $K_{24} = 0$ and $\mathscr{B}$ is the unit ball B in $\mathbb{R}^3$.

Uniform Director

For nematic liquid crystals $q_0 = 0$ and Ericksen's inequalities (1.8) require $W(\boldsymbol{n}, \nabla\boldsymbol{n})$ in (1.3) to attain its minimum on an undistorted configuration, which makes $W(\boldsymbol{n}, \nabla\boldsymbol{n})$ identically 0. Thus, Ericksen's inequalties imply a positive distortional cost (1.1) associated with any distortion of the natural state, which also ensures the positivity of the second variation of $\mathscr{F}$ at any constant vector field $\boldsymbol{n}$. Here, we prove that also the reverse is true. To this aim, we apply the formula found in (4.43) to the constant director field $\boldsymbol{n}_0$ taken as to coincides with the unit vector $\boldsymbol{e}_z$ of a standard Cartesian frame $(\boldsymbol{e}_x, \boldsymbol{e}_y, \boldsymbol{e}_z)^1$; the second variation of $\mathscr{F}$ at $\boldsymbol{n}_0$ reduces to

$$
\delta^2\mathscr{F}(\boldsymbol{n}_0)[\boldsymbol{v}_0] = \int_{\mathscr{B}}\left\{(K_{11} - 2K_{24})(\operatorname{div}\boldsymbol{v}_0)^2 + K_{22}(\boldsymbol{n}\cdot\operatorname{curl}\boldsymbol{v}_0)^2 + K_{33}|\boldsymbol{n}\times\operatorname{curl}\boldsymbol{v}_0|^2\right.
$$
$$
\left. + 2K_{24}\operatorname{tr}(\nabla\boldsymbol{v}_0)^2\right\}dV. \tag{4.44}
$$

---

[1]We recall that $W(\boldsymbol{n}, \nabla\boldsymbol{n})$ is frame-indifferent and the case presented in this Section covers all the other cases of possible constant vector fields.

The gradient of the perturbation $\boldsymbol{v}_0$ of $\boldsymbol{n}_0$, whose transpose annihilates $\boldsymbol{n}_0$ to satisfy the constraint $\boldsymbol{v}_0 \cdot \boldsymbol{n}_0 = 0$, is expressed as

$$\nabla \boldsymbol{v}_0 := \boldsymbol{e}_x \otimes \boldsymbol{a} + \boldsymbol{e}_y \otimes \boldsymbol{b}, \tag{4.45}$$

with $\boldsymbol{a}$ and $\boldsymbol{b}$ arbitrary vector fields[2]. We get from (4.45)

$$\operatorname{div} \boldsymbol{n}_0 = a_x + b_y; \tag{4.46a}$$

$$\boldsymbol{n}_0 \cdot \operatorname{curl} \boldsymbol{v}_0 = b_x - a_y; \tag{4.46b}$$

$$\boldsymbol{n}_0 \times \operatorname{curl} \boldsymbol{v}_0 = -a_z \boldsymbol{e}_x - b_z \boldsymbol{e}_y; \tag{4.46c}$$

$$\operatorname{tr} (\nabla \boldsymbol{n}_0)^2 = a_x^2 + 2a_y b_x + b_y^2; \tag{4.46d}$$

where a_i and b_i for $i = x$, y, z are the components of $\boldsymbol{a}$ and $\boldsymbol{b}$ in the frame $(\boldsymbol{e}_x, \boldsymbol{e}_y, \boldsymbol{e}_z)$, and so we arrive at the following form of (4.44):

$$\delta^2 \mathscr{F}(\boldsymbol{n}_0)[\boldsymbol{v}_0] = \int_{\mathscr{B}} \left\{ K_{11} \left(a_x^2 + b_y^2 \right) + 2 \left(K_{11} - K_{22} - K_{24} \right) a_x b_y \right.$$
$$\left. + K_{22} \left(a_y^2 + b_x^2 \right) + 2K_{24} a_y b_x + K_{33} \left(a_z^2 + b_z^2 \right) \right\} \mathrm{d}V. \tag{4.47}$$

The right-hand side of (4.47) is the sum of three independent quadratic functions, and so $\delta^2 \mathscr{F}(\boldsymbol{n}_0)[\boldsymbol{v}_0]$ is positive whenever all these functions are not negative. The last one is so if, and only if, the Ericksen's inequalities (1.8) are satisfied.

For the frame-indifference of $W(\boldsymbol{n}, \nabla \boldsymbol{n})$, there is no loss in restricting the admissible perturbations $\boldsymbol{v}_0$ to those with $b_z = 0$, and we note that in the special case in which the gradient of the perturbation $\boldsymbol{v}_0$ of $\boldsymbol{n}_0$ is assumed to be constant, that is when $\boldsymbol{a}$ and $\boldsymbol{b}$ in (4.45) are arbitrary constant vectors in $\mathcal{V}$, the second variation of $\mathscr{F}$ at any constant vector fields, (4.44), corresponds to the quadratic form (15) in [30] obtained by Ericksen by defining a local distortion of the ground state.

Hedgehog

In the special case of the radial hedgehog, $\boldsymbol{n}_r = \boldsymbol{e}_r$, $\operatorname{curl} \boldsymbol{n} = 0$, and $\operatorname{div} \boldsymbol{n} = 2r$, so that (4.43) reduces to

$$\delta^2 \mathscr{F}(\boldsymbol{n}_r)[\boldsymbol{v}] = \int_{\mathscr{B}} \left\{ (K_{11} - 2K_{24}) \left[(\operatorname{div} \boldsymbol{v})^2 - \frac{2}{r^2} v^2 \right] + K_{22} (\boldsymbol{n} \cdot \operatorname{curl} \boldsymbol{v}) \right.$$
$$+ 2K_{22} q_0 \boldsymbol{v} \cdot \operatorname{curl} \boldsymbol{v} + K_{33} |\boldsymbol{n} \times \operatorname{curl} \boldsymbol{v}|^2$$
$$\left. + 2K_{24} \left[\operatorname{tr} (\nabla \boldsymbol{v})^2 - \frac{2}{r^2} v^2 \right] \right\} \mathrm{d}V, \tag{4.48}$$

which when $q_0 = 0$, $K_{24} = 0$ and $\mathscr{B}$ is the unit ball B in $\mathbb{R}^3$ coincides with formula (2.3) of Kinderlehrer & Ou in [64]. Here, they prove that if

$$8 (K_{22} - K_{11}) + K_{33} \geq 0, \tag{4.49}$$

then the second variation (4.48) is positive in the class of perturbations $\boldsymbol{v} \in \mathcal{H}^1 \left(B, \mathbb{R}^3 \right) \cap L^\infty \left(B, \mathbb{R}^3 \right)$ with compact support and satisfying $\boldsymbol{v} \cdot \boldsymbol{n}_r = 0$. This ensures the local stability of $\boldsymbol{n}_r$ when (4.49) holds.

---

[2]Especially, $\boldsymbol{a}$ and $\boldsymbol{b}$ correspond to $\nabla (v_0)_x$ and $\nabla (v_0)_y$, respectively, where $(v_0)_i$ is the component along $\boldsymbol{e}_i$ of $\boldsymbol{v}_0$ for $i = x$, y.

4.4 Local Stability of ET Equilibrium Solutions

As said above, both solutions (1.42) and (1.43) exist only if $k_{24} > 1$. Detailed experimental investigations of the elastic properties were reported for ordinary chromonic liquid crystals in [141, 140, 142] and it was found that K_{22} is smaller than both K_{11} and K_{33}. We thus restrict attention to $k_1 \geq 1$ and $k_3 \geq 1$[3]. This means that K_{11} is allowed to be smaller than K_{24} and so to violate a further Ericksen's inequality[4], but it is always greater than K_{22}.

As K_{24} increases beyond K_{22}, and thus as k_{24} increases beyond 1, (1.44) decreases continuously from zero, making the uniform configuration energetically disfavoured and unstable (as proved in Sec. 4.3.1). The aim of this Section is to explore the stability within the Oseen-Frank's theory of the ET configurations when the CLC is confined in a cylinder, though the free-energy functional (1.1) is unbounded below when a Ericksen's inequality is violated. Hereafter we restrict attention to the increasing branch of the solution given by (1.42), though the outcome of our analysis would not be different for (1.43). Let $\boldsymbol{n}_{\mathrm{B}}$ be the equilibrium director field defined by

$$\boldsymbol{n}_{\mathrm{B}} = \sin \beta_0(\rho)\boldsymbol{e}_\theta + cos\beta_0(\rho)\,\boldsymbol{e}_z, \tag{4.50}$$

where $\beta_0 = \beta_0(\rho)$ is the strictly increasing branch of the equilibrium solution as in (1.42). The study of the stability of the ET configuration is based on the analysis of the second variation of $\mathscr{F}$ at $\boldsymbol{n}_{\mathrm{B}}$, whose expression is found in Section 1.2 and is given by (4.43). We take the vector field $\boldsymbol{v}$ which perturbs $\boldsymbol{n}_{\mathrm{B}}$ to preserve the cylindrical symmetry of the problem; it depends on ρ in (1.26) and it is given by

$$\boldsymbol{v} := \boldsymbol{v}(\rho) = f(\rho)\boldsymbol{e}_r - g(\rho)\cos\beta_0(\rho)\boldsymbol{e}_\theta + g(\rho)\sin\beta_0(\rho)\boldsymbol{e}_z, \tag{4.51}$$

where the functions $f = f(\rho)$ and $g = g(\rho)$ are absolutely continuous on $[0, 1]$. We note that $\boldsymbol{v}$ in (4.51) satisfies $\boldsymbol{v} \cdot \boldsymbol{n}_B = 0$. Degenerate planar anchoring conditions at the capillary surface (1.6) let $g(1)$ free to vary and prevent $\boldsymbol{v}$ from having a component along $\boldsymbol{e}_r$, so

$$f(1) = 0. \tag{4.52}$$

The requirement of integrability sets

$$f(0) = g(0) = 0. \tag{4.53}$$

It is shown in Appendix 4.B how to derive the following reduced functional which is an appropriate dimensionless form of $\delta^2\mathscr{F}(\boldsymbol{n}_{\mathrm{B}})(\boldsymbol{v})$ in the class of orientation fields and perturbations described by (4.50) and (4.51):

$$\delta^2\mathcal{F}(\boldsymbol{n}_{\mathrm{B}})[\boldsymbol{v}] = \frac{\delta^2\mathscr{F}(\boldsymbol{n}_{\mathrm{B}})(\boldsymbol{v})}{2\pi L K_{22}} =$$

$$=2\int_0^1 \left\{ \left[-2\cos^2\beta_0\sin^2\beta_0 + \frac{\left(-\sin^2\beta_0 + \cos^2\beta_0\right)^2}{2} + k_3\left(-\sin^2\beta_0 + 3\cos^2\beta_0\right)\sin^2\beta_0 \right] \frac{g^2}{\rho} \right.$$

$$\left. +\frac{\rho g'^2}{2} \right\} \mathrm{d}\rho + (1 - 2k_{24})\left(-\sin^2\beta_0 + \cos^2\beta_0\right)g^2(1)$$

$$+\int_0^1 \left\{ \left[k_1 - 2\left(\rho\beta_0' + \cos\beta_0\sin\beta_0\right)^2 + k_3\left(\rho^2\beta_0'^2 + \sin^2\beta_0 + 4\cos\beta_0\sin\beta_0\beta_0' - 2\sin^4\beta_0\right) \right] \frac{f^2}{\rho} \right.$$

$$\left. +k_1\rho f'^2 \right\} \mathrm{d}\rho. \tag{4.54}$$

---

[3]For completeness the argument in Appendix 4.C also covers the values of $k_3 \in (0, 1)$.

[4]The material parameters of SSY are $K_{11} = 4.3$pN, $K_{22} = 0.7$pN and $K_{33} = 6.1$pN [141], and so $k_1 = 6$ and $k_3 = 8.7$. Davidson [19] gave a remarkable value of $k_{24} = 22.5$. The obtained value of K_{24} is at odds with both Ericksen's inequalities involving it.

Integrations by parts have been performed in (4.54) by considering that $f(\rho)$ vanishes at both end-points of the interval $[0, 1]$ and $g(\rho)$ vanishes at $\rho = 0$.

In (4.54) the pairs (g, g') and (f, f') are decoupled and $\delta^2 \mathcal{F}(\boldsymbol{n}_B)[\boldsymbol{v}]$ can be regarded as a sum of two independent functionals of one of the two pairs. The former functional associated with the pair (g, g') corresponds to the second variation $\delta^2 \mathcal{F}$ at $\boldsymbol{n}_B$ for azimuthal perturbations

$$\boldsymbol{v}_{\theta z} := g(\rho) \left[-\cos \beta_0(\rho) \boldsymbol{e}_\theta + \sin \beta_0(\rho) \boldsymbol{e}_z \right], \tag{4.55}$$

while the latter deals with radial perturbations

$$\boldsymbol{v}_r := f(\rho) \boldsymbol{e}_r. \tag{4.56}$$

Sections 4.4.1 and 4.4.2 are devoted to their illustration and to the study of their positivity, which guarantees the local stability of the ET configuration with respect to these two types of perturbations. This ensures the local stability of the ET configuration.

4.4.1 Azimuthal Perturbations

The stability of the ET solution for azimuthal perturbations of the type (4.55) is guaranteed by the non-negativity of the following functional which depends on the pair (g, g'):

$$\delta^2 \mathcal{F}_{\theta z}(\boldsymbol{n}_B)(\boldsymbol{v}_{\theta z}) = \frac{\delta^2 \mathcal{F}(\boldsymbol{n}_B)(\boldsymbol{v})}{2\pi L K_{22}} =$$

$$= 2 \int_0^1 \left\{ \left[-2 \cos^2 \beta_0 \sin^2 \beta_0 + \frac{\left(-\sin^2 \beta_0 + \cos^2 \beta_0 \right)^2}{2} + k_3 \left(-\sin^2 \beta_0 + 3 \cos^2 \beta_0 \right) \sin^2 \beta_0 \right] \frac{g^2}{\rho} \right.$$

$$\left. + \frac{\rho g'^2}{2} \right\} \mathrm{d}\rho + (1 - 2k_{24}) \left(-\sin^2 \beta_0 + \cos^2 \beta_0 \right) g(1)^2, \tag{4.57}$$

where the functions $g = g(\rho)$ in the domain of $\delta^2 \mathcal{F}_{\theta z}(\boldsymbol{n}_B)(\boldsymbol{v}_{\theta z})$ are absolutely continuous functions on $[0, 1]$ and satisfy $g(0) = 0$, (4.53). The function $\beta_0(\rho)$ defined by (1.42) is strictly increasing on $[0, 1]$ and induces a change of variables which maps $[0, 1]$ onto $[0, \beta_0^1]$, where

$$\beta_0^1 := \beta_0(1) = \arctan \left(\frac{2\sqrt{k_{24}(k_{24} - 1)}}{\sqrt{k_3}} \right). \tag{4.58}$$

In the new variable, $g = g(\rho)$, which is an arbitrary function of ρ, can be regarded as an absolute continuous function $\hat{g}$ on $[0, \beta_0^1]$ defined by

$$\hat{g}(\beta_0(\rho)) := g(\rho), \tag{4.59}$$

with $\hat{g}(0) = 0$, since (4.53) holds. With the aid of (4.59) and of

$$\mathrm{d}\rho = \frac{\rho}{\sin \beta_0 \sqrt{\cos^2 \beta_0 + k_3 \sin^2 \beta_0}} \mathrm{d}\beta_0 \tag{4.60}$$

the functional in (4.57) can be given the form

$$\delta^2 \mathcal{F}_{\theta z}(\boldsymbol{n}_B)(\boldsymbol{v}_{\theta z}) = \int_0^{\beta_0^1} \left\{ \frac{1}{\sin \beta_0 \sqrt{\cos^2 \beta_0 + k_3 \sin^2 \beta_0}} \left[(-\sin^2 \beta_0 + \cos^2 \beta_0)(\cos^2 \beta_0 + (2k_3 - 1) \sin^2 \beta_0) \right. \right.$$

$$\left. + 4(k_3 - 1) \cos^2 \beta_0 \sin^2 \beta_0 \right] \hat{g}^2 + \sin \beta_0 \sqrt{\cos^2 \beta_0 + k_3 \sin^2 \beta_0} \hat{g}'^2 \right\} \mathrm{d}\beta_0$$

$$+ (1 - 2k_{24}) \left[-\sin^2 \beta_0^1 + \cos^2 \beta_0^1 \right] \hat{g}(\beta_0^1)^2, \tag{4.61}$$

where the prime denotes differentiation with respect to β_0. As is clear from (4.58), the extreme of integration β_0^1 depends on k_3 and on k_{24} and to resettle this dependence into the integrand, we define another change of variables $\beta_0 \to u(\beta_0)$ as follows

$$u(\beta_0) := \frac{\sin \beta_0}{A}, \tag{4.62}$$

which is increasing for $\beta_0 \in [0, \beta_0^1]$ with $\beta_0^1 < \pi/2$ and where the parameter $A \in (0, 1)$ is related to both k_3 and k_{24} through

$$A := \sin \beta_0^1 = \sin \beta_0(1) = \frac{2\sqrt{k_{24}(k_{24} - 1)}}{\sqrt{k_3 + 4k_{24}(k_{24} - 1)}}. \tag{4.63}$$

We do not consider both values $A = 0$ and $A = 1$, since the former corresponds to $k_{24} = 1$ for which Ericksen's inequalities still hold and the ET configuration coincides with the trivial one, while the latter is reached by $k_{24} = \infty$ when $k_3 > 0$. The change of variables (4.62) maps the interval $[0, \beta_0^1]$ onto $[0, 1]$ and, in the new variable, $\hat{g}$ becomes a function on $[0, 1]$, which is defined by

$$U(u(\beta_0)) := \hat{g}(\beta_0), \tag{4.64}$$

and belongs to the class

$$\mathcal{A}_{\theta z}^U := \{U \in \mathcal{AC}[0, 1] : \ U(0) = 0\}. \tag{4.65}$$

Inserting (4.64) into (4.61) and by use of

$$\mathrm{d}\beta_0 = \frac{A}{\sqrt{1 - (Au)^2}} \, \mathrm{d}u, \tag{4.66}$$

we give $\delta^2 \mathcal{F}_{\theta z}(\boldsymbol{n}_{\mathrm{B}})(\boldsymbol{v}_{\theta z})$ the following form:

$$\delta^2 \mathcal{F}_{\theta z}(\boldsymbol{n}_{\mathrm{B}})(\boldsymbol{v}_{\theta z}) = \int_0^1 \left\{ \frac{1}{u\sqrt{1 - (Au)^2}\sqrt{1 + (k_3 - 1)(Au)^2}} \left[\left(1 - 2(Au)^2\right) \left(1 + 2(k_3 - 1)(Au)^2\right) \right. \right.$$
$$\left. + 4(k_3 - 1)(1 - (Au)^2)(Au)^2 \right] U^2 + u\sqrt{1 - (Au)^2}\sqrt{1 + (k_3 - 1)(Au)^2}U'^2 \Bigg\} \mathrm{d}u$$
$$+ (1 - 2k_{24})(1 - 2A^2)U(1)^2, \tag{4.67}$$

where a prime now denotes differentiation with respect to the variable u.

We wish to discuss the role played by the constitutive parameters $k_3 \in [1, \infty)$ and $k_{24} \in (1, \infty)$ in determining the non-negativity of (4.67). To this end the structure of the second variation (4.67) suggests to study the problem through the independent parameters (k_3, A) ranging in the strip $\mathsf{S} := \{(k_3, A) : 1 \leq k_3 < \infty, 0 < A < 1\}$. Indeed, by regarding k_{24} as the strictly increasing function of A given by

$$k_{24} = \frac{\sqrt{1 - A^2} + \sqrt{1 + (k_3 - 1)A^2}}{2\sqrt{1 - A^2}}, \tag{4.68}$$

that k_3 is independent of A follows from the one-to-one correspondence between the pairs $(k_3, k_{24}) \in [1, \infty) \times (1, \infty)$ and $(k_3, A) \in \mathsf{S}$ ensured by the non vanishing Jacobian determinant of the coordinate conversion

$$J := \frac{k_3}{2} \frac{A}{(1 - A^2)^{3/2}\sqrt{1 + (k_3 - 1)A^2}}. \tag{4.69}$$

By (4.68) we easily express (4.67) in terms of $(k_3, A) \in \mathsf{S}$ as

$$\delta^2 \mathcal{F}_{\theta z}(\boldsymbol{n}_{\mathrm{B}})(\boldsymbol{v}_{\theta z}) = \int_0^1 \left[\frac{\varphi(k_3, A, u)}{\gamma(k_3, A, u)} U(u)^2 + \gamma(k_3, A, u)U'(u)^2 \right] \mathrm{d}u + q_0(k_3, A)U(1)^2, \tag{4.70}$$

where, we have employed the following notations

$$\varphi = \varphi(k_3, A, u) := \left(1 - 2(Au)^2\right)\left(1 + 2(k_3 - 1)(Au)^2\right) + 4(k_3 - 1)(1 - (Au)^2)(Au)^2, \quad (4.71a)$$

$$\gamma = \gamma(k_3, A, u) := u\sqrt{1 - (Au)^2}\sqrt{1 + (k_3 - 1)(Au)^2}, \quad (4.71b)$$

$$q_0 := q_0(k_3, A) := -\frac{(1 - 2A^2)\sqrt{1 + (k_3 - 1)A^2}}{\sqrt{1 - A^2}}. \quad (4.71c)$$

A condition for the positivity of the functional (4.70) arises when we treat U and U' as independent variables. In this case, the coefficients of U^2, U'^2 and $U(1)^2$ are required to be positive, i.e. $\gamma(k_3, A, u)$, $\varphi(k_3, A, u)$ and $q_0(k_3, A)$ must be so. Since $\gamma(k_3, A, u)$ is non-negative for every $(k_3, A, u) \in \mathsf{S} \times [0, 1]$ and $q_0(k_3, A) > 0$ whenever $A \geq 1/\sqrt{2}$ and vanishes at $A = 1/\sqrt{2}$, the non-negativity of (4.70) is ensured for those values of $(k_3, A) \in [1, \infty) \times [1/\sqrt{2}, 1)$ whereby $\varphi(k_3, A, u)$ is positive for every $u \in [0, 1]$. This happens whenever

$$A \leq A_p(k_3) := \sqrt{\frac{3k_3 - 4 + \sqrt{(3k_3 - 4)^2 + 8(k_3 - 1)}}{8(k_3 - 1)}}, \quad \text{for } k_3 \geq 1, \quad (4.72)$$

and, since $A_p(1) = 1/\sqrt{2}$, the stability of the ET solution is trivially guaranteed for

$$(k_3, A) \in [1, \infty) \times \left[\frac{1}{\sqrt{2}}, A_p(k_3)\right]. \quad (4.73)$$

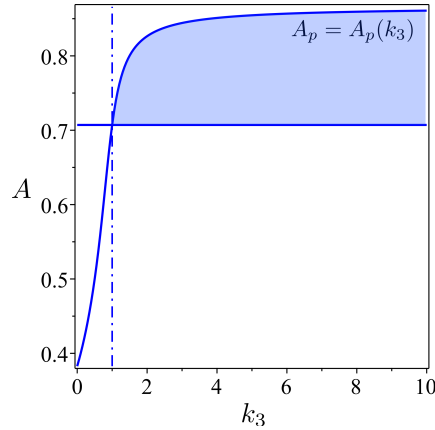This region of the strip S is illustrated in Figure 4.3.

Figure 4.3: The blue region between the graph of A_p against k_3 for $k_3 \geq 1$ and the horizontal line $A = 1/\sqrt{2}$ (the first curve crosses the second one at $k_3 = 1$) represents the values of k_3 and A for which both functions φ and q_0 are positive. This is a trivial condition which ensures the positivity of (4.70).

The stability of the ET solution is proved for every $(k_3, A) \in \mathsf{S}$ through [71, Lemma 2.1] for $c = p = 2$. This Lemma is stated below in the form needed to our development:

Lemma 1. [71, Lemma 2.1] Suppose $[a, b]$ interval in $\mathbb{R}$. Let $\widetilde{U} = \widetilde{U}(u) \in AC[a, b]$ and there exists two functionals $Q(u, t)$ and $G(u, t)$ satisfying the following conditions:

- t is in the range of the function $\widetilde{U} = \widetilde{U}(u)$;

- $Q(u, \widetilde{U}(u))$ *is integrable for* $u \in [a, b]$;

- $G(u, \widetilde{U}(u))$ *is absolutely continuous for* $u \in [a, b]$.[5]

Then

$$\int_a^b Q(u, \widetilde{U}(u))\widetilde{U}'(u)^2 \, du \geq - \int_a^b \left[Q(u, \widetilde{U}(u))^{-1} G_{\widetilde{U}}^2 + 2G_u \right] du + 2 \left[G(b, \widetilde{U}(b)) - G(a, \widetilde{U}(a)) \right],$$

(4.74)

where $G_{\widetilde{U}} = \partial G(u, \widetilde{U})/\partial \widetilde{U}$ *and* $G_u = [\partial G(u, t)/\partial u]\,|_{t=\widetilde{u}}$.

Since

$$[\sqrt{\gamma} U]' = \frac{\gamma'}{2\sqrt{\gamma}} U + \sqrt{\gamma} U',$$

(4.75)

the integration over $[0, 1]$ of the term $\gamma U'^2$ in (4.70) yields

$$\int_0^1 \gamma U'^2 \, du = \int_0^1 \left\{ [(\sqrt{\gamma} U)']^2 - \frac{\gamma'^2}{4\gamma} U^2 - \gamma' U U' \right\} du$$

(4.76)

where the dependence of U and U' on u and of γ and γ' on k_3, A and u has been omitted.

The functions

$$\widetilde{U} = \sqrt{\gamma} U, \quad Q(u, \widetilde{U}) = 1, \quad G(u, \widetilde{U}) = \frac{3}{4} \frac{\gamma'}{\gamma} \widetilde{U}^2 = \frac{3}{4} \gamma' U^2,$$

(4.77)

obey the conditions (i), (ii) and (iii) of Lemma 1 when $U \in \mathcal{A}_{\theta z}^U$ and γ is as in (4.71b), and so the lower estimate (4.74) applies to the first addend on the right-hand side of (4.77);

$$\int_0^1 [(\sqrt{\gamma} U)']^2 \, du \geq - \int_0^2 \left[\frac{3}{4} \frac{\gamma'^2}{\gamma} + \frac{3}{2} \gamma'' \right] U^2 \, dU + \frac{3}{2} \gamma'|_{u=1} U(1)^2.$$

(4.78)

Making use of (4.78) in (4.75) and integrating by parts its third addend with the boundary condition $U(0) = 0$ for $U \in \mathcal{A}_{\theta z}^U$, the following inequality holds:

$$\int_0^1 \gamma U'^2 \, du \geq \int_0^1 \left[-\frac{\gamma'^2}{\gamma} - \gamma'' \right] U^2 \, du + \gamma'|_{u=1} U(1)^2.$$

(4.79)

This shows that for all values of $(k_3, A) \in \mathsf{S}$ the scaled functional (4.70) which represents the second variation $\delta^2 \mathcal{F}$ at $\boldsymbol{n}_\mathrm{B}$ for azimuthal perturbations is bounded from below in $\mathcal{A}_{\theta z}^U$ as follows:

$$\delta^2 \mathcal{F}_{\theta z}(\boldsymbol{n}_\mathrm{B})[\boldsymbol{v}_{\theta z}] \geq \int_0^1 \left[\frac{\varphi(k_3, A, u)}{\gamma(k_3, A, u)} - \frac{\gamma'(k_3, A, u)^2}{\gamma(k_3, A, u)} - \gamma''(k_3, A, u) \right] U(u)^2 \, du$$
$$+ \left[q_0(k_3, A) + \gamma'(k_3, A, 1) \right] U(1)^2.$$

(4.80)

Consequently, $\delta^2 \mathcal{F}_{\theta z}(\boldsymbol{n}_\mathrm{B})(\boldsymbol{v}_{\theta z})$ is certainly positive when the coefficient of U^2 and the surface term are positive, and so when both of the following inequalities hold

$$\frac{\varphi(k_3, A, u)}{\gamma(k_3, A, u)} - \frac{\gamma'(k_3, A, u)^2}{\gamma(k_3, A, u)} - \gamma''(k_3, A, u) \geq 0, \quad q_0(k_3, A) + \gamma'(k_3, A, 1) \geq 0.$$

(4.81)

---

[5]If $p - 1$ is not a quotient of two positive odd integers, then $G(u, t)$ is assumed to be also increasing with respect to t. Here $p - 1 = 2 - 1 = 1$ and this condition can be omitted.

Substituting the expression given in (4.71) for φ, γ and q_0 we get that this happens whenever

$$\frac{7A^2u}{\sqrt{1+(k_3-1)(Au)^2}\sqrt{1-(Au)^2}}\left[\frac{4}{7}+(k_3-1)(Au)^2\right]\geq 0, \tag{4.82a}$$

$$\frac{A^2(1-A^2)}{\sqrt{1+(k_3-1)(Au)^2}\sqrt{1-(Au)^2}}(k_3-1)\geq 0, \tag{4.82b}$$

i.e. for every $(k_3,A)\in\mathsf{S}$. Thus, the ET solutions given by (1.42) and (1.43) are locally stable for the Oseen-Frank's free-energy $\mathscr{F}$ with respect to azimuthal perturbations for every value of $(k_3,k_{24})\in[1,\infty)\times(1,\infty)$, which are all the admissible values of the scaled elastic constants for CLCs. In this range, $\delta^2\mathcal{F}_{\theta z}(\boldsymbol{n}_{\mathrm{B}})(\boldsymbol{v}_{\theta z})$ is strictly positive for all functions $U\neq 0$ in $\mathcal{A}_{\theta z}^U$ and, only in the limiting case when $A=0$, i.e. when $K_{24}=K_{22}$, there can exists functions $U\neq 0$ that make it vanish (e.g. $U(u)=\sqrt{3}u$). This complies with the validity of the Ericksen's inequalities when $A=0$; this value marks the onset of the bifurcation of the ET solutions from the trivial one and the minimum of the free-energy is zero.

Only values of k_3 characteristic of CLCs have been taken into account in our discussion. In Appendix 4.C the local stability of the ET configurations is explored through spectral methods.

4.4.2   Radial Perturbations

Following the same lines of thought outlined in Section 4.4.1, we deduce the local stability of the ET solution for radial perturbations of the type (4.56) by proving that the scaled functional in (4.54) associated with the pair (f,f')

$$\delta^2\mathcal{F}_r(\boldsymbol{n}_{\mathrm{B}})[\boldsymbol{v}_r]=\int_0^1\left\{\left[k_1-2\left(\rho\beta_0'+\cos\beta_0\sin\beta_0\right)^2+k_3\left(\rho^2\beta_0'^2+\sin^2\beta_0\right.\right.\right.$$
$$\left.\left.\left.+4\cos\beta_0\sin\beta_0\beta_0'-2\sin^4\beta_0\right)\right]\frac{f^2}{\rho}+k_1\rho f'^2\right\}\mathrm{d}\rho \tag{4.83}$$

is not negative for any absolutely continuous function $f=f(\rho)$ satisfying (4.53) and (4.52). The terms in (4.83) multiplied by k_1 are positive and we can lower $\mathcal{F}_r(\boldsymbol{n}_{\mathrm{B}})[\boldsymbol{v}_r]$ if we replace k_1 by the lower admissible value for ordinary LCLCs, i.e. 1. We then apply the change of variables (4.66) employed in Section 4.4.1, and for $k_1=1$ (4.83) can be rewritten as

$$\delta^2\mathcal{F}_r(\boldsymbol{n}_{\mathrm{B}})(\boldsymbol{v}_r)=\int_0^1\left[\frac{\varphi_r(k_3,A,u)}{\gamma(k_3,A,u)}U_r(u)^2+\gamma(k_3,A,u)U_r'(u)^2\right]\mathrm{d}u. \tag{4.84}$$

The functions admissible for (4.84) are members of the class

$$\mathcal{A}_r^{U_r}:=\left\{U_r\in\mathcal{AC}[0,1]:\ U_r(0)=U_r(1)=0\right\}. \tag{4.85}$$

Here, $\gamma=\gamma(k_3,A,u)$ coincides with the function found for azimuthal perturbation whose expression is given in (4.71b), while φ_r accords with

$$\varphi_r=\varphi_r(k_3,A,u):=1+2(k_3-2)(Au)^2+(k_3-4)(k_3-1)(Au)^4$$
$$+4(k_3-1)(Au)^2\sqrt{1-(Au)^2}\sqrt{1+(k_3-1)(Au)^2}. \tag{4.86}$$

Here the trivial condition for the positive definiteness of the density of (4.83), which arises when U and U' are treated as independent variables, amounts to the positivity of the term multiplied by U^2, and so of $\varphi_r=\varphi_r(k_3,A,u)$. Whenever $k_3<2.61$, the values of $(k_3,A)\in\mathsf{S}$ for which this function is positive for every $u\in[0,1]$ corresponds to region below the graph in Figure 4.4 , while whenever $k_3\geq 2.61$ this happens for every $A\in(0,1)$.

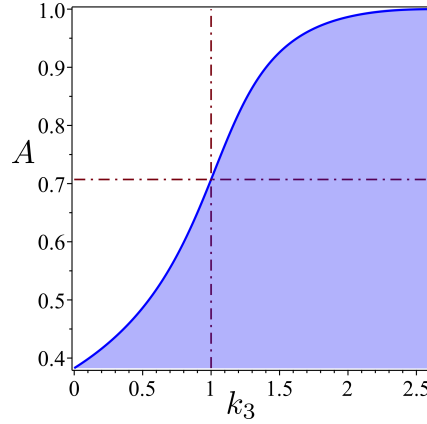**Figure 4.4:** The blue region below the graph represents the values of k_3 and A for which the positivity of (4.84) is ensured by the positivity of the function $\widetilde{\varphi}$ which is the trivial condition for the positivite definiteness of the density of (4.70). The function illustrated here reaches 1 at $k_3 = 2.61$ and whenever $k_3 > 2.61$ $\delta^2 \mathcal{F}_r(\boldsymbol{n}_\mathrm{B})(\boldsymbol{v}_r)$ is positive for every $A \in (0,1)$.

Following the same lines described above, where the pivotal role is played by [71, Lemma 2.1], the same lower bound (4.80) found in Section 4.4.1 for the second variation holds also when the perturbations are radial, and so when U_r belongs to $\mathcal{A}_r^{U_r}$, (4.85). Thus (4.84) is lowered by

$$\delta^2 \mathcal{F}_r(\boldsymbol{n}_\mathrm{B})(\boldsymbol{v}_r) \geq \int_0^1 \left[\frac{\varphi_r(k_3, A, u)}{\gamma(k_3, A, u)} - \frac{\gamma'(k_3, A, u)^2}{\gamma(k_3, A, u)} - \gamma''(k_3, A, u) \right] U_r(u)^2 \, \mathrm{d}u. \tag{4.87}$$

and to make $\delta^2 \mathcal{F}_r(\boldsymbol{n}_\mathrm{B})(\boldsymbol{v}_r)$ positive in the appropriate class of perturbations, the following inequality, where use has been made of (4.86) and (4.71b), is requested to be satisfied

$$\frac{\varphi_r}{\gamma} - \frac{\gamma'^2}{\gamma} - \gamma'' = \frac{4A^2 u}{\sqrt{1-(Au)^2}\sqrt{1+(k_3-1)(Au)^2}} \left[(k_3 - 1)\sqrt{1-(Au)^2}\sqrt{1+(k_3-1)(Au)^2} \right.$$

$$\left. + \frac{1}{4}(Au)^2(k_3+11)(k_3-1) - k_3 + 2 \right] \geq 0. \tag{4.88}$$

This happens whenever for every $(k_3, A) \in \mathsf{S}$. The values of $k_3 \in (0,1)$ are considered in Appendix 4.C.1

4.A   Mathematical Tools

Here I recall all the mathematical tools that are extensively employed in deriving the general formula for the second variation of Oseen-Frank's free-energy.

$$\mathrm{div}\,(\alpha \boldsymbol{n}) = \alpha \, \mathrm{div}\, \boldsymbol{n} + \boldsymbol{n} \cdot \nabla \alpha, \tag{4.89a}$$

$$\mathrm{curl}\,(\alpha \boldsymbol{n}) = \alpha \, \mathrm{curl}\, \boldsymbol{n} + \nabla \alpha \times \boldsymbol{n}, \tag{4.89b}$$

$$\boldsymbol{a} \times (\boldsymbol{b} \times \boldsymbol{c}) = \boldsymbol{b}\,(\boldsymbol{a} \cdot \boldsymbol{c}) - \boldsymbol{c}\,(\boldsymbol{a} \cdot \boldsymbol{b}), \tag{4.89c}$$

$$\nabla\,(\alpha \boldsymbol{n}) = \alpha \nabla \boldsymbol{n} + \boldsymbol{n} \otimes \nabla \alpha, \tag{4.89d}$$

$$\mathrm{tr}(\alpha \boldsymbol{A}) = \alpha \, \mathrm{tr}\, \boldsymbol{A}, \tag{4.89e}$$

$$\mathrm{tr}(\boldsymbol{a} \otimes \boldsymbol{b}) = \boldsymbol{a} \cdot \boldsymbol{b}, \tag{4.89f}$$

which hold for every $\alpha \in \mathbb{R}$, $\boldsymbol{a}$ and $\boldsymbol{b}$ in the translation space $\mathcal{V}$ and $\boldsymbol{A}$ in $\mathcal{L}\,(\mathcal{V}) := \{\boldsymbol{L} : \mathcal{V} \to \mathcal{V} : \boldsymbol{L} \text{ is linear}\}$.

4.B   Distortions

In this Appendix, we justify the expression for the reduced functional (4.54) which is an appropriate dimensionless form of $\delta^2 \mathscr{F}(\boldsymbol{n}_\mathrm{B})(\boldsymbol{v})$ in the class of orientation fields and perturbations described by (4.50) and (4.51). It follows from (4.50) and (4.51) that

$$\nabla \boldsymbol{n}_\mathrm{B} = \frac{1}{R}\left(-\frac{\sin\beta_0}{\rho}\boldsymbol{e}_r\otimes\boldsymbol{e}_\theta + \cos\beta_0\beta_0'\boldsymbol{e}_\theta\otimes\boldsymbol{e}_r - \sin\beta_0\beta_0'\boldsymbol{e}_z\otimes\boldsymbol{e}_r\right), \tag{4.90a}$$

$$\operatorname{div}\boldsymbol{n}_\mathrm{B} = 0, \tag{4.90b}$$

$$\boldsymbol{n}_\mathrm{B}\cdot\operatorname{curl}\boldsymbol{n}_\mathrm{B} = \frac{1}{R}\left(\beta_0' + \frac{\cos\beta_0\sin\beta_0}{\rho}\right), \tag{4.90c}$$

$$\boldsymbol{n}_\mathrm{B}\times\operatorname{curl}\boldsymbol{n}_\mathrm{B} = \frac{1}{R}\left(\frac{\sin^2\beta_0}{\rho}\right)\boldsymbol{e}_r, \tag{4.90d}$$

$$\operatorname{tr}(\nabla\boldsymbol{n}_\mathrm{B})^2 = \frac{1}{R^2}\left(-\frac{2\cos\beta_0\sin\beta_0\beta_0'}{\rho}\right), \tag{4.90e}$$

$$\nabla\boldsymbol{v} = \frac{1}{R}\left[f'\boldsymbol{e}_r\otimes\boldsymbol{e}_r + \frac{g\cos\beta_0}{\rho}\boldsymbol{e}_r\otimes\boldsymbol{e}_\theta + \left(g\sin\beta_0\beta_0' - \cos\beta g'\right)\boldsymbol{e}_\theta\otimes\boldsymbol{e}_r\right.$$
$$\left.+\frac{f}{\rho}\boldsymbol{e}_\theta\otimes\boldsymbol{e}_\theta + \left(\sin\beta_0 g' + g\cos\beta_0\beta_0'\right)\boldsymbol{e}_z\otimes\boldsymbol{e}_r\right], \tag{4.91a}$$

$$\operatorname{div}\boldsymbol{v} = \frac{1}{R}\left(f' + \frac{f}{\rho}\right), \tag{4.91b}$$

$$\boldsymbol{v}\cdot\operatorname{curl}\boldsymbol{v} = \frac{1}{R}\left[g^2\left(\beta_0' - \frac{\sin\beta_0\cos\beta_0}{\rho}\right)\right], \tag{4.91c}$$

$$v^2 = f^2 + g^2, \tag{4.91d}$$

$$\nabla v^2 = \frac{1}{R^2}\left(2ff' + 2gg'\right), \tag{4.91e}$$

$$\operatorname{tr}(\nabla\boldsymbol{v})^2 = \frac{1}{R^2}\left[f'^2 + \frac{f^2}{\rho^2} + \frac{2g\cos\beta_0}{\rho}\left(g\sin\beta_0\beta_0' - \cos\beta_0 g'\right)\right], \tag{4.91f}$$

$$\boldsymbol{v}\cdot\operatorname{curl}\boldsymbol{n}_\mathrm{B} = \frac{1}{R}\left(\frac{g\sin\beta_0^2}{\rho}\right), \tag{4.92a}$$

$$\boldsymbol{n}\cdot\operatorname{curl}\boldsymbol{v} = \frac{1}{R}\left[-g' - \frac{g\cos^2\beta_0}{\rho}\right], \tag{4.92b}$$

$$\boldsymbol{v}\times\operatorname{curl}\boldsymbol{n}_\mathrm{B} = \frac{1}{R}\left[-g\left(\beta_0' + \frac{\sin\beta_0\cos\beta_0}{\rho}\right)\boldsymbol{e}_r - f\left(\frac{\sin\beta_0}{\rho} + \cos\beta_0\beta_0'\right)\boldsymbol{e}_\theta\right.$$
$$\left.+f\sin\beta_0\beta_0'\boldsymbol{e}_z\right], \tag{4.92c}$$

$$\boldsymbol{n}_\mathrm{B}\times\operatorname{curl}\boldsymbol{v} = \frac{1}{R}\left[g\left(\beta_0' - \frac{\sin\beta_0\cos\beta_0}{\rho}\right)\boldsymbol{e}_r\right], \tag{4.92d}$$

$$(\boldsymbol{v}\times\operatorname{curl}\boldsymbol{v})\cdot\boldsymbol{e}_r = \frac{1}{R}\left(gg' + \frac{g^2\cos^2\beta_0}{\rho}\right), \tag{4.92e}$$

where a prime denotes the differentiation with respect to ρ. By the change of variables $r \to \rho(r)$ where $\rho = \rho(r)$ is given by (1.26) and making use of (4.90), (4.91) and (4.92) in (4.43), we arrive at the reduced functional in (4.54).

4.C Legendre Polynomials for $k_3 < 1$

We rewrite the functional $\delta^2 \mathcal{F}_{\theta z}(\boldsymbol{n}_B)(\boldsymbol{v}_{\theta z})$ given by (4.70) in Section 4.4.1, i.e. the dimensionless form of the second variation at $\boldsymbol{n}_B$ for azimuthal perturbations $\boldsymbol{v}_{\theta z}$, in a form which is especially expedient to the application of the principal results of [47, Ch. 6] for the class of *singular Sturm-Liouville Eigenvalue Problems-II* with separated boundary conditions:

$$\delta^2 \mathcal{F}_{\theta z}(\boldsymbol{n}_B)(\boldsymbol{v}_{\theta z}) = \int_0^1 \left[q(k_3, A, u)U(u)^2 + p(k_3, A, u)U'(u)^2 \right] \mathrm{d}u + q_0(k_3, A)U(1)^2, \qquad (4.93)$$

where we have employed the following notations

$$q(k_3, A, u) = \frac{\widetilde{\varphi}(k_3, A, u)}{u}, \quad \text{where} \quad \widetilde{\varphi}(k_3, A, u) := \frac{\left(1 - 2(Au)^2\right)\left(1 + 2(k_3 - 1)(Au)^2\right)}{\sqrt{1 - (Au)^2}\sqrt{1 + (k_3 - 1)(Au)^2}}, \qquad (4.94a)$$

$$p(k_3, A, u) = u\widetilde{\gamma}, \quad \text{where} \quad \widetilde{\gamma}(k_3, A, u) := \sqrt{1 - (Au)^2}\sqrt{1 + (k_3 - 1)(Au)^2}, \qquad (4.94b)$$

and $q_0 = q_0(k_3, A)$ as in (4.71c). The prime denotes differentiation with respect to u and we note that $\widetilde{\varphi}$ and $\widetilde{\gamma}$ reads in the notation introduced in (4.71) as $u\varphi/\gamma$ and γ/u, respectively. The Euler-Lagrange equations of (4.93) subject to the constraint that the L^2-norm of the admissible functions $U = U(u)$ in the class $\mathcal{A}_{\theta z}$ is held fixed to 1, i.e.

$$\int_0^1 U(u)^2 \, \mathrm{d}u = 1, \qquad (4.95)$$

corresponds to the eigenvalue problem for a Sturm-Liouville differential equation, which here is in the form

$$- \left[p(k_3, A, u)U'(u) \right]' + q(k_3, A, u)U(u) = \lambda U(u) \quad \text{for } u \in (0, 1), \qquad (4.96a)$$

$$U(0) = 0, \qquad (4.96b)$$

$$p(k_3, A, 1)U'(1) + q_0(k_3, A)U(1) = 0. \qquad (4.96c)$$

Here, λ is an arbitrary scalar field defined in $[0, 1]$ which can be interpreted as the Lagrange multiplier associated with the isoperimetric constraint (4.95).

The functions $\widetilde{\varphi}$ and $\widetilde{\gamma}$ in (4.94), $U \in \mathcal{A}_{\theta z}^U$ and q_0 in (4.71c) obey the steading assumptions of the singular Sturm-Liouville Eigenvalue Problems-II stated in [47, Ch. 6] for $[a, b] = [0, 1]$ and $r(u) = 1$ (for every $u \in [0, 1]$); indeed, $\widetilde{\varphi}$ is real valued and continuous on $[0, 1]$ and do not vanish at $u = 0$, $\widetilde{\gamma}$ is positive and continuous on $[0, 1]$, $|U(0)| < \infty$ and $|\gamma(1)| + |q_0| \neq 0$.

We reproduce below the main results (c.f. [47, Lemma 176, Theorem 182, Theorem 184]) of [47, Ch. 6] concerning the classification of the eigenvalues λ of (4.96) and the regularity of the corresponding eigenvectors $U = U(u) \neq 0$[6].

Theorem 1. *[47, Lemma 176, Theorem 182, Theorem 184] If $U(u)$ is an eigenfunction of (4.96), then $U(u)$ is continuous on $[0, 1]$, $U(0) = 0$, $\lim_{u \to 0} p(k_3, A, u)U'(u) = 0$ and $U(u)$ is continuously differentiable on $0 < u \leq 1$ and satisfies the Sturm-Liouville differential equation (4.96a) there. In particular, the Sturm-Liouville eigenvalue problem (4.96) has an infinite sequence of real eigenvalues $\{\lambda_n\}_{n=0}^{\infty}$ and a corresponding sequence of real-valued eigenfunctions $\{U_n\}_{n=0}^{\infty}$ with the following properties:*

(i) Each eigenvalue is simple (has both algebraic and geometric multiplicity 1). Moreover,

---

[6]$U = U(u)$ is the eigenfunction corresponding to λ if (4.96) is satisfied for the pair λ and U.

- *if $p(k_3, A, 1)q_0 \geq 0$, i.e. if $A \geq 1/\sqrt{2}$ by (4.94b) and (4.71c), at most a finite number of the eigenvalues are negative and the sequence of eigenvalues is unbounded; hence, the eigenvalues can be listed as $\lambda_0 < \lambda_1 < .. < \lambda_n < ..$, with $\lambda_n \to \infty$ as $n \to \infty$,*

- *$p(k_3, A, 1)q_0 < 0$, i.e. if $0 < A < 1/\sqrt{2}$, the preceding property is established in the weaker form that the eigenvalues are real, simple, and can be listed by increasing absolute value as $|\lambda_0| < |\lambda_1| < .. < |\lambda_n| < ..$, with $|\lambda_n| \to \infty$ as $n \to \infty$;*

(ii) *The corresponding eigenfunctions can be chosen real-valued and orthonormal with weight function 1,*

$$\int_0^1 U_j(u)U_k(u)\, \mathrm{d}u = \delta_{j,k}, \tag{4.97}$$

where $\delta_{j,k}$ is the Kronecker delta. If, in addition to the standing assumptions, the singular Sturm-Liouville eigenvalue problem (4.96) satisfies $p(k_3, A, 1)q_0 \geq 0$, i.e. $A \geq 1/\sqrt{2}$, the eigenfunctions $\{U_n\}_{n=0}^{\infty}$ can be chosen such that they form a Tchebycheff system on $[0, 1]$ for each n. Consequently, the following oscillatory and approximation properties hold:

- *U_n has n nodal (counted once) zeros in $(0, 1)$ and no other zeros there.*

- *The zeros of U_{n-1} and U_n strictly interlace on $(0, 1)$.*

The smallest eigenvalue λ_m of the singular eigenvalue problem (4.96) satisfies the minimum of the second variation functional (4.93) over all functions $U \neq 0$ satisfying the isoperimetric constraint (4.95), (4.96b) and the Robin condition at $u = 1$ (4.96c). This minimum is achieved by the eigenfunction U_m corresponding to the smallest eigenvalue λ_m. The instability of the Burylov solution against azimuthal perturbations occurs whenever (4.93) is negative for some functions in the class $\mathcal{A}_{\theta z}^U$, and thus, within the Sturm-Liouville theory, whenever the sign of λ_m is negative. To determine the smallest eigenvalue λ_m of (4.96), we study a Sturm-Liouville Problem with a finite spectrum. We regard the possible eigenfunction $U = U(u)$ corresponding to λ_m as the sum of n odd Legendre harmonics $P_{2i-1}(u)$ for $i = 1..n$,

$$U(u) = \sum_{i=0}^{n} c_{2i-1}P_{2i-1}(u), \tag{4.98}$$

in order to satisfy the requirements posited on U, i.e. (4.95), (4.96b) and (4.96c) above. This argument is justified within the Sturm-Liouville theory, since Theorem 1 concerns the lower bound on the sequence of eigenvalues at least when $A \geq 1/\sqrt{2}$ and ensures the regularity of the eigenfunctions of (4.96) (c.f. properties (ii) and (iii)). Each of the $P_{2i-1}(u)$ vanishes at $u = 0$ to make sure that $U(u) = 0$ and is taken to be subject to the isoperimetric constraint (4.95); thus it can be expressed as

$$P_{2i-1} = P_{2i-1}(u) := \frac{\sqrt{4i-1}}{2^{2i-1}(2i-1)!}\frac{\mathrm{d}^{2i-1}}{\mathrm{d}u^{2i-1}}\left[(u^2-1)^{2i-1}\right]. \tag{4.99}$$

To satisfy the Robin condition at $u = 1$ (4.96c) a linear constraint on the constants c_{2i-1} for $i = 1..n$ arises

$$\sum_{i=0}^{n} c_{2i-1}\sqrt{4i-1}\, i(2i-1) = \frac{1-2A^2}{1-A^2}\sum_{i=0}^{n} c_{2i-1}\sqrt{4i-1} \tag{4.100}$$

where use has been made of the expression for $p = p(k_3, A, u)$ and $q_0 = q_0(k_3, A)$ given by (4.94b) and (4.71c).

By (4.99), the constraint on the L^2-norm of $U = U(u)$ (4.95) results in a non-linear condition on the c_{2i-1}

$$\sum_{i=0}^{n} (c_{2i-1})^2 = 1. \tag{4.101}$$

Equilibrium is attained whenever the functional $\delta^2 \mathcal{F}_{\theta z}(\boldsymbol{n}_{\mathrm{B}})(\boldsymbol{v}_{\theta z})$ in (4.93) subject the constraints on the length of $U = U(u)$ (4.95) and on its boundary condition at $u = 1$ (4.96c) is minimized. To this end, let $\delta^2 \mathcal{F}_{\theta z}^*(\boldsymbol{n}_{\mathrm{B}})(\boldsymbol{v}_{\theta z})$ be the functional defined by

$$\delta^2 \mathcal{F}_{\theta z}^*(\boldsymbol{n}_{\mathrm{B}})(\boldsymbol{v}_{\theta z}) = \delta^2 \mathcal{F}_{\theta z}(\boldsymbol{n}_{\mathrm{B}})(\boldsymbol{v}_{\theta z}) - \lambda \left[\int_0^1 U(u)^2 \, \mathrm{d}u - 1 \right] - \mu \left[p(1)U'(1) + q_0 U(1) \right] \tag{4.102}$$

where λ and μ are the Lagrange multipliers associated with the two constraints, respectively. Since, as obtained in Section 4.3, the second variation is a quadratic functional in the perturbation $\boldsymbol{v}$ of $\boldsymbol{n}$, substituting for $U = U(u)$ the function given by (4.98) in (4.102) leads us to a quadratic form of the constants c_{2i-1} for $i = 1 \ldots n$, whose differentiation with respect to them gets $n + 1$ linear equations in the c_{2i-1}. Hence, we consider the extended linear homogeneous system constituted by those $n - 1$ equations and by the Robin condition (4.100) in the $n + 1$ unknowns c_{2i-1} for $i = 1 \ldots n$ and μ. Considering λ as a parameter of the system, the finite number of eigenvalues of the Sturm-Liouville problem posed above is found through the request that the system is underdetermined to enable non trivial solutions in addiction to the trivial one where all the unknown c_{2i-1} for $i = 1 \ldots n$ and μ are zero. Thus, the eigenvalues are the roots of the polynomial in λ defined by the determinant of the augmented matrix which represents the system. The smallest root λ_m corresponds to the minimum eigenvalue of $\delta^2 \mathcal{F}_{\theta z}(\boldsymbol{n}_{\mathrm{B}})(\boldsymbol{v}_{\theta z})$ in (4.93) and we study its sign by varying $(k_3, A) \in \mathsf{S}_0 := \{(k_3, A) : 0 < k_3 \leq 1, 0 < A < 1\}$. Figure 4.5 represents the trend of the minimum eigenvalue computed numerically for $n = 6$ for which Legendre armonics up the the degree 11 are considered. When $A = 0$, i.e. $k_{24} = 1$, the ET solutions (1.42) and (1.43) correspond to the uniform solution and we expect that the minimum eigenvalue is 0.
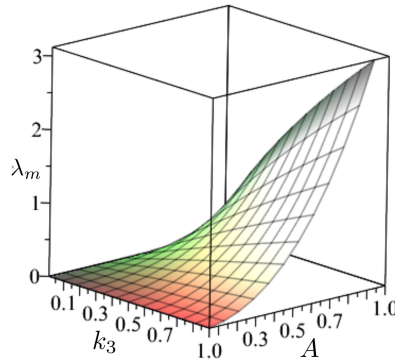

Figure 4.5: $n = 6$: graph of the smallest eigenvalue against S_0, obtained by seeking the smallest root of the polynomial in λ defined by the determinant of the augmented matrix which represents the linear system considered in the main text and here composed by 7 equations in the in the 7 unknowns c_{2i-1} for $i = 1 \ldots 6$ and μ.

We intend to give a qualitative picture of the features of λ_m for small values of the parameter A for which the outcome of the numerical exploration are uncertain. Thus, we carry out an

asymptotic analysis to arrive to an explicit formula of the smallest eigenvalue at least when $n = 3$.

For $A = \varepsilon \ll 1$, we write the functional (4.93) as a formal series in ε truncated at the second order

$$\delta^2 \mathcal{F}_{\theta z}(\boldsymbol{n}_{\mathrm{B}})(\boldsymbol{v}_{\theta z}) \approx \delta^2 \mathcal{F}^\varepsilon_{\theta z}(\boldsymbol{n}_{\mathrm{B}})[\boldsymbol{v}_{\theta z}] := \int_0^1 \left[\frac{U(u)^2}{u} + u U'(u)^2 \right] du - U(1)^2$$

$$+ \varepsilon^2 \left\{ \int_0^1 \frac{u}{2} \left[u^2 (k_3 - 2) U'(u)^2 + (11 k_3 - 14) U(u)^2 \right] du - \frac{k_3 - 4}{2} U(1)^2 \right\}. \quad (4.103)$$

When $n = 2$ in (4.98), (4.99) and in (4.100), the eigenfunction $U = U(u)$ for (4.103) can be approximated by

$$U(u) = c_1 \sqrt{3} u + c_3 \frac{\sqrt{7}}{2} u \left(5u^2 - 3 \right) + c_5 \frac{\sqrt{11}}{8} u \left(63 u^4 - 70 u^2 + 15 \right) \quad (4.104)$$

and obey the Robin condition at $u = 1$ only if

$$5 c_3 \sqrt{7} + 14 c_5 \sqrt{11} + \varepsilon^2 \left(c_1 \sqrt{3} + c_3 \sqrt{7} + c_5 \sqrt{11} \right) = 0. \quad (4.105)$$

Substituting (4.104) for $U = U(u)$ in (4.103) and making use of (4.105) and (4.95) lead us to express the formal series of (4.102) in ε in the form

$$\delta^2 \mathcal{F}^*_{\theta z}(\boldsymbol{n}_{\mathrm{B}})(\boldsymbol{v}_{\theta z}) \approx \frac{175}{6} c_3^2 + \frac{32879}{240} c_5^2 + \frac{245 \sqrt{7} \sqrt{11}}{24} c_3 c_5 - \lambda \left(c_1^2 + c_3^2 + c_5^2 \right) - \mu \left(5 c_3 \sqrt{7} + 14 c_5 \sqrt{11} \right)$$

$$+ \varepsilon^2 \left\{ 3 k_3 c_1^2 + \frac{7}{16} (31 k_3 - 40) c_3^2 + \frac{11}{64} (358 k_3 - 637) c_5^2 + \frac{\sqrt{7}}{\sqrt{3}} (k_3 + 5) c_1 c_3 \right.$$

$$\left. - \frac{\sqrt{11}}{24} c_5 \left[-\frac{15 \sqrt{7}}{2} (16 k_3 - 25) c_3 + c_1 (k_3 - 49) \sqrt{3} \right] - \mu \left(c_1 \sqrt{3} + c_3 \sqrt{7} + c_5 \sqrt{11} \right) \right\}. \quad (4.106)$$

Thus, the extended linear homogeneous system in the unknowns c_1, c_3, c_5 and μ is constituted by the three equations obtained through the partial derivatives of (4.106) with respect to c_1, c_3 and c_5, respectively, and by the Robin condition (4.105):

$$\begin{cases} (-2\lambda + 6\varepsilon^2 k_3) c_1 + \sqrt{\frac{7}{3}} (k_3 + 5) \varepsilon^2 c_3 - \frac{\sqrt{3}\sqrt{11}}{24} (k_3 - 49) \varepsilon^2 c_5 - \sqrt{3} \varepsilon^2 \mu = 0, \\ \frac{\sqrt{7}}{\sqrt{3}} (k_3 + 5) \varepsilon^2 c_1 + \left\{ \frac{175}{3} - 2\lambda + \varepsilon^2 \left[\frac{7}{8} (31 k_3 - 40) \right] \right\} c_3 + \frac{5\sqrt{7}\sqrt{11}}{24} \left[49 + \frac{3}{2} (16 k_3 - 25) \varepsilon^2 \right] c_5 + \\ \qquad - \sqrt{7} (5 + \varepsilon^2) \mu = 0, \\ -\frac{\sqrt{3}\sqrt{11}}{24} (k_3 - 49) \varepsilon^2 c_1 + \frac{5\sqrt{7}\sqrt{11}}{24} \left[49 + \frac{3}{2} (16 k_3 - 25) \varepsilon^2 \right] c_3 + \left[\frac{32879}{120} - 2\lambda + \frac{11}{32} (358 k_3 - 637) \varepsilon^2 \right] c_5 + \\ \qquad - \sqrt{11} \left(14 + \varepsilon^2 \right) \mu = 0, \\ 5 c_3 \sqrt{7} + 14 c_5 \sqrt{11} + \varepsilon^2 \left(c_1 \sqrt{3} + c_3 \sqrt{7} + c_5 \sqrt{11} \right) = 0. \end{cases}$$

$$(4.107)$$

Here, the determinant of the augmented matrix which represents (4.107) results to be a polynomial in λ whose expansion in ε truncated at the second order is

$$\det := 9324 \lambda^2 - \frac{509355}{4} \lambda + \varepsilon^2 \left[1512 \lambda^2 + \left(-\frac{641655}{8} k_3 + \frac{713097}{16} \right) \lambda + \frac{1528065 k_3}{4} \right]. \quad (4.108)$$

The series expansion about $\varepsilon = 0$ of the smallest root for (4.108) exhibits the following asymptotic behaviour near 0:

$$\lambda_m^{n=3} \approx 3k_3\varepsilon^2. \tag{4.109}$$

This means that the smallest eigenvalue of $\delta^2\mathcal{F}_{\theta z}(\boldsymbol{n}_{\mathrm{B}})[\boldsymbol{v}_{\theta z}]$ is always positive for small values of A and decreases to 0 as A approaches 0. Numerical explorations show that also for higher order or n, in the limit as $A = \varepsilon > 0$ tends to 0, the smallest eigenvalue is asymptotically equivalent to (4.109).

4.C.1   Radial Perturbations

The same conclusions based on the Sturm-Liouville analysis carried out in Section 4.C are reached for the dimensionless form of the second variation at $\boldsymbol{n}_{\mathrm{B}}$ for radial perturbations $\boldsymbol{v}_r$, (4.84) in Section 4.4.2, since it is a simplified form of (4.70), since, here, $U \in \mathcal{A}_r^U$ is subject to strong anchoring conditions on the end-points of the interval $[0, 1]$, at which it vanishes.

The trend of smallest eigenvalue λ_m of $\delta^2\mathcal{F}_{\theta z}(\boldsymbol{n}_{\mathrm{B}})(\boldsymbol{v}_r)$ computed numerically for $n = 6$ is illustrated in Figure 4.6. Here, when $A = 0$, i.e. $k_{24} = 1$, the minimum eigenvalue λ_m is not 0 as in 4.C, since U is constrained at $u = 1$, but it exhibits the following asymptotic behaviour as A tends to 0:

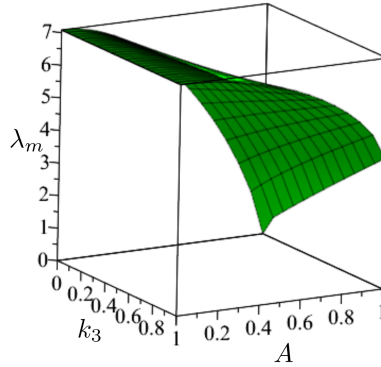$$\lambda_m \approx 7.08 + (3.82k_3 - 5.76)\,A^2. \tag{4.110}$$

Figure 4.6: $n = 6$: graph of the smallest eigenvalue of $\delta^2\mathcal{F}_{\theta z}(\boldsymbol{n}_{\mathrm{B}})(\boldsymbol{v}_r)$, i.e. the dimensionless form of the second variation at $\boldsymbol{n}_{\mathrm{B}}$ for radial perturbations $\boldsymbol{v}_r$, against S_0.

Chapter 5

Paradoxes for Chromonics

We learned in the preceding Chapter that Oseen-Frank's free-energy stored in a cylinder subject to planar degenerate anchoring attains its minimum at the ET configurations (1.42) and (1.43). This fact is a result of boundary conditions and confinement, which cannot accommodate a double-twist configuration. It is for free-boundary problems or when material surfaces inside the confinement lead to jump discontinuities of the nematic director that the frustration of the system could be relaxed (at least partially) and cause paradoxes within Oseen-Frank's theory.

5.1   Introduction

Despite the apparent justification of the applicability of Oseen-Frank's theory to CLCs provided by the local stability of escaped twist solutions (1.42) and (1.43) explored in Chapter 4, a number of mathematical issues tackled in this Chapter show that Oseen-Frank's free-energy is not suitable to describe the elasticity of CLCs. Indeed, two paradoxes arise in cylindrical symmetry if the relevant Ericksen's inequality $K_{22} > K_{24}$ is violated.

   To highlight the deficiencies of Oseen-Frank's theory when it is used to rationalize the experimental results of confined CLCs, Section 5.2 concerns a free boundary problem, where a given quantity of CLC occupying the volume V_0 (liquid crystals are to be regarded as incompressible fluids), can take any desired shape, while the director field within it is free to vary in a class of cylindrically symmetric orientations which satisfy planar degenerate boundary conditions (1.6), as when the confinement was a cylinder. We construct a sequence of configurations $(\mathscr{B}_k, \boldsymbol{n}_k)$ along which the limiting value of Oseen-Frank's free-energy functional diverges to $-\infty$ as soon as the ratio between K_{24} and K_{22} exceeds a value greater than 1, but which is still lower than that observed experimentally [32]. Especially, $\mathscr{B}$ belongs to a family of tactoidal droplets subject to the isoperimetric constraint (1.19) and parametrized in μ given by (3.8), that is, the ratio between the length of the semi-axis and the linear dimension of the droplet. According to the value of this parameter, prolate from oblate shapes are distinguished. The director field inside the droplet, which also depends on the value of μ (when μ diverges to ∞ the corresponding configuration is (1.42) or (1.43) adjusted to accomplish the strong boundary conditions), solve the equilibrium equation for Oseen-Frank's free-energy associated with these tactoidal shapes within a special class of cylindrically symmetric orientation satisfying strong anchoring conditions. It possesses two point defects at poles (boojums with equal topological charge $m = \pm 1$). When K_{24}/K_{22} is lower than this critical value, but still greater than 1, a regime of shape bistability is predicted; prolate and oblate shape coexist in equilibrium. We find that in the limit as μ tends to ∞, the free-energy evaluated on the given configuration of the sequence diverges to $-\infty$. This means that in the indefinite space, when the droplet is free to adjust its shape to the surrounding environment, it would stabilize as a spindle-shape droplet with an infinite height related to the

linear dimension of the droplet without changing its volume and with a double-twist arrange-ment inside which prevents the elastic frustration of the system. The paradox arises thanks to the unboundedness of the domain. Confining the droplet between two plates may turn the ill posed problem into a problem which admits an energy minimizer. Section 5.2.2 is devoted to this issue; since the double twisted configuration can be constructed only locally around the axis of the drop, the director will be geometrically frustrated away from the axis. The energy cost associated with the distortion of the director from the ground state can be always reduced by disassembling the drop into an appropriate multitude of subdroplets whose overall volume is V_0. In this resulting situation, despite the admissible region is confined between two plates, every droplet consists, in the limit, in its axis inside which the director field degenerates in the ground state; the energy of the resulting system diverges to $-\infty$.

In Section 5.3 we relax the assumption of strong anchoring conditions to let the director field be tangent to the boundary and oriented in any direction. By considering the droplet's profile described by the optimal function of the problem in the preceding section, the failure of Oseen-Frank's free-energy in describing the elasticity of CLCs is proved whenever Ericksen's inequality $K_{22} \geq K_{24}$ is violated.

A second paradox arises by inserting inside the starting cylinder a new hollow cylinder of smaller radius. The new configuration into which the nematic director relaxes has a discontinu-ity on the material surface which separates the two regions into which the starting cylinder is divided and the resulting system has less energy than the original one.

5.2   Free-boundary Problems: Strong Anchoring Conditions

In this section we construct a family of droplets and associated director fields where the free-energy does not attain a minimum for sufficiently high value of k_{24} in (1.30). We assume that the boundary $\partial \mathscr{B}$ is obtained by rotating the graph of a function of class $\mathcal{C}^1$, $R = R(z)$, which describes the radius of the drop's cross section at height $z \in [-R_0, R_0]$. R is taken to be an even function and to vanish on the z axis at the points $z = \pm R_0$ (the poles of the drop).

In analogy with Burylov case in Section 1.2 when the droplet is confined in a cylinder, we seek the minimizers of the bulk free-energy functional within the class of orientation fields $\boldsymbol{n}$ of the form (1.25), where β is assumed here to depend on the dimensionless coordinate[1](it does not vary along the meridian of the droplet):

$$\rho = \frac{r}{R(z)}. \tag{5.1}$$

Here, unlike the case of the cylinder, $\boldsymbol{e}_r$ and the unit normal $\boldsymbol{\nu}$ to the boundary do not coincide on the whole of $\partial \mathscr{B}$; to accomplish the anchoring conditions and to prevent the director from having a component along $\boldsymbol{e}_r$ inside the drop, we require that $\boldsymbol{n}$ and $\boldsymbol{e}_\theta$ coincide on the boundary through

$$\beta(1) = \frac{\pi}{2}, \tag{5.2}$$

which causes the director field to possess two point defects at the poles. The cylindrical symmetry sets

$$\beta(0) = 0, \quad \beta(1) = \frac{\pi}{2}, \tag{5.3}$$

and the director field produced with such a geometric construction possesses two point defects at the poles; they are two boojums with equal topological charge $m = \pm 1$.

---

[1]With an abuse of language we keep the name unaltered when R does not depend on z, as in the cylindrical confinement previously considered.

The case where $\boldsymbol{n}$ has a component along $\boldsymbol{e}_r$ in order to be tangent to the boundary but free to orient in any direction orthogonal to $\boldsymbol{\nu}$ will be considered in Sec. 5.3.

We call R_e the radius of the equivalent sphere, which has volume V_0, and we rescale to this length r, z and $R(z)$, keeping their names unaltered. Letting as in Chapters 2 and 3 the dimensionless length of the semi-axis of the drop

$$\mu := \frac{R_0}{R_e} > 0, \tag{5.4}$$

it is shown in Appendix 5.A that for any given function $\beta = \beta(\rho)$ satisfying (5.3) and (5.2), the optimal dimensionless shape of the drop subject to the isoperimetric constraint in scaled variables,

$$\int_{-\mu}^{\mu} R^2(z)\,\mathrm{d}z = \frac{4}{3}, \tag{5.5}$$

belongs to the family of *tactoids*, or spindle-shaped droplets, parametrized in μ:

$$R_{\mathrm{m}}(z) = \frac{2}{\sqrt{3}\mu} \cos\left(\frac{\pi z}{2\mu}\right). \tag{5.6}$$

As also illustrated in Appendix 5.A, the variational problem we thus face can be phrased as follows: find a positive $\mu > 0$ and a function $\beta = \beta(\rho)$ which obeys (5.3) and (5.2) so as to minimize the following reduced functional which is an appropriate dimensionless form of Oseen-Frank's functional $\mathscr{F}_b$ associated with the equilibrium shapes (5.6):

$$\mathcal{F}^\mu[\beta](k_{24}) = \frac{\mathscr{F}_B}{2\pi K_{22} R_e} = \frac{1}{\mu^2} \int_0^1 \frac{\pi^2}{6} \rho^3 \beta'^2 \left(k_1 \sin^2\beta + k_3 \cos^2\beta\right)\,d\rho$$
$$\mu\left[\int_0^1 \left(\rho\beta'^2 + \frac{1}{\rho}\cos^2\beta\sin^2\beta + \frac{k_3}{\rho}\sin^4\beta\right)\,d\rho + (1 - 2k_{24})\right]. \tag{5.7}$$

The following scaled elastic constant have been introduced in (5.7),

$$k_1 := \frac{K_{11}}{K_{22}}, \tag{5.8}$$

while k_3 and k_4 are given in (1.30). Oseen-Frank's theory applied to chromonics requires $k_{24} > 1$ (which violates Ericksen's inequalities (1.8)), while k_1 and k_3 are non negative. In [32] it has been considered a cylindrical cavity with degenerate planar anchoring filled with 14.0% (wt/wt) nematic disodium cromoglycate (DSCG) at 21.5°C, and the estimation of the twist angle at the capillary wall $\beta(1)$ allows, through (1.42) or (1.43) for $\rho = 1$, the measurement of k_{24}. In particular, assuming $k_3 = 30$ [142], they found $k_{24} = 7.5$. Hereafter we also take $k_1 = k_3$, conforming the measurements of the elastic constants in lyotropic chromonic liquid crystals [142, 26] which provide K_{11} and K_{33} of the same order. Qualitatively, this scenario remains the same for different values of k_1 and k_3.

The limiting vatiational problems when $\mu = \infty$ and $\mu = 0$ consist in the minimization of the terms of (5.7) multiplied by μ and $1/\mu^2$, respectively, among the functions $\beta = \beta(\rho)$ satisfying the strong anchoring conditions (5.3) and (5.2). When $\mu = +\infty$ the functional to be minimized corresponds to the dimensionless form of the bulk free-energy (1.29) found when the confinement was a cylinder but scaled to R_e instead of L. Its equilibrium configuration which obeys (5.3) and (5.2) is the ET configuration (1.42) adjusted to accomplish the strong boundary conditions (5.3) (By taking $\beta(1) = -\pi/2$, the equilibrium configuration which obeys (5.3) when $\mu = +\infty$ is

the mirror image of (5.9)). The case for $\mu = 0$ is treated Appendix 5.A. Here we recall that the equilibrium configurations subject to (5.3) for the cases $mu = \infty$ and $\mu = 0$ are, respectively,

$$\beta_{\mathrm{m}}^{\infty} = \beta_m^{\infty}(\rho) := \arctan\left(\frac{1}{\sqrt{k_3}}\frac{2\rho}{1-\rho^2}\right), \tag{5.9}$$

and when $k_1 = k_3$

$$\beta_{\mathrm{m}}^0(\rho) = \begin{cases} 0 & \rho = 0 \\ \dfrac{\pi}{2} & \rho \in (0, 1] \end{cases}. \tag{5.10}$$

The director field $\boldsymbol{n}$ in (1.25) which corresponds to is oriented in the same direction of $\boldsymbol{e}_\theta$ and has a disclination line along the axis of the droplet.

For any given value of $\mu \in (0, +\infty)$ we numerically find the solution $\beta_{\mathrm{m}}^{\mu} = \beta_{\mathrm{m}}^{\mu}(\rho)$ of the Euler Lagrange equation for the functional $\mathcal{F}^{\mu}[\beta](k_{24})$ (see (5.50) in Appendix 5.A) which satisfies the prescribed boundary conditions (5.3) (see Figure 5.1). For the limiting cases $\mu = +\infty$ and $\mu = 0$ the solution coincides with $\beta_{\mathrm{m}}^{\infty}$ (5.9) and β_{m}^0 (5.2), respectively, and we expect that when μ is close to 0, β_{m}^{μ} closely resembles a smooth approximation of β_{m}^0, whereas the more μ exceeds 0, the more β_{m}^{μ} appreciably deviates from β_{m}^0 and tends to $\beta_{\mathrm{m}}^{\infty}$. This argument is supported by the graphs of β_{m}^{μ} shown in Fig. 5.1 for a sequence of values of μ^2.
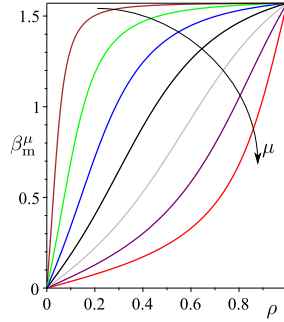

Figure 5.1: Equilibrium solutions $\beta_{\mathrm{m}}^{\mu}(\rho)$ for $k_3 = k_1 = 30$ for different values of μ, namely $\mu = 0.2, 0.4, 0.7, 1, 1.5, 2.5, +\infty$ (according to the arrow)

We evaluate numerically the functional (5.7) on the above configurations $\beta_{\mathrm{m}}^{\mu}(\rho)$ as a reduced function:

$$\mathcal{F}(\mu, k_{24}) := \mathcal{F}^{\mu}[\beta_{\mathrm{m}}^{\mu}](k_{24}) \tag{5.11}$$

on $\mathsf{T} := \{(\mu, k_{24}) : 0 < \mu < \infty, k_{24} > 1\}$. Fig. 5.2 illustrates the graph of (6.38) for $k_1 = k_3 = 30$ and different fixed values of $k_{24} > 1$, where we express the dimensionless functional as a function of $\xi := 1/\mu \in (0, +\infty)$:

$$\hat{\mathcal{F}}(\xi, k_{24}) := \mathcal{F}(1/\xi, k_{24}). \tag{5.12}$$

There exists a value of $k_{24} > 1$, i.e. k_{24}^{∞} (e.g. for $k_1 = k_3 = 30$, $k_{24}^{\infty} = 4.86$), that could be interpreted to mark the value of k_{24} above which the energy becomes negative. This critical value of k_{24} distinguishes two situations qualitatively different from one another. For every $k_{24} < k_{24}^{\infty}$, the reduced functional $\mathcal{F}(\mu, k_{24})$, (6.38), diverges to $+\infty$ as μ approaches both 0 and ∞ (as ξ goes to ∞ and 0) and it possesses two minima, one for $\mu > 1.1$ ($\xi < 0.9$) and the other for $\mu < 1.1$ ($\xi > 0.9$), whose corresponding equilibrium shapes are prolate and oblate, respectively[3].

---

[2]The same argument holds for the mirror images of β_{m}^{μ}, β_{m}^0 and $\beta_{\mathrm{m}}^{\infty}$ when $\beta(1)$ is assumed to be equal to $-\pi/2$.

[3]The prolate shapes are characterized by having height larger than width. i.e. by $\mu \geq R(0)$. By (5.6) this inequality becomes $\mu \geq 1.1$, i.e. $\xi \leq 0.9$.
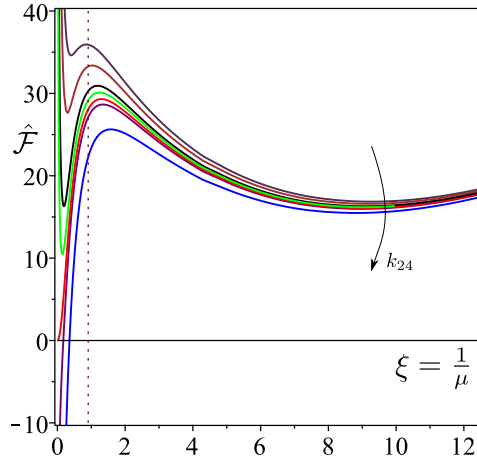
Figure 5.2: Graph of $\hat{\mathcal{F}}(\xi,_{24})$ in (6.39), corresponding to the dimensionless functional (5.7) evaluated numerically on the equilibrium configurations $\beta_m^\mu(\rho)$ and expressed as a function of $\xi = 1/\mu \in (0, \infty)$ for $k_1 = k_3 = 30$ and a sequence of values of $k_{24} > 1$, namely $k_{24} = 1.3, 2.5, k_{24}^{\mathrm{b}} = 3.86, 4.36, k_{24}^\infty = 4.86, 5.3, 7.5$ (according to the arrow). The graphs do not overlap and approach the midway graph for $k_{24} = k_{24}^\infty$ as ξ tends to ∞, i.e. as μ approaches 0. Whenever $k_{24} > k_{24}^\infty$, $\hat{\mathcal{F}}$ is not bounded from below and diverges to $-\infty$ as ξ tends to 0 while for $1 < k_{24} < k_{24}^\infty$ it has an opposite tendency in 0 and goes to $+\infty$. The barrier marking transitions from prolate to oblate shapes is represented by a vertical dashed line.

Upon decreasing values of $k_{24} < k_{24}^\infty$ the minimum for $\mu > 1.1$ ($\xi < 0.9$) corresponds to the minimum value of $\mathcal{F}(\mu, k_{24})$ and so remains stable until decreasing k_{24} crosses k_{24}^{b}, for which a *bistability phenomenon* occurs and the two minima have the same value of the energy. The critical value k_{24}^{b} marks a first-order transition of the absolute minimum of $\mathcal{F}$, which jumps from a value of $\mu > 1.1$ ($\xi < 0.9$) to a value of $\mu < 1.1$ ($\xi > 0.9$). The corresponding optimal shapes are illustrated in Fig. 5.3.

In the limiting case for $k_{24} = k_{24}^\infty$, $\mathcal{F}$ attains its absolute minimum at $\mu = \infty$ ($\xi = 0$) where it vanishes, and so the optimal drop is a filament of infinite length and volume V_0 inside which the orientation of the director (1.25) is given in terms of the angle β as in (5.9).

For every $k_{24} > k_{24}^\infty$ in the limit as μ tends to ∞ (ξ tends to 0), the free-energy evaluated on the equilibrium solutions β_{m}^μ does not attain its minimum for $\mu > 1$ ($\xi < 1$), but diverges to $-\infty$. The metastable minumum for $\xi > 1$ is still attained.

This means that for every $k_{24} \geq k_{24}^\infty$ the problem is ill-posed and shows the deficiencies of Oseen-Frank's theory in studying CLCs. The local stability of escaped twist solutions (1.42) and (1.43) explored in Chapter 4 confirms that these solutions rationalize the configurations of the confinement-induced ground state of CLCs and so they manifest the elastic frustration of the ideal double twisted configuration when requested to occupy the cylinder and to obey degenerate boundary conditions. The paradox hidden in the theory arises when the droplet of CLC is free to adjust its shape to the surrounding environment. In this case, we proved that Oseen-Frank's free-energy does not attain a minimum on the class of selected configurations (R, β) taken at the beginning of the Section, where R describes the profile of the droplet and β is the angle between $\boldsymbol{n}$ and its axis. Indeed, we find the family of configurations $(R_{\mathrm{m}}, \beta_{\mathrm{m}}^\mu)$ generated by letting μ vary in $(0, +\infty)$; the functional $\mathcal{F}(\mu, k_{24})$ evaluated on this family (5.7) is not bounded from below in the limit as μ tends to infinity. Hence, we have constructed a sequence of configurations along which the limiting value of Oseen-Frank's free-energy diverges to $-\infty$.
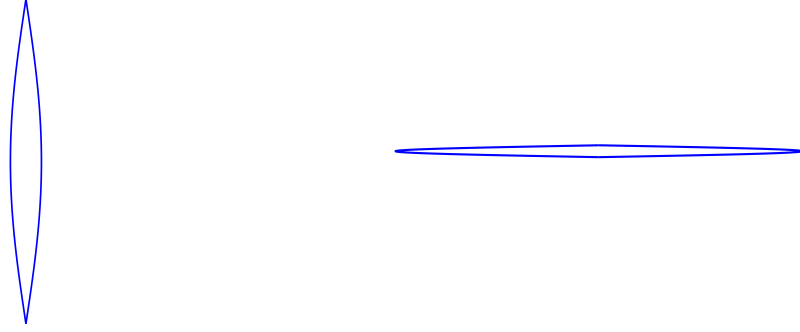
(a) Cross-section of the prolate equilibrium shape corresponding through (5.6) to the minimizer of $\hat{\mathcal{F}}$ for $\xi < 0.9$, i.e. $\mu > 1.1$. In particular $\xi = 0.19$, for $k_3 = k_1 = 30$ and $k_{24} = k_{24}^{\mathrm{b}} = 3.86$

(b) Cross-section of the oblate equilibrium shape corresponding through (5.6) to the minimizer of $\hat{\mathcal{F}}$ for $\xi < 0.9$, i.e. $\mu > 1.1$. In particular $\xi = 9.1$, for $k_3 = k_1 = 30$ ans $k_{24} = k_{24}^{\mathrm{b}} = 3.86$

Figure 5.3: Bistability phenomenon: the two minima, the former for $\xi < 0.9$ and the latter for $\xi > 0.9$ minimize $\hat{\mathcal{F}}$. For $k_1 = k_3 = 30$, it occurs at $k_{24} = k_{24}^{\mathrm{b}} = 3.86$.

5.2.1 Surface Contribution to the Free-Energy

Actually, the drop comes in contact with the isotropic environment that surrounds it and the bulk free-energy must be supplemented by a *Rapini Papoular*-type interfacial energy concentrated on the boundary $\partial \mathscr{B}$ due to the $I - N$ interface (1.16).

The normalized surface free-energy associated with the family of equilibrium shapes (5.6) reads as

$$\mathcal{F}_s^\alpha[\mu] := \frac{\mathscr{F}_s}{2\pi K_{22} R_\mathrm{e}} = \alpha \left[\frac{2\mu^2}{\pi^2} \ln \left(\frac{\pi + \sqrt{3\mu^3 + \pi^2}}{-\pi + \sqrt{3\mu^3 + \pi^2}} \right) + \frac{4}{3\pi\mu} \sqrt{3\mu^3 + \pi^2} \right], \tag{5.13}$$

where

$$\alpha := \frac{\gamma R_\mathrm{e}}{K_{22}} \tag{5.14}$$

is the reduced (dimensionless)[4] volume and $\gamma > 0$ is the isotropic surface tension. For any given value of R_e, which corresponds to a fixed volume, $\mathcal{F}_s^\alpha$ in (5.13) diverges to $+\infty$ like $\sqrt{\mu}$ as $\mu \to +\infty$, which means that the surface contribution coud be responsible for the shape of the drop, but only moves the pathology to larger values of μ. Indeed, the energy functional remains unbounded from below whenever $k_{24} > k_{24}^\infty$, since for these values of k_{24} $\mathcal{F}(\mu, k_{24})$ diverges to $-\infty$ as $\mu \to +\infty$.

5.2.2 Crumbling Paradox

We confine attention to the values of $k_{24} > k_{24}^\infty$ for which the paradox in the preceding section occurs.

When the drop is confined between two plates, $2\bar{R}_0$ apart, a new constraint on the semi-axis of the drop arises because it could not be longer than $\bar{R}_0$, and so it never reaches an infinite

---

[4]Here the normalization elastic constant is K_{22} instead of K_{11} as in Chapters 2 and 3.

length as would be preferred whenever $k_{24} > k_{24}^\infty$. This results in a barrier in μ, (5.4), which can not be overcome:

$$\bar{\mu} = \frac{\bar{R}_0}{R_e}. \tag{5.15}$$

Although this avoids the degeneration of the drop into a filament of infinite height, we now show that the problem is nevertheless ill-posed and that the director field will tend to fill the available region with an infinity of pure double twisted configurations whose associated energy is unbounded below.

As previously found in Sec. 5.2, the drop of volume V_0 acquires at equilibrium a tactoidal shape (5.6) with a dimensionless height μ that here depends on the barrier $\bar{\mu}$ imposed by the constraint (5.15) as illustrated in in Figure 5.4 for $k_1 = k_3 = 30$ and $k_{24} = 7.5$([32]); the scaled functional $\mathcal{F}(\mu, k_{24})$ is unbounded below and we identify two characteristic values of μ: μ_{rel} corresponding to the metastable minimum of $\mathcal{F}(\mu, k_{24})$ for $\mu < 1.1$ and $\widetilde{\mu}$ at which the functional reaches again the same value of the energy attained at μ_{rel} upon further increasing values of μ. For every barrier $\bar{\mu} > 0$ the minimizer of $\mathcal{F}(\mu, k_{24})$ is to be found in the admissible range $(0, \bar{\mu})$; according to whether the barrier $\bar{\mu}$ ranges in $(0, \mu_{\text{rel}}]$, or $(\mu_{\text{rel}}, \widetilde{\mu})$ or $[\widetilde{\mu}, \infty)$, the minimizer is the barrier, i.e. the biggest value of μ available, or μ_{rel} or again the barrier (as suggested by the arrows in Figure 5.4).

Then, according to the minimizing value of μ the director field inside the droplet relaxes in the configuration corresponding to $\beta_{\text{m}}^\mu = \beta_{\text{m}}^\mu(\rho)$. When the given barrier $\bar{\mu}$ coincides with $\widetilde{\mu}$ there are two equilibrium configurations which could arise with the same probability, i.e. $\beta_{\text{m}}^{\mu_{\text{rel}}}$ and $\beta_{\text{m}}^{\widetilde{\mu}}$.
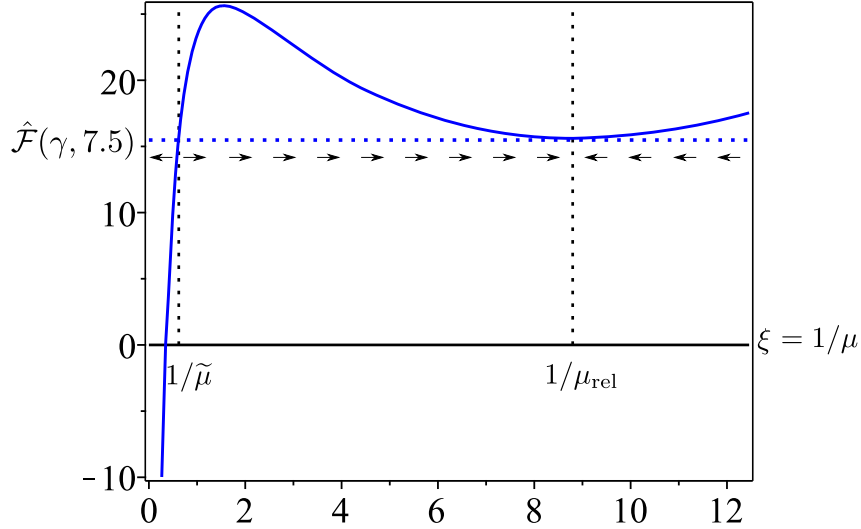

Figure 5.4: For $k_1 = k_3 = 30$ and for $k_{24} = 7.5$, according to the measurements in [32], the crumbling paradox occurs. Here the graph of $\hat{\mathcal{F}}$, (6.39), against ξ for $k_{24} = 7.5$ and $k_1 = k_3 = 30$. The arrows suggest where the functional attains its minimum according to if the barrier $\bar{\xi} = 1/\bar{\mu}$, for $\bar{\mu}$ as in (5.15), is placed after $1/\mu_{\text{rel}}(7.5)$, between $1/\widetilde{\mu}(7.5)$ and $1/\mu_{\text{rel}}$, or before $1/\widetilde{\mu}(7.5)$.

However, despite the shape and director configuration found minimize the functional $\mathcal{F}(\mu, k_{24})$ when the drop is subject to the constraint (5.15), there is always a strategy to split the initial drop into subdroplets whose overall volume is V_0 which lowers the energy of the starting system.

We start by splitting the initial drop into two sub droplets whose total volume is V_0, and so by changing the single domain's volume occupied by the CLC. The barriers (5.15) of the two

resulting drops shift towards larger values of μ, since their volumes, and so their equivalent radii, are reduced; for clarity, the starting drop is broken into two subdroplets of volume $V_1 = V_0/2$ and equivalent radii R_1 such that

$$R_1 = 2^{-1/3} R_{\mathrm{e}}. \tag{5.16}$$

Hence, making use of (5.16) in (5.15), the barriers of the two subdroplets result ats

$$\bar{\mu}_1 = \frac{\bar{\mathrm{R}}_0}{R_1} = 2^{1/3} \frac{\bar{\mathrm{R}}_0}{R_{\mathrm{e}}} = 2^{1/3} \bar{\mu}, \tag{5.17}$$

and so at a value greater than $\bar{\mu}$, the barrier of the starting droplet. Accordingly, the total free-energy of the new system is expressed as the sum of the free-energies associated with the two resulting sub-droplets whose equivalent radii and barriers in μ are given by (5.16) and (5.17):

$$\mathscr{F}^1 = 2\pi K_{22} \left[2R_1 \min_{\mu \in (0,\bar{\mu}_1]} \mathcal{F}(\mu, k_{24}) \right] = 2\pi K_{22} R_{\mathrm{e}} \left[2^{2/3} \min_{\mu \in (0,\bar{\mu}_1]} \mathcal{F}(\mu, k_{24}) \right] \tag{5.18}$$

where we recall that $\mathcal{F}(\mu, k_{24})$ in (6.38) corresponds to the functional (5.7) evaluated on the equilibrium configurations $\beta_{\mathrm{m}}^{\mu}(\rho)$ obtained for the given value of μ.

Equilibrium is attained whenever $\mathcal{F}(\mu, k_{24})$ is minimized among the value of $\mu < \bar{\mu}_1$ and since $\bar{\mu}_1 > \bar{\mu}$, the equilibrium value of $\mathcal{F}$ associated with the resulting drops is always lower than or equal to that of the starting droplet

$$\min_{\mu \in (0,\bar{\mu}_1]} \mathcal{F}(\mu, k_{24}) \leq \min_{\mu \in (0,\bar{\mu}]} \mathcal{F}(\mu, k_{24}). \tag{5.19}$$

According to the graph in Fig. 5.4, the equality holds only when the equilibrium of the starting and the resulting droplets is attained at $\mu = \mu_{\mathrm{rel}}$, and so only if $\bar{\mu}$ and $\bar{\mu}_1$ belong to the range $[\mu_{\mathrm{rel}}, \widetilde{\mu}]$. Making use of (5.19) in (5.18), we get

$$\mathscr{F}^1 \leq 2\pi K_{22} R_{\mathrm{e}} \left[2^{2/3} \min_{\mu \in (0,\bar{\mu}]} \mathcal{F}(\mu, k_{24}) \right]. \tag{5.20}$$

According to the graphs in Figure 5.2, for every given value of $k_{24} > k_{24}^{\infty}$, $\mathcal{F}(\mu, k_{24})$ is strictly decreasing in $(\widetilde{\mu}, +\infty)$, it reaches the μ−axis at $\mu = \mu_0 > \widetilde{\mu}$ and diverges to $-\infty$ as μ goes to $+\infty$. Thus, when the barrier $\bar{\mu}$ is placed at a greater value than μ_0, the inequality in (5.20) is strict, and the minimum value of $\mathcal{F}(\mu, k_{24})$ is negative. Thus

$$\mathscr{F}^1 < 2\pi K_{22} R_{\mathrm{e}} \left[\min_{\mu \in (0,\bar{\mu}]} \mathcal{F}(\mu, k_{24}) \right] = \mathscr{F}^0 \quad \bar{\mu} > \mu_0 \tag{5.21}$$

Then, whenever $\bar{\mu} > \mu_0$, the recursive application of the above procedure to every resulting droplet always leads to an energetic gain, which is preserved for all the subsequent divisions. Indeed, employing n times the split procedure described for the starting drop to every droplet in the configuration at each step, the starting drop results crumbled into 2^n tactoidal droplets of radius R_n and barrier $\bar{\mu}$ whose overall volume is V_0. We prove in Appendix 5.B that the total free-energy of this new system obey:

$$\mathscr{F}^n \leq 2\pi K_{22} 2^{2/3} \left[2^{n-1} R_{n-1} \min_{\mu \in (0,\bar{\mu}_{n-1}]} \mathcal{F}(\mu, k_{24}) \right]. \tag{5.22}$$

Provided that the barriers $\bar{\mu}_n$ shift towards larger values of μ than μ_{n-1} (see (5.60)) and that quilibrium value of $\mathcal{F}(\mu, k_{24})$ is always negative, the free-energy of the system is lowered at every step.

According to the graphs in Figure 5.2, for every given value of $k_{24} > k_{24}^{\infty}$, $\mathcal{F}(\mu, k_{24})$ is strictly decreasing in $(\widetilde{\mu}, +\infty)$, it reaches the μ−axis at $\mu = \mu_0 > \widetilde{\mu}$ and diverges to $-\infty$ as μ goes to

$+\infty$. When $\bar{\mu} < \mu_0$ the split of the initial drop could entail a waste of energy and the initial droplet may appear in apparent equilibrium. When $\bar{\mu} < \mu_0$, the crumbling paradox occurs at least when n is great enough, which means that we need to split the starting drop into a sufficient number of sub droplets, before they start to spontaneously crumble. This is shown in Appendix 5.B and the argument resides on the fact that the functional $\mathcal{F}(\mu, k_{24})$ evaluated on the family $(R_{\mathrm{m}}, \beta_{\mathrm{m}}^{\mu})$ generated by letting μ vary in $(0, +\infty)$ is not bounded from below in the limit as μ tends to infinity.

The droplet confined between two plates can not lead its dimensionless height to an infinite value without changing its volume. The double twist can be constructed only locally around the axis of the drop, and the director will be geometrically frustrated away from the axis; this causes an energy cost associated with this distortion from the ground state which can be reduced by disassembling the drop into a multitude of subdroplets whose equilibrium dimensionless height μ is ∞. Thus, despite the admissible region is confined between two plates, every droplet consists in an axis inside which the director field degenerates in its ground state.

5.3   Degenerate Planar Anchoring Conditions

When $\beta(1)$ is subject to the strong anchoring condition in (5.3), the crumbling paradox happens only for $k_{24} > k_{24}^{\infty}$. Actually, by letting $\beta(1)$ free to vary in order to ensure a planar degenerate anchoring at the boundary $\partial \mathcal{B}$, the unsuitableness of Oseen-Frank's energy in describing the elasticity of CLCs is proved whenever the Ericksen's inequality $K_{22} - K_{24} \geq 0$ is violated, i.e. whenever $k_{24} > 1$.

To this end, we consider here the class of orientation fields $\boldsymbol{n}$ that are represented, in term of $\beta = \beta(\rho)$ and the angle between the director projection on the plane $r\theta$ and $\boldsymbol{e}_r$ [5]$\alpha = \alpha(z)$, in the form

$$\boldsymbol{n} = \cos \alpha(z) \sin \beta(\rho) \boldsymbol{e}_r + \sin \alpha(\rho) \sin \beta(\rho) \boldsymbol{e}_\theta + \cos \beta(\rho) \boldsymbol{e}_z. \tag{5.23}$$

The only requirement for the optic axis $\boldsymbol{n}$ at the free surface of the drop is to fulfil

$$\boldsymbol{n} \cdot \boldsymbol{\nu}|_{\rho=1} = 0, \tag{5.24}$$

where $\boldsymbol{\nu}$ is the outer unit normal to $\partial \mathcal{B}$

$$\boldsymbol{\nu} = \frac{\boldsymbol{e}_r - R' \boldsymbol{e}_z}{\sqrt{1 + R'^2}}. \tag{5.25}$$

The boundary conditions (5.24), with the aid of (5.25), are satisfied by (5.23) only if

$$\alpha(z) = \arccos \left(\frac{R'}{\tan \beta(1)} \right) \tag{5.26}$$

and a new constraint on R' arises:

$$- \tan \beta(1) \leq R' \leq \tan \beta(1). \tag{5.27}$$

By the change of variables (1.26) and by rescaling to R_{e} both $R(z)$ and z, keeping their name unaltered, we get the dimensionless form of bulk free-energy is

---

[5]To guarantee that $\boldsymbol{n}$ could rotate freely on the local tangent plane at the drop's surface without flip out of it, we need to consider a component of $\boldsymbol{n}$ along $\boldsymbol{e}_r$ besides those along $\boldsymbol{e}_\theta$ and $\boldsymbol{e}_z$ in (1.25). Since the admissible droplet's profiles $R = R(z)$ are functions of the height $z \in [-R_0, R_0]$, the angle α in (1.25) must also depend on the coordinate z when the droplet taken into account is not a cylinder. For simplicity, however, α is assumed to not depend on ρ.

$$\mathcal{F}_{\mathrm{p}}^{\mu}[R,\beta](k_{24}) = \frac{\mathscr{F}}{2\pi K_{22}R_{\mathrm{e}}} = \int_{-\mu}^{\mu} R'^2 \, \mathrm{d}z \int_0^1 \left\{ \frac{1}{\tan^2 \beta(1)} \left[\frac{\beta'^2}{2} \left(k_1 \cos^2 \beta + k_3 \sin^2 \beta - 1 \right) \right. \right.$$

$$+ \frac{1}{2\rho^2} \left(k_1 \sin^2 \beta - \cos^2 \beta \sin^2 \beta + k_3 \sin^4 \beta \right) + \frac{\beta'}{\rho} \cos \beta \sin \beta (k_1 - 1) \right]$$

$$+ \frac{1}{\tan \beta(1)} \left[\rho \cos \beta \sin \beta \beta'^2 (k_1 - k_3) + \sin^2 \beta \beta'(k_1 - 1) + \frac{1}{\rho} \cos \beta \sin^3 \beta (k_3 - 1) \right]$$

$$+ \frac{\rho^2 \beta'^2}{2} \left(k_1 \sin^2 \beta + k_3 \cos^2 \beta \right) \bigg\} \rho \, \mathrm{d}\rho$$

$$+ \int_{-\mu}^{\mu} \frac{R''^2 R^2}{\tan^2 \beta(1) - R'^2} \, \mathrm{d}z \int_0^1 \frac{\sin^2 \beta}{2} \left(k_3 \sin^2 \beta + k_3 \cos^2 \beta \right) \rho \, \mathrm{d}\rho$$

$$+ 2\mu \left\{ \int_0^1 \left[\frac{\beta'^2}{2} + \frac{1}{2\rho^2} \cos^2 \beta \sin^2 \beta + \frac{k_3}{2\rho^2} \sin^4 \beta \right] \rho \, \mathrm{d}\rho + \frac{(1 - 2k_{24})}{2} \sin^2 \beta(1) \right\}. \quad (5.28)$$

We assume that the drop's profile is described by the optimal function $R_{\mathrm{m}} = R_{\mathrm{m}}(z)$ in (5.6) obtained when $\beta(1) = \pi/2^6$, and we consider the reduced functional (5.28) associated with this family of shapes:

$$\mathcal{F}_{\mathrm{p,m}}^{\mu}[\beta](k_{24}) = \mathcal{F}_{\mathrm{p}}^{\mu}[R_{\mathrm{m}}, \beta](k_{24}). \quad (5.29)$$

For every $k_3 > 0$, only the null solution satisfies the Euler-Lagrange equations for the functional (5.29) when the Ericksen's inequality $K_{22} - K_{24} > 0$, holds. As soon as K_{24} increases beyond K_{22}, i.e. $k_{24} > 1$, two equilibrium double-twisted configurations with their mirror images of opposite handedness arise at $\mu_0 = \mu_0(k_{24})$ and persist for all the subsequent values of μ. The two solutions with the same chirality coincide at $\mu_0 = \mu_0(k_{24})$ and upon further increasing values of μ they split into two branches whose value in $\rho = 1$ progressively decreases in modulus (red lines in Fig 5.5a) or increases in modulus (blue lines in Fig 5.5a), respectively, from that characterizing the case $\mu = \mu_0(k_{24})$. Especially, the more μ exceeds $\mu_0(k_{24})$, the more the two branches tend respectively to the uniform solution or to the escaped twist solution ((1.42) or (1.43) according to the chirality).

For $k_{24} < 1$ the trivial solution is the only equilibrium solution and it is necessarily stable. As soon as $k_{24} > 1$ an exchange of stability occurs at $\mu = \mu_0(k_{24})$ where the four twisted director field configurations share the same energy (5.29) which is negative. Whenever $\mu > \mu_0(k_{24})$ the equilibrium solutions which converge to the ET configurations with the corresponding handedness (1.42) (1.43) are always stable and the dimensionless functional $\mathcal{F}_{\mathrm{p,m}}^{\mu}$ (5.29) evaluated on them diverges to $-\infty$ as μ tends to $+\infty$, as is clear by the graph in Figure 5.5 (blue lines). The energy associated with the other double twisted configurations converging to the trivial solution is strictly decreasing and approaches zero as μ goes to $+\infty$.

---

[6]Finding the optimal function $R = R(z)$ for each feasible function $\beta = \beta(\rho)$ satisfying planar degenerate anchoring at the interface is not straightforward as in the preceding case where $\beta(1)$ was fixed equal to $\pi/2$. We are interested in highlighting the instability of the system whenever $k_{24} > 1$, and so in the large values of the dimensionless height μ for which we expect that functional (5.28) is minimum mainly if the term multiplied by μ is. This term appears also in (5.7) when the anchoring is strong, and its stable equilibrium configurations subject to (5.24) are the ET solutions (1.42) and (1.43), to which the optimal solutions of (5.28) closely resemble when μ is great enough. Therefore, for the values of μ we are interested in, the optimal values in $\rho = 1$ are close to $\pi/2$ as that of the ET solutions, and we assume that the drop's profile is described by the optimal function.
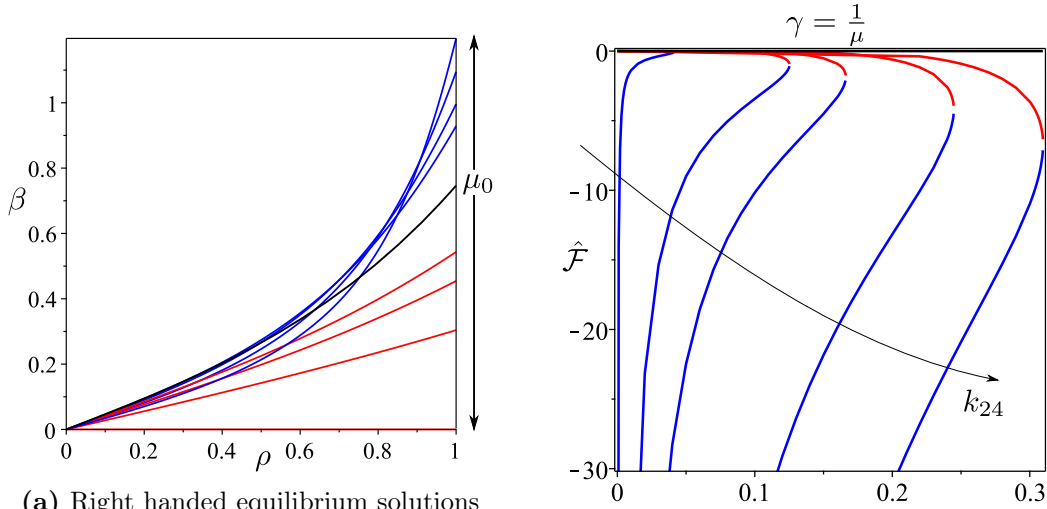
(a) Right handed equilibrium solutions for $k_{24} = 7.5$ and different values of $\mu \geq \mu_0(7.5) \approx 3$, i.e. $3, 3.5, 3.7, 4.5, \infty$. These solution coincide at $\mu > \mu_0$ and upon further increasing values of μ, one of them(blue lines) converges to the ET solution with the same chirality, according to the arrow pointing upwards, while the other (red lines) converges to the trivial solution according to arrow pointing downwards.

(b) Graphs of the dimensionless functional in (5.29) evaluated numerically on the equilibrium configurations as a function of $\xi = 1/\mu$, for $k_1 = k_3 = 30$ and a sequence of values of $k_{24} > 1$, namely $k_{24} = 1.3, 2.5, 3.3, 5.3, 7.5$ (according to the arrow). The energies of the four equilibrium double-twisted solutions are always negative and coincide when the solutions do at $\mu = \mu_0(k_{24})$. The energies of the two solutions which converge to the ET solutions (blue lines) are unbounded from below as μ goes to ∞.

Figure 5.5: Whenever $k_{24} > 1$ two equilibrium solutions for the functional (5.29) with their mirror images with opposite chirality arise at $\mu > \mu_0(k_{24})$, where they coincide, and persist for every $\mu > \mu_0(k_{24})$.

5.4   Coaxial Cylinders

We adopt a new model, where a hollow cylinder of radius R_0 is introduced inside the starting hollow cylinder with radius $R > R_0$ so that their axes, taken parallel to the $\boldsymbol{e}_z$-axis, coincide. The director field inside the two portions of $\mathscr{B}$ is free to vary in a class of cylindrical symmetric orientations which satisfy planar degenerate conditions at all the surfaces. The total free-energy is given by the sum of the elastic free energies distributed over the inner cylinder of radius R_0 and the outer cylinder with inner and outer radius R_0 and R.

   Whenever $k_{24} > 1$, the director field inside the inner cylinder relaxes in a ET configuration with right or left handed chirality, as this case can be regarded as that studied in [10] with $R = R_0$. Thus, the free-energy stored in the inner cylinder is exactly that given in (1.44), since it depends linearly on the length L and not on its radius.

   For the outer cylinder we extend the analysis in Chapter 4 slightly. The class of admissible mappings for $\mathscr{F}$ are described by (1.25), where here the dimensionless coordinate ρ corresponds to the radial coordinate r scaled to the major radius R and spans $[\eta, 1]$, where

$$\eta := \frac{R_0}{R}. \tag{5.30}$$

The degenerate anchoring conditions at the inner and outer surfaces of the outer cylinder allow $\beta(\eta)$ and $\beta(1)$ to be free to vary. The bulk free-energy of the orientation field described by (1.25)

over the outer capillary is obtained by analogous considerations just applied to $\mathscr{F}$ in (1.29)

$$\mathscr{F}^\eta = 2\pi K_{22} L \left\{ \int_\eta^1 \left[\frac{\beta'^2}{2} + \frac{1}{2\rho^2} \cos^2 \beta \sin^2 \beta + \frac{k_3}{2\rho^2} \sin^4 \beta \right] \rho \, d\rho + \frac{(1 - 2k_{24})}{2} \sin^2 \beta(1) \right\}, \quad (5.31)$$

which is reduced to the analogous autonomous dynamical problem by the change of variables $t(\rho) := -\ln(\rho)$:

$$\mathscr{F}^\eta = 2\pi K_{22} L \left\{ \int_0^{T_\eta} \left(\frac{\dot{b}^2}{2} + \phi(b) \right) dt + \frac{(1 - 2k_{24})}{2} \left[\sin^2 b(0) - \sin^2 b(T_\eta) \right] \right\}, \quad (5.32)$$

where $T_\eta := -\ln(\eta)$. Here, we have employed the notation given in (4.5).

$$\phi(b) := \frac{\sin^2 b \cos^2 b}{2} + \frac{k_3 \sin^4 b}{2}. \quad (5.33)$$

The *orbits* are obtained by solving (4.13) by separation of variables, where c is an integration constant, and obey the natural boundary conditions (4.11) at both initial al final times $\{0, T_\eta\}$. We read the equations (4.13) and (4.11) in the phase space $(b, \dot{b})$; the phase diagram of this system for the representative values $k_3 = 30$ and $k_{24} = 7.5$ is illustrated in Figure 5.6.
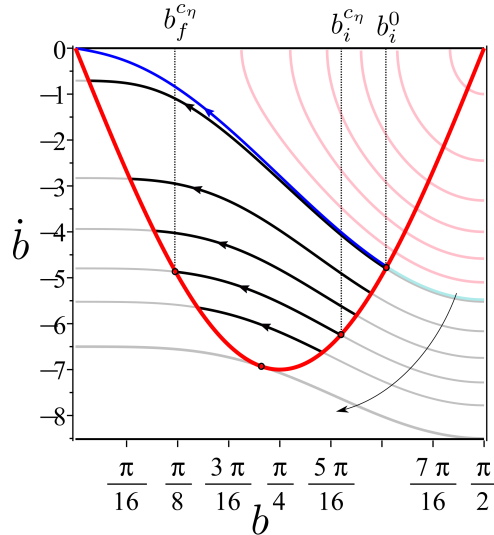

Figure 5.6: Reduced elastic constants are $k_3 = 30$ and $k_{24} = 7.5$; phase portrait for $b \in [0, \pi/2]$ of the dynamical system generated by the minimized Lagrangian. Here, the orbits for $c = 0$ (blue line) and $c = 0.5, 8, 15.5, 23, 30.5, c_{max} = 42.5$ (black lines according to the arrow) have been underlined, with attention to the orientation. For a outer cylinder of inner and outer radius R_0 and R with $\eta = R_0/R \in [0, 1]$, the optimal solution of the dynamical problem is the orbit corresponding to $c = c_\eta$ such that the time lapse T in (5.36) needed to traverse the contour line from one point of intersection with (4.11) to the other one is exactly $T_\eta = -\ln \eta$. This orbit departs from the curve of natural condition (4.11) for $b(0) = b_i^{c_\eta}$ and reaches again the curve (4.11) at $b(T_\eta) = b_f^{c_\eta}$. Especially, when η takes the value 0, $T_\eta \to +\infty$ and the optimal orbit of the infinite horizon variational problem is that individuated in Chapter 4 for $c = 0$ (blue line); it is exactly the right-handed ET-configuration by the change of variables $t = -\ln \rho$ and $b(t) = \beta(e^{-t})$.

To ensure the validity of (4.11), the motion follows the level curves in the phase space (4.13) departing at $t = 0$ from a point $(b_i^c, \dot{b}_n(b_i^c))$ on the curve (4.11) and arriving at $T = T_\eta$ to

another point $(b_f^c, \dot{b}_n(b_f^c))$ on the same curve. We assume that the initial configuration b_i^c ranges in $(0, \pi/2)$ and thus that $\dot{b}_n(b_i^c) < 0$ and the minus sign initially holds in (4.13); the restrinction of b_i^c to this interval excludes the mirror symmetric solutions, which could be retrieved by taking $b_i^c \in (\pi/2, \pi)$. When $c \in (-k_3, 0)$, the corresponding orbits cross again the curve of the natural conditions only if b traverses the same values attained before crossing the b-axis. To avoid these cases of non-injectivity, we restrict attention to non negative values of c; actually not all values of $c \geq 0$ guarantee the existence of an initial value b_i^c at which the corresponding orbit crosses two times the natural conditions. Indeed, the intersections between the manifold (4.11) and the negative branch of solution (4.13) are respectively

$$b_i^c := \arcsin \sqrt{\frac{2k_{24}(k_{24} - 1) + \sqrt{4k_{24}^2(k_{24} - 1)^2 - c[k_3 + 4k_{24}(k_{24} - 1)]}}{k_3 + 4k_{24}(k_{24} - 1)}}, \tag{5.34a}$$

$$b_f^c := \arcsin \sqrt{\frac{2k_{24}(k_{24} - 1) - \sqrt{4k_{24}^2(k_{24} - 1)^2 - c[k_3 + 4k_{24}(k_{24} - 1)]}}{k_3 + 4k_{24}(k_{24} - 1)}} \tag{5.34b}$$

and they exist when the range of the admissible values of c is bounded from above by

$$c_{\max} := \frac{4k_{24}^2(k_{24} - 1)^2}{[k_3 + 4k_{24}(k_{24} - 1)]}. \tag{5.35}$$

When $c = 0$, b_f^0 degenerates into 0, while for $c = c_{max}$ the initial and the final configurations coincide.

By (4.13), the time lapse needed for b to go backwards from b_i^c to b_f^c is delivered by

$$T := - \int_{b_i^c}^{b_f^c} \frac{1}{\sqrt{2\phi(\eta) + c}} \, d\eta. \tag{5.36}$$

Thus, (5.36) is infinite when the denominator vanishes at b_f^c and $\phi'(b_f^c) = 0$; this happens only for $c = 0$, while for every $c \in (0, c_{max}]$ it is finite and equals zero when $c = c_{max}$. We call c_η the value of $c \in [0, c_{max}]$ ensuring $T = T_\eta$ in (5.36); this defines a bijective correspondence between $\eta \in [0, 1]$ and $c_\eta \in [0, c_{max}]$, which associates η to the orbit corresponding to $c = c_\eta$ which departs from the curve of natural condition (4.11) for $b(0) = b_i^{c_\eta}$ and reaches again the curve (4.11) at $b(T_\eta) = b_f^{c_\eta}$. In particular, for the inner cylinder η takes the value 0 which corresponds to the level curve for $c_0 = 0$, which is exactly the right-handed ET-configuration[7]. Thus, the elastic free-energy stored in a outer cylinder with inner and outer radius R_0 and R corresponds through the dynamical analogy to (5.32) evaluated on the equilibrium solution for $c = c_\eta$ with η as in (5.30):

$$\mathscr{F}_\eta := 2\pi K_{22} L \left\{ \int_{b_f^{c_\eta}}^{b_i^{c_\eta}} \left[\sqrt{2\phi(b) + c_\eta} - \frac{c_\eta}{2\sqrt{2\phi(b) + c_\eta}} \right] db \right.$$
$$\left. + (1 - 2k_{24}) \frac{\sqrt{4k_{24}^2(k_{24} - 1)^2 - c_\eta[k_3 + 4k_{24}(k_{24} - 1)]}}{k_3 + 4k_{24}(k_{24} - 1)} \right\}, \tag{5.37}$$

where use has been made of (4.13) in (5.32). As we expected, when η is 0, i.e. the inner surface degenerates into the axis of the cylinder, then $c_0 = 0$ and $\mathscr{F}_0$ is exactly (1.44) for the ET configuration. Whenever $\eta \neq 0$, $\mathscr{F}_\eta$ is always greater than $\mathscr{F}_0$ and decreases towards it as

---

[7]By taking the initial configuration $b(0) \in (\pi/2, \pi)$ we obtain the mirror image solution.
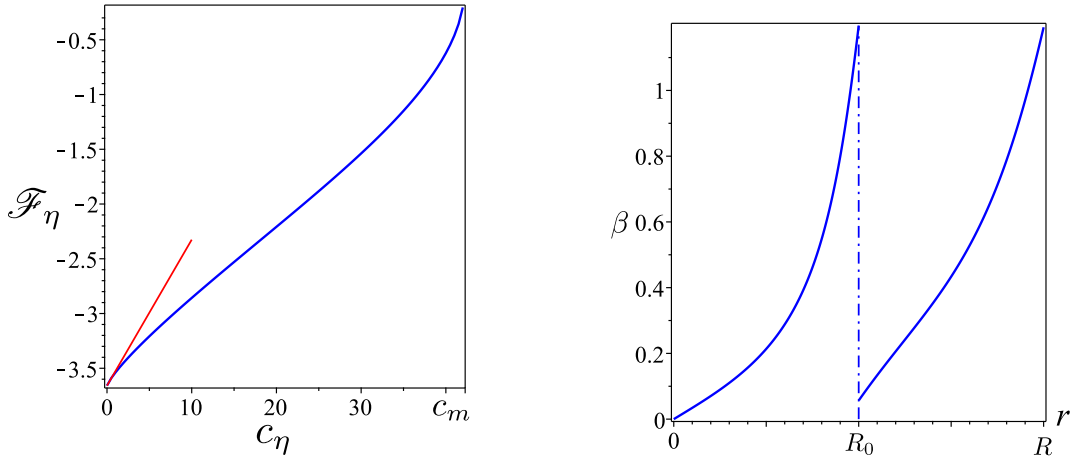
(a) Graph of $\mathscr{F}_\eta$ versus $c_\eta \in [0, c_{max}]$. For $\eta = 0$, i.e. $c_0 = 0$, $\mathscr{F}_0$ coincides with (1.44), while for $\eta = 1$, i.e. $c = c_{max}$, it equals 0. The red line corresponds to the straight line $y = \mathscr{F}_0 + c_\eta/(4k_{24})$: it is the asymptotic behaviour of $\mathscr{F}_\eta$ as η, and thus c_η, approaches 0.

(b) We find that, at equilibrium, the director field suffers a jump discontinuity on this material surface which separates two regions. Making use of $\rho = e^{-t}$ and $b(t) = \beta(e^{-t})$, we reproduce the configuration into which the director relaxes as a function of the radial coordinate. Here η is taken equal to $1/2$ and the dot line at $r = R_0$ represents the material barrier.

Figure 5.7: $k_3 = 30$ and $k_{24} = 7.5$, according to the measurement in [32]; the insertion of a cylinder of radius $R_0 < R$ such that $\eta = R_0/R$ from (5.30) corresponds to the appearance of a material surface, which separate the initial initial cylinder of radius R into two regions; an inner cylinder of radius R_0 and an outer cylinder of inner and outer radius R_0 and R.

η approaches 0; indeed, the series expansion about $c_\eta = 0$ truncated at the first order of the difference between the free-energy functionals evaluated on the solutions corresponding to $c_\eta \neq 0$ and $c_\eta = 0$ exhibits the following asymptotic behaviour:

$$\mathcal{F}_{c_\eta} - \mathcal{F}_0 \approx \frac{c_\eta}{4k_{24}} > 0. \tag{5.38}$$

This result has been obtained by the help of the *mean value theorem*. A graph of $\mathscr{F}_\eta$ versus $c_\eta \in [0, c_{max}]$ for $k_3 = 30$ and $k_{24} = 7.5$, [32] is illustrated in Fig. 5.7a. When c_η is sufficiently small, the graph of $\mathscr{F}_\eta$ is very similar to the red line corresponding to $y = \mathscr{F}_0 + c_\eta/(4k_{24})$; this confirms its good agreement with the asymptotic behaviour studied in (5.38).

The free-energy of the total configuration is given by

$$\mathscr{F} := \mathscr{F}_0 + \mathscr{F}_{c_\eta} < \mathscr{F}_0 \tag{5.39}$$

and since $\mathscr{F}_\eta$ is always negative whenever $c_\eta < c_{max}$ the insertion of a new cylinder in the starting system allows the director to suffer a jump discontinuity on the material surface which separates two regions and this lowers the total free-energy (see Fig. 5.7b)[8]. Now, work is required in inserting the material cylinder into the starting one since this process requires the displacement of the liquid crystal molecules that previously occupied the place now taken by the new cylinder. In the absence of dissipation one would expect an increase in the internal energy, Here, however, the internal energy further decreases: a paradoxical phenomenon which we ascribe to the lack of boundedness from below of the elastic free-energy density.

---

[8]The stability of the ET configuration has been proved against AC perturbations.

5.4.1   Additional Remark

We employ n times the procedure described above to the innermost cylinder at every step in order to ensure $\eta = R_{i-1}/R_i$ for every $i = 0 .. n$ where R_0 is the radius of the inner cylinder and $R_n = R$ is that of the starting one. Then, the total free-energy at the step n is given by

$$\mathscr{F}^n := \mathscr{F}_0 + n\mathscr{F}_\eta = \mathscr{F}_\eta + \mathscr{F}^{n-1} < \mathscr{F}^{n-1}; \tag{5.40}$$

it decreases of the quantity $\mathscr{F}_\eta$ with respect to the step before, and this energetic gain is preserved for all the subsequent iterations until the free-energy of the resulting system diverges to $-\infty$.

Actually, inserting a new cylinder leads to an increase of the surface exposed to the liquid crystal, and we should ask whether the surface contribution to the bulk energy of the configuration at every step could inhibit the paradox. For every inserted cylinder of radius R_0, both sides of the surface $\partial\mathscr{B}_0$ of the cylinder have to be taken into account and the additional surface contribution is proportional to their area, i.e.

$$\mathscr{F}_s^{add} = 2\gamma A(\partial\mathscr{B}_0) = 2\left(2\pi L\gamma R_0\right) = 2\pi K_{22}L\left[2\alpha\frac{R_0}{R}\right] = 2\pi K_{22}L\left[2\alpha\eta^n\right]. \tag{5.41}$$

where use has been make of the relation between the radii of the cylinders in the interior of the starting one

$$\frac{R_0}{R} = \frac{R_0}{R_1}\frac{R_1}{R_2} .. \frac{R_{i-1}}{R_i} .. \frac{R_{n-1}}{R} = \eta^n. \tag{5.42}$$

In (5.41), $\gamma > 0$ is the *nematic-nematic isotropic surface tension*, while α is the dimensionless volume define by

$$\alpha := \frac{\gamma R}{K_{22}}. \tag{5.43}$$

Thus, the surface free-energy at the step n is given by the sum of all the contributions originating by the exposed surfaces of the n inserted cylinders, i.e. by

$$\mathscr{F}_s^n = 2\pi K_{22}L\left[2\alpha\left(1 + \eta + \eta^2 + .. \eta^n\right)\right]. \tag{5.44}$$

For $\eta \in (0, 1)$, in the limit as n tends to ∞, (5.44) does not prevail over the bulk free-energy of the resulting system, since it converges to the finite value

$$\mathscr{F}_s^n = 2\pi K_{22}L\left(\frac{2\alpha}{1 - \eta}\right) < +\infty. \tag{5.45}$$

5.A   Strong Anchoring Conditions: Variational Problem

This technical Appendix concerns the mathematical details relative to the variational problem stated in Section 5.2 when a strong anchoring is imposed on the boundary of the region $\mathscr{B}$ that is given by a 2π rotation around the z- axis of the smooth function $R = R(z)$ vanishing at the extremes $z = \pm R_0$.

Frank's free-energy density associated with the particular class of distortions described by (1.25) reads as

$$f_{\mathrm{OF}} = \frac{K_{22}}{R^2}\left[\frac{R'^2\beta'^2\rho^2}{2}\left(k_1\sin^2\beta + k_3\cos^2\beta\right) + \frac{1 - k_{24}}{2}\left(\beta' + \frac{1}{\rho}\sin\beta\cos\beta\right)^2\right.$$
$$\left. + \frac{k_{24}}{2}\left(\beta' - \frac{1}{\rho}\sin\beta\cos\beta\right)^2 + \frac{k_3}{2\rho^2}\sin^4\beta\right], \tag{5.46}$$

where the scaled elastic constants k_1, k_3, k_{24} are as in (5.8).

We rescale the lengths r, z and $R(z)$, keeping their name unaltered, to the length dictated by the isotropic constraint (1.19) R_e, and by the use of (5.46), (5.3) and the change of variables (5.1), we arrive at the following reduced functional, $\mathcal{F}_\mu[R, \beta]$

$$\mathcal{F}_\mu[R, \beta] := \frac{\mathscr{F}_B}{2\pi K_{22} R_e} = \int_{-\mu}^{\mu} R'(z)^2 \, dz \int_0^1 \frac{\rho^2 \beta'^2}{2} \left(k_1 \sin^2 \beta + k_3 \cos^2 \beta\right) \rho \, d\rho$$

$$+ 2\mu \left\{ \int_0^1 \left[\beta'^2 + \frac{1}{\rho^2} \cos^2 \beta \sin^2 \beta + \frac{k_3}{\rho^2} \sin^4 \beta\right] \rho \, d\rho. + (1 - 2k_{24}) \right\}. \quad (5.47)$$

For any given function $\beta = \beta(\rho)$ satisfying (5.3), the optimal shape of the drop which minimizes $\mathcal{F}_\mu[R, \beta]$ in (5.47) subject to the isoperimetric constraint in scaled variables (5.5) is obtained by minimizing the unique term of (5.47), which depends on R among the smooth functions that obey:

$$R(-\mu) = R(\mu) = 0. \quad (5.48)$$

These hypothesis on R allow the use of *Wirtinger's Inequality*, which with the aid of (5.5) gives

$$\int_{-\mu}^{\mu} R'(z)^2 \, dz \geq \frac{\pi^2}{(2\mu)^2} \int_{-\mu}^{\mu} R(z)^2 = \frac{\pi}{3\mu^2}, \quad (5.49)$$

and the minimum is reached by (5.6) in the main text.

Thus, the normalized free-energy (5.47) associated with the family of the equilibrium shapes (5.6), $\mathcal{F}^\mu[\beta](k_{24})$, reads as in (5.7) in the main text. For any given value of $\mu \in (0, +\infty)$ its Euler Lagrange equation for $\rho \in (0, 1)$ reduces to

$$\frac{1}{\mu^2} \frac{\pi^2}{6} \left[\rho^2 \beta'^2 \sin \beta \cos \beta (k_1 - k_3) + (3\rho\beta' + \rho^2 \beta'') \left(k_1 \sin^2 \beta + k_3 \cos^2 \beta\right)\right]$$

$$+ \mu \left\{ \beta'' + \frac{1}{\rho} \beta' - \frac{1}{\rho^2} \sin \beta \cos \beta \left[1 + 2(k_3 - 1) \sin^2 \beta\right] \right\} = 0, \quad \rho \in (0, 1) \quad (5.50)$$

and it is subject to the conditions at the end-points of the interval $[0, 1]$ (5.3).

We consider in the following two subsections the two limiting problems $\mu = \infty$ and $\mu = 0$, which are slightly easier to solve than the general equilibrium problem proposed in the main text.

$\mu = 0$

In the limit as μ tends to 0 the term of the energy multiplied by $1/\mu^2$ prevails over the other term, and for $\mu = 0$ the free-energy is minimized only if

$$\mathcal{F}^0[\beta] = \int_0^1 \frac{\pi^2}{6} \rho^3 \beta'^2 \left(k_1 \sin^2 \beta + k_3 \cos^2 \beta\right) d\rho \quad (5.51)$$

is minimized among the functions $\beta = \beta(\rho)$ satisfying the strong anchoring conditions (5.3).

The Euler Lagrange Equation for the free-energy functional (5.51) in the bulk is

$$\rho^2 \beta'^2 \sin \beta \cos \beta (k_1 - k_2) + (3\rho\beta' + \rho^2 \beta'') \left(k_1 \sin^2 \beta + k_3 \cos^2 \beta\right) = 0, \quad (5.52)$$

and, multiplying both sides by $\rho^4 \beta'$, (5.52) has an integral of motion (has a first integral):

$$\frac{1}{2}\rho^6\beta'^2 \left(k_1 \sin^2 \beta + k_3 \cos^2 \beta\right) = \text{const.} \tag{5.53}$$

The Euler Lagrange equation in the strong form does not admit a regular solution in the interval $(0, 1)$ subject to the strong anchoring conditions (5.3).

Conforming to the experimental data in [32] and more generally to the recent measurements of the elastic constants in lyotropic chromonic liquid crystals as in [142] or in [26], we assume $k_1 = k_3$ and we confine the problem just stated to the interval (a, b) for $0 < a < b \le 1$ with the following conditions at the end points of this interval

$$\beta(a) = 0, \quad \beta(b) = \frac{\pi}{2}. \tag{5.54}$$

The Euler Lagrange equation (5.52) in the interval (a, b), making use of (5.53) and taking into account the boundary conditions (5.54), are solved by:

$$\beta_{a,b}(\rho) = \frac{\pi}{2} \frac{b^2 \left(\rho^2 - a^2\right)}{\rho^2 \left(b^2 - a^2\right)}, \quad \rho \in (a, b). \tag{5.55}$$

We consider a new family of variational problems phrased as follow: Find a and b, which satisfy $0 < a < b \le 1$, so as to minimize the free-energy (5.51) associated to the family of absolute continuous solutions parametrized in a and b (see e.g. Fig. 5.8):

$$\beta_{a,b}^0(\rho) = \begin{cases} 0 & \rho \in [0, a) \\ \dfrac{\pi}{2} \dfrac{b^2 \left(\rho^2 - a^2\right)}{\rho^2 \left(b^2 - a^2\right)} & \rho \in [a, b] \\ \dfrac{\pi}{2} & \rho \in (b, 1] \end{cases} \tag{5.56}$$

which reads:

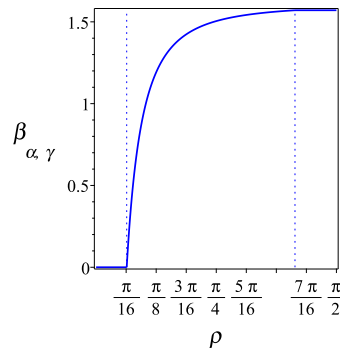$$\mathcal{F}^0\left[\beta_{a,b}^0\right] = k_1 \frac{\pi^2 a^2 b^2}{2\left(b^2 - a^2\right)}. \tag{5.57}$$

Figure 5.8: An example of AC solutions $\beta_{a,b}^0$, for $a = 0.2$ and $b = 1.3$.

For any $a \in (0, b)$, $\mathcal{F}^0\left[\beta_{a,b}^0\right]$ (5.57) is a strictly decreasing functions of b, and, taking $b = 1$, we construct the sequence of functions $\{\beta_{a,1}^0\}_a$ along which the value of the functional (5.57) tends to 0 as a approaches 0. The limiting solution to which the sequence converges when a goes to 0 is given by (5.2) in the main text and it is not an AC function due to the discontinuity in $\rho = 0$ with $\beta'(\rho) = \delta_{\{0\}} \left(\beta(0)^+ - \beta(0)^-\right)$.

5.B Crumbling Paradox

Employing n times the split procedure described for the starting drop in Section 5.2.2 to every droplet in the configuration at each step, the starting drop results crumbled into 2^n tactoidal droplets of equal volume and whose overall volume is V_0. If V_{n-1} and R_{n-1} are the volumes and the equivalent radii of all the 2^{n-1} drops at the step $n-1$, the volumes and the radii of the two sub-droplets into which every drop is splitted at step n (keeping the total volume unchanged) are, respectively

$$V_n = V_{n-1}/2 \tag{5.58}$$

and

$$R_n = 2^{-1/3} R_{n-1}. \tag{5.59}$$

Then, by (5.59) the equivalent radii corresponding to each of the two subdroplets at the step n are lowered with respect to that of the generating droplets at the step $n-1$, and so the barriers shift towards larger values of μ relative to μ_{n-1}, where the barriers of the drops at the step $n-1$ are placed. Making use of (5.15) and (5.59), the new barriers will be placed in

$$\bar{\mu}_n = \frac{\bar{R}_0}{R_n} = (2)^{1/3} \frac{\bar{R}_0}{R_{n-1}} = (2)^{1/3} \bar{\mu}_{n-1} > \bar{\mu}_{n-1}. \tag{5.60}$$

Accordingly, the free-energy at step n expressed as the sum of the free-energies associated to the resulting 2^n sub-droplets whose equivalent radii and barriers in μ are given by (5.59) and (5.60) results:

$$\mathscr{F}^n = 2\pi K_{22} 2^n \left[R_n \min_{\mu \in (0, \bar{\mu}_n]} \mathcal{F}(\mu, k_{24}) \right] = 2\pi K_{22} 2^n 2^{1/3} R_{n-1} \left[\min_{\mu \in (0, \bar{\mu}_n]} \mathcal{F}(\mu, k_{24}) \right] \tag{5.61}$$

where we recall that $\mathcal{F}(\mu, k_{24})$, (6.38), is the functional (5.7) evaluated on the equilibrium configurations $\beta_m^\mu(\rho)$ obtained for the given value of μ.

Equilibrium is attained whenever $\mathcal{F}(\mu, k_{24})$ is minimized among the value of $\mu < \bar{\mu}_n$ and since $\bar{\mu}_n > \bar{\mu}_{n-1}$ by (5.60), the value of $\mathcal{F}$ associated with the i-th drop at the step $n-1$ at equilibrium is always greater than or equal to that of the generating droplets associated with every resulting drops at the step n is always lower than or equal to that of the

$$\min_{\mu \in (0, \bar{\mu}_n]} \mathcal{F}(\mu, k_{24}) \leq \min_{\mu \in (0, \mu_{n-1}]} \mathcal{F}(\mu, k_{24}). \tag{5.62}$$

According to the graph in Fig. 5.4, the equality holds only when the equilibrium of the generating and the resulting droplets is is attained at $\mu = \mu_{\text{rel}}$, and so only if $\bar{\mu}_n$ and $\bar{\mu}_{n-1}$ belong to the range $[\mu_{\text{rel}}, \widetilde{\mu}]$. Making use of (5.62) in (5.61), we get (5.22) in the main text. According to the graphs in Figure 5.2, for every given value of $k_{24} > k_{24}^\infty$, $\mathcal{F}(\mu, k_{24})$ is strictly decreasing in $(\widetilde{\mu}, +\infty)$, it reaches the μ−axis at $\mu = \mu_0 > \widetilde{\mu}$ and diverges to $-\infty$ as μ goes to $+\infty$. When $\bar{\mu} < \mu_0$ the split of the initial drop could entail a waste of energy and the initial droplet may appear in apparent equilibrium. When $\bar{\mu} < \mu_0$, the crumbling paradox occurs at least when n is great enough, which means that we need to split the starting drop into a sufficient number of sub droplets, before they start to spontaneously disaggregate. By (5.60) there exist a step $\bar{n}$ at which the barriers of each of the droplet in the configuration are placed at a greater value than μ_0, i.e. $\bar{\mu}_{\bar{n}} > \mu_0$ and by (5.22) the total free-energy of the system at the step $\bar{n}+1$ obeys:

$$\mathscr{F}^{\bar{n}+1} \leq 2\pi K_{22} 2^{2/3} \left[2^{n-1} R_{\bar{n}} \min_{\mu \in (0, \bar{\mu}_{\bar{n}}]} \mathcal{F}(\mu, k_{24}) \right]. \tag{5.63}$$

The minimum value of $\mathcal{F}(\mu, k_{24})$ in $(0, \bar{\mu}_n)$ is negative and so by (5.63)

$$\mathscr{F}^{\bar{n}+1} < 2\pi K_{22} \left[2^{\bar{n}} R_{\bar{n}} \min_{\mu \in (0, \bar{\mu}_{\bar{n}}]} \mathcal{F}(\mu, k_{24}) \right] = \mathscr{F}^{\bar{n}} \tag{5.64}$$

By (5.62) and (5.60) this happens for every $n \geq \bar{n}$. Indeed for every subsequent splitting, the barriers increases and the equilibrium value of $\mathcal{F}(\mu, k_{24})$ is always negative.

Chapter 6

Quartic Theory

We propose a quartic theory to avoid the shortcomings of the existing one. The new quartic free-energy density is minimized by the (non uniform) local double-twist ground state, the assumed ground state of CLCs, and it turns out to be suitable to reproduce the experiments.

6.1 Introduction

The unboundedness below of Oseen-Frank's free-energy in $3D$ Euclidean space when $K_{22} < K_{24}$ seems to be the only responsible for the paradoxes shown in Chapter 5. Taking for a fact that the ground state of CLCs is a characteristic double twist, a continuum model for these particular materials should primarily cure that pathology. We do so by resorting to a higher-order theory. There are essentially two avenues towards a higher-order theory, that is, to allow either for higher spatial derivatives of $\boldsymbol{n}$ in the elastic free-energy density or for higher powers of its spatial gradient. Here, to stabilize the free-energy so that it cannot decrease without limit when $K_{22} < K_{24}$ we introduce a quartic power of the spatial gradient of $\boldsymbol{n}$. Examples of fourth-order densities were proposed in [3, 128, 21]. The idea here is to justify the occurrence of non-uniform, modulated nematic phases as ground states. Other theories are known as "quartic", [46], but they owe this name to an elastic term globally quartic in the order tensor and its derivatives, added to the commonly considered version of the Landau de Gennes theory. This version is capable of recovering the full Oseen-Frank's energy-density, avoiding the degeneracy $K_{11} = K_{33}$ typical of the original theory.

In Section 6.2 we look for a minimalistic free-energy density that agrees with Oseen-Frank's at the lower order and is minimized by a characteristic double-twist configuration.

In Section 6.3 we put to the test the ability of the new theory to reproduce the experiments with CLCs under confinement. A scale length a is introduced in the model which measures the extent of the distortions. This characteristic length, which we estimate of the order of $10 - 100$nm and the radius of the cylinder of the experiments are well separated and the non trivial solutions of the Euler Lagrange equations for the new functional have opposite chirality and closely resemble the ET solution (1.42) or its mirror image (1.43). Despite the new theory describes the assumed ground state of CLCs, this state could be attained in $3D$ space only in the non physical case of a cylinder whose radius is considerably smaller than a. Otherwise, the confinement prevents the realization of the spontaneous value of the double twist away from the axis.

Also the study of the extended phase space of a dynamical system associated with the quartic free-energy density shows in Section 6.4 a good agreement between the new theory and Oseen-Frank's in rationalizing the experimental investigations of CLCs confined in cylindrical geometry.

Section 6.5 illustrates that for the sequence of configurations $(\mathscr{B}_k, \boldsymbol{n}_k)$ leading to the free-boundary paradox described in Chapter 5, the limiting value of the new functional as $k \to \infty$ does not diverge to $-\infty$.

6.2 Quartic Formula

Since the ground state of CLCs is not the uniform field, as in classical nematics, but a characteristic double-twist, a well-posed elastic theory for chromonics should penalize distortions departing from the (non-uniform) local state characterized by

$$S = 0, \quad T = T_0, \quad B = 0, \quad 2q = 0. \tag{6.1}$$

We posit a quartic energy density promoting a double-twist configuration and penalizing all departures from it

$$W_{\text{chr}}(\boldsymbol{n}, \nabla \boldsymbol{n}) = \frac{1}{2}\kappa_1 S^2 + \frac{1}{2}\kappa_2 T^2 + \frac{1}{2}\kappa_2'(2q)^2 + \frac{1}{2}\kappa_3 B^2 + \frac{1}{4}\kappa_4 T^4. \tag{6.2}$$

The leading terms in (6.2) are the only terms that need to be positive definite, and since (S, T, B, q) are all independent measures of distortions, it readily follows that we shall take κ_1, κ_2', κ_3, κ_4 all positive. The sign of κ_2 could be arbitrary.

Comparing W_{chr} in (6.2) and the form of f_{OF} given in (1.13), one can easily see quadratic theory agrees with Oseen-Frank's energy at lower order. In particular:

$$\kappa_1 = K_{11} - K_{24} > 0, \quad \kappa_2 = K_{22} - K_{24} \in \mathbb{R}, \quad \kappa_3 = K_{33} > 0, \quad \kappa_2' = K_{24} > 0, \quad \kappa_4 > 0. \tag{6.3}$$

It is worth noting that this choice makes W_{chr} depend only on five elastic constants, just one more than in Oseen-Frank's formula. While K_{11}, K_{22}, K_{33} and K_{24} have physical dimensions of force, κ_4 has dimension of force times length squared. We shall set

$$k_4 = K_{22}a^2, \tag{6.4}$$

where a is a *characteristic length* (possibly of molecular origin). Indeed, since the ground state for the quartic energy is not uniform, this scale length is introduced into the model and measures the locality of the distortion[1]; it could be closely related to the persistence length of the molecular order, which characterizes the flexibility of CLC aggregates[2]. We estimate a on the order of tens-hundreds of nm [139].

Whenever the inequalities in (6.3) hold, the free-energy density intended here for chromonics (6.2) would induce a double-twist distortion characterized by (6.1), which realizes the the state of minimum energy. The unboundedness below of Oseen-Frank's free-energy which was responsible for the paradoxes found in Chapter 5, is here prevented by the positive definiteness of the leading terms in (6.2) and the problem of minimizing (6.2) with respect to the double-twist pseudoscalar reduces to

$$T^2 = T_0^2 := -\frac{k_2}{k_4} = -\frac{K_{22} - K_{24}}{K_{22}}\frac{1}{a^2} = -\frac{1 - k_{24}}{a^2} > 0 \tag{6.5}$$

where use has been made of (6.3) and (1.30). Thus, the free-energy has a minimum at $T = \pm|T_0|$, provided that k_{24} in (1.30) is greater than 1, which is also the range of validity of the escaped twist solutions in the quadratic theory.

---

[1]It is perhaps worth noting that also in the elastic model proposed in [128], whose quadratic free-energy can admit as ground state either of the two families of uniform director fields (1.15), i.e. two conjugated heliconical fields with opposite chirality, a length scale is hidden in the theory from the start; it will reappear in the equilibrium pitch and the distortion state characterized by this preferential length is the same everywhere.

[2]The persistence length of self-assembled flexible aggregates is a length over which unit vectors tangential to the aggregates lose correlation.

6.3 Minimization Problem

We write the elastic free-energy functional for CLCs as

$$\mathscr{F}_{chr}[\mathscr{B}, \boldsymbol{n}] := \int_{\mathscr{B}} W_{chr}(\boldsymbol{n}, \nabla \boldsymbol{n}) \, \mathrm{d}V = \mathscr{F}_{\mathrm{b}}[\mathscr{B}, \boldsymbol{n}] + \mathscr{F}_{k_4}[\mathscr{B}, \boldsymbol{n}], \tag{6.6}$$

where $\mathscr{F}_{\mathrm{b}}$ is Oseen-Frank's free-energy functional and

$$\mathscr{F}_{k_4}[\mathscr{B}, \boldsymbol{n}] := \frac{K_{22} a^2}{4} \int_{\mathscr{B}} (\boldsymbol{n} \cdot \operatorname{curl} \boldsymbol{n})^4 \, \mathrm{d}V \tag{6.7}$$

is the higher-order contribution.

The length a is characteristic of the material and it is thus held fixed; R is the radius of the cylinder confining the CLC and on physical grounds it is expected to range in the interval $[a, \infty)$. With a physicist's mind, one could reason by saying that if $R \gg a$, the quartic term in (6.2) does not broadly contribute to energy density of the quadratic theory, and so to the equilibrium equations. We thus expect the minimizers of the new energy functional (6.6) to be either 0 or two solutions with opposite chirality which closely resemble the ET solution (1.42) or its mirror immage (1.43). To study the intermediate regime in which R and a are comparable is also of interest.

We follow the same line of thought outlined in Chapter 1 when Oseen-Frank's free-energy was employed to rationalize the configuration of the confinement-induced ground state. Thus, the region $\mathscr{B}$ occupied by the CLCs in the N phase is a cylinder of radius R and height L; the director field is defined by (1.25), where $\beta = \beta(\rho)$ describes how the directors twist along a radius of the cylinder and it is assumed to depend only on r through $\rho = r/R$ in (1.26). This angle obeys $\beta(0) = 0$ for the integrability of the energy density, while $\beta(1)$ is free to vary, since $\boldsymbol{n}$ in the form (1.25) can always accommodate degenerate boundary conditions. By the change of variable $r \to \rho$ and making use of the distortion characteristics (1.28) in the new free-energy functional for CLCs (6.6), we arrive at the following reduced functional, which is an appropriate dimensionless form of $\mathscr{F}_{chr}[\boldsymbol{n}]$ in (6.6) and agrees with that found within Oseen-Frank's theory, $\mathcal{F}[\beta]$ in (1.29), at lower order

$$\mathcal{F}_{chr}[\beta] := \frac{\mathscr{F}_{chr}}{2\pi K_{22}} = \mathcal{F}[\beta] + \mathcal{F}_{k_4}[\beta] \tag{6.8}$$

where

$$\mathcal{F}_{k_4}[\beta] := \varepsilon^2 \int_0^1 \frac{\rho}{4} \left(\beta' + \frac{1}{\rho} \sin \beta \cos \beta \right)^4 \mathrm{d}\rho, \tag{6.9}$$

and

$$\varepsilon := \frac{a}{R}. \tag{6.10}$$

As before, we seek the orientation fields $\boldsymbol{n}$ which make the elastic free-energy stationary within the class described by (1.25) subject to $\boldsymbol{n}|_{\rho=0} = \boldsymbol{e}_z$, under the assumption that $\boldsymbol{n}$ is at least a map of class $\mathcal{C}^2$. This amounts to seek the functions $\beta = \beta(\rho)$ of class $\mathcal{C}^2$ in $[0, 1]$ which satisfy the condition at $\rho = 0$ and make (1.29) stationary. The strong forms of the Euler Lagrange equations reduce here to

$$\frac{1}{\rho^2} \cos \beta \sin \beta \left[1 + 2(k_3 - 1) \sin^2 \beta \right] - \frac{\beta'}{\rho} - \beta''$$

$$+ \varepsilon^2 \left(\beta' + \frac{\sin \beta \cos \beta}{\rho} \right)^2 \left[\frac{4 \sin^2 \beta \beta'}{\rho} - \frac{3\beta'}{\rho} - 3\beta'' + \frac{\sin \beta \cos \beta}{\rho^2} \left(3 - 2 \sin^2 \beta \right) \right] = 0, \tag{6.11}$$

and

$$\left[(1 - 2k_{24})\cos\beta\sin\beta + \beta' + \varepsilon^2\left(\beta' + \frac{\sin\beta\cos\beta}{\rho}\right)^3\right]\Bigg|_{\rho=1} = 0. \tag{6.12}$$

When ε equals 0 the quartic term is neglected and this theory effectively reduces to Frank's; the non-uniform equilibrium configurations for the free-energy functionals subjects to the boundary conditions are the escaped twist solutions (1.42) and (1.43). Whenever $\varepsilon > 0$, (6.11) has not a first integral and the solutions of (6.11) and (6.12) fail to be made explicit. Thus, for a given choice of the parameter ε and of the elastic parameters (k_3, k_{24}) we numerically find the solutions of (6.11) and (6.12), which satisfies $\beta(0) = 0$. We consider one or three equilibrium solutions according to the value of k_{24}: the uniform solution $\beta(\rho) = 0$ (1.41) which exists for every $k_{24} > 0$, with the director $\boldsymbol{n}$ parallel to the capillary axis, and two other non-uniform configurations $\beta_\varepsilon(\rho)$ and $\pi - \beta_\varepsilon(\rho)$ with right- and left- handed chirality according to whether the integral lines of the nematic director spiral clockwise or counter-clockwise. By evaluating numerically the functional $\mathcal{F}_{chr}[\beta]$ in (6.8) on these last two equilibrium configurations, we find that the uniform configuration is always energetically disfavoured; this justifies the spontaneous emergence of chirality in the nematic director texture in the absence of molecular chirality. Actually, director equilibrium configurations in which the director winds around the radial direction a larger number of times than these latter also exist. They are both energetically disfavoured and lacking in physical meaning; we neglect them.

Though equation (6.11) is too complicated to lend itself to analytic solutions, we can still explore the asymptotic behaviour near $\rho = 0$ of the solutions branching off the trivial one. We take in (6.11)

$$\beta(\rho) = A\rho^\alpha, \tag{6.13}$$

where A is an arbitrary constant and $\alpha > 1/2$ makes (6.9) compatible with the requirement of integrability. In the limit as ρ tends to 0, (6.11) can be given the following asymptotic form:

$$3A^2(\alpha - 1)(\alpha + 1)\rho^{4\alpha-3}\varepsilon^2 + (\alpha - 1)(\alpha + 1)\rho^{2\alpha-1} + O(\rho^{6\alpha-3}, \rho^{4\alpha-1}) = 0, \tag{6.14}$$

where $O(\rho^{6\alpha-3}, \rho^{4\alpha-1})$ means that $6\alpha - 3$ is the lower order in ρ for $\alpha \in (1/2, 1)$, $4\alpha - 1$ otherwise. For every $A \in \mathbb{R}$ and $\varepsilon > 0$, $\alpha = 1$ solves equation (6.14) at the lowest order and the non trivial solutions of (6.11) shows the following asymptotic behaviour as ρ tends to 0

$$\beta(\rho) \approx \beta'(0)\rho. \tag{6.15}$$

6.3.1 Cylindrical Symmetry and Extensions

Hereafter we restrict attention to the positive branch of the solution $\beta = \beta_\varepsilon(\rho)$. Since the extrapolation length a is kept fixed, the family of solutions $\{\beta_\varepsilon(\rho)\}_\varepsilon$ is thus generated by letting R vary in the admissible interval $[a, \infty)$, which corresponds through (6.10) to the interval $[0, 1]$ spanned by ε.

We first explore the ability of the new free-energy functional (6.2) to reproduce the experiments on CLCs under cylindrical confinement. Good agreement with Oseen-Frank's theory is also expected.

In [19, 32], the experimental study of CLCs confined in cylinders are carried out for radii R of the order of tens-hundreds micrometers, $R \sim 10 - 100\mu$m, and since we consider a of molecular order, the corresponding value of ε is $\ll 1$. We take as reference value $\varepsilon = 10^{-2}$. Figure 6.1 illustrates than when ε is around this value, the equilibrium solution with right-handed chirality closely resembles the ET configuration with the same chirality, as expected. The same argument holds for the mirror image with left-handed chirality. They share the same energy and are likely to characterize the two-fold pseudo ground state of CLCs within the new theory.
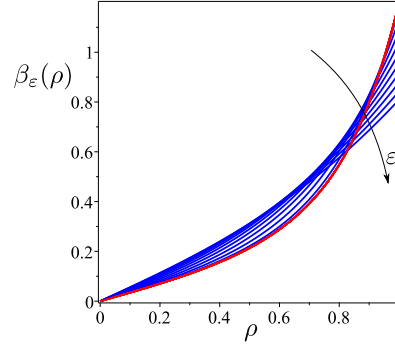
Figure 6.1: Right-handed equilibrium solutions for $k_3 = 30$, $k_{24} = 7.5$ [32] for different values of ε, namely $\varepsilon = 10^{-2}$, 6×10^{-2}, 0.1, 0.2, 0.3, 0.4, 0.5, 0.6, 0.8, 0.9, 1(according to the arrow). Red line represents the ET solution with positive chirality, (1.42).

The minima $\pm T_0$ $(T_0 > 0)$ of the free-energy in (6.5) are determined by the value of a. To explore the core of a size around the axis of the cylinder, we find it useful to introduce the new scaled variable

$$\xi := \frac{r}{a} \in \left[0, \frac{1}{\varepsilon}\right]. \tag{6.16}$$

As ξ spans the interval $[0, 1]$, we remain within the molecular distance a from the axis. Here ξ is related to $\rho \in [0, 1]$ in (1.26) through the formula

$$\xi(\rho) = \frac{\rho}{\varepsilon}, \tag{6.17}$$

providing a change of variables which maps $[0, 1]$ onto $[0, 1/\varepsilon]$. In the new variable β_ε becomes a function on $[0, 1/\varepsilon]$ defined by

$$b_\varepsilon(\xi(\rho)) := \beta_\varepsilon(\rho), \tag{6.18}$$

and such that

$$b'_\varepsilon(\xi) := \varepsilon\beta'_\varepsilon(\rho) = \varepsilon\beta'_\varepsilon(\varepsilon\xi), \tag{6.19}$$

where $'$ always denotes differentiation with respect to the argument. Inserting (6.18) and (6.19) (with $T > 0$) in (1.28), we give the distortion characteristics of the right-handed equilibrium solution the following dimensionless form as function of ξ:

$$aS_\varepsilon = 0, \tag{6.20a}$$

$$aT_\varepsilon = b'_\varepsilon(\xi) + \frac{\cos b_\varepsilon(\xi) \sin b_\varepsilon(\xi)}{\xi}, \tag{6.20b}$$

$$2aq_\varepsilon = b'_\varepsilon(\xi) - \frac{\cos b_\varepsilon(\xi) \sin b_\varepsilon(\xi)}{\xi}, \tag{6.20c}$$

$$aB_\varepsilon = \frac{\sin^2 b_\varepsilon(\xi)}{\xi}. \tag{6.20d}$$

In particular, the ratio between T_ε and $+T_0$ does not depend on a and is given by

$$\frac{T_\varepsilon}{T_0} = \frac{1}{\sqrt{k_{24} - 1}} \left(b'_\varepsilon(\xi) + \frac{\cos b_\varepsilon(\xi) \sin b_\varepsilon(\xi)}{\xi}\right). \tag{6.21}$$

When $a \ll R$, and so $\varepsilon \ll 1$, the confinement is placed at a great distance from the cylinder of molecular radius a. The ideal state with $T = T_0$ is sought for away from the cylinder's axis (see

Fig. 6.2a) for different values of ε. The spontaneous value of the double-twist is prevented from being attended along the axis.

The distortion characteristics for $b_\varepsilon = b_\varepsilon(\xi)$ near the axis are justified by the asymptotic analysis carried out for the non trivial equilibrium solutions in Section 6.3. Making use of (6.15) in (6.18), we arrive at the following explicit formula for b_ε when ξ is near 0

$$b_\varepsilon(\xi) \approx \varepsilon \beta'(0)\xi, \tag{6.22}$$

from which it readily follows that both $2aq$ in (6.20c) and aB in (6.20d) vanish at $\xi = 0$. The value of T_ε/T_0 along the axis of the is given by

$$\left.\frac{T_\varepsilon}{T_0}\right|_{\xi=0} = \frac{2\varepsilon\beta'(0)}{\sqrt{k_{24} - 1}}, \tag{6.23}$$

which, by (6.18) and (6.19), vanishes only for $\varepsilon = 0$. As soon as ε differs from 0, T_ε/T_0 along the axis starts to increase toward 1, reaching only a fraction of it for $\varepsilon = 1$. In particular, the computed values for (6.23) as a function of $\varepsilon \in [0, 1]$ when $k_3 = 30$ and $k_{24} = 7.5$ [32] are reported in Fig. 6.3.   For the physically meaningful values of ε, the equilibrium double-twist T_ε never
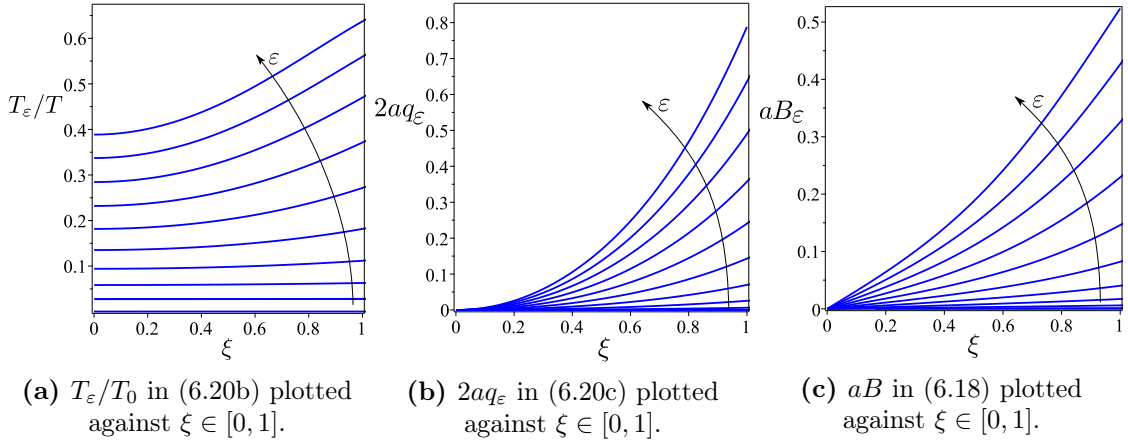

<div align="center">

(a) T_ε/T_0 in (6.20b) plotted against $\xi \in [0, 1]$.   (b) $2aq_\varepsilon$ in (6.20c) plotted against $\xi \in [0, 1]$.   (c) aB in (6.18) plotted against $\xi \in [0, 1]$.

</div>

Figure 6.2: $k_3 = 30$, $k_{24} = 7.5$ and increasing values of ε, namely $\varepsilon = 10^{-2}, 6 \times 10^{-2}, 10^{-1}\, 0.2, 0.3, 0.4, 0.5, 0.6, 0.8, 0.9, 1$(according to the arrow). These graphs investigate how the elastic mode of the right-handed equilibrium solution behave within the cylinder of molecular radius a enclosing the axis of the confinement. They are expressed in terms of the auxiliary variable $\xi \in [0, 1]$ in (6.16).

reaches the spontaneous value T_0, a clear sign of elastic frustration. It should be noted that the value predicted here for the double twist T at equilibrium along the cylinder's axis is in stark contrast with that read off from (1.45) within Oseen-Frank's theory. Consider now, at curiosity, the case $R < a$: the confinement of the CLC becomes virtual as it enters the cylinder of radius a. Thus the auxiliary variable suitable for the study of the virtual situation is $\rho \in [0, 1]$ in (1.26), and the dimensionless distortion characteristics of the right-handed equilibrium solution are:

$$aS_\varepsilon = 0, \tag{6.24a}$$

$$aT_\varepsilon = \varepsilon\left(\beta'_\varepsilon(\rho) + \frac{\cos\beta_\varepsilon(\rho)\sin\beta_\varepsilon(\rho)}{\rho}\right), \tag{6.24b}$$

$$2aq_\varepsilon = \varepsilon\left(\beta'_\varepsilon(\rho) - \frac{\cos\beta_\varepsilon(\rho)\sin\beta_\varepsilon(\rho)}{\rho}\right), \tag{6.24c}$$

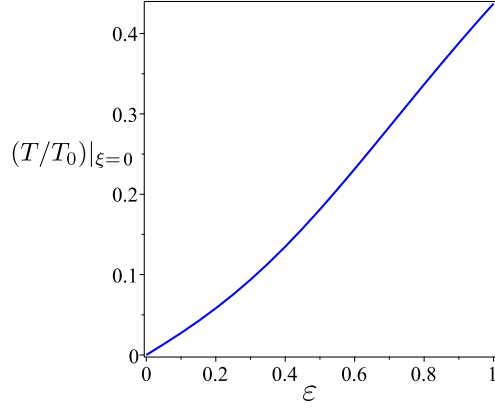$$aB_\varepsilon = \varepsilon\frac{\sin^2\beta_\varepsilon(\rho)}{\rho}. \tag{6.24d}$$

Figure 6.3: The value of the ratio T_ε/T_0 at the origin is plotted against $\varepsilon \in [0,1]$. Reduced elastic constants are $k_3 = 30$, $k_{24} = 7.5$.

As ε increases beyond 1, we notice in Fig. 6.4 that an increase of ε is associated with a reduction of the frustration in the confined system and to a tendency to uniformity of the confinement-induced ground state. Indeed, the graphs in Figures 6.4c and 6.4b show a reduction of both bend and octupolar splay. Moreover, Fig 6.4a represents the trend toward uniformity of the double twist, which converges to the minimum T_0 in (6.5) of the free-energy.
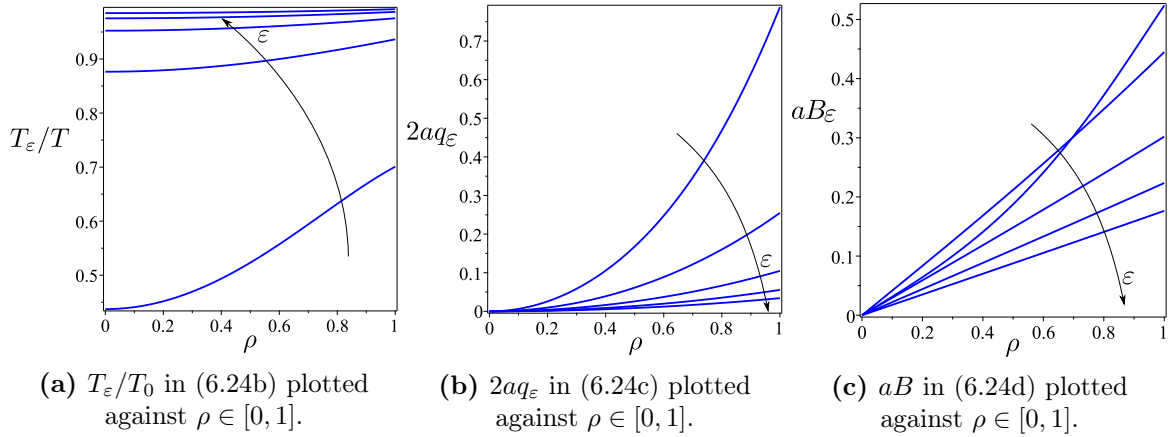

(a) T_ε/T_0 in (6.24b) plotted against $\rho \in [0,1]$.

(b) $2aq_\varepsilon$ in (6.24c) plotted against $\rho \in [0,1]$.

(c) aB in (6.24d) plotted against $\rho \in [0,1]$.

Figure 6.4: $k_3 = 30$, $k_{24} = 7.5$. For increasing values of $\varepsilon > 1$, a trend toward a double-twist configuration (6.1) with T_0 given by the positive minimum of the quartic free-energy (6.5) is observed. Here, the dimensionless distortion characteristics are plotted against $\rho \in [0,1]$ for increasing values of ε, namely $\varepsilon = 1, 3, 5, 7, 9$ (according to the arrow).

6.4   Dynamical Analogy

Here the problem tackled in the previous Section is reduced to an analogous infinite horizon variational problem. Contrary to the case for $\varepsilon = 0$ in Chapter 4, the dynamical system is not autonomous. The new bulk free-energy density is mechanically interpreted as the Lagrangian of this peculiar dynamical system given by the sum of a kinetic and a potential energy and the features of these motions are illustrated through the extended phase diagram of the system, with the time as third coordinate. We thus extend the analysis in Chapter 4 slightly.

Since W_{chr} in (6.2) agrees with Oseen-Frank's energy density at lower order, we study only the contribution of the term of higher order which supplements those just found in Chapter 4.

The functional (6.9) is reduced to the analogous dynamical problem by the change of variables $t(\rho) := -\ln(\rho)$ in (4.1), where t has the meaning of artificial time and maps $[0,1]$ onto $[0, +\infty]$. Moreover β becomes a function on $[0, \infty)$, which is defined by $b(t(\rho)) := \beta(\rho)$ and we give $\mathcal{F}_{k_4}[\beta]$ the following dimensionless form:

$$\mathcal{F}_{k_4}[b] := \frac{1}{4} \int_0^\infty \left(\varepsilon e^t\right)^2 \left(-\dot{b} + \sin b \cos b\right)^4 \mathrm{d}t \tag{6.25}$$

This functional is to be added to $\mathcal{F}[b]$ in (5.47), and the dynamical analogous of $\mathcal{F}_{\text{chr}}[\beta]$ in (6.8) results in:

$$\mathcal{F}_{chr}[b] := \mathcal{F}[b] + \mathcal{F}_{k_4}[b] = \int_0^\infty \left[\frac{\dot{b}^2}{2} + \phi(b) + \frac{1}{4}\left(\varepsilon e^t\right)^2 \left(-\dot{b} + \sin b \cos b\right)^4\right] \mathrm{d}t - \varphi_0(b(0)), \tag{6.26}$$

where $\phi(b)$ and $\varphi_0(b)$ are given as in (4.5) and (4.6), respectively. Unlike the quadratic case, this dynamical problem is not autonomous and the Lagrangian of this peculiar system is given by

$$\mathcal{L}_{chr} := \frac{\dot{b}^2}{2} + \phi(b) + \frac{1}{4}\left(\varepsilon e^t\right)^2 \left(-\dot{b} + \sin b \cos b\right)^4. \tag{6.27}$$

Here, the equation of motion (4.8) for $\mathcal{L}_{chr}$ reads as

$$\ddot{b} + (\varepsilon e^t)^2(-\dot{b} + \sin b \cos b)^2 \left[3\ddot{b} + 4\dot{b}\sin^2 b + \sin b \cos b(2\sin^2 b - 3)\right] = \phi'(b) \tag{6.28}$$

while the natural condition at the boundary (4.10) is given by

$$\dot{b} - (\varepsilon e^t)^2(-\dot{b}\sin b \cos b)^3 - (1 - 2k_{24})\sin b \cos b = 0. \tag{6.29}$$

The phase diagram of this system for the representative values $k_3 = 30$ and $k_{24} = 7.5$ is illustrated in Figure 6.5.

The phase space, although the problem is no longer autonomous, has the same structure of that for $\varepsilon = 0$ in Chapter 4. The intersection of orbits does not contradict the theorem of existence and uniqueness of the solutions of dynamical systems as the system is non autonomous and time makes these trajectories not self-intersecting in the extended phase space. This confirms that the quartic theory as long as ε is small is exactly superimposable to Oseen-Frank's theory; indeed, the orbits on the phase space for the quadratic and the quartic theories are only quantitatively (but not qualitatively) different.

6.5   Chromonic Droplets

The aim of this section is to prove that the quartic theory proposed here prevent the shortcomings of Oseen-Frank's theory highlighted in Chapter 5. As an example, we illustrate that for the sequence of configurations $(\mathscr{B}_k, \boldsymbol{n}_k)$ leading to the free-boundary paradox we have constructed in Chapter 5, the limiting value of the new functional as $k \to \infty$ does not diverge to $-\infty$.

We recall the setting of the paradox. The drop's boundary $\partial\mathscr{B}$ is obtained by rotating the graph of a function of class $\mathcal{C}^1$, $R = R(z)$, which describes the radius of the drop's cross-section at height $z \in [-R_0, R_0]$. R is taken to be an even function and to vanish on the z axis at the points $z = \pm R_0$ (the poles of the drop). Orientation fields $\boldsymbol{n}$ are of the form given in (1.25),
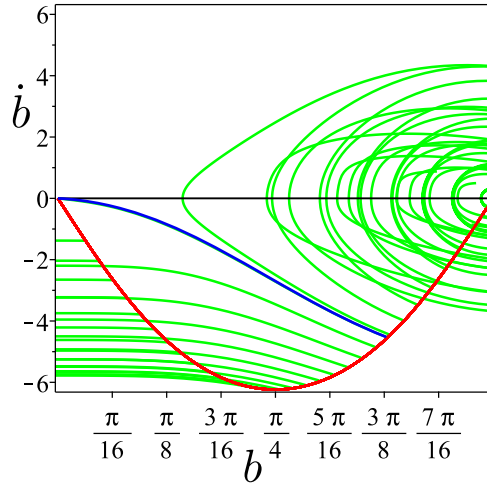
Figure 6.5: Reduced elastic constants are $k_3 = 30$ and $k_{24} = 7.5$. $\varepsilon = 10^{-2}$, value taken as representative of the experiments on CLCs under cylindrical confinement; phase portrait for $b \in [0, \pi]$ of the dynamical system generated by the minimized nemerically Lagrangian. The optimal solution of the infinite dynamical problem is the orbit corresponding to $c = 0$.

where β is assumed to depend on the dimensionless coordinate $\rho = r/R(z)$ in (5.1)[3](it does not vary along the meridian of the droplet). Moreover $\beta = \beta(\rho)$ obeys strong anchoring conditions (5.3) and (5.2).

More precisely, the incriminated sequence corresponds to the family of configurations (R_m^μ, β_m^μ) generated by letting μ vary in $(0, +\infty)$, where $R_m^\mu = R_m^\mu(z)$ is the family of tactoids parametrized in μ and given by (5.6) and $\beta_m^\mu = \beta_m(\rho)$ is the equilibrium solution of the Euler Lagrange equation for the functional $\mathcal{F}_\mu[R, \beta]$ in (5.6) and satisfying the strong anchoring conditions. Here the functions β_m^μ will be the equilibrium configurations for the appropriate dimensionless form of the functional $\mathscr{F}_{chr}$ in (6.6) over the special family of shapes (5.6).

Since W_{chr} in (6.2) agrees with Oseen-Frank's energy density at lower order, we study only the contribution of the term of higher order which supplements those just found in Chapter 5. By rescaling the length r, R and z to that dictated by the volume constraint R_e, the appropriate dimensionless form of $\mathscr{F}_{k_4}$ in (6.7) associated with the particular class of distortions under condideration is given by

$$\mathcal{F}_{k_4}^\mu[R, \beta] := \frac{\mathscr{F}_{k_4}}{2\pi K_{22} R_e} = \varepsilon^2 \int_{-\mu}^{\mu} \frac{1}{R(z)^2} \, dz \int_0^1 \frac{\rho}{4} \left(\beta' + \frac{\sin\beta \cos\beta}{\rho} \right)^4 d\rho. \qquad (6.30)$$

This functional is to be added to $\mathcal{F}_\mu[R, \beta]$ in (5.47), and the variational problem we thus face can be phrased as follows: find a positive and even function $R = R(z)$ vanishing at $z = \pm\mu$ and a function $\beta = \beta(\rho)$ which obeys (5.3) and (5.2) so as to minimize the following reduced functional which is an appropriate dimensionless form of $\mathscr{F}_{chr}[\mathscr{B}, \boldsymbol{n}]$ in (6.6) associated with the equilibrium shapes (5.6):

---

[3]With an abuse of language we keep the name unaltered when R does not depend on z, as in the cylindrical confinement treated in [10] or in [19].

$$\mathcal{F}_{chr}[R,\beta] := \frac{\mathscr{F}_{chr}}{2\pi K_{22}R_{e}} = \int_{-\mu}^{\mu} R'(z)^2\, dz \int_0^1 \frac{\rho^2\beta'^2}{2} \left(k_1 \sin^2\beta + k_3 \cos^2\beta\right)\rho\, d\rho$$

$$+ \varepsilon^2 \int_{-\mu}^{\mu} \frac{1}{R(z)^2}\, dz \int_0^1 \frac{\rho}{4}\left(\beta' + \frac{\sin\beta\cos\beta}{\rho}\right)^4 d\rho$$

$$+ 2\mu \left\{ \int_0^1 \left[\beta'^2 + \frac{1}{\rho^2}\cos^2\beta\sin^2\beta + \frac{k_3}{\rho^2}\sin^4\beta\right]\rho\, d\rho. + (1 - 2k_{24})\right\}. \tag{6.31}$$

Here k_1, k_3 and k_4 are given in (5.8) and (1.30). The new theory requires $k_{24} > 1$ (which violates Ericksen's inequalities (1.8)), while k_1 and k_3 are non negative.

In the new theory the defects at the poles of the director field (1.25) subject to strong anchoring conditions (5.3) and (5.2) possess infinite energy. Here the culprits are the twist and the splay contributions; at least one of the two integrands $R'(z)^2$ or $1/R(z)^2$ is not integrable at $z = \pm\mu$. This is seen by the following inequality, which is built on *Hölder's inequality*:

$$|\ln R(z) |_0^\mu | = \left|\int_0^\mu \frac{R'(z)}{R(z)}\, dz\right| \leq \int_0^\mu \left|\frac{R'(z)}{R(z)}\right|\, dz \leq \left(\int_0^\mu R'(z)^2\, dz\right)^{1/2}\left(\int_0^\mu \frac{1}{R(z)^2}\, dz\right)^{1/2}. \tag{6.32}$$

Especially, the contribution of the splay distortion to the functional (6.31) diverges for smooth shapes, while twist contribution becomes unbounded for pointed shapes.

We thus resume the argument of Chapter 3 for two-dimensional droplets and we imagine that the energy concentration near defects causes a localized transition to the isotropic phase, which constitutes a defect core. Moreover, for simplicity, instead of considering a circular core, which is the most common choice, we take it in the shape of the tapering drop's tip. Letting r_c denote the core's size letting r_c, we set $r_c = \varepsilon R_e$, where ε is the dimensionless parameter defined in (6.10), and restrict z to the interval $[-\eta, \eta]$ where η is defined by

$$R(\eta) = R(-\eta) = \varepsilon. \tag{6.33}$$

The integral in (6.31) will hereafter be limited to the interval $[-\eta, \eta]$, so that it will always converge. The extra energy stored in the defects, being approximately constant, will play no role.

We investigate the value of (6.31) evaluated on the family of tactoids parametrized in μ whose profile is given by $R_m = R_m(z)$ in (5.6). Thus, making use of (5.6) in (6.33), η results as a decreasing function of ε whose expression is given by

$$\eta = \frac{2\mu}{\pi}\arccos\left(\frac{\sqrt{3\mu}}{2}\varepsilon\right). \tag{6.34}$$

The admissible value of μ are thus bounded above by

$$\mu_{\max} := 4/(3\varepsilon^2), \tag{6.35}$$

value at which the energy concentration near defects would cause the transition to the isotropic phase of all the droplet. This limiting value of μ is thus forbidden.

Making use of (5.6) and (6.34) in (6.31) (the integral has been limited to the interval $[-\eta, \eta]$), we arrive at

$$\mathcal{F}_{\text{chr}}^{\mu}[R, \beta] = 2 \left\{ -\frac{\pi}{12\mu^2} \left[\sqrt{3\mu}\varepsilon\sqrt{4 - 3\mu\varepsilon^2} - 4\arccos\left(\frac{\sqrt{3\mu}\varepsilon}{2}\right) \right] A[\beta] \right.$$
$$\left. + \varepsilon\frac{\mu^{3/2}}{2\pi}\sqrt{3}\sqrt{4 - 3\mu\varepsilon^2}B[\beta] + \eta\,C[\beta](k_{24}) \right\}, \tag{6.36}$$

where use has been made of the notation:

$$A[\beta] := \int_0^1 \frac{\rho^3}{2}\beta'^2\left(k_1\sin^2\beta + k_3\cos^2\beta\right)\mathrm{d}\rho, \tag{6.37a}$$

$$B[\beta] := \int_0^1 \frac{\rho}{4}\left(\beta' + \frac{1}{\rho}\sin\beta\cos\beta\right)^4\mathrm{d}\rho, \tag{6.37b}$$

$$C[\beta](k_{24}) := \frac{1}{2}\left\{\int_0^1 \left[\rho\beta'^2 + \frac{1}{\rho}\cos^2\beta\sin^2\beta + \frac{k_3}{\rho}\sin^4\beta\right]\mathrm{d}\rho + (1 - 2k_{24}).\right\}, \tag{6.37c}$$

$C[\beta](k_{24})$ is negative whenever $k_{24} > k_{24}^{\infty}$ as inferred in Chapter 5. Following the same argument illustrated in Chapter 5, for any given value of $\mu \in (0, \mu_{\text{max}})$ we numerically find the solution $\beta = \beta_{\text{m}}^{\mu}(\rho)$ of the Euler Lagrange equation for the functional $\mathcal{F}_{\text{chr}}^{\mu}[\beta](k_{24})$ in (6.36) which satisfies the prescribed boundary conditions (5.3) and (5.2). We then evaluate numerically the functional (6.36) on these configurations as a reduced function:

$$\mathcal{F}_{\text{chr}}(\mu, k_{24}) := \mathcal{F}_{\text{chr}}^{\mu}[\beta_{\text{m}}^{\mu}](k_{24}) \tag{6.38}$$

on $\mathrm{T} := \{(\mu, k_{24}) : 0 < \mu < \mu_{\text{max}}, k_{24} > 1\}$. Fig. 6.6 illustrates the graph of (6.38) for $k_1 = k_3 = 30$ and different fixed values of $k_{24} > 1$, where to confine attention to large values of μ we express the dimensionless functional as a function of $\xi := 1/\mu \in (0, 1/\mu_{\text{max}})$:

$$\hat{\mathcal{F}}_{\text{chr}}(\xi, k_{24}) := \mathcal{F}_{\text{chr}}\left(1/\xi, k_{24}\right). \tag{6.39}$$
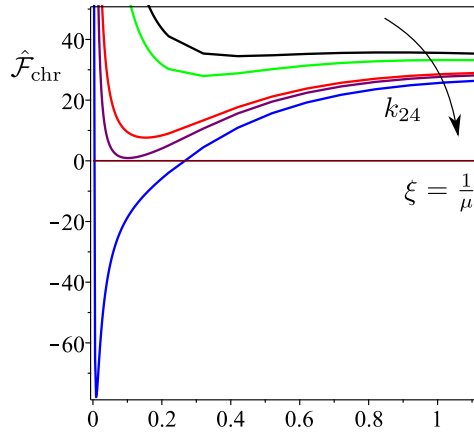

Figure 6.6: Graph of $\hat{\mathcal{F}}_{\text{chr}}(\xi, k_{24})$ in (6.39), corresponding to the dimensionless functional (5.7) evaluated numerically on the equilibrium configurations $\beta_m^{\mu}(\rho)$ and expressed as a function of $\xi = 1/\mu \in (0, \infty)$ for $k_1 = k_3 = 30$ and a sequence of values of $k_{24} > 1$, namely $k_{24} = 1.3, 2.5, k_{24}^{\infty} = 4.86, 5.3, 7.5$ (according to the arrow). For every $k_{24} > 1$, $\hat{\mathcal{F}}_{\text{chr}}$ has a minimum that always occurs at $\mu < \mu_{\text{max}}$.

Whenever $k_{24} > k_{24}^{\infty}$, $\hat{\mathcal{F}}_{\text{chr}}$ is no more unbounded below, but the quartic term gives rise to a minimum in the functional of the energy that always occurs at $\mu < \mu_{max}$.

6.5.1   Conclusions and Future Explorations

Strictly speaking, above we have only proved the non-occurrence of the free-boundary paradox for the special sequence of configurations on which Oseen-Frank's theory failed. In order to effectively cure the paradox, we should be able to guarantee that the new theory attains a minimum on the whole class of configurations parametrized by (R, β) where the even function R describes the profile of the droplet and β is the angle between $\boldsymbol{n}$ in (1.25) and its axis and depends on ρ in (5.1). The subject of a future study will be the attempt to establish the existence of minimizers for the functional $\mathscr{F}_{\mathrm{chr}}$ introduced in (6.6).

Furthermore, a quartic theory raises intriguing regularity issues, such as the following. What type of defects would be compatible with the new theory? What would be the optimal dimension of the singular set? We briefly recall two results proved in [112] and [49] on the space dimension of defects in the minimizers of Oseen-Frank's energy functional. In the one-constant approximation $K_{11} = K_{22} = K_{33}$ and $K_{24} = 0$ any minimizer for the energy functional is an harmonic mapping of $\mathcal{A}(\boldsymbol{n}_0)$, where

$$\mathcal{A}(\boldsymbol{n}_0) := \left\{ \boldsymbol{n} \in H^1\left(\mathscr{B}, \mathbb{S}^2\right) \mid \boldsymbol{n}_0 \text{ is the trace of } \boldsymbol{n} \text{ on } \partial\mathscr{B} \right\}, \qquad (6.40)$$

and is smooth in $\mathscr{B}$ except possibly for a finite number of point defects [112] at points $x_0 \in \mathscr{B}$ with degree $+1$ or -1. In the vicinity of them

$$\boldsymbol{n}(x) \approx \boldsymbol{R}_{x_0} \boldsymbol{n}_{x_0}, \qquad (6.41)$$

where $\boldsymbol{R}_{x_0}$ is an orthogonal tensor depending on x_0, and $\boldsymbol{n}_{x_0}$ is the radial hedgehog located at x_0

$$\boldsymbol{n}_{x_0} = \frac{x - x_0}{|x - x_0|}. \qquad (6.42)$$

For general elastic constants it is not known whether minimizers can only have a finite number of point defects, though by the partial regularity result in [49] the set of singularities has one-dimensional Hausdorff measure zero.

There is no indication as to whether the conclusions about the regularity of energy minimizers reached above apply also when the free-energy density is given in the form (6.6), where an higher order term is added. Surely the noteworthy results of Hardt, Kinderlehrer and Lin [49] are to be revisited and possibly extended to the newly envisaged setting. There could exist defects successfully explained within Oseen-Frank's theory, but incompatibly with the quartic theory. If this is the case, to validate our theory, we have to contrast these defects to the experimentally observed ones.

To posit the quartic free-energy in an achiral scenario, basic invariants under central inversion and complying with the nematic symmetry are built in [128] starting from the measures of distortion $(S, T, \boldsymbol{b}, \boldsymbol{D})$; they are listed below:

$$\left\{ S^2, T^2, B^2, \operatorname{tr} \boldsymbol{D}^2, S\boldsymbol{b} \cdot \boldsymbol{D}\boldsymbol{b}, T\boldsymbol{b} \cdot \boldsymbol{D}(\boldsymbol{n} \times \boldsymbol{b}) \right\}. \qquad (6.43)$$

Their multiplication up to the fourth power of $\nabla \boldsymbol{n}$ forms a general quartic theory. In this case, T^4 is the only genuine quartic contribution needed to accommodate (6.1) as local ground state.

Given the nature of a null Lagrangian of the saddle-splay term (1.5), geometrical confinements with finite principal curvatures inducing degenerate tangential anchoring on the nematic director inhibit the divergence of Oseen-Frank's free-energy to $-\infty$ when $K_{22} < K_{24}$ or $K_{11} < K_{24}$ and turn an ill-posed problem into a problem which admits an energy minimizer. This is the case for CLCs in cylinders first studied within Oseen-Frank's theory by Burylov [10]; the ET configurations (1.42) and (1.43) realize the minimum of the free-energy. Thus, according to

the boundedness below of the quadratic energy and to the perturbative nature of the quartic term in W_{chr} when $a \ll R$, the equilibrium solution for the quartic functional with right- or left-handed chirality closely resemble the ET configuration with the same chirality. However, it has to be noted that the relevant feature which makes the difference between the two theories in rationalizing the experimental data is the value of the double twist along the axis of the cylinder; this cannot be detected experimentally.

On the other hand, as we learned in Chapter 5, problems where the region in space is allowed to vary may accommodate an ET configuration, but the associated quadratic energy is not bounded from below. An higher order term can be used to overcome the deficiencies of Oseen-Frank's free-energy density for CLCs when the saddle-splay constant exceeds the twist constant.

We still lack the solution of this free-boundary problem within the quartic theory. On the other hand, the corrections to Oseen-Frank's formula when the boundary conditions prevent the onset of pathologies are negligible in all practical situations. To really see the difference between the two theories, we must conceive an experimentally attainable situation where the violation of the inequality $K_{22} > K_{24}$ entails the existence of minimizers only within the new theory, while those for Oseen-Frank's functional fail to exist.

Bibliography

[1] D. G. A. L. Aarts, M. Schmidt, and H. N. W. Lekkerkerker. Direct visual observation of thermal capillary waves. *Science*, 304(5672):847–850, 2004.

[2] D. A. Balzarini, D. A. Dunmur, and P. Palffy-Muhoray. High voltage birefringence measurements of elastic constants. *Mol. Cryst. Liq. Cryst.*, 102(2):35–41, 1984.

[3] G. Barbero and I. Lelidis. Fourth-order nematic elasticity and modulated nematic phases: a poor man's approach. *Liq. Cryst.*, 46(4):535–542, 2019.

[4] F. C. Bawden, N. W. Pirie, J. D. Bernal, and I. Fankuchen. Liquid crystalline substances from virus-infected plants. *Nature*, 138:1051–1052, 1936.

[5] J. D. Bernal and I. Fankuchen. X-ray and crystallographic studies of plant virus preparations: I. Introduction and preparation of specimens. II. Modes of aggregation of the virus particles. *J. Gen. Physiol.*, 25:111–146, 1941.

[6] C. P. Brangwynne, C. R. Eckmann, D. S. Courson, A. Rybarska, C. Hoege, J. Gharakhani, F. Jülicher, and A. A. Hyman. Germline p granules are liquid droplets that localize by controlled dissolution/condensation. *Science*, 324(5935):1729–1732, 2009.

[7] H. Brezis. *Functional Analysis, Sobolev Spaces and Partial Differential Equations*. Universitext. Springer New York, 2010.

[8] J. Brugués and D. Needleman. Physical basis of spindle self-organization. *Proceedings of the National Academy of Sciences*, 111(52):18496–18500, 2014.

[9] J. D. Bunning, T. E. Faber, and P. L. Sherrell. The Frank constants of nematic 5CB at atmospheric pressure. *J. de Phys.*, 42(8):1175–1182, 1981.

[10] S. Burylov. Equilibrium configuration of a nematic liquid crystal confined to a cylindrical cavity. *J. Exp. Theor. Phys*, 85(1):873–886, 1997.

[11] S. Candau, P. L. Roy, and F. Debeauvais. Magnetic field effects in nematic and cholesteric droplets suspended in a isotropic liquid. *Mol. Cryst. Liq. Cryst.*, 23:283–297, 1973.

[12] F. Chami and M. R. Wilson. Molecular order in a chromonic liquid crystal: A molecular simulation study of the anionic azo dye sunset yellow. *J. Am. Chem. Soc.*, 132(22):7794–7802, 2010.

[13] S. Chandrasekhar. Surface tension of liquid crystals. *Mol. Cryst.*, 2(1–2):71–80, 1966.

[14] W. Chen and D. G. Gray. Interfacial tension between isotropic and anisotropic phases of a suspension of rodlike particles. *Langmuir*, 18:633–637, 2002.

[15] W. Chen, T. Sato, and A. Teramoto. Measurement of the interfacial tension between coexisting isotropic and nematic phases of a lyotropic polymer liquid crystal. *Macromolecules*, 29:4283–4286, 1996.

[16] W. Chen, T. Sato, and A. Teramoto. Interfacial tension between coexisting isotropic and nematic phases for a lyotropic polymer liquid crystal: Poly(n-hexyl isocyanate) solutions. *Macromolecules*, 31:6506–6510, 1998.

[17] W. Chen, T. Sato, and A. Teramoto. Interfacial tension between coexisting isotropic and cholesteric phases for aqueous solutions of Schizophyllan. *Macromolecules*, 32:1549–1553, 1999.

[18] P. J. Collings, P. van der Asdonk, A. Martinez, L. Tortora, and P. H. J. Kouwer. Anchoring strength measurements of a lyotropic chromonic liquid crystal on rubbed polyimide surfaces. *Liq. Cryst.*, 44(7):1165–1172, 2017.

[19] Z. S. Davidson, L. Kang, J. Jeong, T. Still, P. J. Collings, T. C. Lubensky, and A. G. Yodh. Chiral structures and defects of lyotropic chromonic liquid crystals induced by saddle-splay elasticity. *Physical Review E*, 91(5), May 2015.

[20] P. G. de Gennes and J. Prost. *The Physics of Liquid Crystals*, volume 83 of *The International Series of Monographs on Physics*. Clarendon Press, Oxford, 2nd edition, 1993.

[21] G. De Matteis, L. Martina, C. Naya, and V. Turco. Nonuniform localized distortions in generalized elasticity for liquid crystals. *Phys. Rev. E*, 102:042705, 2020.

[22] B. Demé, D. Hess, M. Tristl, L. Lee, and E. Sackmann. Binding of actin filaments to charged lipid monolayers: Film balance experiments combined with neutron reflectivity. *Eur. Phys. J.*, 2:125–136, 2000.

[23] A. J. Dickinson, N. D. LaRacuente, C. B. McKitterick, and P. J. Collings. Aggregate structure and free energy changes in chromonic liquid crystals. *Mol. Cryst. Liq. Cryst.*, 509(1):751–762, 2009.

[24] I. Dierking and A. Martins Figueiredo Neto. Novel trends in lyotropic liquid crystals. *Crystals*, 10(7), 2020.

[25] C. F. Dietrich, P. J. Collings, T. Sottmann, P. Rudquist, and F. Giesselmann. Extremely small twist elastic constants in lyotropic nematic liquid crystals. *Proc. Natl. Acad. Sci. USA*, 117(44):27238–27244, 2020.

[26] C. F. Dietrich, P. J. Collings, T. Sottmann, P. Rudquist, and F. Giesselmann. Extremely small twist elastic constants in lyotropic nematic liquid crystals. *Proc. Natl. Acad. Sci. USA*, 117(44):27238–27244, 2020.

[27] E. Dubois-Violette and O. Parodi. Émulsions nématiques. Effects de champ magnétiques et effects piézoélectriques. *J. Phys. Colloq.*, 30:C4.57–C4.64, 1969.

[28] S. Elbaum-Garfinkle, Y. Kim, K. Szczepaniak, C. C.-H. Chen, C. R. Eckmann, S. Myong, and C. P. Brangwynne. The disordered p granule protein laf-1 drives phase separation into droplets with tunable viscosity and dynamics. *Proceedings of the National Academy of Sciences*, 112(23):7189–7194, 2015.

[29] J. L. Ericksen. Nilpotent energies in liquid crystal theory. *Arch. Rational Mech. Anal.*, 10(1):189–196, 1962.

[30] J. L. Ericksen. Inequalities in liquid crystal theory. *Phys. Fluids*, 9(6):1205–1207, 1966.

[31] J. L. Ericksen. Liquid crystals with variable degree of orientations. *Archive for Rational Mechanics and Analysis*, 113(2):97–120, 1991.

[32] J. Eun, S.-J. Kim, and J. Jeong. Effects of chiral dopants on double-twist configurations of lyotropic chromonic liquid crystals in a cylindrical cavity. *Phys. Rev. E*, 100:012702, Jul 2019.

[33] S. Faetti. Anchoring at the interface between a nematic liquid crystal and an isotropic substrate. *Mol. cryst. liq. cryst. inc. nonlinear opt.*, 179(1):217–231, 1990.

[34] S. Faetti and V. Palleschi. Measurements of the interfacial tension between nematic and isotropic phase of some cyanobiphenyls. *J. Chem. Phys.*, 81(12):6254–6258, 1984.

[35] S. Faetti and V. Palleschi. Nematic-isotropic interface of some members of the homologous series of 4-cyano-4′-(n-alkyl)biphenyl liquid crystals. *Phys. Rev. A*, 30:3241–3251, Dec 1984.

[36] T. P. Fraccia and T. Z. Jia. Liquid crystal coacervates composed of short double-stranded dna and cationic peptides. *ACS Nano*, 14(11):15071–15082, 2020. PMID: 32852935.

[37] S. Fraden, A. J. Hurd, R. B. Meyer, M. Cahoon, and D. L. D. Caspar. Magnetic-field-induced alignment and instabilities in ordered colloids of tobacco mosaic virus. *J. Phys. (Paris) Colloq.*, 46(C3):C3/85–C3/113, 1985.

[38] F. C. Frank. On the theory of liquid crystals. *Discuss. Faraday Soc.*, 25:19–28, 1958.

[39] Friedel, G. Les états mésomorphes de la matière. *Ann. Phys.*, 9(18):273–474, 1922.

[40] G. Gaeta and E. G. Virga. The symmetries of octupolar tensors, 2018.

[41] Gaeta, Giuseppe and Virga, Epifanio G. Octupolar order in three dimensions. *Eur. Phys. J. E*, 39(11):113, 2016.

[42] F. Gittes, B. Mickey, J. Nettleton, and J. Howard. Flexural rigidity of microtubules and actin filaments measured from thermal fluctuations in shape. *J. Cell Biol.*, 120:923–934, 1993.

[43] M. H. Godinho. When the smallest details count. *Science*, 369(6506):918–919, 2020.

[44] D. Golovaty. A model problem for nematic-isotropic transitions with highly disparate elastic constants. *Arch. Ration. Mech. Anal.*, 236(3):1739–1805, 2020.

[45] D. Golovaty, Y.-K. Kim, O. D. Lavrentovich, M. Novack, and P. Sternberg. Phase transitions in nematics: textures with tactoids and disclinations. *Math. Model. Nat. Phenom.*, 15(8):1–21, 2020.

[46] D. Golovaty, M. Novack, and P. Stenberg. A novel landau-de gennes model with quartic elastic terms. *Eur. J. Appl. Math.*, 32(1):177–198, 2021.

[47] R. Guenther and J. Lee. *Sturm-Liouville Problems. Theory and Numerical Implementation.* Monographs and Research Notes in Mathematics. CRC Press, Boca Raton, FL, 2019.

[48] T. Guo, X. Zheng, and P. Palffy-Muhoray. Surface anchoring energy of cholesteric liquid crystals. *Liq. Cryst.*, 47(4):477–480, 2020.

[49] R. Hardt, D. Kinderlehrer, and F. H. Lin. Stable defects of minimizers of constrained variational principles. *Annales de l'I.H.P. Analyse non linéaire*, 5(4):297–322.

[50] A. J. Hurd, S. Fraden, F. Lonberg, and R. B. Meyer. Field-induced transient periodic structures in nematic liquid crystals: the splay Frederiks transition. *J. Phys. France*, 46:905–917, 1985.

[51] K. Ichimura, Y. Akita, H. Akiyama, K. Kudo, and Y. Hayashi. Photoreactivity of polymers with regioisomeric cinnamate side chains and their ability to regulate liquid crystal alignment. *Macromolecules*, 30(4):903–911, 1997.

[52] H. Isambert, P. Venier, A. C. Maggs, A. Fattoum, R. Kassab, D. Pantaloni, and M.-F. Carlier. Flexibility of actin filaments derived from thermal fluctuations: Effect of bound nucleotide, phalloidin, and muscle regulatory proteins. *J. Biol. Chem*, 270(19):11437–11444, 1995.

[53] S. Itou, K. Tozaki, and N. Komatsu. Lyotropic liquid crystalline structures of synthetic polypeptide 2. Measurements of elastic constants and coupling constants of Poly(γ-Benzyl L-Glutamate) solutions by the Freedericksz transition. *Jpn. J. Appl. Phys.*, 30(6):1230–1234, 1991.

[54] A. Javadi, J. Eun, and J. Jeong. Cylindrical nematic liquid crystal shell: effect of saddle-splay elasticity. *Soft Matter*, 14:9005–9011, 2018.

[55] J. Jeong, Z. S. Davidson, P. J. Collings, T. C. Lubensky, and A. G. Yodh. Chiral symmetry breaking and surface faceting in chromonic liquid crystal droplets with giant elastic anisotropy. *Proc. Natl. Acad. Sci. USA*, 111(5):1742–1747, 2014.

[56] J. Jeong, L. Kang, Z. S. Davidson, P. J. Collings, T. C. Lubensky, and A. G. Yodh. Chiral structures from achiral liquid crystals in cylindrical capillaries. *Proc. Natl. Acad. Sci. USA*, 112(15):E1837–E1844, 2015.

[57] M. Kahlweit and W. Ostner. An estimation of the interfacial tension between the nematic and isotropic states of a liquid crystal. *Chem. Phys. Lett.*, 18(4):589–591, 1973.

[58] P. P. Karat and N. V. Madhusudana. Elastic and optical properties of some 4'-n-Alkyl-4-Cyanobiphenyls. *Mol. Cryst. Liq. Cryst.*, 36(1-2):51–64, 1976.

[59] P. P. Karat and N. V. Madhusudana. Elasticity and orientational order in some 4'-n-Alkyl-4-Cyanobiphenyls: Part II. *Mol. Cryst. Liq. Cryst.*, 40(1):239–245, 1977.

[60] A. V. Kaznacheev, M. M. Bogdanov, and S. A.Taraskin. The nature of prolate shape of tactoids in lyotropic inorganic liquid crystals. *J. Exp. Theor. Phys.*, 95:57–63, 2002.

[61] A. V. Kaznacheev, M. M. Bogdanov, and A. S. Sonin. The influence of anchoring energy on the prolate shape of tactoids in lyotropic inorganic liquid crystals. *J. Exp. Theor. Phys.*, 97:1159–1167, 2003.

[62] J. Y. Kim, K. Nayani, H. S. Jeong, H.-J. Jeon, H.-W. Yoo, E. H. Lee, J. O. Park, M. Srinivasarao, and H.-T. Jung. Macroscopic alignment of chromonic liquid crystals using patterned substrates. *Phys. Chem. Chem. Phys.*, 18:10362–10366, 2016.

[63] Y.-K. Kim, S. V. Shiyanovskii, and O. D. Lavrentovich. Morphogenesis of defects and tactoids during isotropic-nematic phase transition in self-assembled lyotropic chromonic liquid crystals. *J. Phys.: Condens. Matter*, 25(40):404202, 2013.

[64] D. Kinderlehrer and B. Ou. Second variation of liquid crystal energy at x/|x|. *Proceedings: Mathematical and Physical Sciences*, 437(1900):475–487, 1992.

[65] M. Kleman and O. D. Lavrentovich. *Soft Matter Physics: An Introduction*. Partially Ordered Systems (Springer). Springer, Verlag, New York, 2003.

[66] V. Koning, B. C. van Zuiden, R. D. Kamien, and V. Vitelli. Saddle-splay screening and chiral symmetry breaking in toroidal nematics. *Soft Matter*, 10:4192–4198, 2014.

[67] M. V. Kurik and D. Lavrentovich. Negative-positive monople transitions in cholesteric liquid crystals. *JETP Lett.*, 35:444–447, 1982. Pis'ma Zh. Eksp. Teor. Fiz. **35**(1982), 362–365.

[68] D. Langevin and M. A. Bouchiat. Molecular order and surface tension for the nematic-isotropic interface of MBBA, deduced from light reflectivity and light scattering measurements. *Mol. Cryst. Liq. Cryst.*, 22(3–4):317–331, 1973.

[69] S. Lee and R. B. Meyer. Computations of the phase equilibrium, elastic constants, and viscosities of a hard-rod nematic liquid crystal. *J. Chem. Phys.*, 84(6):3443–3448, 1986.

[70] S.-D. Lee and R. B. Meyer. Crossover behavior of the elastic coefficients and viscosities of a polymer nematic liquid crystal. *Phys. Rev. Lett.*, 61:2217–2220, 1988.

[71] H. J. Li and C. C. Yeh. Inequalities for a function involving its integral and derivative. *Proceedings of the Royal Society of Edinburgh: Section A Mathematics*, 125(1):133, 1995.

[72] J. Lydon. Chromonic liquid crystal phases. *Current Opinion in Colloid & Interface Science*, 3(5):458–466, 1998.

[73] J. Lydon. Chromonic review. *J. Mater. Chem.*, 20:10071–10099, 2010.

[74] J. Lydon. Chromonic liquid crystalline phases. *Liq. Cryst.*, 38(11–12):1663–1681, 2011.

[75] T. Machon and G. P. Alexander. Umbilic lines in orientational order. *Phys. Rev. X*, 6:011033, Mar 2016.

[76] P. Mariani, F. Spinozzi, F. Federiconi, H. Amenitsch, L. Spindler, and I. Drevensek-Olenik. Small angle X-ray scattering analysis of deoxyguanosine 5'-monophosphate self-assembing in solution: Nucleation and growth of G-quadruplexes. *J. Phys. Chem. B*, 113(22):7934–7944, 2009.

[77] A. W. Marris. Universal solutions in the hydrostatics of nematic liquid crystals. *Arch. Rational Mech. Anal.*, 67:251–303, 1978.

[78] C. Maze. Determination of nematic liquid crystal elastic and dielectric properties from the shape of a capacitance-voltage curve. *Mol. Cryst. Liq. Cryst.*, 48(3-4):273–287, 1978.

[79] N. D. Mermin. The topological theory of defects in ordered media. *Rev. Mod. Phys.*, 51:591–648, Jul 1979.

[80] R. Mezzenga, J.-M. Jung, and J. Adamcik. Effects of charge double layer and colloidal aggregation on the isotropic-nematic transition of protein fibers in water. *Langmuir*, 26(13):10401–10405, 2010. PMID: 20509704.

[81] S. W. Morris, P. Palffy-Muhoray, and D. A. Balzarini. Measurements of the bend and splay elastic constants of octyl-cyanobiphenyl. *Mol. Cryst. Liq. Cryst.*, 139(3-4):263–280, 1986.

[82] P. C. Mushenheim, R. R. Trivedi, D. Weibel, and N. Abbott. Using liquid crystals to reveal how mechanical anisotropy changes interfacial behaviors of motile bacteria. *Biophysical journal*, 107 1:255–65, 2014.

[83] V. Naggiar. Phénomènes d'orientation dans les liquides nématiques. Une nouvelle méthode de mesure de la tension superficielle applicable à ces liquides. *Ann. Phys. (France)*, 11:5–55, 1943.

[84] M. Nakata, G. Zanchetta, B. D. Chapman, C. D. Jones, J. O. Cross, R. Pindak, T. Bellini, and N. A. Clark. End-to-end stacking and liquid crystal condensation of 6- to 20-base pair DNA duplexes. *Science*, 318(5854):1276–1279, 2007.

[85] Y. A. Nastishin, H. Liu, T. Schneider, V. Nazarenko, R. Vasyuta, S. V. Shiyanovskii, and O. D. Lavrentovich. Optical characterization of the nematic lyotropic chromonic liquid crystals: Light absorption, birefringence, and scalar order parameter. *Phys. Rev. E*, 72:041711, Oct 2005.

[86] K. Nayani, R. Chang, J. Fu, P. W. Ellis, A. Fernandez-Nieves, J. O. Park, and M. Srinivasarao. Spontaneous emergence of chirality in achiral lyotropic chromonic liquid crystals confined to cylinders. *Nature Communications*, 6(1), 8 2015.

[87] J. Nehring and A. Saupe. On the elastic theory of uniaxial liquid crystals. *The Journal of Chemical Physics*, 54(1):337–343, 1971.

[88] J. Nehring and A. Saupe. Calculation of the elastic constants of nematic liquid crystals. *The Journal of Chemical Physics*, 56(11):5527–5528, 1972.

[89] P. W. Oakes, J. Viamontes, and J. X. Tang. Growth of tactoidal droplets during the first-order isotropic to nematic phase transition of f-actin. *Phys. Rev. E*, 75:061902, Jun 2007.

[90] T. Odijk. Elastic constants of nematic solutions of rod-like and semi-flexible polymers. *Liq. Cryst.*, 1(6):553–559, 1986.

[91] C. S. Ogilvy. *Excursions in geometry*. Taylor and Francis, Mineola, NY, USA, 1990. (Unabridged and corrected republication of the work originally published by Oxford University Press, New York).

[92] T. Ogolla and P. J. Collings. Assembly structure and free energy change of a chromonic liquid crystal formed by a perylene dye. *Liq. Cryst.*, 46(10):1551–1557, 2019.

[93] T. Ogolla, R. S. Paley, and P. J. Collings. Temperature dependence of the pitch in chiral lyotropic chromonic liquid crystals. *Soft Matter*, 15:109–115, 2019.

[94] K. Okano, N. Matsuura, and S. Kobayashi. Alignment of a liquid crystal on an anisotropic substrate. *Japanese Journal of Applied Physics*, 21(Part 2, No. 2):L109–L110, 1982.

[95] L. Onsager. The effects of shape on the interaction of colloidal particles. *Ann. N. Y. Acad. Sci.*, 51(4):627–659, 1949.

[96] Orsay Liquid Crystal Group. Recent experimental investigations in nematic and cholesteric mesophases. In J. F. Johnson and R. S. Porter, editors, *Liquid Crystals and Ordered Fluids: Proceedings of an American Chemical Society Symposium on Ordered Fluids and Liquid Crystals, held in New York City, September 10-12, 1969*, pages 447–453. Plenum Press, New York, 1970.

[97] C. W. Oseen. The theory of liquid crystals. *Trans. Faraday Soc.*, 29(4):883–899, 1933.

[98] E. Paineau, A. M. Philippe, K. Antonova, I. Bihannic, P. Davidson, I. Dozov, J. C. P. Gabriel, M. Impéror-Clerc, P. Levitz, F. Meneau, and L. J. Michot. Liquid–crystalline properties of aqueous suspensions of natural clay nanosheets. *Liq. Cryst. Rev.*, 1(2):110–126, 2013.

[99] S. Paparini and E. G. Virga. Nematic tactoid population. *Phys. Rev. E*, 103:022707, 2021.

[100] S. Paparini and E. G. Virga. Shape bistability in 2d chromonic droplets. *J. Phys. Condens Matter*, 33(49):495101, 2021.

[101] J. Parsons. A molecular theory of surface tension in nematic liquid crystals. *J. Phys. France*, 37(10):1187–1195, 1976.

[102] A. Pedrini and E. G. Virga. Instability of toroidal nematics. *Liq. Cryst.*, 45(13-15):2054–2064, 2018.

[103] A. Pedrini and E. G. Virga. Liquid crystal distortions revealed by an octupolar tensor. *Phys. Rev. E*, 101:012703, Jan 2020.

[104] C. Peng and O. D. Lavrentovich. Chirality amplification and detection by tactoids of lyotropic chromonic liquid crystals. *Soft Matter*, 11:7221–7446, 2015.

[105] P. Prinsen and P. van der Schoot. Shape and director-field transformation of tactoids. *Phys. Rev. E*, 68:021701, Aug 2003.

[106] P. Prinsen and P. van der Schoot. Continuous director-field transformation of nematic tactoids. *Euro. Phys. J. E*, 13:35–41, 2004.

[107] P. Prinsen and P. van der Schoot. Parity breaking in nematic tactoids. *J. P.: Condens. Matter*, 16:8835–8850, 2004.

[108] N. Puech, E. Grelet, P. Poulin, C. Blanc, and P. van der Schoot. Nematic droplets in aqueous dispersions of carbon nanotubes. *Phys. Rev. E*, 82:020702, Aug 2010.

[109] A. Rapini and M. Papoular. Distorsion d'une lamelle mématique sous champ magnétique conditions d'ancrage aux parois. *J. Phys. Colloq.*, 30(C4):C4.54–C4.56, 1969.

[110] A. Saupe. Die Biegungselastizität der nematischen Phase von Azoxyanisol. *Z. Naturforschg.*, 15a:815–822, 1960.

[111] A. Saupe. Temperaturabhängigkeit und Größe der Deformationskonstanten nematischer Flüssigkeiten. *Z. Naturforschg.*, 15a:810–814, 1960.

[112] R. M. Schoen and K. K. Uhlenbeck. Boundary regularity and the dirichlet problem for harmonic maps. *Journal of Differential Geometry*, 18:253–268, 1983.

[113] W. M. Schwartz and H. W. Moseley. The surface tension of liquid crystals. *J. Phys. Chem.*, 51(3):826–837, 1947.

[114] J. V. Selinger. Interpretation of saddle-splay and the Oseen-Frank free energy in liquid crystals. *Liq. Cryst. Rev.*, 6(2):129–142, 2018.

[115] J. V. Selinger. Director deformations, geometric frustration, and modulated phases in liquid crystals. *Annual Review of Condensed Matter Physics*, 13(1):null, 2022.

[116] K. Skarp, S. T. Lagerwall, and B. Stebler. Measurements of hydrodynamic parameters for nematic 5CB. *Mol. Cryst. Liq. Cryst.*, 60(3):215–236, 1980.

[117] A. S. Sonin. Inorganic lyotropic liquid crystals. *J. Mater. Chem.*, 8:2557–2574, 1998.

[118] W. M. Stanley. Isolation of a crystalline protein possessing the properties of tobacco-mosaic virus. *Science*, 81(2113):644–645, 1935.

[119] A. Stroobants, H. N. W. Lekkerkerker, and T. Odijk. Effect of electrostatic interaction on the liquid crystal phase transition in solutions of rodlike polyelectrolytes. *Macromolecules*, 19(8):2232–2238, 1986.

[120] S.-W. Tam-Chang and L. Huang. Chromonic liquid crystals: properties and applications as functional materials. *Chem. Commun.*, 44:1957–1967, 2008.

[121] V. G. Taratuta, A. J. Hurd, and R. B. Meyer. Light-scattering study of a polymer nematic liquid crystal. *Phys. Rev. Lett.*, 55:246–249, 1985.

[122] V. G. Taratuta, F. Lonberg, and R. B. Meyer. Anisotropic mechanical properties of a polymer nematic liquid crystal. *Phys. Rev. A*, 37:1831–1834, 1988.

[123] L. Tortora and O. D. Lavrentovich. Chiral symmetry breaking by spatial confinement in tactoidal droplets of lyotropic chromonic liquid crystals. *Proc. Natl. Acad. Sci. USA*, 108(13):5163–5168, 2011.

[124] A. A. Verhoeff, I. A. Bakelaar, R. H. J. Otten, P. van der Schoot, and H. N. W. Lekkerkerker. Tactoids of plate-like particles: Size, shape, and director field. *Langmuir*, 27(1):116–125, 2011.

[125] J. Viamontes, S. Narayanan, A. R. Sandy, and J. X. Tang. Orientational order parameter of the nematic liquid crystalline phase of f-actin. *Phys. Rev. E*, 73:061901, 2006.

[126] E. G. Virga. Drops of nematic liquid crystals. *Arch. Rational Mech. Anal.*, 107:371–390, 1989. Reprinted in [**?**].

[127] E. G. Virga. *Variational Theories for Liquid Crystals*, volume 8 of *Applied Mathematics and Mathematical Computation*. Chapman & Hall, London, 1994.

[128] E. G. Virga. Uniform distortions and generalized elasticity of liquid crystals. *Phys. Rev. E*, 100:052701, 2019.

[129] G. E. Volovik and D. Lavrentovich. Topological dynamics of defects: boojums in nematic drops. *Sov. Phys. JETP*, 58:1159–1166, 1983. Zh. Eksp. Teor. Fiz. **85**(1983), 1997–2010.

[130] J. H. L. Watson, W. Heller, and W. Wojtowicz. Comparative electron and light microscopic investigations of tactoid structures in V_2O_5-sols. *Science*, 109(2829):274–278, 1949.

[131] K. L. Weirich, S. Banerjee, K. Dasbiswas, T. A. Witten, S. Vaikuntanathan, and M. L. Gardel. Liquid behavior of cross-linked actin bundles. *PNAS*, 114(9):2131–2136, 2017.

[132] R. D. Williams. Nematic liquid crystal droplets. Technical Report RAL-85-028, Rutherford Appleton Laboratory, Chilton, UK, 1985. `https://lib-extopc.kek.jp/preprints/PDF/1986/8606/8606437.pdf`.

[133] R. D. Williams. Two transitions in tangentially anchored nematic droplets. *J. Phys. A: Math. Gen.*, 19:3211–3222, 1986.

[134] D. C. Wright and N. D. Mermin. Crystalline liquids: the blue phases. *Rev. Mod. Phys.*, 61:385–432, Apr 1989.

[135] G. Wulff. Zur Frage der Geschwindigkeit des Wachsthums und der Auflösung der Kristallflächen. *Z. Kristallographie und Mineralogie*, 34:449–530, 1901.

[136] Y. Yi and N. A. Clark. Orientation of chromonic liquid crystals by topographic linear channels: multi-stable alignment and tactoid structure. *Liq. Cryst.*, 40(12):1736–1747, 2013.

[137] H. Yokoyama, S. Kobayashi, and H. Kamei. Boundary dependence of the formation of new phase at the isotropic-nematic transition. *Mol. Cryst. Liq. Cryst.*, 99(1):39–52, 1983.

[138] G. Zanchetta, M. Nakata, M. Buscaglia, T. Bellini, and N. A. Clark. Phase separation and liquid crystallization of complementary sequences in mixtures of nanodna oligomers. *Proc. Natl. Acad. Sci. USA*, 105(4):1111–1117, 2008.

[139] S. Zhou. *Lyotropic Chromonic Liquid Crystals*. Springer Theses. Springer, Cham, Switzerland, 2017.

[140] S. Zhou, A. J. Cervenka, and O. D. Lavrentovich. Ionic-content dependence of viscoelasticity of the lyotropic chromonic liquid crystal sunset yellow. *Phys. Rev. E*, 90:042505, 2014.

[141] S. Zhou, Y. A. Nastishin, M. M. Omelchenko, L. Tortora, V. G. Nazarenko, O. P. Boiko, T. Ostapenko, T. Hu, C. C. Almasan, S. N. Sprunt, J. T. Gleeson, and O. D. Lavrentovich. Elasticity of lyotropic chromonic liquid crystals probed by director reorientation in a magnetic field. *Phys. Rev. Lett.*, 109:037801, Jul 2012.

[142] S. Zhou, K. Neupane, Y. A. Nastishin, A. R. Baldwin, S. V. Shiyanovskii, O. D. Lavrentovich, and S. Sprunt. Elasticity, viscosity, and orientational fluctuations of a lyotropic chromonic nematic liquid crystal disodium cromoglycate. *Soft Matter*, 10:6571–6581, 2014.

[143] H. Zocher. Über freiwillige Strukturbildung in Solen. (Eine neue Art anisotrop flüssiger Medien.). *Z. anorg. allg. Chem.*, 147(1):91–110, 1925.

[144] H. Zocher. The effect of a magnetic field on the nematic state. *Trans. Faraday Soc.*, 29:945–957, 1933.

[145] H. Zocher. Taktosole und Mesophasen. *Kolloid-Z.*, 139:81–85, 1954.

[146] H. Zocher. II. Nematic and smectic phases of higher order. *Mol. Cryst.*, 7(1):177–180, 1969.

[147] H. Zocher and K. Jacobsohn. Über Taktosole. *Kolloidchem. Beihefte*, 28:167–206, 1929.

[148] H. Zocher and C. Török. Neuere Beiträge zur Kenntnis der Taktosole. *Kolloid-Zeit.*, 170:140–144, 1960.